

University of Groningen

Quantitative diffusion-weighted imaging in breast and liver tissue

Dijkstra, Hildebrand

IMPORTANT NOTE: You are advised to consult the publisher's version (publisher's PDF) if you wish to cite from it. Please check the document version below.

Document Version

Publisher's PDF, also known as Version of record

Publication date:

2016

[Link to publication in University of Groningen/UMCG research database](#)

Citation for published version (APA):

Dijkstra, H. (2016). *Quantitative diffusion-weighted imaging in breast and liver tissue*. Rijksuniversiteit Groningen.

Copyright

Other than for strictly personal use, it is not permitted to download or to forward/distribute the text or part of it without the consent of the author(s) and/or copyright holder(s), unless the work is under an open content license (like Creative Commons).

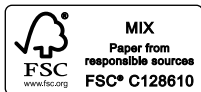
The publication may also be distributed here under the terms of Article 25fa of the Dutch Copyright Act, indicated by the "Taverne" license. More information can be found on the University of Groningen website: <https://www.rug.nl/library/open-access/self-archiving-pure/taverne-amendment>.

Take-down policy

If you believe that this document breaches copyright please contact us providing details, and we will remove access to the work immediately and investigate your claim.

Downloaded from the University of Groningen/UMCG research database (Pure): <http://www.rug.nl/research/portal>. For technical reasons the number of authors shown on this cover page is limited to 10 maximum.

Quantitative Diffusion-Weighted Imaging in Breast and Liver Tissue



Hildebrand Dijkstra
Quantitative Diffusion-Weighted Imaging in Breast and Liver Tissue
PhD thesis University of Groningen, with a summary in Dutch

ISBN: 978-90-367-9097-0 (printed version)
ISBN: 978-90-367-9096-3 (electronic version)

Copyright © Hildebrand Dijkstra

No part of this thesis may be reproduced, stored, or transmitted in any form or by any means, without permission from the author.

Cover design and layout: Hildebrand Dijkstra

Photo on the cover was modified: CC Image courtesy of andrew_annemarie on Flickr

Printed by: Ipskamp Drukkers Enschede B.V.

The publication of this thesis was financially supported by:
University of Groningen, University Medical Center Groningen, Department of Radiology,
Guerbet Nederland BV, Bracco Imaging Europe BV, Center for Medical Imaging - NEN.



rijksuniversiteit
 groningen

Quantitative Diffusion-Weighted Imaging in Breast and Liver Tissue

Proefschrift

ter verkrijging van de graad van doctor aan de
Rijksuniversiteit Groningen
op gezag van de
rector magnificus prof. dr. E. Sterken
en volgens besluit van het College voor Promoties.

De openbare verdediging zal plaatsvinden op
woensdag 2 november 2016 om 16.15 uur

door

Hildebrand Dijkstra

geboren op 12 maart 1983
te Smalingerland

Promotor

Prof. dr. M. Oudkerk

Copromotor

Dr. P.E. Sijens

Beoordelingscommissie

Prof. dr. G.A.P. Hospers

Prof. dr. J. Stoker

Prof. dr. T. Leiner



voor Gonda en Kirsten

Er is niets nieuws onder de zon. Is er iets, waarvan men zegt: „Kijk iets nieuws” - dan is het er sinds langvervlogen tijden al geweest.

-Prediker-

Contents

I	Introduction	1
1	General Introduction	3
II	Liver	29
2	Effects of microperfusion in hepatic diffusion-weighted imaging	31
3	Assessment of the link between quantitative biexponential DWI and CE-MRI in the liver	51
4	Clinical implications of non-steatotic hepatic fat fractions on quantitative DWI of the liver	71
5	Diminished liver microperfusion in Fontan patients: a biexponential DWI study	93
III	Breast	111
6	Effects of b-values and pre-admission of contrast media on the diagnostic accuracy of 1.5T breast DWI: a systematic review and meta-analysis	113
7	Semi-automated quantitative IVIM analysis and its implementation in breast DWI	139
8	Quantitative DWI implemented after DCE-MRI yields increased specificity for BI-RADS 3 and 4 breast lesions	163
IV	Appendix	181
A	Summary	183
B	Nederlandse Samenvatting	191
C	Dankwoord	199
D	Bibliography	203
E	Curriculum Vitae	207

Abbreviations and acronyms

ACC	Accuracy
ADC	Apparent Diffusion Coefficient
ALP	Arterial Liver Perfusion
ALT	Alanine aminotransferase
AST	Aspartate aminotransferase
AUC	Area Under the Curve
b	Factor summarizing the setup of the gradients in DWI
BIRADS	Breast Imaging-Reporting and Data System
BMI	Body Mass Index
BOPTA	Gadobenated dimeglumine
CE-	Contrast-Enhanced
CI	Confidence Interval
DCE-	Dynamic Contrast-Enhanced
DWI	Diffusion-Weighted Imaging
D_{fast}	Microperfusion
D_{slow}	Molecular diffusion
DSC	Dice Similarity Coefficient
EDV	End Diastolic Volume
EF	Ejection Fraction
EPI	Echo-Planar Imaging
FETS	Fast Exchange Two-State
FA	Flip Angle
F_{fast}	Fraction of microperfusion
F_{slow}	Fraction of molecular diffusion
Fib-4	Fibrosis-4 score
Fo	Optimal Fraction
FN	False Negative
FP	False Positive
FNH	Focal Nodular Hyperplasia
G	Gradient strength
Gd-DTPA	Gadopentate dimeglumine
Gd-DOTA	Gadoterate meglumine
Gd-EOB-DTPA	Gadoxetate disodium

GRAPPA	GeneRalised Auto-calibrating Partially Parallel Acquisition
HCC	HepatoCellular Carcinoma
HFF	Hepatic Fat Fraction
HPI	Hepatic Perfusion Index
IDC	Invasive Ductal Carcinoma
ILC	Invasive Lobular Carcinoma
IP	In-Phase
IRB	Institutional Review Board
IVIM	Intravoxel Incoherent Motion Model
MELDIXI	Model for Endstage Liver Disease eXcluding the International normalised ratio
MRI	Magnetic Resonance Imaging
NAFLD	Non-Alcoholic Fatty Liver Disease
NMR	Nuclear Magnetic Resonance
NPV	Negative Predictive Value
OP	Out-of-Phase
PT	Prothrombin Time
QUADAS	Quality Analysis of Data from Any Sensor
ROC	Receiver Operator Characteristics
ROI	Region of Interest
SPAIR	Spectral Adiabatic Inversion Recovery
SPGR	Spoiled Gradient Recalled
SS-EPI	Single Shot Echo-planar Imaging
T1	Longitudinal relaxation
T2	Transversal relaxation
TE	Echo Time
TH	ThresHold
TR	Repetition Time
TN	True Negative
TP	True Positive
US	UltraSonic
VCI	Vena Cava Inferior

Part I

Introduction

General Introduction

1.1 Principles of diffusion

Molecules or small particles are constantly moving due to thermal energy. Einstein showed in 1905 that the kinetic energy of a particle is related to its velocity v and mass m :

$$\frac{1}{2}mv^2 = \frac{1}{2}kT \quad (1.1)$$

where T is the temperature and k is Boltzmann's constant. The velocity of a particle can therefore be easily calculated in units of mm/s when m and T are known variables. This relation however assumes no obstructions, such as in a vacuum conditions. When the particle is emerged in water, it bumps against other water molecules, resulting in a random walk (Fig. 1.1), or Brownian motion (1).

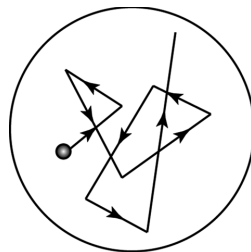


Figure 1.1: Example of Brownian motion.

Brown's model is a probabilistic description of the trajectory of particles due to random collisions with neighboring particles (2). The average displacement r of a particle

in a 3D volume is therefore a probability distribution which depends on the diffusion coefficient D , and the diffusion time t (3):

$$\langle r^2 \rangle = 6Dt \quad (1.2)$$

where D is defined by Fick's laws of diffusion and expressed in the Stokes-Einstein equation:

$$D = \frac{kT}{6\pi\eta R} \quad (1.3)$$

which demonstrates the dependency of D on the temperature T , the viscosity η of the liquid, and the radius R of the particle. Consequently, the diffusion coefficient is given in units of mm^2/s . This can be understood by picturing an infinitesimal small sphere where a particle is initially concentrated. When the particle diffuses away, the surface area [m^2] of the sphere (the probable location of the particle) grows linearly with time [s].

Diffusion occurs in all fluids. In a glass of water, the H_2O molecules with their two hydrogen protons, move around freely in all directions, in a random fashion defined as isotropic diffusion. The net movement or diffusion of protons from one area to another can be measured. At room temperature (20 °C), the diffusion in a glass of water is around $2.02 \times 10^{-3} \text{ mm}^2/\text{s}$ (4). And as the diffusion increases with temperature, the diffusion coefficient of pure water in the human body is higher, approximately $3 \times 10^{-3} \text{ mm}^2/\text{s}$ at 37 °C (5).

Obstacles can cause restriction of diffusion. In the human body these obstacles include macromolecules (e.g. lipids or proteins) located in the extracellular space, increasing the viscosity (6). Also the cellularity (ratio of volume occupied by the cells to the volume of the extracellular space) has a large impact on the diffusion in biological tissues. When the number of cells increases, as in cancer, there is less extracellular space to allow diffusion, thus the diffusion drops. The same is true for an increase in cell volume caused for example by ischemia. The opposite can be observed when the extracellular space increases (interstitial edema) due to inflammation, causing an increase in diffusion.

1.2 Origin of diffusion-weighted imaging

Diffusion can be measured very accurately using a nuclear magnetic resonance (NMR) spectrometer, nowadays routine equipment in large physics or chemistry labs (Fig. 1.2).

In 1950, Hahn used a NMR system to show that the T₂ relaxation time of fluids is affected by molecular diffusion (7). The first direct NMR measurement of diffusion was performed several years later by Carr and Purcell, who demonstrated a good agreement between the diffusion of water at 25° measured using NMR and previous literature values (8). NMR measurement of diffusion was improved by Stejskal and Tanner who developed the gradient echo technique to solve some technical limitations with the timing of the spin-echo technique introduced by Hahn (9). It took two more decades before the measurement of diffusion was also introduced in the imaging domain by using a 0.35 Tesla (T) small animal magnetic resonance (MR) imager, by Wesbey et al. (10).



Figure 1.2: Example of a modern NMR system.

Diffusion-weighted imaging (DWI) as a clinical application of MR imaging (MRI) finds its origin in the early 1980s, when the brains of healthy subjects and patients with neurological pathology were compared in terms of the molecular diffusion measured at 0.5T using a whole-body MR system and head coil (11). The technique was further improved by Tuner et al. who integrated the diffusion measurement into a fast echo planar imaging (EPI) sequence, which is less sensitive to bulk motion such as cardiac pulsation, respiratory movement, involuntary movements and flow (12). Clinical applications of DWI were soon realized, at first mainly in the brain. Different diffusion speeds were distinguished between brain tumor components (cystic regions, edema, necrosis), and another clinical application, still used today, was recognized in the strong decrease of the molecular diffusion after acute stroke (Fig. 1.3) (13, 14).

The first applications of DWI outside the brain were shown in 1994 by in vivo measurements of the molecular diffusion in the liver, spleen, kidney, muscles and the human heart, revealing differences between diseased and normal tissue (15, 16). Several years later, DWI was applied in the human breast to visually separate fibroglandular

and fatty tissue owing to differences in diffusion (17).

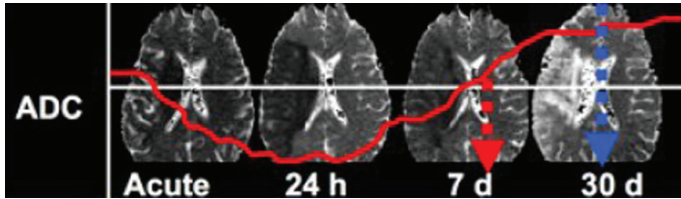


Figure 1.3: Example of strong decrease of apparent diffusion coefficient (ADC) after acute stroke in the brain. © radiologyassistant.nl.

1.3 Acquisition of diffusion-weighted imaging

MRI is based on a homogeneously distributed magnetic field strength in the imaging plane (18) (Fig. 1.4). In DWI, initially, all protons experience a similar magnetic field strength and therefore have a similar rate of precession (64 MHz on a 1.5T system). This condition, when protons spin at a similar rate, is defined as “in phase” and results in a high MR signal (Fig. 1.5).



Figure 1.4: Example of a Siemens Aera 1.5T whole-body MRI system.

The homogeneity of the magnetic field can be disturbed by applying magnetic gradient fields (Fig. 1.6). The magnetic gradients induce an increase or decrease of the local magnetic field and thereby affect the proton precession rate. When neighboring protons have a different precession rate they lose coherence. This condition is defined as “out of phase” or “dephasing”, and results in a loss of MR signal.

However, by applying so called inverse magnetic field gradients (which have a negative magnetization), the loss of coherence or dephasing can be reversed such that the

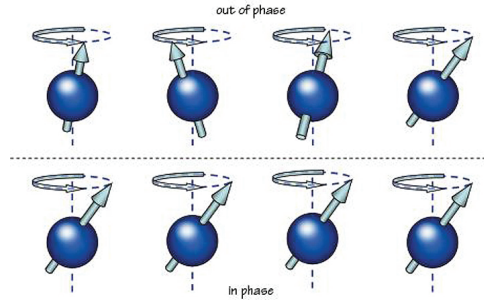


Figure 1.5: Protons are “in-phase” when they spin at a similar rate (bottom). When gradients are applied they lose coherence and become “out-of-phase” (top). © MRI at a Glance, C. Westbrook.

initial in phase condition is obtained again; this process is defined as “rephasing”. In DWI the pulse sequence, which describes the technical instructions to the MR system, is constructed out of several blocks of magnetic field gradients to induce dephasing and rephasing (Fig. 1.7).

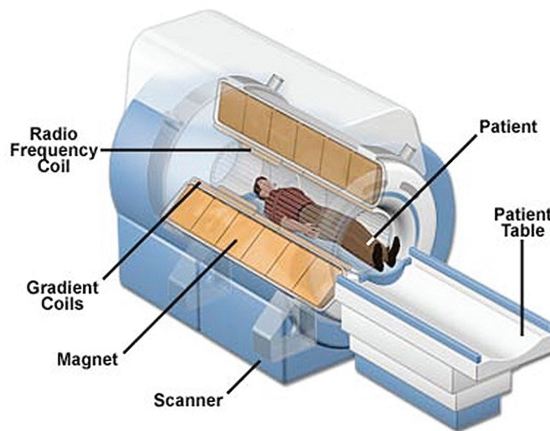


Figure 1.6: Diagram of the internal components of a MRI system.

The principle of DWI is described most easily when a water containing voxel (e.g. $1.0 \times 1.0 \times 1.0 \text{ mm}^3$) is considered. In the first example it is assumed that diffusion inside the voxel is absent. Next, a dephasing magnetic gradient is applied followed shortly (i.e. after 50 ms) by a rephasing gradient. First the MR signal is lost by dephasing, and then restored again by rephasing. The net effect is that the resulting MR signal is high when the DWI sequence is finished. In the second example it is assumed that diffusion inside the voxel is fast. Again a dephasing and rephasing gradient are applied. However,

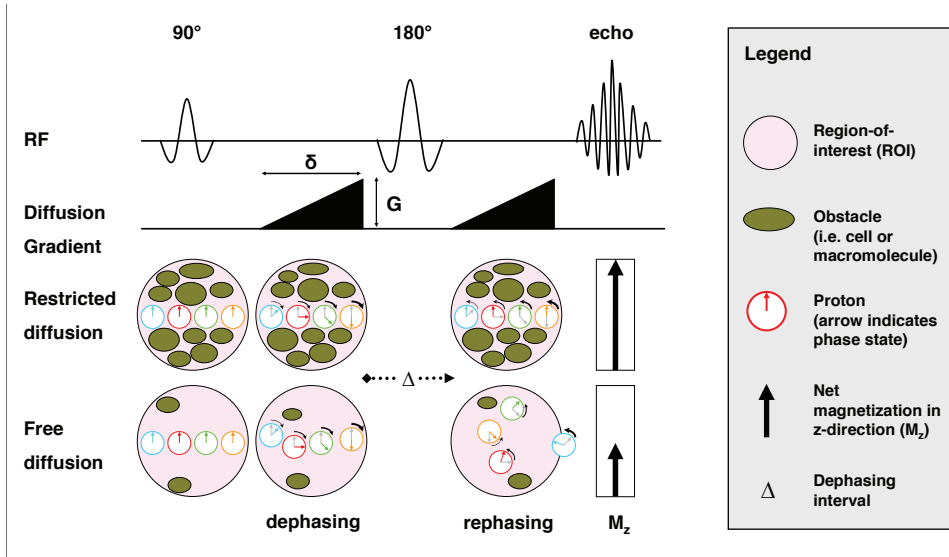


Figure 1.7: Schematic representation of a DWI sequence demonstrating dephasing and rephasing for restricted and free diffusion. Initially, all protons experience a similar magnetic field strength and therefore have a similar rate of precession defined as “in phase” (all arrows point upwards). The first diffusion gradient disturbs the magnetic field causing dephasing or loss of coherence (arrows point in various directions). Depending on environment in the region-of-interest (ROI), the protons reside at approximately the same position (restricted diffusion), or diffuse to other positions, even possibly outside the ROI (free diffusion). The sensitivity of the DWI sequence for diffusion (the b-value) is a function of the gradient pulse duration (δ), the gradient strength (G), and the time of the dephasing interval (Δ). After the dephasing interval the second gradient rephases the protons. For restricted diffusion the phase of most protons is reversed to the initial state (all arrows pointing upwards), yielding a high net magnetization in the z-direction M_z and thus a high signal. For free diffusion, however, the protons experience differing gradient field strengths and can not be rephased completely therefore yielding a low M_z and respective low signal. When the diffusion signal is measured for each voxel within a slice the result is a qualitative diffusion weighed image, acquired for a specific b-value. This image is not quantitative by itself. At least two images are required to calculate the quantitative diffusion for each voxel in terms of the apparent diffusion coefficient (ADC), or intravoxel incoherent motion (IVIM) model (Fig. 1.8 and 1.9).

during the interval Δ of 50 ms between the two gradients, the protons diffuse out of the voxel and are therefore not rephased again or only partially rephased. In the latter case a loss of MR signal reflects the rate of diffusion. Low diffusion (example 1) is observed as hyperintense (high signal) on DW images, and fast diffusion appears as hypointense (low signal; example 2).

Besides the interval between the gradients, Δ (ms), also the magnetic field gradient strength G (T/m), the magnetic field gradient duration δ (ms) and the gyromagnetic ratio γ are parameters affecting the sensitivity of the DWI sequence to the rate of diffu-

sion. The most direct effect is observed when changing interval Δ . When Δ is prolonged, there is more time for the protons to diffuse, yielding a DWI sequence with higher sensitivity for slow diffusion. During a 50 ms interval the protons travel approximately 30 μm (19). In general, the sensitivity of the DWI sequence for diffusion, also called the diffusion-weighting, is summarized into one parameter: the b-value (s/mm^2)

$$b = \gamma^2 G^2 \delta^2 \left(\Delta - \frac{\delta}{3} \right) \quad (1.4)$$

The b-value is a function of the gradient pulse duration (δ) and the gradient strength (G), and is also affected by the time between the onsets of the diffusion gradients (Δ). Typically, b-values up to $1500 \text{ s}/\text{mm}^2$ are clinically used.

1.4 Modeling DWI data

The acquisition of the quantitative diffusion coefficient can be performed with two b-values (i.e. 0 and $500 \text{ s}/\text{mm}^2$) when a mono-exponential model is assumed.

$$\frac{S}{S_0} = e^{-b \cdot \text{ADC}} \quad (1.5)$$

By acquiring the signal (S_0) of a reference DW image without diffusion-weighting ($b = 0 \text{ s}/\text{mm}^2$) and the signal (S) of a second DW image with diffusion-weighting (i.e. $b = 500 \text{ s}/\text{mm}^2$), a quantitative diffusion coefficient in units of mm^2/s can be obtained. The mono-exponential model hypothesizes that the diffusion signal S decreases log-linearly with the diffusion-weighting (Fig. 1.8).

The quantitative diffusion coefficient is then obtained by calculating the slope of the signal plot. However, in clinical practice, most tissues do not demonstrate pure mono-exponential diffusion. The quantitative diffusion coefficient resulting from the mono-exponential model is therefore historically entitled as “seemingly or apparently”: the apparent diffusion coefficient (ADC). This implies that the quantitative outcome of DWI (the ADC), is affected by the acquisition parameters (the choice of b-values), when the diffusion signal is not purely mono-exponential. This has been demonstrated in various studies since the introduction of the ADC (20). Also the quest for the optimal set of b-values for each tissue type has been conducted ever since (21).

The concept of the ADC however has been derived from the more complex intravoxel incoherent motion (IVIM) model, which fits a bi-exponential model to multiple DW images using multiple b-values (Fig. 1.9) (22):

$$\frac{S}{S_0} = f_{fast} \cdot e^{-b \cdot D_{fast}} + f_{slow} \cdot e^{-b \cdot D_{slow}} \quad (1.6)$$

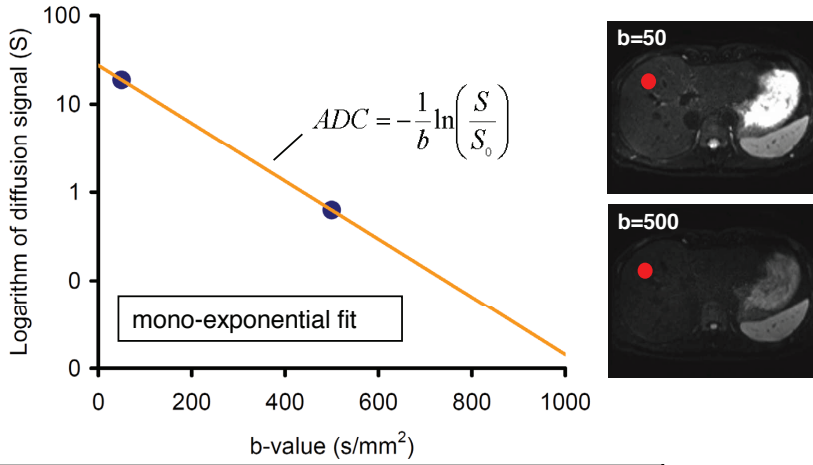


Figure 1.8: Mono-exponential fit of the diffusion signal (S) with two b -values (50 and 500 s/mm^2). When S is plotted on a logarithmic scale, the apparent diffusion coefficient (ADC) can be calculated from the slope of the fit.

Besides a slow diffusion coefficient, the bi-exponential model assumes an additional fast diffusion parameter, which is also referred to as “microperfusion”. The IVIM model

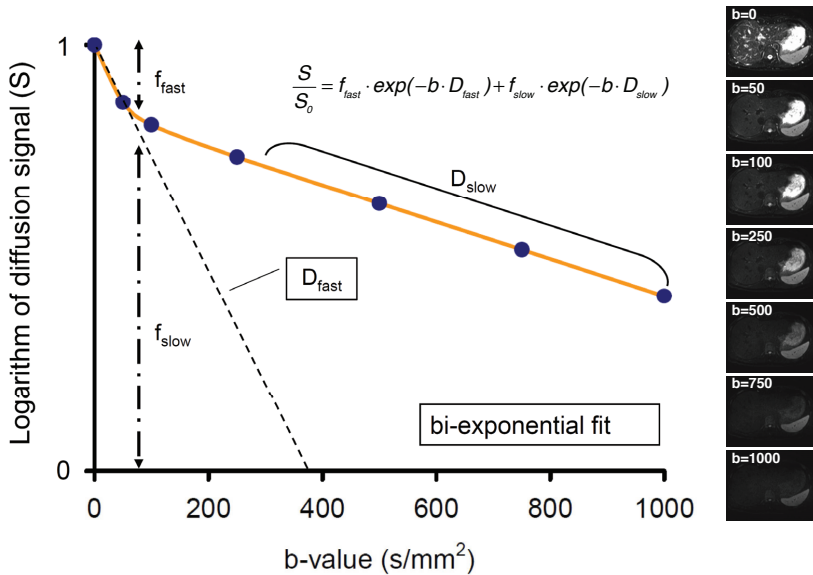


Figure 1.9: Bi-exponential fit of the diffusion signal (S) indicating molecular diffusion (D_{slow}), microperfusion (D_{fast}) and its fractions (f_{slow} and f_{fast}). In this example seven b -values between 0 and 1000 s/mm^2 were acquired to allow bi-exponential fitting.

separates these two diffusion parameters to obtain pure and separate images of molecular diffusion D_{slow} and microperfusion D_{fast} . The ADC equals D_{slow} when the diffusion signal of a tissue is pure mono-exponential and only molecular diffusion is present. However, because most tissues demonstrate bi-exponential diffusion due to the presence of microperfusion, the ADC effectively integrates molecular diffusion and microperfusion effects in one parameter. In figure 1.10 an example is shown with the diffusion signal of water at 37 °C, liver tissue and gray matter.

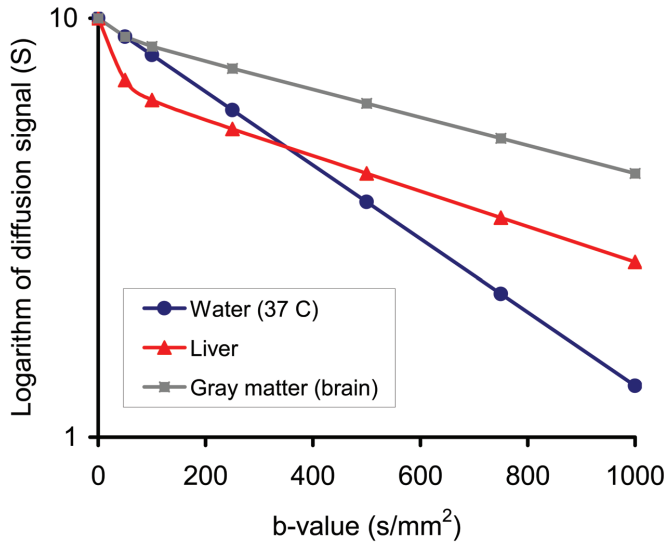


Figure 1.10: Example of the diffusion signal for water at 37 °C (mono-exponential diffusion; $D_{\text{slow}} = 2.02 \times 10^{-3} \text{ mm}^2/\text{s}$; no microperfusion component), for the liver (bi-exponential diffusion; $D_{\text{slow}} = 0.97 \times 10^{-3} \text{ mm}^2/\text{s}$; $D_{\text{fast}} = 35.9 \times 10^{-3} \text{ mm}^2/\text{s}$; $f_{\text{fast}} = 30.6\%$) and gray matter (bi-exponential diffusion; $D_{\text{slow}} = 0.77 \times 10^{-3} \text{ mm}^2/\text{s}$; $D_{\text{fast}} = 30.0 \times 10^{-3} \text{ mm}^2/\text{s}$; $f_{\text{fast}} = 10\%$).

1.5 Implementation issues of DWI

1.5.1 Acquisition

The first category of obstacles considers the acquisition of DWI data of the patient performed in the MR scanner. In theory ADC values are independent of the magnetic field strength, which is confirmed by several studies showing no significantly different ADC values in the abdomen between the 1.5T and 3.0T field strength (23–25). One study however reported up to 15.9% higher ADC values at 3.0T compared to 1.5T (26).

Variability of microperfusion parameters (D_{fast} and f_{fast}) derived from the IVIM model is relatively high between the two platforms compared to ADC values (25). In addition, increased image distortions by susceptibility artifacts and field heterogeneities have been shown at the higher field strength (27). Image quality scores of DWI in the abdomen were reported to be significantly lower at 3.0T compared to 1.5T MR systems (24).

Besides field strength, a comprehensive list of other technical specifications of the scanner affects the quantification of diffusion measurements, such as respiratory related techniques (e.g. breath-hold, free breathing, respiratory-triggered), repetition time (TR), echo time (TE), voxel size, number of averages, fat suppression techniques, receiver bandwidth and gradient performance specifications (20).

With the initial introduction of DWI simple spine echo sequences were modified to measure diffusion. However, a list of other sequences can also be adopted for DWI such as stimulated echo, fast spin-echo, gradient echo, line scan diffusion techniques and echo planar imaging (EPI); all those sequences have their specific advantages and disadvantages and thus affect the quantitative outcome (28). EPI is applied frequently to perform DWI because it is very fast and can acquire entire images within 100 milliseconds. It is, however, rather susceptible to magnetic field heterogeneities which are encountered especially in areas with air such as the gastrointestinal tract and the lungs, or near metal medical devices such as stents and clips (29).

Although DWI suffers from challenges like low resolution, gaining optimal signal-to-noise ratio (SNR), acquisition time and susceptibility distortion, technological advancements improved diffusion measurement significantly in recent years (30). Gradients got more powerful and parallel imaging techniques allow for higher resolution, less scan time and reduced artifacts.

1.5.2 Choice of b-values

One of the main parameters affecting diffusion measurements in the acquisition phase are the b-values (Eq. 1.4) applied in the DWI scan protocol. The number of b-values directly affects which model (mono- or bi-exponential) can be used to analyze the data when acquisition is completed. When only two b-values are used during acquisition, the analysis of the data is limited to mono-exponential analysis, resulting in an ADC value.

There is however no such thing as a true ADC value because it depends heavily on which two b-values are used in the setup. A couple of relatively low b-values (i.e. 50 and

400 s/mm²) will result in significantly higher ADC values than when a couple of higher b-values are used (i.e. 500 and 1000 s/mm²). The problem is that besides true molecular diffusion, based on the thermally driven motion of water molecules (mean diffusivity), which is known as Brownian motion, there may be substantial contributions of additional faster components due to contributions of blood vessels (microperfusion) (22).

The microperfusion term reflecting microcirculation of blood in the capillary network is for example substantial in tumors, but almost negligible in normal glandular breast tissue (31). When there is more microperfusion in the tissue, the ADC is affected stronger. This effect is also called “microperfusion contamination” of the ADC (32). This is why in some studies researchers tried to choose b-values not within the microperfusion range (33–38). And in a recent consensus report on DWI, it was recommended to use two b-values (>100 and between 500 and 1000 mm²/s) for ADC assessments (19). It is, however, difficult to choose b-values such that microperfusion contamination of the ADC is avoided, because the microperfusion effects of the tissue are not known a priori.

Microperfusion effects vary substantially between tissues and also throughout tissues, whether or not due to pathology, and render the ADC regionally dependent of the measurement location instead of reflecting a true variance in molecular diffusion.

The bi-exponential intravoxel incoherent motion (IVIM) model was designed to separate these two effects, the microperfusion and molecular diffusion (22). To do this, theoretically four b-values are needed because there are four unknown parameters (D_{slow} , D_{fast} , f_{slow} and f_{fast}), and this reduces further to a minimum number of three b-values when it is assumed that a voxel is a mix of either molecular diffusion or microperfusion, such that $f_{\text{fast}} = 1 - f_{\text{slow}}$.

However, to obtain a perfect fit of the diffusion signal, a large number of b-values have to be sampled. Lemke et al. suggested that at least 10 b-values should be used for current clinical settings, and Ter Voert et al. even argued for a minimum of 16 b-values (39, 40). However a balance is needed between the longer acquisition time and optimal image quality, and that is why Dyvorne et al. concluded that a set of four optimized b-values should be used in the liver, where in the pancreas up to seven b-values are needed (41, 42).

The reproducibility of D_{slow} is generally good (<20%), however f_{fast} (<40%) and D_{fast} (>40%) are subject to high uncertainty due to noise and fitting artefacts (41, 43, 44). Another consideration when implementing the IVIM model is that it assumes a random capillary orientation. For tissues with ordered and structured capillary orienta-

tion, however, such as the myocardium, it is unclear whether the IVIM theory can be applied directly (45).

The mono- and biexponential models generally rely on the acquisition of b-values between 0 and 1000 s/mm². That range of b-values is sufficient to perform accurate fits of either one or two exponential components. The application of DWI however is not restricted to that range and also extends to the use of very high b-values in the order of 5000 s/mm². In that range the use of triexponential analysis demonstrated a potential third component where the molecular diffusion component can be separated into fast (free) diffusion and slow (restricted) diffusion (46–48). The latter has been recognized also in a breast DWI study, where it was shown that the main fast diffusion would represent water signal and the second slow diffusion component would be unsuppressed immobile fat molecules thereby restricting the diffusion of water (trapped water) (31).

1.5.3 Analysis of DWI

There are systematic discrepancies in the determination of the region of interest (ROI) for the calculation of the ADCs between studies. Some studies use circular ROIs with a fixed diameter, or place the ROI in the whole breast lesion; others use the most enhancing area of the lesion. Also, several studies have shown that important information is lost when one relies just on the average values of lesions and that higher sensitivity can be obtained when the minimum diffusion is used instead of average diffusion (49–51). That approach, however, usually depends on just a single voxel which defining the lesion's minimum value and is, therefore, prone to a high degree of uncertainty.

Recently, several authors introduced lesion histogram analysis which adds a whole set of additional histogram parameters such as percentile, minimum, median, mode, skewness and kurtosis (52–55). For example, the histogram mode represents the ADC value in the ROI which is found with the highest frequency. In that way, the ADC measurement is not dependent on only one pixel.

1.5.4 Effects of fat

Already in 1983, it was demonstrated that water diffusion drops six-fold inside of Cheddar and Swiss cheeses (56). However, the effect of fat on hepatic DWI is still subject of debate. In an animal study it was concluded that steatosis may confound determination of hepatic fibrosis with DWI (57). This was confirmed in two clinical studies

where the ADC decreased significantly in patients with hepatic steatosis (58, 59). Similarly, a study which applied the IVIM model demonstrated that steatosis can reduce the molecular diffusion significantly and thus act as a potential confounder when IVIM is used to assess diffuse liver diseases such as cirrhosis (60).

1.5.5 Effects of contrast agents

High concentrations of gadolinium-based complexes hamper the effective motion of water molecules and increase the viscosity (61, 62). Several studies on the liver showed that this may result in decreased ADC values of 3.1%, 5% and 17.8% after injection of respectively Gd-DTPA, Gd-EOB-DTPA and gadodiamide (63–65). Others however observed no change in the ADC after administering Gd-EOB-DTPA (66). In the kidneys decreases of the ADC up to 4.2% were found post-contrast (67). A study by Janka et al. concluded, although a significant post-contrast decrease of the ADC was found, that DWI of the breast may as well be performed after contrast application and they even indicated a slightly better ADC discrimination between benign and malignant lesions after contrast administration (68). However, when the DWI sequence follows the contrast-enhanced sequences, it becomes unclear whether potential decreases of the ADC are due to pathology or due to the presence of contrast agent in the tissue. Most authors therefore recommend acquiring the DWI data before injection of the contrast agent.

1.5.6 Interpretation and standardization

The additional value of IVIM to ADC, for example for the evaluation of hepatic parenchyma and hepatic lesions, has been demonstrated by several studies since the onset of IVIM (69–72). However, there has also been debate about the concept of separating the molecular diffusion and microperfusion by IVIM. With the introduction of IVIM, the molecular diffusion was associated with the diffusion of water in tissue and the microperfusion was associated with microcirculation of blood in the capillary network (referred to as perfusion) (22). The term perfusion, however, was defined rather loosely and any linkage to classical perfusion obtained from techniques such as dynamic contrast enhanced (DCE-) MRI remained unclear (73, 74).

The lack of standardization is one of the greatest challenges to widespread adoption of DWI (75). Because there are so many factors affecting the DWI measurement, several authors raised a call for consensus and the recommendation to specifically describe all

the acquisition parameters (including all b-values) alongside the published DWI measurements (19, 76). This allows comparison of diffusion measurement between different studies, sites and systems in a more structured and reliable matter.

1.6 Current clinical applications of DWI

A major application of DWI is in oncology, and calls have been raised to implement it as routine sequence in the oncologic setting (77). Applications can be found in tumor detection, characterization, discrimination and monitoring and predicting treatment response (75, 78). The cellularity and membrane structure changes when normal tissue turns cancerous. Dense malignant tumors show high cellularity and a low diffusion accordingly.

For focal liver lesions DWI is superior to standard T2-weighted imaging (79). For example, ADCs tend to decrease in the order of cysts, hemangiomas, hepatocellular carcinoma, and metastases (80). Malignant breast tumors demonstrate lower ADC values than the surrounding fibroglandular tissue or cysts (81). Also the tumor aggressiveness is reflected in the membrane integrity and cellularity and hence in the diffusion (82, 83). Lower ADC values have been associated with a more aggressive tumor profile in rectal cancer, and the ADC was marked as a potential imaging biomarker of the tumor aggressiveness profile (82).

Similarly, for prostate and cervical cancer, ADCs were shown to be lower for cancerous tissue compared to normal tissue, and tumor ADCs differed significantly between low- and higher risk localized prostate cancer (83–85). By evaluating tumor aggressiveness using DWI, more effectively tailored treatments can be offered to patients with high risk of occurrence or poorer prognosis. More importantly, this can be achieved in a non-invasive way, thereby enabling additional opportunities such as efficient patient selection, stratification and management in clinical trials (86).

A challenge is the differentiation of recurrent and residual tumors after treatment such as radiotherapy. Initial evaluations in the larynx showed that tissue changes post radiotherapy could be observed, and tumor recurrence was differentiated from treatment-induced complications (87). Effective treatment of tumors results in breakdown of the cell membrane (lysis) and necrosis, thereby increasing the amount of free fluids and consequently an increase of diffusion is observed (88). In a study on colorectal hepatic metastases, the ADC was found to increase in patients who responded to therapy while for the non-responders this increase was absent (89). Also in a lon-

itudinal study on the response in patients with locally advanced breast cancer treated with neoadjuvant chemotherapy it was shown that the ADC is useful for predicting early tumor response (90).

Considering the high costs of cancer treatment, and the major consequences of therapy effectiveness for patients, the field of treatment response prediction has high potential. For rectal carcinoma, cerebral gliomas and colorectal hepatic metastasis it has already been shown that tumors with a low ADC respond better to therapy than tumors with high ADC values at baseline (89, 91, 92).

Also the assessment of liver diseases has gained great benefit of DWI. Liver inflammation (caused by chronic viral hepatitis B and C, or alcohol abuse) causes the generation of more than normal amounts of collagen fibers in the extracellular space thereby hardening the tissue. This process is entitled liver fibrosis and develops in four stages, where in each stage the tissues becomes stiffer and the ADC decreases accordingly. The final stage is known as cirrhosis. Cirrhotic livers can be reliably distinguished from nonfibrotic livers by the decreased ADC seen with cirrhosis (38). Recently also the severity of fibrosis was assessed by DWI, showing that the liver fibrosis stages had a strong negative correlation with the microperfusion obtained with IVIM (93). Earlier studies already showed that the perfusion-related parameters from IVIM demonstrated a larger reduction in cirrhotic livers than the true molecular diffusion, which amplifies the potential of IVIM for liver imaging (43, 70).

Novel applications of DWI can be found in an ever growing field of clinical applications. In Crohn's disease it was demonstrated that quantitative DWI is useful in detecting and assessing inflammatory activity in the colon, but is also effective in predicting the response to therapy (94). In ophthalmology, the majority of orbital masses could be characterized into 3 categories based on an ADC threshold with more than 90% confidence, and was found valuable in monitoring the response of eye-preserving therapies (95, 96). Recently, the ADC was found helpful for distinguishing malignant and benign lesions in the lungs and vertebrae (97, 98).

For the brain, it has been suggested that correlations exist between diffusion abnormalities and damage by multiple sclerosis (99, 100). Also ADC measures turned out to be very sensitive in detecting differences between schizophrenia patients and healthy volunteers even in a relatively small sample (101). For other brain diseases such as Alzheimer's disease it has been suggested that DWI is useful for early detection (102).

1.7 Opportunities and challenges for IVIM

Although DWI found a wide range of applications, its use in clinic practice is mostly qualitative and based on visual assessment of DWI images. When DWI is applied quantitatively, usually the ADC is used. IVIM is a niche in clinical practice because it is not implemented in commercially available software, and depends on off-line analysis in custom software. Moreover, still challenges exist considering the implementation and interpretation of IVIM.

IVIM theoretically describes diffusion and perfusion effects; however the confirmation in clinical practice seems cumbersome. Since the onset of IVIM, the relationship between the conventional assessment of perfusion and IVIM related perfusion has been discussed and investigated (74). For example, no convincing support has been found for a relationship between perfusion measured by DCE-MRI and IVIM on 1.5T systems (43, 103, 104). Recently, however, using a 3.0T system a strong correlation was found between microperfusion fraction f of the IVIM model and enhancement amplitude of DCE-MRI (105). Also, there have been indications that quantitatively derived DCE-MRI parameters such as K_{trans} correlate with the microperfusion fraction f of the IVIM model in cervical cancer (106). Another challenge of IVIM is that the repeatability of IVIM parameter values is lower than that of the ADC, with microperfusion D_{fast} being worst among the IVIM parameters (107).

However, there are opportunities for IVIM that cannot be reached with just the ADC. Recently, in the brain it was demonstrated that microperfusion measured with IVIM reflects the perfusion situation in cerebral tissues (108). It was observed that microperfusion decreased in ischemic penumbrae compared to normal brain tissue while the diffusion remained the same. Also, IVIM proved as high potential for non-invasive assessment of acute clinical stroke and performed better than mono-exponential ADC (109).

In the liver, while the ADC was not associated with histological aspects of non-alcoholic fatty liver disease (NAFLD), IVIM derived parameters were significantly affected: diffusion decreased with steatosis and the fraction of microperfusion decreased with fibrosis (110). Correlations with fibrosis stage were strongest for IVIM derived microperfusion compared to the ADC (111, 112). Also in a rat model it was demonstrated that IVIM is better for the evaluation of fibrosis stages than the ADC (113).

Besides mono- and biexponential models, also more complex models have been studied such as the triexponential, stretched exponential, Gaussian and kurtosis models (46, 114). Also, on a voxel-by-voxel level, not all voxels may be best described by the

same model. These considerations require the development of novel algorithms to describe the complex behavior of diffusion and perfusion related properties of the tissue, but also provide great potential for future clinical applications.

1.8 Purpose and outline

Diffusion-weighted imaging (DWI) has been clinically available for some decades now. There are still numerous questions, however, how it should be implemented and interpreted. The quantitative end results of DWI depend on several factors acting during the acquisition, the data modeling and data analysis. Also patient related properties such as the amount of contrast agent and fat fractions affect quantitative DWI. This thesis aims to identify these confounders and assess their effect on DWI and the clinical workflow in the liver and breast.

Currently, clinical hepatic DWI generally relies on mono-exponential diffusion expressed in the apparent diffusion coefficient (ADC). However, a significant amount of microperfusion can be expected in the liver. In **chapter 2** the aim was therefore to demonstrate that diffusion of normal liver tissue measured by ADC is contaminated by microperfusion, and that analysis by the bi-exponential intravoxel incoherent motion (IVIM) model is required. A further understanding of what is measured by IVIM is investigated in **chapter 3**. Especially the linkage to classical perfusion obtained from techniques such as contrast-enhanced MRI is assessed by correlating to microperfusion parameters resulting from IVIM.

One of the confounders in hepatic DWI is steatosis. The ADC decreases significantly in patients with hepatic steatosis and this may hamper for example the determination of hepatic fibrosis with DWI. However, detailed insights in the dependency of IVIM parameters on normal (non-steatotic) fat fractions have not been reported yet. The diagnostic implications of non-steatotic hepatic fat fractions on quantitative DWI were therefore assessed in **chapter 4**.

Cirrhotic livers are characterized by the significantly lower ADC compared to normal livers, and negative correlations between fibrosis stages and ADC values have been demonstrated. However, it is unclear whether this is a true decrease of molecular diffusion, or rather reflects decreased microperfusion due to decreased portal blood flow. In **chapter 5** this topic is investigated by assessing patients with a Fontan circulation who are known for alterations in hepatic perfusion.

The potential additional value of IVIM compared to the ADC was further investi-

gated in the breast. DWI can help to differentiate between benign and malignant breast lesions. However, the ADC of breast lesions and the subsequently derived ADC thresholds show considerable variation. Therefore, a systematic review and meta-analysis was performed in **chapter 6** to assess the effect of the choice of b-values, and the effect of contrast agents, on the ADCs of breast lesions.

In **chapter 7** an optimization and validation study was conducted to improve IVIM for the semi-automated analysis of breast lesions. The aim was to exclude cancer by maximizing specificity while maintaining sensitivity at 100%. This approach aims at reducing the number of biopsies and surgical removals of breast lesions turning out to be benign, which was investigated in **chapter 8**.

1.9 References

- (1) Brown, R. (1828). On the general existence of active molecules in organic and inorganic bodies. *Phil Mag* 4, 161–73.
- (2) Basser, P. J. In, Atlas, W. A., Ed., 4th; Magnetic Resonance Imaging of the Brain and Spine; LWW: 2008, pp 1752–67.
- (3) Berg, H. C. In, Revised edition; Random Walks in Biology; Princeton University Press: 1993, pp 5–12.
- (4) Tofts, P. S. et al. (2000). Test liquids for quantitative MRI measurements of self-diffusion coefficient in vivo. *Magnetic resonance in medicine* 43, 368–374.
- (5) Koh, D. M., and Thoeny, H. C., *Diffusion-Weighted MR Imaging: Applications in the Body*; Springer: 2010.
- (6) Fornasa, F. (2011). Diffusion-weighted Magnetic Resonance Imaging: What Makes Water Run Fast or Slow? *Journal of clinical imaging science* 1, 27.
- (7) Hahn, E. L. (1950). Spin Echoes. *Phys Rev* 80, 580.
- (8) Carr, H. Y., and Purcell, E. M. (1954). Effects of Diffusion on Free Precession in Nuclear Magnetic Resonance Experiments. *Phys Rev* 94, 630.
- (9) Stejskal, E. O., and Tanner, J. E. (1965). Spin Diffusion Measurements: Spin Echoes in the Presence of a Time Dependent Field Gradient. *J Chem Phys* 42, 288.
- (10) Wesbey, G. E., Moseley, M. E., and Ehman, R. L. (1984). Translational molecular self-diffusion in magnetic resonance imaging. II. Measurement of the self-diffusion coefficient. *Investigative radiology* 19, 491–498.
- (11) Bihan, D. L., Breton, E., Lallemand, D., Grenier, P., Cabanis, E., and Laval-Jeantet, M. (1986). MR imaging of intravoxel incoherent motions: application to diffusion and perfusion in neurologic disorders. *Radiology* 161, 401–407.
- (12) Turner, R., Bihan, D. L., Maier, J., Vavrek, R., Hedges, L. K., and Pekar, J. (1990). Echo-planar imaging of intravoxel incoherent motion. *Radiology* 177, 407–414.
- (13) Bihan, D. L., Turner, R., Douek, P., and Patronas, N. (1992). Diffusion MR imaging: clinical applications. *AJR.American journal of roentgenology* 159, 591–599.
- (14) Moseley, M. E. et al. (1990). Diffusion-weighted MR imaging of acute stroke: correlation with T2-weighted and magnetic susceptibility-enhanced MR imaging in cats. *AJNR.American journal of neuroradiology* 11, 423–429.

- (15) Muller, M. F., Prasad, P., Siewert, B., Nissenbaum, M. A., Raptopoulos, V., and Edelman, R. R. (1994). Abdominal diffusion mapping with use of a whole-body echo-planar system. *Radiology* 190, 475–478.
- (16) Edelman, R. R. et al. (1994). In vivo measurement of water diffusion in the human heart. *Magnetic resonance in medicine* 32, 423–428.
- (17) Englander, S. A., Ulug, A. M., Brem, R., Glickson, J. D., and van Zijl, P. C. (1997). Diffusion imaging of human breast. *NMR in biomedicine* 10, 348–352.
- (18) Mori, S., and Barker, P. B. (1999). Diffusion magnetic resonance imaging: its principle and applications. *The Anatomical Record* 257, 102–109.
- (19) Padhani, A. R. et al. (2009). Diffusion-weighted magnetic resonance imaging as a cancer biomarker: consensus and recommendations. *Neoplasia (New York, N.Y.)* 11, 102–125.
- (20) Zhang, J. L. et al. (2010). Variability of renal apparent diffusion coefficients: limitations of the monoexponential model for diffusion quantification. *Radiology* 254, 783–792.
- (21) Dyvorne, H. A. et al. (2013). Diffusion-weighted imaging of the liver with multiple b values: effect of diffusion gradient polarity and breathing acquisition on image quality and intravoxel incoherent motion parameters—a pilot study. *Radiology* 266, 920–929.
- (22) Bihan, D. L., Breton, E., Lallemand, D., Aubin, M. L., Vignaud, J., and Laval-Jeantet, M. (1988). Separation of diffusion and perfusion in intravoxel incoherent motion MR imaging. *Radiology* 168, 497–505.
- (23) Matsuoka, A. et al. (2008). Comparison of 3.0- and 1.5-tesla diffusion-weighted imaging in the visibility of breast cancer. *Radiation Medicine* 26, 15–20.
- (24) Rosenkrantz, A. B., Oei, M., Babb, J. S., Niver, B. E., and Taouli, B. (2011). Diffusion-weighted imaging of the abdomen at 3.0 Tesla: image quality and apparent diffusion coefficient reproducibility compared with 1.5 Tesla. *Journal of magnetic resonance imaging : JMRI* 33, 128–135.
- (25) Cui, Y., Dyvorne, H., Besa, C., Cooper, N., and Taouli, B. (2015). IVIM Diffusion-weighted Imaging of the Liver at 3.0T: Comparison with 1.5T. *European Journal of Radiology Open* 2, 123–128.
- (26) Dale, B. M., Braithwaite, A. C., Boll, D. T., and Merkle, E. M. (2010). Field strength and diffusion encoding technique affect the apparent diffusion coefficient measurements in diffusion-weighted imaging of the abdomen. *Investigative radiology* 45, 104–108.
- (27) Bernstein, M. A., 3rd, J. H., and Ward, H. A. (2006). Imaging artifacts at 3.0T. *Journal of magnetic resonance imaging : JMRI* 24, 735–746.
- (28) Bammer, R. (2003). Basic principles of diffusion-weighted imaging. *European Journal of Radiology* 45, 169–184.
- (29) Bihan, D. L., Poupon, C., Amadon, A., and Lethimonnier, F. (2006). Artifacts and pitfalls in diffusion MRI. *Journal of magnetic resonance imaging : JMRI* 24, 478–488.
- (30) Chilla, G. S., Tan, C. H., Xu, C., and Poh, C. L. (2015). Diffusion weighted magnetic resonance imaging and its recent trend—a survey. *Quantitative imaging in medicine and surgery* 5, 407–422.
- (31) Baron, P., Dorrius, M. D., Kappert, P., Oudkerk, M., and Sijens, P. E. (2010). Diffusion-weighted imaging of normal fibroglandular breast tissue: influence of microperfusion and fat suppression technique on the apparent diffusion coefficient. *NMR in biomedicine* 23, 399–405.
- (32) Moteki, T., and Horikoshi, H. (2011). Evaluation of noncirrhotic hepatic parenchyma with and without significant portal vein stenosis using diffusion-weighted echo-planar MR on the basis of multiple-perfusion-components theory. *Magnetic resonance imaging* 29, 64–73.
- (33) Chan, J. H. et al. (2001). Diffusion-weighted MR imaging of the liver: distinguishing hepatic abscess from cystic or necrotic tumor. *Abdominal Imaging* 26, 161–165.

- (34) Murtz, P., Flacke, S., Traber, F., van den Brink, J. S., Gieseke, J., and Schild, H. H. (2002). Abdomen: diffusion-weighted MR imaging with pulse-triggered single-shot sequences. *Radiology* 224, 258–264.
- (35) Boulanger, Y. et al. (2003). Diffusion-weighted MR imaging of the liver of hepatitis C patients. *NMR in biomedicine* 16, 132–136.
- (36) Bruegel, M. et al. (2008). Characterization of focal liver lesions by ADC measurements using a respiratory triggered diffusion-weighted single-shot echo-planar MR imaging technique. *European radiology* 18, 477–485.
- (37) Perman, W. H., Balci, N. C., Akduman, I., and Kuntz, E. (2009). Magnetic resonance measurement of diffusion in the abdomen. *Topics in magnetic resonance imaging : TMRI* 20, 99–104.
- (38) Sandrasegaran, K. et al. (2009). Value of diffusion-weighted MRI for assessing liver fibrosis and cirrhosis. *AJR.American journal of roentgenology* 193, 1556–1560.
- (39) Lemke, A., Stieltjes, B., Schad, L. R., and Laun, F. B. (2011). Toward an optimal distribution of b values for intravoxel incoherent motion imaging. *Magnetic resonance imaging* 29, 766–776.
- (40) Voert, E. E. T., Delso, G., Porto, M., Huellner, M., and Veit-Haibach, P. (2016). Intravoxel Incoherent Motion Protocol Evaluation and Data Quality in Normal and Malignant Liver Tissue and Comparison to the Literature. *Investigative radiology* 51, 90–99.
- (41) Dyvorne, H., Jajamovich, G., Kakite, S., Kuehn, B., and Taouli, B. (2014). Intravoxel incoherent motion diffusion imaging of the liver: optimal b-value subsampling and impact on parameter precision and reproducibility. *European Journal of Radiology* 83, 2109–2113.
- (42) Gurney-Champion, O. J. et al. (2015). Minimizing the Acquisition Time for Intravoxel Incoherent Motion Magnetic Resonance Imaging Acquisitions in the Liver and Pancreas. *Investigative radiology*.
- (43) Patel, J., Sigmund, E. E., Rusinek, H., Oei, M., Babb, J. S., and Taouli, B. (2010). Diagnosis of cirrhosis with intravoxel incoherent motion diffusion MRI and dynamic contrast-enhanced MRI alone and in combination: preliminary experience. *Journal of magnetic resonance imaging : JMRI* 31, 589–600.
- (44) Andreou, A. et al. (2013). Measurement reproducibility of perfusion fraction and pseudodiffusion coefficient derived by intravoxel incoherent motion diffusion-weighted MR imaging in normal liver and metastases. *European radiology* 23, 428–434.
- (45) Abdullah, O. M., Gomez, A. D., Merchant, S., Heidinger, M., Poelzing, S., and Hsu, E. W. (2015). Orientation dependence of microcirculation-induced diffusion signal in anisotropic tissues. *Magnetic resonance in medicine*.
- (46) Ueda, Y. et al. (2016). Triexponential function analysis of diffusion-weighted MRI for diagnosing prostate cancer. *Journal of magnetic resonance imaging : JMRI* 43, 138–148.
- (47) Rosenkrantz, A. B. et al. (2016). Prostate Cancer Detection Using Computed Very High b-value Diffusion-weighted Imaging: How High Should We Go? *Acad Radiol*.
- (48) Hayashi, T. et al. (2013). Diffusion Analysis with Triexponential Function in Liver Cirrhosis. *J Magn Reson Imaging* 38, 148–53.
- (49) Hirano, M., Satake, H., Ishigaki, S., Ikeda, M., Kawai, H., and Naganawa, S. (2012). Diffusion-weighted imaging of breast masses: comparison of diagnostic performance using various apparent diffusion coefficient parameters. *AJR.American journal of roentgenology* 198, 717–722.
- (50) Mori, N. et al. (2013). Detection of invasive components in cases of breast ductal carcinoma in situ on biopsy by using apparent diffusion coefficient MR parameters. *European radiology* 23, 2705–2712.
- (51) Baltzer, P. A. et al. (2011). Diffusion tensor magnetic resonance imaging of the breast: a pilot study. *European radiology* 21, 1–10.
- (52) Guan, Y. et al. (2015). Whole-Lesion Histogram Analysis of Apparent Diffusion Coefficient for the Assessment of Cervical Cancer. *Journal of computer assisted tomography*.

- (53) Choi, M. H. et al. (2015). Diffusion-weighted imaging: Apparent diffusion coefficient histogram analysis for detecting pathologic complete response to chemoradiotherapy in locally advanced rectal cancer. *Journal of magnetic resonance imaging : JMRI*.
- (54) Xu, X. Q. et al. (2016). Orbital Indeterminate Lesions in Adults:: Combined Magnetic Resonance Morphometry and Histogram Analysis of Apparent Diffusion Coefficient Maps for Predicting Malignancy. *Academic Radiology* 23, 200–208.
- (55) Cho, G. Y. et al. (2015). Evaluation of breast cancer using intravoxel incoherent motion (IVIM) histogram analysis: comparison with malignant status, histological subtype, and molecular prognostic factors. *European radiology*.
- (56) Callaghan, P. T., Jolley, K. W., and Humphrey, R. S. (1983). Diffusion of fat and water in cheese as studied by pulsed field gradient nuclear magnetic resonance. *Journal of colloid and interface science* 93, 521–529.
- (57) Anderson, S. W. et al. (2011). Effect of disease progression on liver apparent diffusion coefficient values in a murine model of NASH at 11.7 Tesla MRI. *Journal of magnetic resonance imaging : JMRI* 33, 882–888.
- (58) Poyraz, A. K., Onur, M. R., Kocakoc, E., and Ogur, E. (2012). Diffusion-weighted MRI of fatty liver. *Journal of magnetic resonance imaging : JMRI* 35, 1108–1111.
- (59) Wignall, O., Scurr, E., Collins, D., Thng, C. H., and Koh, D. M. (2008). Hepatic steatosis results in a reduction in the apparent diffusion coefficient (ADC) of liver parenchyma. *Proc. Intl. Soc. Mag. Reson. Med.* 16.
- (60) Guiu, B. et al. (2012). Intravoxel incoherent motion diffusion-weighted imaging in nonalcoholic fatty liver disease: a 3.0-T MR study. *Radiology* 265, 96–103.
- (61) Ogura, A., Hayakawa, K., Miyati, T., and Maeda, F. (2008). The effect of susceptibility of gadolinium contrast media on diffusion-weighted imaging and the apparent diffusion coefficient. *Academic Radiology* 15, 867–872.
- (62) Jost, G., Lenhard, D. C., Sieber, M. A., Lengsfeld, P., Hutter, J., and Pietsch, H. (2011). Changes of renal water diffusion coefficient after application of iodinated contrast agents: effect of viscosity. *Investigative radiology* 46, 796–800.
- (63) Choi, J. S., Kim, M. J., Choi, J. Y., Park, M. S., Lim, J. S., and Kim, K. W. (2010). Diffusion-weighted MR imaging of liver on 3.0-Tesla system: effect of intravenous administration of gadoxetic acid disodium. *European radiology* 20, 1052–1060.
- (64) Chiu, F. Y. et al. (2005). Effect of intravenous gadolinium-DTPA on diffusion-weighted magnetic resonance images for evaluation of focal hepatic lesions. *Journal of computer assisted tomography* 29, 176–180.
- (65) Saremi, F., Sefidbakht, S., Quane, L., Maria, J. S., Khararjian, A., and Jalili, M. (2011). Effect of intravenous extracellular gadolinium based contrast medium on renal diffusion weighted images. *Academic Radiology* 18, 174–183.
- (66) Saito, K. et al. (2010). Effect of Gd-EOB-DTPA on T2-weighted and diffusion-weighted images for the diagnosis of hepatocellular carcinoma. *Journal of magnetic resonance imaging : JMRI* 32, 229–234.
- (67) Wang, C. L. et al. (2011). Effect of gadolinium chelate contrast agents on diffusion weighted MR imaging of the liver, spleen, pancreas and kidney at 3 T. *European Journal of Radiology* 80, e1–7.
- (68) Janka, R., Hammon, M., Geppert, C., Nothhelfer, A., Uder, M., and Wenkel, E. (2014). Diffusion-weighted MR imaging of benign and malignant breast lesions before and after contrast enhancement. *RoFo : Fortschritte auf dem Gebiete der Rontgenstrahlen und der Nuklearmedizin* 186, 130–135.
- (69) Yamada, I., Aung, W., Himeno, Y., Nakagawa, T., and Shibuya, H. (1999). Diffusion coefficients in abdominal organs and hepatic lesions: evaluation with intravoxel incoherent motion echo-planar MR imaging. *Radiology* 210, 617–623.

- (70) Luciani, A. et al. (2008). Liver cirrhosis: intravoxel incoherent motion MR imaging—pilot study. *Radiology* 249, 891–899.
- (71) Cohen, A. D., Schieke, M. C., Hohenwarter, M. D., and Schmainda, K. M. (2014). The effect of low b-values on the intravoxel incoherent motion derived pseudodiffusion parameter in liver. *Magnetic resonance in medicine : official journal of the Society of Magnetic Resonance in Medicine / Society of Magnetic Resonance in Medicine*.
- (72) Kakite, S. et al. (2014). Hepatocellular carcinoma: Short-term reproducibility of apparent diffusion coefficient and intravoxel incoherent motion parameters at 3.0T. *Journal of magnetic resonance imaging : JMRI*.
- (73) Bihan, D. L., and Turner, R. (1992). The capillary network: a link between IVIM and classical perfusion. *Magnetic resonance in medicine : official journal of the Society of Magnetic Resonance in Medicine / Society of Magnetic Resonance in Medicine* 27, 171–178.
- (74) Henkelman, R. M. (1990). Does IVIM measure classical perfusion? *Magnetic resonance in medicine : official journal of the Society of Magnetic Resonance in Medicine / Society of Magnetic Resonance in Medicine* 16, 470–475.
- (75) Koh, D. M., and Collins, D. J. (2007). Diffusion-weighted MRI in the body: applications and challenges in oncology. *AJR.American journal of roentgenology* 188, 1622–1635.
- (76) Guiu, B., and Cercueil, J. P. (2011). Liver diffusion-weighted MR imaging: the tower of Babel? *European radiology* 21, 463–467.
- (77) Bozgeyik, Z., Onur, M. R., and Poyraz, A. K. (2013). The role of diffusion weighted magnetic resonance imaging in oncologic settings. *Quantitative imaging in medicine and surgery* 3, 269–278.
- (78) Malayeri, A. A. et al. (2011). Principles and applications of diffusion-weighted imaging in cancer detection, staging, and treatment follow-up. *Radiographics : a review publication of the Radiological Society of North America, Inc* 31, 1773–1791.
- (79) Parikh, T. et al. (2008). Focal liver lesion detection and characterization with diffusion-weighted MR imaging: comparison with standard breath-hold T2-weighted imaging. *Radiology* 246, 812–822.
- (80) Goshima, S. et al. (2008). Diffusion-weighted imaging of the liver: optimizing b value for the detection and characterization of benign and malignant hepatic lesions. *Journal of magnetic resonance imaging : JMRI* 28, 691–697.
- (81) Sinha, S., Lucas-Quesada, F. A., Sinha, U., DeBruhl, N., and Bassett, L. W. (2002). In vivo diffusion-weighted MRI of the breast: potential for lesion characterization. *Journal of magnetic resonance imaging : JMRI* 15, 693–704.
- (82) Curvo-Semedo, L., Lambregts, D. M., Maas, M., Beets, G. L., Caseiro-Alves, F., and Beets-Tan, R. G. (2012). Diffusion-weighted MRI in rectal cancer: apparent diffusion coefficient as a potential noninvasive marker of tumor aggressiveness. *Journal of magnetic resonance imaging : JMRI* 35, 1365–1371.
- (83) deSouza, N. M. et al. (2008). Diffusion-weighted magnetic resonance imaging: a potential non-invasive marker of tumour aggressiveness in localized prostate cancer. *Clinical radiology* 63, 774–782.
- (84) Issa, B. (2002). In vivo measurement of the apparent diffusion coefficient in normal and malignant prostatic tissues using echo-planar imaging. *Journal of magnetic resonance imaging : JMRI* 16, 196–200.
- (85) Naganawa, S., Sato, C., Kumada, H., Ishigaki, T., Miura, S., and Takizawa, O. (2005). Apparent diffusion coefficient in cervical cancer of the uterus: comparison with the normal uterine cervix. *European radiology* 15, 71–78.
- (86) Bollineni, V. R., Kramer, G., Liu, Y., Melidis, C., and deSouza, N. M. (2015). A literature review of the association between diffusion-weighted MRI derived apparent diffusion coefficient and tumour aggressiveness in pelvic cancer. *Cancer treatment reviews* 41, 496–502.

- (87) Vandecaveye, V. et al. (2006). Evaluation of the larynx for tumour recurrence by diffusion-weighted MRI after radiotherapy: initial experience in four cases. *The British journal of radiology* 79, 681–687.
- (88) Moffat, B. A. et al. (2004). Diffusion imaging for evaluation of tumor therapies in preclinical animal models. *Magma (New York, N.Y.)* 17, 249–259.
- (89) Koh, D. M. et al. (2007). Predicting response of colorectal hepatic metastasis: value of pretreatment apparent diffusion coefficients. *AJR.American journal of roentgenology* 188, 1001–1008.
- (90) Sharma, U., Danishad, K. K., Seenu, V., and Jagannathan, N. R. (2009). Longitudinal study of the assessment by MRI and diffusion-weighted imaging of tumor response in patients with locally advanced breast cancer undergoing neoadjuvant chemotherapy. *NMR in biomedicine* 22, 104–113.
- (91) Dzik-Jurasz, A. et al. (2002). Diffusion MRI for prediction of response of rectal cancer to chemoradiation. *Lancet (London, England)* 360, 307–308.
- (92) Mardor, Y. et al. (2004). Pretreatment prediction of brain tumors' response to radiation therapy using high b-value diffusion-weighted MRI. *Neoplasia (New York, N.Y.)* 6, 136–142.
- (93) Chung, S. R. et al. (2015). Intravoxel incoherent motion MRI for liver fibrosis assessment: a pilot study. *Acta Radiologica (Stockholm, Sweden : 1987)* 56, 1428–1436.
- (94) Buisson, A. et al. (2015). Diffusion-weighted magnetic resonance enterocolonography in predicting remission after anti-TNF induction therapy in Crohn's disease. *Digestive and liver disease : official journal of the Italian Society of Gastroenterology and the Italian Association for the Study of the Liver*.
- (95) Sepahdari, A. R., Politi, L. S., Aakalu, V. K., Kim, H. J., and Razek, A. A. (2014). Diffusion-weighted imaging of orbital masses: multi-institutional data support a 2-ADC threshold model to categorize lesions as benign, malignant, or indeterminate. *AJNR.American journal of neuroradiology* 35, 170–175.
- (96) de Graaf, P. et al. (2012). Single-shot turbo spin-echo diffusion-weighted imaging for retinoblastoma: initial experience. *AJNR.American journal of neuroradiology* 33, 110–118.
- (97) Shen, G., Jia, Z., and Deng, H. (2016). Apparent diffusion coefficient values of diffusion-weighted imaging for distinguishing focal pulmonary lesions and characterizing the subtype of lung cancer: a meta-analysis. *European radiology* 26, 556–566.
- (98) Luo, Z. et al. (2016). Standard-b-value vs low-b-value DWI for differentiation of benign and malignant vertebral fractures: a meta-analysis. *The British journal of radiology* 89, 20150384.
- (99) Rovaris, M. et al. (2005). Diffusion MRI in multiple sclerosis. *Neurology* 65, 1526–1532.
- (100) Inglese, M., and Bester, M. (2010). Diffusion imaging in multiple sclerosis: research and clinical implications. *NMR in biomedicine* 23, 865–872.
- (101) Baumann, P. S. et al. (2012). High b-value diffusion-weighted imaging: a sensitive method to reveal white matter differences in schizophrenia. *Psychiatry research* 201, 144–151.
- (102) Defrancesco, M. et al. (2014). Changes in white matter integrity before conversion from mild cognitive impairment to Alzheimer's disease. *PloS one* 9(8), e106062.
- (103) Marzi, S., Stefanetti, L., Sperati, F., and Anelli, V. (2016). Relationship between diffusion parameters derived from intravoxel incoherent motion MRI and perfusion measured by dynamic contrast-enhanced MRI of soft tissue tumors. *NMR in biomedicine* 29, 6–14.
- (104) Wang, L. L. et al. (2014). Intravoxel incoherent motion diffusion-weighted MR imaging in differentiation of lung cancer from obstructive lung consolidation: comparison and correlation with pharmacokinetic analysis from dynamic contrast-enhanced MR imaging. *European radiology* 24, 1914–1922.
- (105) Jia, Q. J. et al. (2014). Initial experience of correlating parameters of intravoxel incoherent motion and dynamic contrast-enhanced magnetic resonance imaging at 3.0 T in nasopharyngeal carcinoma. *European radiology* 24, 3076–3087.

- (106) Lee, E. Y. et al. (2015). Relationship between intravoxel incoherent motion diffusion-weighted MRI and dynamic contrast-enhanced MRI in tissue perfusion of cervical cancers. *Journal of magnetic resonance imaging : JMRI* 42, 454–459.
- (107) Lee, Y. et al. (2015). Intravoxel incoherent motion diffusion-weighted MR imaging of the liver: effect of triggering methods on regional variability and measurement repeatability of quantitative parameters. *Radiology* 274, 405–415.
- (108) Hu, L. B., Hong, N., and Zhu, W. Z. (2015). Quantitative Measurement of Cerebral Perfusion with Intravoxel Incoherent Motion in Acute Ischemia Stroke: Initial Clinical Experience. *Chinese medical journal* 128, 2565–2569.
- (109) Suo, S. et al. (2016). Stroke assessment with intravoxel incoherent motion diffusion-weighted MRI. *NMR in biomedicine*.
- (110) Murphy, P. et al. (2015). Associations between histologic features of nonalcoholic fatty liver disease (NAFLD) and quantitative diffusion-weighted MRI measurements in adults. *Journal of magnetic resonance imaging : JMRI* 41, 1629–1638.
- (111) Ichikawa, S. et al. (2015). MRI-based staging of hepatic fibrosis: Comparison of intravoxel incoherent motion diffusion-weighted imaging with magnetic resonance elastography. *Journal of magnetic resonance imaging : JMRI* 42, 204–210.
- (112) Wu, C. H. et al. (2015). Assessing hepatic fibrosis: comparing the intravoxel incoherent motion in MRI with acoustic radiation force impulse imaging in US. *European radiology* 25, 3552–3559.
- (113) Hu, G. et al. (2015). Intravoxel incoherent motion MRI evaluation for the staging of liver fibrosis in a rat model. *Journal of magnetic resonance imaging : JMRI* 42, 331–339.
- (114) Koh, D. M., Collins, D. J., and Orton, M. R. (2011). Intravoxel incoherent motion in body diffusion-weighted MRI: reality and challenges. *AJR. American journal of roentgenology* 196, 1351–1361.

Part II

Liver

Effects of microperfusion in hepatic diffusion-weighted imaging

Hildebrand Dijkstra
Paul Baron
Peter Kappert
Matthijs Oudkerk
Paul E. Sijens

Published in European Radiology
2012, vol. 22, no. 4, pp. 891-899.

2.1 Abstract

Purpose: Clinical hepatic diffusion weighted imaging (DWI) generally relies on mono-exponential diffusion. The aim was to demonstrate that mono-exponential diffusion in the liver is contaminated by microperfusion and that the bi-exponential model is required.

Materials and Methods: Nineteen fasting healthy volunteers were examined with DWI (seven b-values) using fat suppression and respiratory triggering (1.5 T). Five different regions in the liver were analysed regarding the mono-exponentially fitted apparent diffusion coefficient (ADC), and the bi-exponential model: molecular diffusion (D_{slow}), microperfusion (D_{fast}) and the respective fractions ($f_{\text{slow/fast}}$). Data were compared using ANOVA and Kruskal–Wallis tests. Simulations were performed by repeating our data analyses, using just the DWI series acquired with b-values approximating those of previous studies.

Results: Median mono-exponentially fitted ADCs varied significantly ($p < 0.001$) between 1.107 and $1.423 \times 10^{-3} \text{ mm}^2/\text{s}$ for the five regions. Bi-exponential fitted D_{slow} varied between 0.923 and $1.062 \times 10^{-3} \text{ mm}^2/\text{s}$ without significant differences ($p = 0.140$). D_{fast} varied significantly, between 17.8 and $46.8 \times 10^{-3} \text{ mm}^2/\text{s}$ ($p < 0.001$). F-tests showed that the diffusion data fitted the bi-exponential model significantly better than the mono-exponential model ($F > 21.4$, $p < 0.010$). These results were confirmed by the simulations.

Conclusion: ADCs of normal liver tissue are significantly dependent on the measurement location because of substantial microperfusion contamination; therefore the bi-exponential model should be used.

2.2 Introduction

Diffusion weighted imaging (DWI) started with the introduction of intravoxel incoherent motion (IVIM) imaging by Le Bihan et al. in the late 1980s (1). IVIM was developed to quantify microscopic translational motions in a voxel by defining the apparent diffusion coefficient (ADC), which integrates the effects of both molecular diffusion and microperfusion of blood in the capillary network (2). The ADC is sensitive to all intravoxel incoherent motions and equals the diffusion coefficient D_{slow} if only molecular diffusion is present. However, ADCs of brain tissue were often higher than expected because of microperfusion contamination. Therefore, the IVIM theory was extended to a bi-exponential model that was used to obtain pure and separate images of molecular diffusion D_{slow} and microperfusion D_{fast} (3).

DWI was introduced in the abdominal organs from the early 1990s (4); before that, it was primarily limited to the brain (1–3, 5). Subsequently, DWI of liver parenchyma and liver abnormalities was performed, however mainly by application of ADC quantification using the mono-exponential model (6–8). Yamada et al. then demonstrated that the effect of microperfusion significantly contributes to the ADCs of abdominal organs and hepatic lesions (9). They concluded by application of the bi-exponential model that the molecular diffusion coefficient D_{slow} and microperfusion fraction f are useful parameters for the characterisation of hepatic lesions. This was supported by later studies that showed the additional value of using the bi-exponential model for the clinical evaluation of hepatic parenchyma and hepatic lesions (10–14).

However, we noticed that most liver studies up to now rely on the ADC as a measure for molecular diffusion without taking into account microperfusion contamination (15–17). Only a few liver studies avoided microperfusion contamination by choosing only higher b-values starting from 50 s/mm^2 for the calculation of ADCs (18–23). Others showed that besides the MRI technique and field strength, the location of the measurement can influence the ADC significantly (21, 24–26). We, however, suspected that the variation of ADCs in different regions of the liver was due to microperfusion contamination.

Thus, the purpose of this study was to demonstrate that mono-exponential diffusion in the liver is contaminated by microperfusion and that the bi-exponential model is required.

2.3 Materials and methods

2.3.1 Study population

The protocol of the study was approved by the hospital's institutional review board, and informed consent was obtained from all subjects. The study population comprised of 10 men and 9 women ($n = 19$) ranging from 20 to 62 years old (mean 32.9 years). All subjects were healthy volunteers, without relevant medical history, with a body mass index (BMI) ranging from 20 to 32 kg/m². The only preparation before the examination was an 8-h fasting period.

2.3.2 MR protocols

All subjects were prospectively examined using MR imaging at 1.5 T (Magnetom Avanto, Siemens Medical Solutions, Erlangen, Germany). The body coil served as a transmitter and a six element spine matrix coil in combination with the body matrix as a receiver. After routine localiser- and T2-weighted imaging a series ($b = 0, 50, 100, 250, 500, 750, 1000$ s/mm²) of isotropic diffusion weighted images (DWI) were acquired using a spin echo based echo-planar imaging (EPI) sequence in combination with spectral adiabatic inversion recovery (SPAIR) fat suppression. The acquisition was gated using PACE respiratory triggering (TR = 3100–6500 ms) and was tuned with the following parameters: TE 75 ms; slice-thickness 6 mm; slice-gap 18 mm; FOV 379x284 mm; matrix 192x144; bandwidth 1735 Hz/pixel; averages 2 and parallel acquisition technique GRAPPA with acceleration factor 2. Diffusion gradients (25 mT/m) were applied in the phase, read, and z-directions separately.

In total 9 transverse slices were acquired with an 18 mm slice gap to cover the whole liver within an average total acquisition time of 8.1 minutes (range; 4.7 - 11.1 minutes). The image acquisition took place in an interleaved mode; first slices 1, 4 and 7 were consecutively acquired with $b=0$ value, then the same slices with $b=50$ value and so on up to $b=1000$. Subsequently, slices 2, 5 and 8 were acquired in the same way, and finally slices 3, 6 and 9 also.

2.3.3 Image analysis

A programmable graphical and calculus environment was used (Matlab, The Mathworks, Natick, MA, USA) to develop a tool for analysing the DWI series using mono- and bi-exponential fitting procedures. First, the DWI data were loaded and the five liver regions were defined for all 19 datasets by drawing circular regions-of-interest (ROIs) with a diameter of 22.3 mm on selected transverse 6-mm slices (Fig. 2.1).

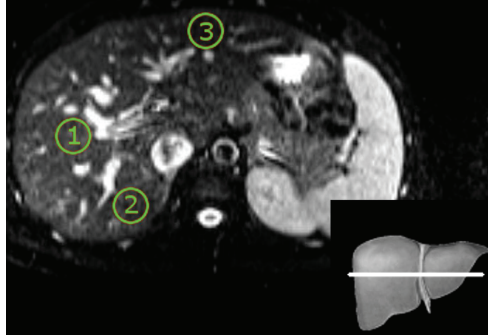


Figure 2.1: Diffusion in the liver was measured in five locations (ROI 1 to 5) with a diameter of 22.3 mm. A. Transverse plane of the medial liver with ROI 1 central in the right lobe (segments 5/8), ROI 2 dorso-lateral in the right lobe (segments 6/7) and ROI 3 ventral in the left lobe (segments 2/3). B. Transverse plane of the cranial liver with ROI 4 dorso-lateral in the right lobe (segment 7) C. Transverse plane of the caudal liver with ROI 5 near the gallbladder (segment 5)

For each dataset three slices at three different levels were selected; medial at the level of the right portal vein, cranial above the level of the left portal vein and caudal at the level of the splenic vein. The first three regions were drawn in the medial liver slice: central in the right lobe (ROI 1, segments 5/8), dorso-lateral in the right lobe (ROI 2, segments 6/7) and ventral in the left lobe (ROI 3, segments 2/3). The fourth region was drawn in the cranial liver slice, dorso-lateral in the right lobe (ROI 4, segment 7), and the last region in the caudal liver slice, near the gallbladder (ROI 5, segment 5). Any nearby visible vascular and biliary structures were avoided. For each ROI and all seven b-values the average signal intensity S was calculated and stored. Then, the signal intensities S and all seven b-values were fitted to the bi-exponential model [3]:

$$\frac{S}{S_0} = f_{fast} \cdot e^{-b \cdot D_{fast}} + f_{slow} \cdot e^{-b \cdot D_{slow}} \quad (2.1)$$

where S_0 is the maximum signal intensity, D_{fast} is the fast component representing microperfusion, f_{fast} is the fraction of microperfusion, D_{slow} is the slow component repre-

senting molecular diffusion and f_{slow} is the fraction of molecular diffusion ($f_{\text{slow}} = 1 - f_{\text{fast}}$).

Equation 1 was fitted by the Nelder-Mead simplex direct search method with bound constraints (Table 2.1), which performs a constrained non-linear minimisation of the sum of the squared residuals (27, 28). Finally, the conventional ADC was determined using linear regression analysis of the natural log of signal intensities S versus all seven b -values, where A is the intercept of the signal (2):

$$S = Ae^{-b \cdot ADC} \quad (2.2)$$

Table 2.1: Fitting parameters. *Number of parameters

Bi-exponential fit (p = 3)*	Lower-bound	Higher-bound	Initial guess
f_{fast} (unitless)	1,00E-08	1	0.4
D_{fast} ($\times 10^{-3}$ mm ² /s)	1,00E-05	100	10
D_{slow} ($\times 10^{-3}$ mm ² /s)	1,00E-05	10	1

2.3.4 Parametric maps

For one subject, parametric maps of ADC and D_{slow} were calculated by fitting the diffusion signal of a 4 by 4 pixels area to the mono- and bi-exponential model. The area was then moved 4 pixels until the whole liver matrix (192x144) was covered, resulting in a parametric map of 48x36. Subsequently, the parametric map was rescaled to the original matrix size by linear interpolation.

2.3.5 Influence of blood vessels

To illustrate the effects of microperfusion on the mono- and bi-exponential models, an ROI was drawn in one subject and blood vessels were included in the ROI. Then the same ROI was moved slightly until the blood vessels were excluded from the ROI. In both cases ADC, D_{slow} , D_{fast} and f were calculated and the curves presented in a figure for comparison.

2.3.6 Simulation study

A systematic literature search was performed in order to compare our results with previous findings. We included multi-region DWI liver studies that determined the ADC for healthy liver tissue for at least 20 patients and published a p-value for the significance of the ADC difference among the regions. Then the results of the reviewed studies were simulated by performing mono- and bi-exponential analyses on our data using the b-values and regions mentioned in the review studies. The ADC, D_{slow} , D_{fast} , f_{slow} and f_{fast} resulting from the simulation were then compared with those of the reviewed studies.

2.3.7 Statistical analysis

Statistical analysis was performed using SPSS (SPSS 18, Chicago, IL, USA). All data were tested for normality using Shapiro–Wilk tests. For normally distributed data (ADC and D_{slow}) one-way ANOVA tests were used to compare measurements between different liver regions. For non-normally distributed data (D_{fast} and f) the differences between liver regions were determined using non-parametric Kruskal–Wallis tests. The central tendency and variability of the data were quantified by the median and the median deviation (29) where

$$\sigma_{1/2} = \text{median}(|x_i - \mu_{1/2}|) \quad (2.3)$$

For each individual fitting procedure the coefficient of correlation (goodness-of-fit) R^2 was adjusted for the number of parameters p and the number of data points n :

$$R_{adj}^2 = 1 - \frac{(1 - R^2) \cdot (n - 1)}{n - p} \quad (2.4)$$

where $n = 7$ for seven b-values and $p = 2$ or 3 for mono- and bi-exponential models respectively. F-tests were performed to evaluate whether the bi-exponential model was justified over a mono-exponential model:

$$F = \frac{(SSE_{\text{mono}} - SSE_{\text{bi}}) / (DF_{\text{mono}} - DF_{\text{bi}})}{SSE_{\text{bi}} / DF_{\text{bi}}} \quad (2.5)$$

where SSE_{mono} and SSE_{bi} are the sum-of-squared errors (SSE) of the mono- and bi-

exponential fits respectively, and DF_{mono} and DF_{bi} are the degrees of freedom of both analyses ($DF = n - p$). All statistical analyses had a significance level of 5%.

2.4 Results

The mono-exponentially fitted ADCs were significantly different ($p < 0.001$) among the five regions and normally distributed (Tables 2.2 and 2.3). The left lobe showed the highest ADC ($1.423 \times 10^{-3} \text{ mm}^2/\text{s}$) and the lowest ADC was found centrally in the medial right lobe ($1.107 \times 10^{-3} \text{ mm}^2/\text{s}$).

Table 2.2: p values (Shapiro–Wilk tests) indicate deviations from normal distribution ($p < 0.05$). Measurements of D_{fast} and f fractions were non-normally distributed, D_{slow} values were normally distributed

Region	Segment	ADC	D_{slow}	D_{fast}	$f_{\text{slow/fast}}$
1	5/8	0.798	0.929	0.022*	0.761
2	6/7	0.895	0.708	0.086	0.005*
3	2/3	0.814	0.309	0.007*	0.900
4	7	0.208	0.523	0.563	0.023*
5	5	0.230	0.735	0.167	0.663

The bi-exponentially fitted D_{slow} was not shown to be significantly different ($p = 0.140$) among the five regions and were normally distributed (Tables 2.2 and 2.3). The median of the D_{slow} components varied between 0.923 and $1.062 \times 10^{-3} \text{ mm}^2/\text{s}$ for each of the five regions.

The bi-exponentially fitted D_{fast} was significantly different ($p < 0.001$) between the five regions and non-normally distributed (Tables 2.2 and 2.3). The median of the D_{fast} components varied between 17.8 and $46.8 \times 10^{-3} \text{ mm}^2/\text{s}$ for the five regions. The left lobe showed the highest fraction of microperfusion f_{fast} (47%) and the lowest fraction of diffusion f_{slow} (53%). The dorso-lateral right lobe showed the lowest fraction of microperfusion f_{fast} (24%) and the highest fraction of molecular diffusion f_{slow} (76%). The f_{slow} and f_{fast} fractions were significantly different among the five regions ($p < 0.001$) (Table 2.3).

The adjusted R^2 showed that the bi-exponential model fitted better to the diffusion data than the mono-exponential model for each liver region ($R^2_{\text{adj, bi}} > R^2_{\text{adj, mono}}$).

Table 2.3: Data are medians \pm median absolute deviations. Both mono- and bi-exponential fits were determined with seven b values (0, 50, 100, 250, 500, 750 and 1000). R_{adj}^2 is the goodness-of-fit correlation coefficient. p values indicate the significance of differences between different regions in the liver. *One-way ANOVA. † Non-parametric Kruskal-Wallis

		Mono-exponential fit ($R_{adj}^2 = 0.479$)		Bi-exponential fit ($R_{adj}^2 = 0.969$)		
Region	Segment	ADC ($\times 10^{-3}$ mm ² /s)	f_{fast} (%)	D_{fast} ($\times 10^{-3}$ mm ² /s)	f_{slow} (%)	D_{slow} ($\times 10^{-3}$ mm ² /s)
1	5/8	1.107 \pm 0.101	29 \pm 5	33.5 \pm 12.1	71 \pm 5	0.923 \pm 0.148
2	6/7	1.204 \pm 0.055	24 \pm 3	37.8 \pm 11.0	76 \pm 3	1.038 \pm 0.052
3	2/3	1.423 \pm 0.118	47 \pm 9	17.8 \pm 7.1	53 \pm 9	0.900 \pm 0.228
4	7	1.239 \pm 0.090	24 \pm 5	46.8 \pm 19.8	76 \pm 5	1.062 \pm 0.118
5	5	1.107 \pm 0.102	29 \pm 4	43.6 \pm 9.7	71 \pm 4	0.954 \pm 0.120
P-value		<0.001*	<0.001†	<0.001†	<0.001†	0.140*

Furthermore, the F-tests showed that the diffusion data fitted significantly better to the bi-exponential model ($F > 21.4$, $p < 0.010$) than to the mono-exponential model in all individual fitting procedures.

2.4.1 Parametric maps

DWI data of the medial liver of one subject were used to calculate ADC and D_{slow} maps (Fig. 2.2). The D_{slow} map showed a more homogeneous distribution of the bi-exponential fitted slow diffusion throughout the liver. The ADC map showed more differing values between different regions of the liver, especially near blood vessels and in the left lobe.

2.4.2 Influence of blood vessels

In one subject, the effects of microperfusion on the mono- and bi-exponential models were illustrated by including blood vessels in the ROI; this showed a large influence of microperfusion on the ADC (Fig. 2.3). When the blood vessels were excluded from the ROI a decreased ADC was observed. However, D_{slow} was similar to when blood vessels were included in the ROI.

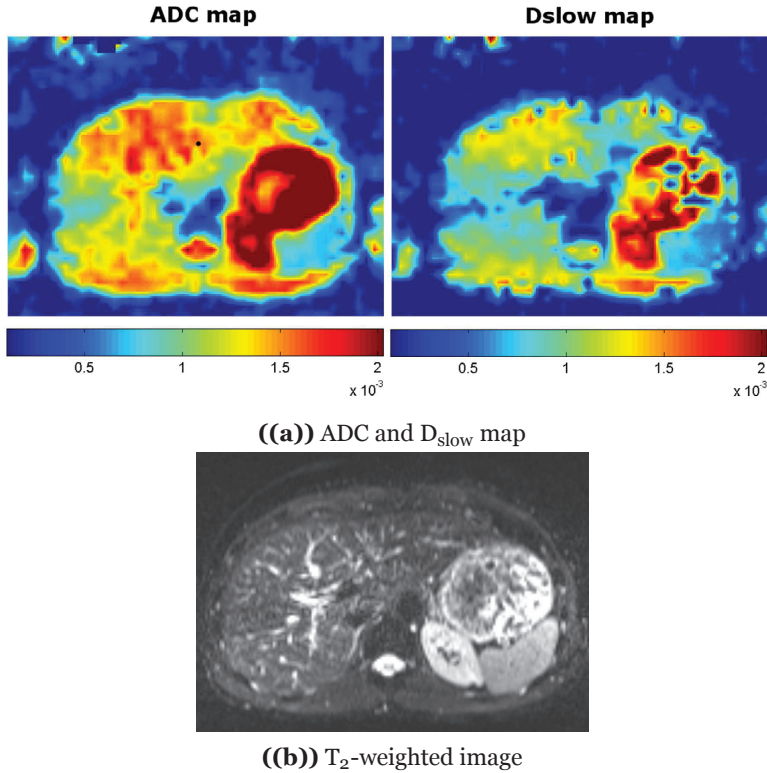


Figure 2.2: An example of ADC and D_{slow} maps of the medial liver. **A)** ADC map (left) and D_{slow} map (right) of the medial liver which were scaled equally from 0.1×10^{-3} to 2×10^{-3} mm^2/s . The D_{slow} map shows a more homogeneous distribution of the bi-exponential fitted slow diffusion component throughout the liver. The ADC map shows significantly different values between different regions of the liver, especially near blood vessels and in the left lobe. **B)** The anatomical position of the ADC and D_{slow} maps

2.4.3 Simulation study

The systematic literature search resulted in six multi-region DWI studies of the liver in which a minimal of 20 patients were included and in which between two and four different regions of healthy liver parenchyma were analysed (13, 19, 21, 25, 26, 30). Studies in which mono-exponential analyses were performed showed ADCs between 1.00 and 2.69×10^{-3} mm^2/s using sets of two, three or five b-value combinations between 0 and 1300 s/mm^2 (Table 2.4). We found ADCs between 0.94 and 2.39×10^{-3} mm^2/s when using the same b-value combinations. All mono-exponential studies reported significantly ($p < 0.05$) different ADCs between the different liver regions, this was confirmed by our simulation study ($p < 0.001$).

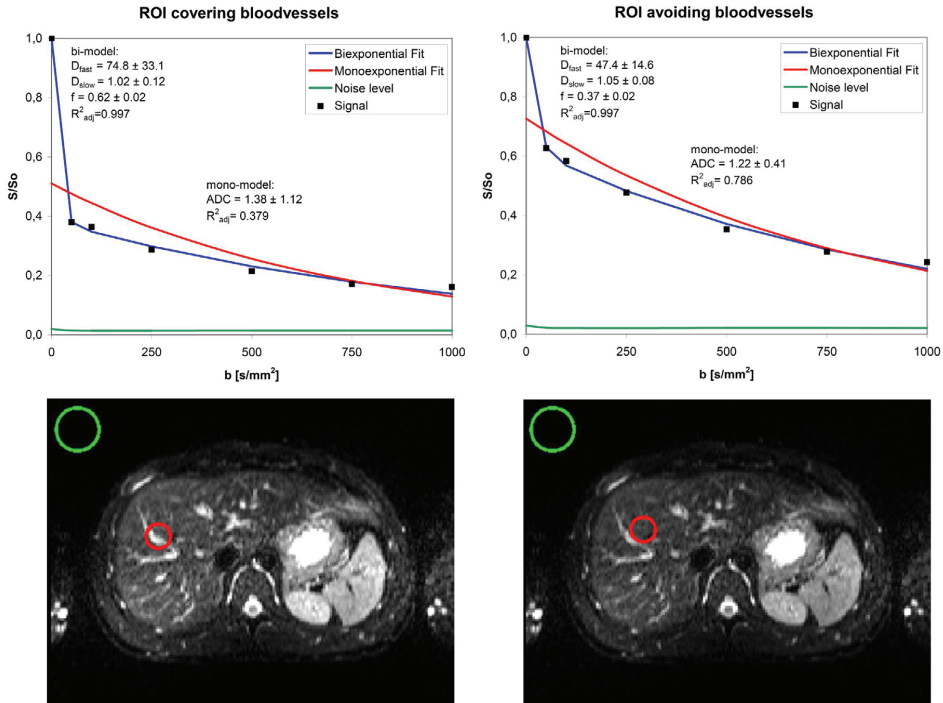


Figure 2.3: An example of the effects of microperfusion on DWI measurements. To illustrate the effects of microperfusion on the mono- and bi-exponential model, blood vessels were included in the ROI (left) which showed a large influence of microperfusion on the ADC. Then the same ROI was moved slightly until the blood vessels were excluded from the ROI (right) which showed a decreased ADC, however D_{slow} was similar to when blood vessels were included in the ROI. The noise was defined as the average signal measured in air (green ROI), away from any visible artefacts

In one study a bi-exponential analysis of two different regions of liver parenchyma was performed using a series of ten b -values between 0 and 800 s/mm^2 (Table 2.5) (13). They did not find significantly different D_{slow} components among different liver regions ($p=0.5$); this was confirmed by our simulation study ($p=0.105$).

2.5 Discussion

The aim of this study was to demonstrate that mono-exponential diffusion in the liver is contaminated by microperfusion. We suspected that variation of ADCs in different regions of the liver is due to microperfusion contamination and that therefore the bi-exponential model is required. We found that the ADC of normal liver tissue is sub-

stantially dependent on the location; however, the bi-exponentially fitted D_{slow} is not dependent on the location of the measurement. We used terminology according to the suggestions of Guiu and Cercueil who convincingly advocated for the use of D_{slow} to describe molecular diffusion properties and D_{fast} to describe microperfusion (31).

Table 2.4: ADCs are means in units of $10^{-3} \text{ mm}^2/\text{s}$. p values (one-way ANOVA) indicate the significance of differences between different regions in the liver. †p value was not mentioned; however the significance level was 5%. *Mürtz et al. [19] did not evaluate regions in the left lobe; therefore we excluded ROI 3 (left lobe) from the simulation

Ref.	n	Reviewed data				Simulated on our data		
		b-values (s/mm ²)	#regions	ADC (range)	p value	b-values (s/mm ²)	ADC (range)	p value
Nasu et al. [25]	30	0, 500	2	1.98-2.69	<0.001	0, 500	1.64-2.39	<0.001
Yoshikawa et al. [30]	45	0, 600	4	1.55-1.63	<0.05†	0, 750	1.38-1.91	<0.001
Kiliçkesmez et al. [26]	50	0, 500, 600	4	1.34-1.77	<0.01	0, 500, 750	1.42-1.98	<0.001
Bruegel et al. [21]	90	50, 300, 600	4	1.12-1.44	<0.001	50, 250, 750	1.02-1.41	<0.001
Mürtz et al. [19]	36	50, 300, 700, 1000, 1300	3	1.00-1.16	<0.05†	50, 250, 750, 1000	0.94-1.10 (only RL)*	0.001

Table 2.5: Data are means. p values indicate the significance of differences between different regions in the liver. *One-way ANOVA. †Non-parametric Kruskal-Wallis

	Reviewed data [13]		Simulated on our data	
	Mean (range)	p value	Mean (range)	p value
N	25		19	
b-values (s/mm ²)	0, 10, 20, 30, 50, 80, 100, 200, 400, 800		0, 50, 100, 250, 500, 750	
#regions	2		5	
f_{fast} (%)	26–31	0.07	26–43	0.000†
D_{fast} ($\times 10^{-3} \text{ mm}^2/\text{s}$)	71.0–85.1	0.1	27.9–57.2	0.001†
f_{slow} (%)	69–74	0.07	57–74	0.000†
D_{slow} (mm ² /s)	1.02–1.16	0.5	0.98–1.18	0.105*

Our results agree with earlier studies reporting significant differences among ADCs obtained in different regions in the liver (19, 21, 25, 26, 30). ADCs in our study (1.107 to $1.423 \times 10^{-3} \text{ mm}^2/\text{s}$) were consistent with those of previous reports, which showed a

large range (0.69 to $2.69 \times 10^{-3} \text{ mm}^2/\text{s}$) of ADCs for normal liver tissue (15, 25, 32). The results on D_{slow} were supported by Luciani et al.; they also found no significant differences between D_{slow} of normal liver tissue (13). They found that D_{slow} varied between 1.02 and $1.16 \times 10^{-3} \text{ mm}^2/\text{s}$; this is comparable to our range (0.98 to $1.18 \times 10^{-3} \text{ mm}^2/\text{s}$) when we simulated their results using our data and similar b-values.

The demonstrated regional dependence of the ADC contrary to the non-regional dependence of D_{slow} can be explained from the differences between the mono- and the bi-exponential models. The mono-exponentially fitted ADC is to a high degree sensitive to microperfusion, which was already shown by Le Bihan et al. in the brain (2). When the DWI sequence contains b-values in the microperfusion range, and the microperfusion is relatively high compared with the diffusion component, then the model will result in a high ADC compared with D_{slow} . When there is no microperfusion, which has been reported for fibroglandular breast tissue, the ADC will be comparable to D_{slow} (33).

Hence the ADC of the liver is to a large extent dependent on microperfusion, especially when the DWI sequence contains several b-values in the microperfusion range (14). This is why in some studies researchers tried to choose b-values not within the microperfusion range (18–23). For example, Perman et al. observed that the ADC value for liver decreased from 1.36 to $0.98 \times 10^{-3} \text{ mm}^2/\text{s}$ when the $b=0$ value was omitted; this is similar to the range of D_{slow} that we found. In a recent consensus report on DWI, it was recommended to use two b-values (>100 and between 500 and 1000 s/mm^2) for ADC assessments (34). It is, however, difficult to choose b-values such that microperfusion contamination of the ADC is avoided, because the microperfusion effects of the tissue are not known beforehand. We demonstrated in our simulation study that, although low b-values were excluded, the ADC of liver tissue was to a large extent contaminated by microperfusion and that this resulted in apparent differences of the diffusion between liver regions.

The simulation study also showed that the variety of ADC values of healthy liver tissue published in the literature, were probably caused by the choice of b-values, and the mono-exponential model itself. This is a pitfall of using the ADC as a measure for molecular diffusion; there is no optimal combination of b-values, because the amount of microperfusion determines the optimal sequence of b-values and this is not known a priori. Recently, a similar simulation study was performed in the kidneys; they also found that the variability of the ADC in the kidneys is caused by the use of the mono-exponential model (35).

The microperfusion component D_{fast} of the bi-exponential model significantly de-

depends on the location of the measurement. This contradicts with the results of Luciani et al., who did not find a location dependency of D_{fast} , possibly because they compared just two regions (left and right lobe) (13). The range ($71.0 - 85.1 \times 10^{-3} \text{ mm}^2/\text{s}$) was higher than what we found ($27.9 - 57.2 \times 10^{-3} \text{ mm}^2/\text{s}$) when we simulated their results using our data and similar b-values. This may reflect the use of different calculation methods. In our study f , D_{fast} and D_{slow} of an ROI were calculated by taking the medians of the underlying b-maps as an input for the fitting procedure, where Luciani et al. first calculated D_{fast} , D_{slow} and f maps on a pixel-by-pixel based fitting procedure, after which the average of an ROI was calculated. In addition, they used six b-values under $100 \text{ s}/\text{mm}^2$ (versus two in our study), which tends to decrease the uncertainty of the fitting algorithm, and increase the slope of the curve close to zero. This might explain the higher D_{fast} and the decreased range of D_{fast} in their study. However, we have shown that even with seven (rather than 16 b-values) the bi-exponential fits are already extremely accurate, which is supported by the nearly identical values of D_{slow} in their study and our simulation study. Too little b-values under $b=100 \text{ s}/\text{mm}^2$ can however hamper an accurate determination of D_{fast} , especially when analysing tissues with high D_{fast} values, which can be expected in pathology or near blood vessels.

The increase in the ADC in the left lobe, which was demonstrated in Fig. 2.2, is usually explained from the increased cardiac motion in the left lobe (19, 25, 36–38). However, we found that the fraction of microperfusion f_{fast} in the left lobe was almost a factor two higher than in other liver locations. Although pseudo-anisotropy is a known artefact of respiratory triggering in the liver (39), we suspect that the increased ADC in the left lobe may be caused by extensive microperfusion contamination of the ADC and to a lesser extent by either cardiac or respiratory artefacts. This is supported by a study on the hepatic perfusion of eight hepatic segments by dual-source computed tomography (40). They found that the hepatic perfusion index (HPI) was significantly higher in segment 3 (left lobe) than in segments 5 to 8 (right lobe), and suggested that this might be related to the anatomy of the liver vessels. Another study using pharmacokinetic analysis of dynamic contrast-enhanced MRI demonstrated that regional variations in liver microcirculation can be displayed by colour-coded parameter maps (41). They found a minor variation of perfusion in an apical section of a transplanted liver. The left part of the liver, corresponding to segment 2, showed a different perfusion rate than the right part of the liver. In an experimental study on rats using perfusion CT, the relative blood flow in the left lobe was 17% higher than in the right lobe of the liver (42). We suspect that these regional variations in the density of small blood vessels and capillaries caused the heterogeneous appearance of microperfusion throughout the liver. This

is supported by our analysis of including a blood vessel in the ROI, which resulted in more microperfusion contamination than when blood vessels were avoided.

2.5.1 Limitations

Some studies have reported on age-related changes in liver structure and function (43, 44). However, Pasquinelli et al. showed no significant variations in liver DWI quantitative parameters according to the age of the subject (45). Therefore, we assumed that the possible effects of age in our cohort are far smaller than the demonstrated significant region dependency of the ADC in the liver. Although the conclusions in this study are drawn from healthy volunteers, we suspect that the effects of microperfusion are much larger in pathology, and should therefore be applicable to patient data also.

2.5.2 Conclusions

In conclusion, the ADC of normal liver tissue is significantly dependent on the measurement location because of substantial microperfusion contamination; therefore the bi-exponential model should be used. Currently, the diagnostic use of DWI for discriminating hepatic masses, liver cirrhosis and fibrosis is mainly based on the ADC, and the discrimination between diseased and healthy tissue may therefore be hampered (6–8, 15–18, 20, 21, 23, 30, 37, 46). Thus, the bi-exponential model is essential for the future development of the clinical diagnostic application of DWI in the liver.

2.6 References

- (1) Bihan, D. L., Breton, E., Lallemand, D., Grenier, P., Cabanis, E., and Laval-Jeantet, M. (1986). MR imaging of intravoxel incoherent motions: application to diffusion and perfusion in neurologic disorders. *Radiology* 161, 401–407.
- (2) Bihan, D. L., Breton, E., Lallemand, D., Aubin, M. L., Vignaud, J., and Laval-Jeantet, M. (1988). Separation of diffusion and perfusion in intravoxel incoherent motion MR imaging. *Radiology* 168, 497–505.
- (3) Bihan, D. L., Turner, R., Moonen, C. T., and Pekar, J. (1991). Imaging of diffusion and microcirculation with gradient sensitization: design, strategy, and significance. *Journal of magnetic resonance imaging : JMRI* 1, 7–28.
- (4) Muller, M. F., Prasad, P., Siewert, B., Nissenbaum, M. A., Raptopoulos, V., and Edelman, R. R. (1994). Abdominal diffusion mapping with use of a whole-body echo-planar system. *Radiology* 190, 475–478.

- (5) Turner, R., Bihan, D. L., Maier, J., Vavrek, R., Hedges, L. K., and Pekar, J. (1990). Echo-planar imaging of intravoxel incoherent motion. *Radiology* 177, 407–414.
- (6) Namimoto, T., Yamashita, Y., Sumi, S., Tang, Y., and Takahashi, M. (1997). Focal liver masses: characterization with diffusion-weighted echo-planar MR imaging. *Radiology* 204, 739–744.
- (7) Ichikawa, T., Haradome, H., Hachiya, J., Nitatori, T., and Araki, T. (1999). Diffusion-weighted MR imaging with single-shot echo-planar imaging in the upper abdomen: preliminary clinical experience in 61 patients. *Abdominal Imaging* 24, 456–461.
- (8) Kim, T., Murakami, T., Takahashi, S., Hori, M., Tsuda, K., and Nakamura, H. (1999). Diffusion-weighted single-shot echoplanar MR imaging for liver disease. *AJR.American journal of roentgenology* 173, 393–398.
- (9) Yamada, I., Aung, W., Himeno, Y., Nakagawa, T., and Shibuya, H. (1999). Diffusion coefficients in abdominal organs and hepatic lesions: evaluation with intravoxel incoherent motion echo-planar MR imaging. *Radiology* 210, 617–623.
- (10) Moteki, T., Horikoshi, H., Oya, N., Aoki, J., and Endo, K. (2002). Evaluation of hepatic lesions and hepatic parenchyma using diffusion-weighted reordered turboFLASH magnetic resonance images. *Journal of magnetic resonance imaging : JMRI* 15, 564–572.
- (11) Moteki, T., and Horikoshi, H. (2006). Evaluation of hepatic lesions and hepatic parenchyma using diffusion-weighted echo-planar MR with three values of gradient b-factor. *Journal of magnetic resonance imaging : JMRI* 24, 637–645.
- (12) Coenegrachts, K. et al. (2009). Evaluation of true diffusion, perfusion factor, and apparent diffusion coefficient in non-necrotic liver metastases and uncomplicated liver hemangiomas using black-blood echo planar imaging. *European Journal of Radiology* 69, 131–138.
- (13) Luciani, A. et al. (2008). Liver cirrhosis: intravoxel incoherent motion MR imaging—pilot study. *Radiology* 249, 891–899.
- (14) Moteki, T., and Horikoshi, H. (2011). Evaluation of noncirrhotic hepatic parenchyma with and without significant portal vein stenosis using diffusion-weighted echo-planar MR on the basis of multiple-perfusion-components theory. *Magnetic resonance imaging* 29, 64–73.
- (15) Taouli, B., and Koh, D. M. (2010). Diffusion-weighted MR imaging of the liver. *Radiology* 254, 47–66.
- (16) Taouli, B., Vilgrain, V., Dumont, E., Daire, J. L., Fan, B., and Menu, Y. (2003). Evaluation of liver diffusion isotropy and characterization of focal hepatic lesions with two single-shot echo-planar MR imaging sequences: prospective study in 66 patients. *Radiology* 226, 71–78.
- (17) Talwalkar, J. A., Yin, M., Fidler, J. L., Sanderson, S. O., Kamath, P. S., and Ehman, R. L. (2008). Magnetic resonance imaging of hepatic fibrosis: emerging clinical applications. *Hepatology (Baltimore, Md.)* 47, 332–342.
- (18) Chan, J. H. et al. (2001). Diffusion-weighted MR imaging of the liver: distinguishing hepatic abscess from cystic or necrotic tumor. *Abdominal Imaging* 26, 161–165.
- (19) Murtz, P., Flacke, S., Traber, F., van den Brink, J. S., Gieseke, J., and Schild, H. H. (2002). Abdomen: diffusion-weighted MR imaging with pulse-triggered single-shot sequences. *Radiology* 224, 258–264.
- (20) Boulanger, Y. et al. (2003). Diffusion-weighted MR imaging of the liver of hepatitis C patients. *NMR in biomedicine* 16, 132–136.
- (21) Bruegel, M. et al. (2008). Characterization of focal liver lesions by ADC measurements using a respiratory triggered diffusion-weighted single-shot echo-planar MR imaging technique. *European radiology* 18, 477–485.
- (22) Perman, W. H., Balci, N. C., Akduman, I., and Kuntz, E. (2009). Magnetic resonance measurement of diffusion in the abdomen. *Topics in magnetic resonance imaging : TMRI* 20, 99–104.
- (23) Sandrasegaran, K. et al. (2009). Value of diffusion-weighted MRI for assessing liver fibrosis and cirrhosis. *AJR.American journal of roentgenology* 193, 1556–1560.

- (24) Dale, B. M., Braithwaite, A. C., Boll, D. T., and Merkle, E. M. (2010). Field strength and diffusion encoding technique affect the apparent diffusion coefficient measurements in diffusion-weighted imaging of the abdomen. *Investigative radiology* 45, 104–108.
- (25) Nasu, K., Kuroki, Y., Sekiguchi, R., Kazama, T., and Nakajima, H. (2006). Measurement of the apparent diffusion coefficient in the liver: is it a reliable index for hepatic disease diagnosis? *Radiation Medicine* 24, 438–444.
- (26) Kilickesmez, O., Yirik, G., Bayramoglu, S., Cimilli, T., and Aydin, S. (2008). Non-breath-hold high b-value diffusion-weighted MRI with parallel imaging technique: apparent diffusion coefficient determination in normal abdominal organs. *Diagnostic and interventional radiology (Ankara, Turkey)* 14, 83–87.
- (27) D'Errico, J. Understanding fminsearchbnd, MATLAB Central File Exchange. Available via <http://www.mathworks.com/matlabcentral/fileexchange/8277-fminsearchbnd>.
- (28) Lagarias, J., Reeds, J., Wright, M., and Wright, P. (1998). Convergence properties of the Nelder-Mead Simplex method in low dimensions. *SIAM J Optim* 9(1), 112–147.
- (29) Hampel, F. (1974). The Influence Curve and Its Role in Robust Estimation. *Journal of the American Statistical Association* 69, 383–393.
- (30) Yoshikawa, T. et al. (2006). ADC measurement of abdominal organs and lesions using parallel imaging technique. *AJR.American journal of roentgenology* 187, 1521–1530.
- (31) Guiu, B., and Cercueil, J. P. (2011). Liver diffusion-weighted MR imaging: the tower of Babel? *European radiology* 21, 463–467.
- (32) Chow, L. C., Bammer, R., Moseley, M. E., and Sommer, F. G. (2003). Single breath-hold diffusion-weighted imaging of the abdomen. *Journal of magnetic resonance imaging : JMRI* 18, 377–382.
- (33) Baron, P., Dorrius, M. D., Kappert, P., Oudkerk, M., and Sijens, P. E. (2010). Diffusion-weighted imaging of normal fibroglandular breast tissue: influence of microperfusion and fat suppression technique on the apparent diffusion coefficient. *NMR in biomedicine* 23, 399–405.
- (34) Padhani, A. R. et al. (2009). Diffusion-weighted magnetic resonance imaging as a cancer biomarker: consensus and recommendations. *Neoplasia (New York, N.Y.)* 11, 102–125.
- (35) Zhang, J. L. et al. (2010). Variability of renal apparent diffusion coefficients: limitations of the monoexponential model for diffusion quantification. *Radiology* 254, 783–792.
- (36) Koh, D. M. et al. (2006). Colorectal hepatic metastases: quantitative measurements using single-shot echo-planar diffusion-weighted MR imaging. *European radiology* 16, 1898–1905.
- (37) Kandpal, H., Sharma, R., Madhusudhan, K. S., and Kapoor, K. S. (2009). Respiratory-triggered versus breath-hold diffusion-weighted MRI of liver lesions: comparison of image quality and apparent diffusion coefficient values. *AJR.American journal of roentgenology* 192, 915–922.
- (38) Kwee, T. C. et al. (2009). Influence of cardiac motion on diffusion-weighted magnetic resonance imaging of the liver. *Magma (New York, N.Y.)* 22, 319–325.
- (39) Nasu, K., Kuroki, Y., Fujii, H., and Minami, M. (2007). Hepatic pseudo-anisotropy: a specific artifact in hepatic diffusion-weighted images obtained with respiratory triggering. *Magma (New York, N.Y.)* 20, 205–211.
- (40) Su, B. Y. et al. (2010). Features of eight segments of liver perfusion with the second generation dual-source computed tomography. *Zhongguo yi xue ke xue yuan xue bao.Acta Academiae Medicinae Sinicae* 32, 655–658.
- (41) Scharf, J. et al. (2007). Assessment of hepatic perfusion in transplanted livers by pharmacokinetic analysis of dynamic magnetic resonance measurements. *Investigative radiology* 42, 224–229.
- (42) Tutcu, S. et al. (2010). Hepatic perfusion changes in an experimental model of acute pancreatitis: evaluation by perfusion CT. *European Journal of Radiology* 75, 203–206.
- (43) Schmucker, D. L. (2005). Age-related changes in liver structure and function: Implications for disease ? *Experimental gerontology* 40, 650–659.

- (44) Schmucker, D. L. (1998). Aging and the liver: an update. *The journals of gerontology. Series A, Biological sciences and medical sciences* 53, B315–20.
- (45) Pasquinelli, F., Belli, G., Mazzoni, L. N., Grazioli, L., and Colagrande, S. (2011). Magnetic resonance diffusion-weighted imaging: quantitative evaluation of age-related changes in healthy liver parenchyma. *Magnetic resonance imaging* 29, 805–812.
- (46) Gourtsoyianni, S., Papanikolaou, N., Yarmenitis, S., Maris, T., Karantanas, A., and Gourtsoyianis, N. (2008). Respiratory gated diffusion-weighted imaging of the liver: value of apparent diffusion coefficient measurements in the differentiation between most commonly encountered benign and malignant focal liver lesions. *European radiology* 18, 486–492.

Assessment of the link between quantitative biexponential DWI and CE-MRI in the liver

Hildebrand Dijkstra
Matthijs Oudkerk
Peter Kappert
Paul E. Sijens

Submitted to Magnetic Resonance Imaging

3.1 Abstract

Purpose: To quantitatively associate intravoxel incoherent motion (IVIM) modeled diffusion-weighted imaging (DWI) measured in liver parenchyma and lesions with semi-quantitative contrast-enhanced (CE-)MRI when using intra- and extracellular contrast-agents.

Materials and Methods: Twenty-five patients underwent IVIM-DWI followed by multiphase CE-MRI using intracellular Gd-EOB-DTPA (n=20) or extracellular Gd-DOTA (n=5) concluded with IVIM-DWI. Diffusion (D_{slow}), microperfusion (D_{fast}), its fraction (f_{fast}), wash-in-rate (R_{early}) and late-enhancement-rate (R_{late}) of Gd-EOB-DTPA were calculated voxel-wise for the liver. Parenchyma and lesions were segmented. Pre-contrast IVIM was compared 1) between low, medium and high R_{early} for parenchyma 2) to post-contrast IVIM substantiated with simulations 3) between low and high R_{late} per lesion type.

Results: D_{fast} and f_{fast} increased ($P < 0.001$) with 25.6% and 33.8% between low and high R_{early} of Gd-EOB-DTPA. D_{slow} decreased (-15.0%; $P < 0.001$) with increasing R_{early} . Gd-DOTA demonstrated similar observations. f_{fast} (+10%; $P < 0.001$) and D_{fast} (+6.6%; $P < 0.001$) increased after Gd-EOB-DTPA, while decreasing after Gd-DOTA (-4.2% and -5.7%, $P < 0.001$) and were confirmed by simulations. For focal nodular hyperplasia lesions (n=5) D_{fast} and f_{fast} increased ($P < 0.001$) with increasing R_{late} , whereas for hepatocellular carcinoma (n=4) and adenoma (n=7) no differences were found.

Conclusion: Microperfusion measured by IVIM reflects perfusion in a way resembling CE-MRI. Also IVIM separated intra- and extracellular MR contrast media. This underlines the potential of IVIM in quantitative liver imaging.

3.2 Introduction

Hepatic diffusion weighted imaging (DWI) has been used from the beginning as a quantitative technique by deploying the apparent diffusion coefficient (ADC) (1). The ADC is obtained by calculating a mono-exponential fit from multiple (at least two) diffusion-weighted images, thereby integrating molecular diffusion and microperfusion effects in one quantitative parameter (2, 3). The concept of the ADC however has been derived from the more complex intravoxel incoherent motion (IVIM) model, which separates molecular diffusion and microperfusion effects by fitting a bi-exponential model to multiple DW images (3).

The additional value of IVIM to ADC, for example for the evaluation of hepatic parenchyma and hepatic lesions, has been demonstrated by several studies (4–8). However, there has been debate about the concept of separating molecular diffusion and microperfusion effects by IVIM. Especially the linkage to classical perfusion obtained from techniques such as (dynamic) contrast enhanced MRI remained unclear (9, 10).

Since then the validation of the microperfusion concept of IVIM has been continued by Wirestam et al. who correlated the IVIM microperfusion fraction to conventional cerebral blood volume obtained with dynamic susceptibility-contrast (DSC-) MRI (11). However, still the need for advanced processing of DWI and investigation of the exact nature of what is measured by IVIM has been stressed by Le Bihan recently (12, 13).

The purpose of this study was therefore to assess if IVIM can be linked to contrast-enhanced (CE-) MRI. This was approached firstly by comparing IVIM parameters (obtained pre-contrast) of liver parenchyma between increasing rates of contrast wash-in during the initial portal-venous phase of intra- and extracellular contrast agents, and secondly by comparing IVIM parameters of liver lesions between increasing rates of enhancement during the late hepatobiliary phase of an intracellular contrast agent. Finally IVIM parameters were compared before and after administering either intra- or extracellular contrast agents.

3.3 Materials and methods

3.3.1 Study population

The protocol of this prospective study was approved by the hospital's Institutional Review Board (IRB) and informed consent was obtained. Between January 2009 and

April 2009, patients with an indication of focal hepatic pathology were consecutively scheduled for MRI and DWI examinations as part of the clinical routine. After exclusion of cirrhotic and resected livers, the patient group ($n=25$) comprised 3 men and 22 women with an average age of 43.2 years (range: 7-69; one paediatric patient). The only preparation before the examination was a 4-h fasting period.

3.3.2 MR protocols

All subjects were examined on a 1.5 T MRI system (Magnetom Avanto, Siemens Medical Solutions, Erlangen, Germany). The body coil served as the transmitter and a 24-element spine matrix coil in combination with a 6-element body matrix as the receiver. After the localiser scans, routine T_1 and T_2 -weighted imaging series were acquired.

Subsequently, the pre-contrast series of diffusion weighted images (DWI) were obtained using a spin echo based single shot echo-planar imaging (SS-EPI) sequence in combination with spectral adiabatic inversion recovery (SPAIR) fat suppression as part of the clinical routine. DWI acquisitions ($b= 0, 50, 100, 250, 500, 750, 1000 \text{ s/mm}^2$) were gated using prospective acquisition correction (PACE) respiratory triggering ($TR = 3200\text{--}6900 \text{ ms}$) and tuned with the following parameters: $TE 75 \text{ ms}$; $FA 90^\circ$; slice-thickness 6 mm ; $FOV 380 \times 285 \text{ mm}^2$; matrix 192×144 ; bandwidth 1735 Hz/pixel ; 2 averages and generalized autocalibrating partially parallel acquisition (GRAPPA) with acceleration factor 2. Between 9 and 23 transverse slices were acquired in sequential mode to cover the liver within a total acquisition time between 1.0 and 2.2 minutes.

In total, 20 patients received intracellular gadoxetate disodium (Gd-EOB-DTPA, Primovist, Bayer, 0.025 mmol/kg) to acquire the multiphase contrast-enhanced (CE-) MRI scans. Both pre-administering contrast agent and 20, 90 and 900 seconds thereafter, T_1 -weighted 3D spoiled gradient echo series were acquired with the following parameters: $TE 2.59 \text{ ms}$; $TR 5.77 \text{ ms}$; $FA 10^\circ$; slice-thickness 3 mm ; $FOV 400 \times 275 \text{ mm}^2$; matrix 256×176 ; bandwidth 250 Hz/pixel ; no averages and GRAPPA with acceleration factor 2.

In total, 5 patients received extracellular gadoterate meglumine (Gd-DOTA, Dotarem, Guerbet, 0.1 mmol/kg) instead as part of the clinical routine. The post-contrast DWI series (with same acquisition parameters as pre-contrast DWI series) were obtained 11 ± 4 minutes after the administration of the contrast agents.

3.3.3 Fitting of DWI signal

Bi-exponential fitting procedures were performed using a programmable graphical and calculus environment (Matlab, The Mathworks, Natick, MA, USA). For all analyses, the diffusion-weighted signal intensities S were fitted bi-exponentially using the parameters prescribed by the intravoxel incoherent motion (IVIM) model (3, 14):

$$\frac{S}{S_0} = f_{fast} \cdot e^{-b \cdot D_{fast}} + f_{slow} \cdot e^{-b \cdot D_{slow}} \quad (3.1)$$

where S_0 is the maximum signal intensity, D_{fast} is the fast pseudodiffusion component referred to as microperfusion, f_{fast} is the fraction of microperfusion, D_{slow} is the slow diffusion component and f_{slow} is the fraction of the slow component ($f_{slow} = 1 - f_{fast}$) as defined previously by Le Bihan et al. (14). D_{slow} is referred to as the molecular diffusion in accordance with the study of Luciani et al. (6). Equation 3.1 was fitted by the Nelder-Mead simplex direct search method with bound constraints, which performs a constrained non-linear minimisation of the sum of the squared residuals (1, 15).

For each individual fitting procedure the coefficient of correlation (goodness-of-fit) R^2 was adjusted for the number of parameters p and the number of data points n :

$$R_{adj}^2 = 1 - \frac{(1 - R^2) \cdot (n - 1)}{n - p} \quad (3.2)$$

where $n = 7$ for seven b -values and $p = 2$ for bi-exponential models.

3.3.4 Semi-quantitative kinetics of CE-MRI

Liver perfusion was quantified using the CE-MRI series by a semi-quantitative analysis of signal intensity changes during the initial portal-venous phase and the late hepatobiliary phase:

$$R_{early} = \frac{1}{T_1^{pre} \cdot r_1} \frac{S_{90} - S_0}{S_0} \frac{1}{\Delta T_{early}} \quad (3.3)$$

$$R_{late} = \frac{1}{T_1^{pre} \cdot r_1} \frac{S_{900} - S_{90}}{S_0} \frac{1}{\Delta T_{late}} \quad (3.4)$$

where T_1^{pre} is the T_1 relaxation time of liver parenchyma (586 ms) pre-contrast, and r_1 is the T_1 relaxivity of Gd-EOB-DTPA (6.9 L/mmol/s). R_{early} (mmol/L/s) reflects the normalized rate of contrast wash-in during the initial portal-venous phase in the time interval $\Delta T_{\text{early}} = 90$ s. R_{late} (mmol/L/s) reflects the normalized rate of contrast enhancement during the late hepatobiliary phase in the time interval $\Delta T_{\text{late}} = 810$ s (only applicable to Gd-EOB-DTPA).

Rigid linear image registration between DWI series and CE-MRI series was performed (Matlab, The Mathworks, Natick, MA, USA) by first rescaling (cubic interpolation) the spatial resolution of the CE-MRI series such that it equaled the spatial resolution of the DWI series, and secondly by aligning both series automatically based on the ImagePositionPatient tag in the DICOM headers.

3.3.5 Comparison of IVIM and CE-MRI kinetics

Parametric maps of pre-contrast IVIM parameters, post-contrast IVIM parameters and contrast kinetics (R_{early} and R_{late}) were calculated for each slice on a voxel-by-voxel basis (Fig. 3.1). To evaluate the liver parenchyma, it was segmented based on the T_1 series by drawing a contour around the liver, and any visible vascular and biliary structures were excluded (Matlab, The Mathworks, Natick, MA, USA). Voxels within the segmented area were collected and only voxels with sufficient goodness-of-fit (eq. 3.2) were included for analysis ($R^2_{\text{adj}} > 0.995$).

The IVIM parameters (measured pre-contrast) were compared between three groups (low, medium and high) of increasing contrast wash-in rate R_{early} during the early phase of Gd-EOB-DTPA and Gd-DOTA after excluding outliers below the 1% percentile and higher than the 99% percentile. The three groups were defined by evenly dividing the range of R_{early} . Additionally, IVIM parameters of liver parenchyma were compared pre- and post-administering either intra- or extracellular contrast agent.

To evaluate the liver lesions, an experienced radiologist (M.O.) with more than 35 years of experience reviewed all the patients using a commercially available dedicated workstation (Leonardo, Siemens Healthcare, Forchheim, Germany) and identified all foci. The observed liver lesions were segmented by drawing a contour around the lesion in each slice, for all patients. For all the voxels within the segmentations, the IVIM parameters (D_{fast} , f_{fast} and D_{slow}) were calculated voxel-wise using the pre-contrast DWI series according to equation 3.1. Per lesion type, the IVIM parameters were compared between two groups of low and high contrast enhancement rates ($R_{\text{late}} > 0$) during the

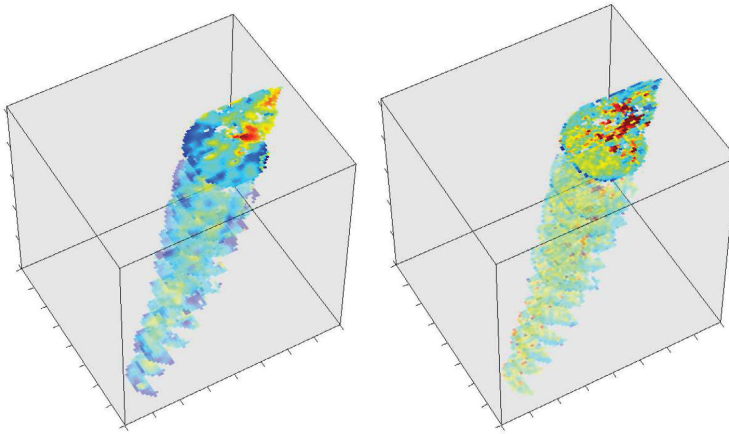


Figure 3.1: Parametric maps of IVIM and contrast kinetics were calculated for each slice on a voxel-by-voxel basis. As an illustration, the left panel shows the fraction (f_{fast}) of microperfusion throughout the liver, and the right panel the contrast wash-in rate (R_{early}) during the portal-venous phase of Gd-EOB-DTPA.

late phase of Gd-EOB-DTPA, where the two groups were divided by the median of R_{late} yielding an equal amount of voxels in both groups. When multiple lesions were observed in one patient, only the largest lesion was evaluated.

3.3.6 Simulation of the effect of intra- and extracellular contrast on IVIM

Equation 1 can be used under the assumption that both slow and fast components have similar T_2 -relaxation times. However, when T_2 -relaxation times are assumed to differ between slow (T_2^{slow}) and fast (T_2^{fast}) component, the echo attenuation in a single voxel is described by:

$$S(TE) = S(0) \cdot [f_{\text{fast}} \cdot e^{-TE/T_2^{\text{fast}}} \cdot e^{-b \cdot D_{\text{fast}}} + f_{\text{slow}} \cdot e^{-TE/T_2^{\text{slow}}} \cdot e^{-b \cdot D_{\text{slow}}}] \quad (3.5)$$

Using equation 3.5 a simulated echo attenuation signal was generated (Matlab, The Mathworks, Natick, MA, USA) of a voxel with different T_2^{fast} and T_2^{slow} relaxation times. For that purpose, D_{slow} and D_{fast} were fixed to $1.0 \times 10^{-3} \text{ mm}^2/\text{s}$ and $10 \times 10^{-3} \text{ mm}^2/\text{s}$ with respective fraction of 70% and 30%. The echo time (TE) was, in accordance to the DWI acquisition, set to 75 ms. T_2 -relaxation times of pre-contrast conditions in the

liver were set to 50 ms (16, 17).

Considering that the extracellular fluid of a 75 kg subject is about 15 liters the extracellular concentration of both agents is 0.125 mmol/l and 0.5 mmol/l for Gd-EOB-DTPA and Gd-DOTA respectively. Given the relaxivity of Gd-EOB-DTPA ($r_2=8.7 \text{ mM}^{-1}\text{s}^{-1}$) and Gd-DOTA ($r_2=4.3 \text{ mM}^{-1}\text{s}^{-1}$), this implicates that for the extracellular space a T_2 relaxation factor of $R_2 = 1.088 \text{ s}^{-1}$ and $R_2 = 2.15 \text{ s}^{-1}$ for Gd-EOB-DTPA and Gd-DOTA respectively. Therefore, in our model it was safe to assume a T_2 shortening of maximally 4 ms for Gd-EOB-DTPA and 6 ms for Gd-DOTA according to the relation $1/T_2 = 1/T_2^0 + R_2$ and $T_2^0 = 50 \text{ ms}$.

Subsequently, for Gd-EOB-DTPA which resides intracellular, T_2^{slow} was shortened from 50 ms to 46 ms in steps of 2 ms while T_2^{fast} was fixed to 50 ms. For Gd-DOTA which remains extracellular, T_2^{fast} was shortened from 50 ms to 44 ms in steps of 2 ms while T_2^{slow} was fixed to 50 ms. The simulated echo attenuation signal was then fitted by the simplified IVIM model (eq. 3.1) resulting in D_{slow} , D_{fast} and f_{fast} and compared to the pre-contrast conditions $T_2^{\text{slow}} = T_2^{\text{fast}} = 50 \text{ ms}$.

3.3.7 Statistical analysis

Statistical analysis was performed using SPSS (SPSS 22, Chicago, IL, USA). Shapiro-Wilk tests were performed to assess the normality of the data. Kruskal-Wallis tests ($\alpha=0.05$) were used to test if pre-contrast IVIM parameters differed significantly between the three groups of low, medium and high R_{early} rates. Intergroup differences were assessed by post-hoc Mann-Whitney U multiple comparisons with Bonferroni type I error correction ($\alpha=0.05/3$). Mann-Whitney U tests were used to test the significance of IVIM parameters between low and high rates of R_{early} in the liver lesions. Wilcoxon Signed rank tests were used to test the significance of the effect of both contrast agents on the IVIM parameters.

3.4 Results

For Gd-EOB-DTPA, R_{early} ranged from 5.4×10^{-4} to 30.0×10^{-4} mmol/L/s and was evenly divided into three groups: low $5.4 \times 10^{-4} < R_{\text{early}} < 13.6 \times 10^{-4}$, medium $13.6 \times 10^{-4} < R_{\text{early}} < 21.8 \times 10^{-4}$ and high $21.8 \times 10^{-4} < R_{\text{early}} < 30.0 \times 10^{-4}$ all in mmol/L/s. For Gd-DOTA, R_{early} ranged from 16×10^{-4} to 135×10^{-4} mmol/L/s and was evenly divided into three groups: low $16 \times 10^{-4} < R_{\text{early}} < 56 \times 10^{-4}$, medium $56 \times 10^{-4} < R_{\text{early}} < 95 \times 10^{-4}$ and

high $95 \times 10^{-4} < R_{\text{early}} < 135 \times 10^{-4}$ all in mmol/L/s.

All pre-contrast IVIM parameters obtained from liver parenchyma differed significantly between the three groups of increasing wash-in rates of Gd-EOB-DTPA during the portal-venous phase (R_{early}), and also the intergroup comparisons were significantly different ($p < 0.001$) (Table 3.1). Both D_{fast} and f_{fast} increased steadily and significantly ($p < 0.001$) with increasing R_{early} , demonstrating an increase of 25.6% and 33.8% respectively between low and high wash-in rates. However, molecular diffusion D_{slow} decreased (-15.0%) significantly with increasing R_{early} ($p < 0.001$). For Gd-DOTA similar observations were made, (Table 3.2), although no significance was found for the difference of D_{fast} between low and high contrast wash-in rates ($p = 0.033$).

Table 3.1: IVIM compared to R_{early} of Gd-EOB-DTPA. IVIM parameters (measured before injection of Gd-EOB-DTPA) were statistically compared between low, medium and high wash-in rate (R_{early} , mmol/L/s) during the initial phase (0-90s) of Gd-EOB-DTPA and post-hoc intergroup differences were assessed. It was observed that D_{fast} and f_{fast} increased significantly from low to high wash-in rates whereas D_{slow} decreased. *P-value indicates significant difference.

Contrast wash-in rate R_{early} (mmol/L/s)							
during initial phase							
of Gd-EOB-DTPA							
	low	medium	high	Intergroup test	Post-hoc multiple comparisons between groups		
					1-2	1-3	2-3
n (voxel)	10502	11290	904				
R_{early} (10^{-4} mmol/L/s)	11.3 (9.8-12.4)	15.8 (14.5-17.5)	23.7 (22.4-25.8)	<0.001*	<0.001*	<0.001*	<0.001*
D_{slow} (10^{-3} mm ² /s)	1.00 (0.84-1.11)	0.96 (0.81-1.09)	0.85 (0.62-1.04)	<0.001*	<0.001*	<0.001*	<0.001*
D_{fast} (10^{-3} mm ² /s)	27.0 (19.0-33.9)	28.8 (20.8-35.8)	33.9 (19.7-46.5)	<0.001*	<0.001*	<0.001*	<0.001*
F_{fast} (%)	25.9 (20.7-32.0)	27.5 (22.5-33.2)	34.7 (27.5-42.1)	<0.001*	<0.001*	<0.001*	<0.001*

Table 3.2: IVIM compared to R_{early} of Gd-DOTA. IVIM parameters (measured before injection of Gd-DOTA) were statistically compared between low, medium and high wash-in rate (R_{early} , mmol/L/s) during the initial phase (0-90s) of Gd-DOTA, and post-hoc intergroup differences were assessed. It was observed that f_{fast} increased significantly from low to high wash-in rates, whereas D_{slow} decreased. *p-value indicates significant difference.

Contrast wash-in rate R_{early} (mmol/L/s)							
during initial phase							
of Gd-DOTA							
	low	medium	high	Intergroup test	Post-hoc multiple comparisons between groups		
					1-2	1-3	2-3
n (voxels)	4099	638	45				
R_{early} (10^{-4} mmol/L/s)	35.2 (26.1-46.1)	61.8 (58.0-67.5)	112.5 (104-125)	<0.001*	<0.001*	<0.001*	<0.001*
D_{slow} (10^{-3} mm ² /s)	0.88 (0.76-0.97)	0.84 (0.71-0.96)	0.65 (0.37-0.79)	<0.001*	<0.001*	<0.001*	<0.001*
D_{fast} (10^{-3} mm ² /s)	28.2 (20.5-35.8)	24.9 (16.3-35.1)	38.9 (19.7-53.1)	<0.001*	<0.001*	0.033	0.001*
F_{fast} (%)	27.2 (22.1-33.6)	30.3 (24.8-35.3)	43.8 (34.3-58.2)	<0.001*	<0.001*	<0.001*	<0.001*

When IVIM parameters of liver parenchyma were compared between pre- and post-contrast conditions of intra- and extracellular contrast agents (Fig. 3.2), f_{fast} increased significantly (10.0%, $p < 0.001$) after administering Gd-EOB-DTPA, instead a significant decrease was found (-4.2%, $p < 0.001$) after Gd-DOTA. Also D_{fast} increased significantly (6.6%, $p < 0.001$) after administering Gd-EOB-DTPA, and a significant decrease was found (-5.7%, $p < 0.001$) after Gd-DOTA. D_{slow} decreased significantly (-3.3%, $p < 0.001$) after Gd-EOB-DTPA and no differences were found after Gd-DOTA (+0.2%, $p = 0.805$).

Simulation of the effect of intra- and extracellular contrast on IVIM parameters of liver parenchyma demonstrated an expected increase of f_{fast} and D_{fast} up to 9.1% and 7.3% respectively compared to pre-contrast conditions of Gd-EOB-DTPA (Fig. 3.3). For Gd-DOTA a decrease of f_{fast} and D_{fast} up to -14.8% and -11.5% respectively were expected compared to pre-contrast conditions. D_{slow} was not affected by different T_2^{fast} and T_2^{slow} relaxation times in the simulation.

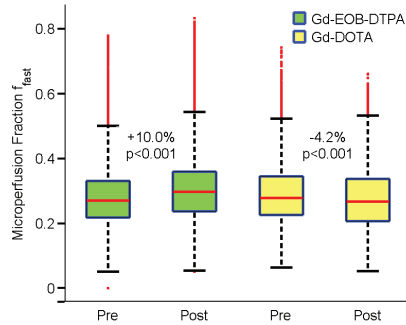
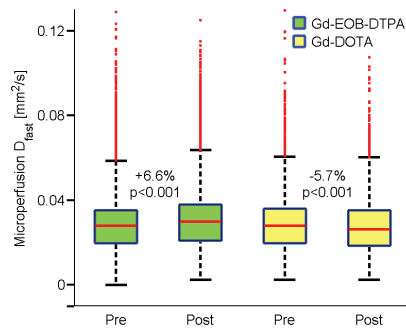
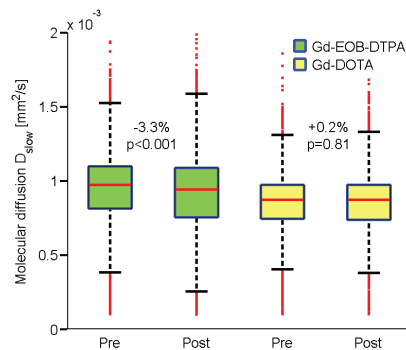
**(a)****(b)****(c)**

Figure 3.2: In liver parenchyma the fraction of microperfusion f_{fast} (%) **(A)** microperfusion D_{fast} (mm^2/s) **(B)** and molecular diffusion D_{slow} ($10^{-3} mm^2/s$) **(C)** were measured *Pre-* and *Post-* administering either a hepatocyte-specific contrast agent (Gd-EOB-DTPA) or an extracellular contrast agent (Gd-DOTA).

The 20 patients receiving Gd-EOB-DTPA were diagnosed with focal nodular hyperplasia (FNH; $n = 5$), hepatocellular carcinoma (HCC, $n = 4$), adenoma ($n = 7$), hemangioma ($n = 2$), hamartoma ($n = 1$) and one patient showed no lesions. The range of R_{late} was from 0 to 32.2×10^{-5} mmol/L/s and was evenly divided into two groups based on the median of R_{late} yielding an equal amount of voxels in both groups: low $0 < R_{late} < 4.0 \times 10^{-5}$ and high $4.0 \times 10^{-5} < R_{late} < 32.2 \times 10^{-5}$ and all in units of mmol/L/s.

All IVIM parameters measured in FNH lesions differed significantly between low and high enhancement rates (R_{late}) of Gd-EOB-DTPA during the late hepatobiliary phase (Fig. 3.4). Both D_{fast} and f_{fast} increased significantly ($p < 0.001$) with increasing R_{late} , demonstrating an increase of 43.2% and 34.1% respectively between low and high enhancement rates. Contrary, the molecular diffusion D_{slow} decreased significantly ($p < 0.001$) with -6.6% between low and high enhancement rates. For HCC lesions and adenoma no significant differences were found between low and high enhancement rates. The hemangioma and hamartoma were not compared due to the low numbers.

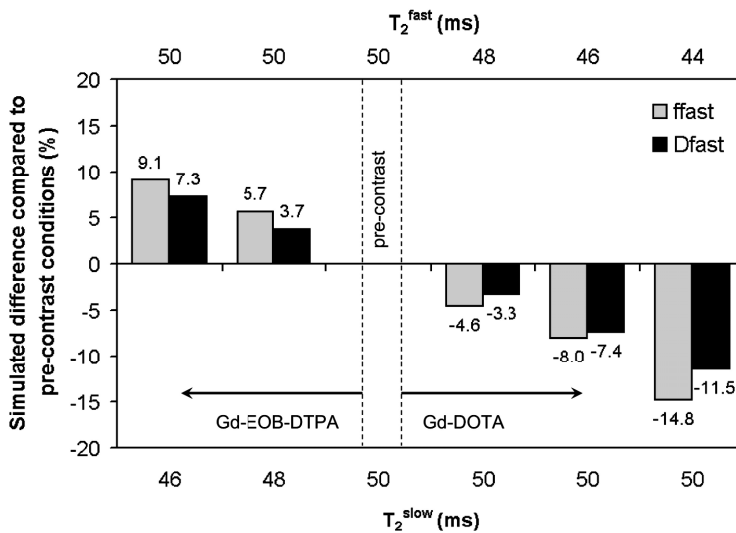


Figure 3.3: Simulation of theoretical effect of intra- and extracellular contrast agents on IVIM parameters of liver parenchyma. In IVIM model slow and fast components are generally assumed to have similar T_2 -relaxation times. However, when T_2 -relaxation times differ between slow (T_2^{slow}) and fast (T_2^{fast}) component (e.g. due to contrast agent), the echo attenuation in a single voxel is described by equation 3.5. After injecting Gd-EOB-DTPA (intracellular agent) T_2^{slow} is expected to be smaller than T_2^{fast} due to entrance in hepatocytes, which results in an apparent increase of f_{fast} and D_{fast} . For Gd-DOTA the effect is opposite because it resides only extracellular.

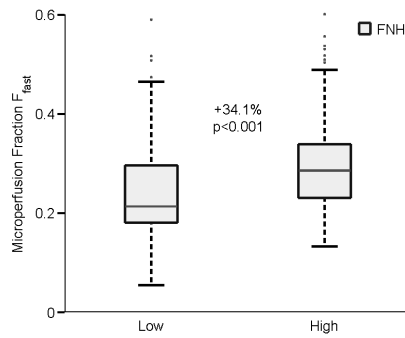
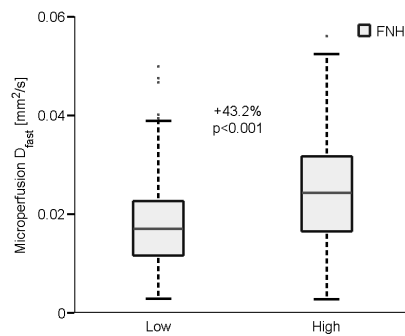
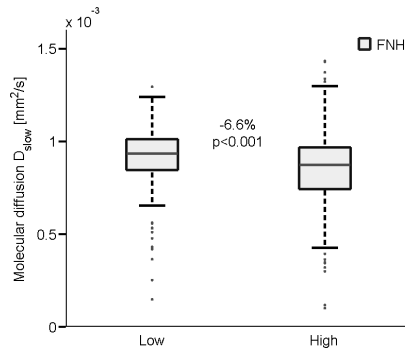
**(a)****(b)****(c)**

Figure 3.4: In focal nodular hyperplasia (FNH) lesions the fraction of microperfusion f_{fast} (%) **(A)** microperfusion D_{fast} (mm^2/s) **(B)** and molecular diffusion D_{slow} ($10^{-3} \text{mm}^2/\text{s}$) **(C)** were measured and compared between *Low* and *High* rates of contrast enhancement in the late hepatobiliary phase of Gd-EOB-DTPA (R_{late}). Similar comparisons were performed for adenoma and hepatocellular carcinoma (HCC), but no significant differences were found between low and high rates of contrast enhancement for those lesions.

3.5 Discussion

In this study we observed that IVIM parameters f_{fast} and D_{fast} measured in pre-contrast conditions in liver parenchyma increased significantly with wash-in rates (R_{early}) of Gd-EOB-DTPA during the portal-venous phase. This indicates that f_{fast} and D_{fast} relate to the same perfusion mechanism responsible for the uptake of Gd-EOB-DTPA.

Previous studies with similar approaches showed various results. Patel et al. found no significant correlation between IVIM and contrast wash-in rate using dynamic-contrast enhanced (DCE-) MRI in cirrhotic livers (18). Using triexponential analysis however a weak but significant correlation ($r=0.372$) was found between perfusion derived by hepatic DWI and contrast enhancement in the portal phase (19). In an isolated dog kidney, f_{fast} increased with renal perfusion with fair correlation ($r=0.683$) (20). In humans, moderate correlation ($r=0.563$) was found between cerebral blood volume and f_{fast} (11). So far, the highest correlations have been reported in human kidneys, showing a good correlation ($r=0.7$) between f_{fast} and the maximum contrast enhancement of renal lesions. For this, they designated f_{fast} as a noninvasive biomarker of tumor vascularity (21).

When several types of liver lesions were analyzed, it was found that f_{fast} and D_{fast} increased significantly with the uptake rate of FNH lesions during the late phase of Gd-EOB-DTPA. This was not observed for adenoma and HCC lesions. FNH lesions are composed of functioning hepatocytes and bile ducts and the majority is either isointense or hyperintense relative to liver parenchyma due to uptake of Gd-EOB-DTPA (22). Adenoma and HCCs generally show less or no uptake of Gd-EOB-DTPA in the late phase due to lack of functional hepatocytes. These observations are in agreement with the hypothesis that f_{fast} and D_{fast} relate to a similar scale of perfusion effects as the uptake of Gd-EOB-DTPA in the late phase. ADC and semi-quantitative perfusion parameters of FNH lesions have been measured previously (23), however no studies are known which investigate the correlations between DWI and contrast uptake. To our knowledge the current study is the first to relate IVIM parameters of liver lesions with semi-quantitative liver specific contrast uptake rates.

The sensitivity of IVIM-DWI for microperfusion effects was additionally investigated by comparing the IVIM parameters between pre- and post-contrast conditions of either hepatospecific (Gd-EOB-DTPA) or extracellular (Gd-DOTA) contrast agent. f_{fast} and D_{fast} increased significantly after administering Gd-EOB-DTPA, instead a significant decrease was found after Gd-DOTA. It has been reported that diffusion decreases after injection of gadolinium based contrast agents. For example, the ADC decreased

respectively 3.1%, 5% and 17.8% after injection of Gd-DTPA, Gd-EOB-DTPA and gadodiamide (24–26).

It is however questionable whether parameters such as diffusion and microperfusion are actually affected biophysically post-contrast, or that the assumptions of the quantitative DWI model are violated. The simplified IVIM model (eq. 3.1) assumes that both the fast component (f_{fast}) and the slow component (f_{slow}) have similar T_2 -relaxation times; however if this hypothesis is not true (i.e. $T_2^{\text{slow}} \neq T_2^{\text{fast}}$) then the IVIM model is described by equation 3.5 (3). A potential violation might be the injection of gadolinium based contrast agents. Gadolinium chelates exhibit positive magnetic susceptibility due to the numerous unpaired electrons which interact with adjacent protons, causing shortening of the longitudinal and transverse relaxation (T_2 -shortening).

Gd-EOB-DTPA enters the hepatocytes during the late phase and therefore shortening of T_2^{slow} was expected to be more persistent than shortening of T_2^{fast} . In a theoretical simulation, these effects were investigated, demonstrating an expected increase of f_{fast} and D_{fast} after administering Gd-EOB-DTPA. This was confirmed by the clinical measurements. It is important to note however that these observations are caused only due to violating the assumption of equation 3.1 that T_2^{slow} and T_2^{fast} are equal, and are probably not related to a biophysical change of f_{fast} or D_{fast} .

Gd-DOTA on the other hand resides only extracellular and was assumed to shorten T_2^{fast} more than T_2^{slow} . In the simulation this resulted in an expected decrease of f_{fast} and D_{fast} , which was supported by clinical results. The different observations between IVIM parameters measured after Gd-EOB-DTPA and Gd-DOTA confirms that IVIM is sensitive for a slow and fast component. Additionally it shows that quantitative DWI should not be performed post-contrast unless the extended IVIM model is used.

The sensitivity of DWI to magnetic susceptibility changes has been observed previously as well (27). ADCs decreased linearly with magnetic susceptibility (T_2 -shortening) after step-wise injection of a superparamagnetic intravascular contrast agent. This supports the observed decrease of f_{fast} after injection of intravascular Gd-DOTA in our study. The observed change in f_{fast} is also in concordance with data of others who suggested that the vasculature's signal is suppressed or altered by contrast agents (28, 29).

Furthermore, it has been reported that f_{fast} is dependent on the echo time (TE) (30); this is due to similar reasons as why f_{fast} is affected differently by intra- and extracellular contrast agents. The simple IVIM model assumes equal relaxation times of tissue and blood, however this is in general not true, and will be noticed when TE is varied.

The excellent study of Lemke et al. combined with our observations of the effect of

contrast agents on f_{fast} demonstrate that the simplified IVIM model should not be used when the assumptions of the model (equal relaxation times) are violated. In addition, it may be arguable that the wide variation of observations in literature of the IVIM parameters in the liver, but also in other organs, is due to the inappropriate use of the simplified IVIM model instead of the full model as described by equation 3.5.

Considering the molecular diffusion, a significant decrease was found after the injection of hepato-specific Gd-EOB-DTPA (-3.3%), while for Gd-DOTA no significant differences were found. We expect that this effect is caused by actual physical hampering of hydrogen molecules by the larger gadolinium compounds. The post-contrast DWI scan was performed about 10 minutes after contrast injection. At that point, a significant part of the liver parenchyma, amounting to 78% of liver volume (31), is filled with Gd-EOB-DTPA for a period of 2 hours (32–34), while Gd-DOTA is cleared from the plasma with a half-life of approximately 90 minutes (35). Therefore the molecular diffusion is hampered more by Gd-EOB-DTPA than by Gd-DOTA.

3.5.1 Limitations

This study was partially limited by the disagreement between resolutions of the DWI and CE-MRI series. CE-MRI was acquired at 1.6 mm spatial resolution while DWI was acquired at 2.0 mm, according to the clinical protocol. Therefore CE-MRI series were rescaled using post-processing such that they equaled the spatial resolution of DWI. Although this study revealed significant increases of D_{fast} and f_{fast} with contrast wash-in rates, we expect that the increases could have been stronger when the spatial resolution of both CE-MRI and DWI would have been equal.

3.5.2 Conclusions

In this study we observed that microperfusion measured by IVIM in the human liver increased significantly with wash-in rates of Gd-EOB-DTPA. Also IVIM separated intra- and extracellular MR contrast media. This underlines the potential of IVIM in quantitative liver imaging.

3.6 References

- (1) Muller, M. F., Prasad, P., Siewert, B., Nissenbaum, M. A., Raptopoulos, V., and Edelman, R. R. (1994). Abdominal diffusion mapping with use of a whole-body echo-planar system. *Radiology* 190, 475–478.
- (2) Namimoto, T., Yamashita, Y., Sumi, S., Tang, Y., and Takahashi, M. (1997). Focal liver masses: characterization with diffusion-weighted echo-planar MR imaging. *Radiology* 204, 739–744.
- (3) Bihan, D. L., Breton, E., Lallemand, D., Aubin, M. L., Vignaud, J., and Laval-Jeantet, M. (1988). Separation of diffusion and perfusion in intravoxel incoherent motion MR imaging. *Radiology* 168, 497–505.
- (4) Yamada, I., Aung, W., Himeno, Y., Nakagawa, T., and Shibuya, H. (1999). Diffusion coefficients in abdominal organs and hepatic lesions: evaluation with intravoxel incoherent motion echo-planar MR imaging. *Radiology* 210, 617–623.
- (5) Dijkstra, H., Baron, P., Kappert, P., Oudkerk, M., and Sijens, P. E. (2012). Effects of microperfusion in hepatic diffusion weighted imaging. *European radiology* 22, 891–899.
- (6) Luciani, A. et al. (2008). Liver cirrhosis: intravoxel incoherent motion MR imaging—pilot study. *Radiology* 249, 891–899.
- (7) Cohen, A. D., Schieke, M. C., Hohenwarter, M. D., and Schmainda, K. M. (2014). The effect of low b-values on the intravoxel incoherent motion derived pseudodiffusion parameter in liver. *Magnetic resonance in medicine : official journal of the Society of Magnetic Resonance in Medicine / Society of Magnetic Resonance in Medicine*.
- (8) Kakite, S. et al. (2014). Hepatocellular carcinoma: Short-term reproducibility of apparent diffusion coefficient and intravoxel incoherent motion parameters at 3.0T. *Journal of magnetic resonance imaging : JMRI*.
- (9) Bihan, D. L., and Turner, R. (1992). The capillary network: a link between IVIM and classical perfusion. *Magnetic resonance in medicine : official journal of the Society of Magnetic Resonance in Medicine / Society of Magnetic Resonance in Medicine* 27, 171–178.
- (10) Henkelman, R. M. (1990). Does IVIM measure classical perfusion? *Magnetic resonance in medicine : official journal of the Society of Magnetic Resonance in Medicine / Society of Magnetic Resonance in Medicine* 16, 470–475.
- (11) Wirestam, R., Borg, M., Brockstedt, S., Lindgren, A., Holtas, S., and Stahlberg, F. (2001). Perfusion-related parameters in intravoxel incoherent motion MR imaging compared with CBV and CBF measured by dynamic susceptibility-contrast MR technique. *Acta Radiologica (Stockholm, Sweden : 1987)* 42, 123–128.
- (12) Bihan, D. L. (2013). Apparent diffusion coefficient and beyond: what diffusion MR imaging can tell us about tissue structure. *Radiology* 268, 318–322.
- (13) Bihan, D. L. (2012). Diffusion, confusion and functional MRI. *NeuroImage* 62, 1131–1136.
- (14) Bihan, D. L., Turner, R., Moonen, C. T., and Pekar, J. (1991). Imaging of diffusion and microcirculation with gradient sensitization: design, strategy, and significance. *Journal of magnetic resonance imaging : JMRI* 1, 7–28.
- (15) Turner, R., Bihan, D. L., Maier, J., Vavrek, R., Hedges, L. K., and Pekar, J. (1990). Echo-planar imaging of intravoxel incoherent motion. *Radiology* 177, 407–414.
- (16) Goldberg, M. A. et al. (1993). Value of T1 and T2 relaxation times from echoplanar MR imaging in the characterization of focal hepatic lesions. *AJR.American journal of roentgenology* 160, 1011–1017.
- (17) de Bazelaire, C. M., Duhamel, G. D., Rofsky, N. M., and Alsop, D. C. (2004). MR imaging relaxation times of abdominal and pelvic tissues measured in vivo at 3.0 T: preliminary results. *Radiology* 230, 652–659.

- (18) Patel, J., Sigmund, E. E., Rusinek, H., Oei, M., Babb, J. S., and Taouli, B. (2010). Diagnosis of cirrhosis with intravoxel incoherent motion diffusion MRI and dynamic contrast-enhanced MRI alone and in combination: preliminary experience. *Journal of magnetic resonance imaging : JMIRI* 31, 589–600.
- (19) Lewin, M. et al. (2007). Diffusion-weighted magnetic resonance imaging for the assessment of fibrosis in chronic hepatitis C. *Hepatology (Baltimore, Md.)* 46, 658–665.
- (20) 3rd, D. R. P., Jolgren, D. L., Lorenz, C. H., Creasy, J. L., and Price, R. R. (1992). Magnetic resonance perfusion/diffusion imaging of the excised dog kidney. *Investigative radiology* 27, 287–292.
- (21) Chandarana, H., Lee, V. S., Hecht, E., Taouli, B., and Sigmund, E. E. (2011). Comparison of biexponential and monoexponential model of diffusion weighted imaging in evaluation of renal lesions: preliminary experience. *Investigative radiology* 46, 285–291.
- (22) Grazioli, L., Morana, G., Kirchin, M. A., and Schneider, G. (2005). Accurate differentiation of focal nodular hyperplasia from hepatic adenoma at gadobenate dimeglumine-enhanced MR imaging: prospective study. *Radiology* 236, 166–177.
- (23) Kreutzer, G., Galindez, E., Bono, H., Palma, C. D., and Laura, J. P. (1973). An operation for the correction of tricuspid atresia. *The Journal of thoracic and cardiovascular surgery* 66, 613–621.
- (24) Choi, J. S., Kim, M. J., Choi, J. Y., Park, M. S., Lim, J. S., and Kim, K. W. (2010). Diffusion-weighted MR imaging of liver on 3.0-Tesla system: effect of intravenous administration of gadoteric acid disodium. *European radiology* 20, 1052–1060.
- (25) Chiu, F. Y. et al. (2005). Effect of intravenous gadolinium-DTPA on diffusion-weighted magnetic resonance images for evaluation of focal hepatic lesions. *Journal of computer assisted tomography* 29, 176–180.
- (26) Saremi, F., Sefidbakht, S., Quane, L., Maria, J. S., Khararjian, A., and Jalili, M. (2011). Effect of intravenous extracellular gadolinium based contrast medium on renal diffusion weighted images. *Academic Radiology* 18, 174–183.
- (27) Does, M. D., Zhong, J., and Gore, J. C. (1999). In vivo measurement of ADC change due to intravascular susceptibility variation. *Magnetic resonance in medicine : official journal of the Society of Magnetic Resonance in Medicine / Society of Magnetic Resonance in Medicine* 41, 236–240.
- (28) Yamada, K. et al. (2002). Effect of intravenous gadolinium-DTPA on diffusion-weighted images: evaluation of normal brain and infarcts. *Stroke; a journal of cerebral circulation* 33, 1799–1802.
- (29) Laissy, J. P. et al. (2000). Hemodynamic effect of iodinated high-viscosity contrast medium in the rat kidney: a diffusion-weighted MRI feasibility study. *Investigative radiology* 35, 647–652.
- (30) Lemke, A., Laun, F. B., Simon, D., Stieltjes, B., and Schad, L. R. (2010). An in vivo verification of the intravoxel incoherent motion effect in diffusion-weighted imaging of the abdomen. *Magnetic resonance in medicine : official journal of the Society of Magnetic Resonance in Medicine / Society of Magnetic Resonance in Medicine* 64, 1580–1585.
- (31) Dancygier, H., *Clinical Hepatology: Principles and Practice of Hepatobiliary Diseases, Volume 1. Page 16. Table 3.2.* Springer: 2009.
- (32) Gschwend, S., Ebert, W., Schultze-Mosgau, M., and Breuer, J. (2011). Pharmacokinetics and imaging properties of Gd-EOB-DTPA in patients with hepatic and renal impairment. *Investigative radiology* 46, 556–566.
- (33) Ba-Ssalamah, A., Uffmann, M., Saini, S., Bastati, N., Herold, C., and Schima, W. (2009). Clinical value of MRI liver-specific contrast agents: a tailored examination for a confident non-invasive diagnosis of focal liver lesions. *European radiology* 19, 342–357.
- (34) Hamm, B. et al. (1995). Phase I clinical evaluation of Gd-EOB-DTPA as a hepatobiliary MR contrast agent: safety, pharmacokinetics, and MR imaging. *Radiology* 195, 785–792.

- (35) Chachuat, A., Molinier, P., Bonnemain, B., Chambon, C., and Gayet, J. L. Pharmacokinetics and tolerance of Gd-DOTA (DOTAREM) in healthy volunteers and in patients with chronic renal failure., 1992.

Clinical implications of non-steatotic hepatic fat fractions on quantitative DWI of the liver

Hildebrand Dijkstra

Astri Handayani

Peter Kappert

Matthijs Oudkerk

Paul E. Sijens

Published in PLoS One
2014, vol. 9, no. 2, e87926.

4.1 Abstract

Background: Diffusion-weighted imaging (DWI) is an important diagnostic tool in the assessment of focal liver lesions and diffuse liver diseases such as cirrhosis and fibrosis. Quantitative DWI parameters such as molecular diffusion, microperfusion and their fractions, are known to be affected when hepatic fat fractions (HFF) are higher than 5.5% (steatosis). However, less is known about the effect on DWI for HFF in the normal non-steatotic range below 5.5%, which can be found in a large part of the population.

Purpose: The aim of this study was therefore to evaluate the diagnostic implications of non-steatotic HFF on quantitative DWI parameters in eight liver segments.

Materials and methods: For this purpose, eleven healthy volunteers (2 men, mean age 31.0) were prospectively examined with DWI and three series of in-/out-of-phase dual-echo spoiled gradient-recalled MRI sequences to obtain the HFF and T2*. DWI data were analyzed using the intravoxel incoherent motion (IVIM) model. Four circular regions ($\varnothing 22.3$ mm) were drawn in each of eight liver segments and averaged. Measurements were divided in group 1 (HFF \leq 2.75%), group 2 (2.75 < HFF \leq 5.5%) and group 3 (HFF > 5.5%). DWI parameters and T2* were compared between the three groups and between the segments.

Results: It was observed that the molecular diffusion (0.85, 0.72 and 0.49 $\times 10^{-3}$ mm²/s) and T2* (32.2, 27.2 and 21.0 ms) differed significantly between the three groups of increasing HFF (2.18, 3.50 and 19.91%). Microperfusion and its fraction remained similar for different HFF. Correlations with HFF were observed for the molecular diffusion ($r = -0.514$, $p < 0.001$) and T2* (-0.714 , $p < 0.001$). Similar results were obtained for the majority of individual liver segments.

Conclusions: It was concluded that fat significantly decreases molecular diffusion in the liver, also in absence of steatosis (HFF \leq 5.5%). Also, it was confirmed that fat influences T2*. Determination of HFF prior to quantitative DWI is therefore crucial.

4.2 Introduction

The effect of fat on the self-diffusion of water has been assessed since the onset of nuclear magnetic resonance. Already in 1983, it was demonstrated that water diffusion drops six-fold inside of Cheddar and Swiss cheeses (1). Later it was observed in vitro that water diffusion is hindered by lipid-rich cores in susceptible plaque (2). The clinical assessment of water diffusion in the liver became feasible with the introduction of diffusion weighted imaging (DWI) in the abdomen (3). DWI reflects the mobility of water molecules (molecular diffusion) in a tissue which can be described by the apparent diffusion coefficient (ADC) or the intravoxel incoherent motion (IVIM) model (4–6). Since then DWI has been successfully applied in the assessment of focal liver lesions and diffuse liver diseases such as cirrhosis, fibrosis and steatosis (7–11).

However, the effect of fat on hepatic DWI is still subject of debate. In an animal study it was concluded that steatosis may confound determination of hepatic fibrosis with DWI (12). This was confirmed in two clinical studies where the ADC decreased significantly in patients with hepatic steatosis (13, 14). Similarly, a study which applied the IVIM model demonstrated that steatosis can reduce the molecular diffusion significantly and thus act as a potential confounder when IVIM is used to assess diffuse liver diseases such as cirrhosis (15).

These studies discussed the effect of hepatic fat on DWI for patients with steatosis, which is defined as fat fractions higher than 5.56% (16). However, a detailed insight in the dependency of IVIM parameters on normal (non-steatotic) fat fractions ranging between 0 and 5.56% has not been reported yet; it has been suggested however, that there might be a nonlinear relationship (15). Also, the relation between the different segmental regions of the liver and the effect of fat on IVIM modelled DWI has not been studied up to now. Considering that fat content has been demonstrated to differ between liver segments, its effect on IVIM modelled DWI may be expected to be location dependent (17). In addition, it has been reported that next to the effects of fat on diffusion, fat also affects T2* estimation (18–20).

The purpose of this study was therefore to evaluate the diagnostic implications of non-steatotic HFF (< 5.5%) on quantitative DWI by assessing the HFF and T2* of healthy subjects in eight liver segments.

4.3 Materials and methods

4.3.1 Ethics statement

The protocol of the study was approved by the Medical Ethics Review Board of the University Medical Center Groningen, and written informed consent was obtained from each volunteer.

4.3.2 Study population

In April 2011, healthy volunteers were randomly selected by local advertisement in the university to ensure a diverse population. Volunteers were required to be without any history of hepatic pathology or any other pathology related to liver function. The minimum age for inclusion was 18 years old. Exclusion criteria included MRI contraindications such as pacemakers, clips, stents and implants. In total, 11 subjects were included (2 men) with an age between 18 to 56 years old (mean 31.0) and a body mass between 55 and 116 kg. Body-mass-index (BMI) ranged between 19.9 and 34.4 kg/m² (mean 25.4 kg/m²). The only preparation before the examination was an 8-h fasting period.

4.3.3 MR protocols

All subjects were prospectively examined on a 1.5 T MRI system (Magnetom Avanto, Siemens Medical Solutions, Erlangen, Germany). The body coil served as transmitter and a 24-element spine matrix coil in combination with a 6-element body matrix as receiver.

After the localiser scans, a series of diffusion weighted images (DWI) were obtained using a spin echo based single shot echo-planar imaging (SS-EPI) sequence in combination with spectral adiabatic inversion recovery (SPAIR) fat suppression. The DWI acquisitions ($b = 0, 50, 100, 250, 500, 750$ and 1000 s/mm²) were gated using PACE respiratory triggering (TR = 3065–5947 ms) and tuned with the following parameters: TE 90 ms; FA 90°; slice-thickness 5 mm; FOV 300×242 mm²; matrix 144×116 ; bandwidth 1335 Hz/pixel; 4 averages and parallel acquisition technique GRAPPA with acceleration factor 2. Diffusion gradients (25 mT/m) were applied in the phase-, read-, and

z-directions separately using bipolar diffusion-encoding schemes. For each subject, 16 transverse slices were acquired in interleaved mode to cover the liver in an acquisition time between 7.2 and 13.5 minutes.

After the DWI scans, a dual-echo spoiled gradient recalled (SPGR) sequence was acquired to obtain two series of in-phase (IP) images with echo times of 4.5 and 18 ms, TR = 220 ms and FA = 70° to calculate T2*. Then, to calculate the hepatic fat fraction (HFF), a second dual-echo SPGR was acquired to obtain two series of both out-phase (OP) and in-phase (IP) images with echo times of 2.38 and 4.76 ms respectively tuned with TR = 206 ms and FA = 70°. Finally, a third series of dual-echo SPGR was acquired with equal TE/TR settings as the second series hence a flip angle of 20°.

All three SPGR scans were acquired with slice-thickness 6 mm; FOV 375 × 196 mm²; matrix 256 × 134; bandwidth 434 Hz/pixel; 1 average and parallel acquisition technique GRAPPA with acceleration factor 2 and an acquisition time between 1.5 and 2.0 minutes. Total acquisition time for DWI and HFF measurements was between 12 and 20 minutes.

4.3.4 Fitting of DWI signal

Bi-exponential fitting procedures and exact positioning of ROIs were performed using a programmable graphical and calculus environment (Matlab, The Mathworks, Natick, MA, USA) according to the instructions of a radiologist (M.O.) with more than 35 years of experience. For all analyses, the diffusion weighted signal intensities S were fitted bi-exponentially using the parameters prescribed by the IVIM model (4, 21):

$$\frac{S}{S_0} = f_{fast} \cdot e^{-b \cdot D_{fast}} + f_{slow} \cdot e^{-b \cdot D_{slow}} \quad (4.1)$$

where S_0 is the maximum signal intensity, D_{fast} is the fast pseudodiffusion component, f_{fast} is the fraction of the fast component, D_{slow} is the slow diffusion component and f_{slow} is the fraction of the slow component ($f_{slow} = 1 - f_{fast}$) as defined previously by Le Bihan et al. (21).

In this study, D_{fast} is referred to as microperfusion, and f_{fast} as the fraction of microperfusion, in accordance with the study of Lemke et al., who suggested that the IVIM-model separates DWI measurements into a “contribution of microperfusion and diffusion” (22). D_{slow} is referred to as the molecular diffusion in accordance with the study of Luciani et al. (23).

Equation 4.1 was fitted by the Nelder-Mead simplex direct search method with

bound constraints, which performs a constrained non-linear minimisation of the sum of the squared residuals (3, 24). The initial guess D_{slow}^0 was estimated by calculating the slope of the asymptote of the slow signal component between $b = 500$ and 1000 s/mm^2 , and D_{slow} was bound between 0.5 and $5 \times D_{\text{slow}}^0 \times 10^{-3} \text{ mm}^2/\text{s}$. The intercept of the asymptote with the y-axis at S_0 resulted in an initial guess f_{fast}^0 , and f_{fast} was bound between $f_{\text{fast}}^0 - 0.02$ and $f_{\text{fast}}^0 + 0.02$. The slope of the signal between $b = 0$ and $b = 100 \text{ s}/\text{mm}^2$ was used to guess the initial value of the fast signal component (D_{fast}^0), and D_{fast} was bound between D_{slow} and $100 \times 10^{-3} \text{ mm}^2/\text{s}$.

4.3.5 Hepatic fat fraction

The hepatic fat fraction (HFF) was calculated by Dixon's in- and out-of-phase SPGR imaging modified with dual flip angles (70° , 20°) as proposed by Hussain et al.: $\text{HFF} = \text{HFF}_{20}$ if $\text{HFF}_{20} \leq \text{HFF}_{70}$ and otherwise $\text{HFF} = 100 - \text{HFF}_{20}$ (25, 26). The second SPGR series with a flip angle of 70 degrees were used to calculate HFF_{70} :

$$\text{HFF}_{70}(\%) = \frac{S_{IP,corr}^{70} - S_{OP}^{70}}{2 \cdot S_{IP,corr}^{70}} \cdot 100 \quad (4.2)$$

where

$$S_{IP,corr}^{70} = S_{IP}^{70} \cdot e^{\frac{\tau}{T2^*}} \quad (4.3)$$

and S_{IP}^{70} and S_{OP}^{70} are the signal intensities of the IP and OP images of the second SPGR series using $\tau = 2.38 \text{ ms}$ ($\text{TE}_{IP} - \text{TE}_{OP}$). Similarly, the calculation of HFF_{20} was done using the third SPGR series with a flip angle of 20° . $T2^*$ was estimated using the first dual echo SPGR series:

$$\frac{1}{T2^*} = \frac{1}{\Delta TE} \cdot \ln\left(\frac{S_{IP1}}{S_{IP2}}\right) \quad (4.4)$$

where $\Delta TE = 13.5 \text{ ms}$ ($\text{TE}_{IP,2} - \text{TE}_{IP,1}$) and $S_{IP,1}$ and $S_{IP,2}$ are the respective signal intensities of both echoes.

4.3.6 Image analysis

First the DWI data were loaded. For each of the 11 subjects, four circular regions-of-interest (ROI) with a diameter of 22.3 mm were drawn in each of the eight segmental regions (II – VIII) according to the Couinaud-Bismuth classification (27, 28). The four ROIs were drawn on four different slices when possible; hence when no additional slices were available a second ROI was drawn on the same slice (yet in another location of the segment). For each ROI the average signal intensity S was obtained and the IVIM-DWI parameters (D_{slow} , D_{fast} and the respective fractions) were fitted.

The exact locations of the ROIs were stored as xy-coordinates, and for each ROI the HFF and $T2^*$ were recorded. Finally, the four ROIs measured in each segment were averaged, resulting in 88 measurements totally (11 subjects, 8 segments). During the assessments, any visible vascular and biliary structures nearby were avoided.

4.3.7 Statistical analysis

Statistical analyses were performed using SPSS (SPSS 20, Chicago, IL, USA). All data were tested for normality using Shapiro–Wilk tests. Non-steatotic measurements ($\text{HFF} \leq 5.5\%$) were divided into two groups: group 1 ($\text{HFF} \leq 2.75\%$) and group 2 ($2.75 < \text{HFF} \leq 5.5\%$). Steatotic measurements ($\text{HFF} > 5.5\%$) were assigned to group 3.

For normally distributed data (D_{slow} , D_{fast} , f_{fast} and $T2^*$) one-way ANOVA tests were used to compare measurements between the three groups. Post-hoc comparisons after ANOVA were implemented using Fisher's LSD tests which provides familywise type I error protection when the number of comparisons equals three, while providing increased power compared to Bonferroni correction (29).

For non-normally distributed data (HFF) the differences between the three groups were determined using non-parametric Kruskal-Wallis tests, whereafter post-hoc Mann-Whitney U multiple comparisons were performed with Bonferroni type I error correction.

Guiu et al. reported a potential nonlinear effect between D_{slow} and HFF, especially for HFF below 3% (15). To investigate whether the relationship between HFF and D_{slow} , D_{fast} , f_{fast} and $T2^*$, was linear or potentially nonlinear, Pearson's correlations for all data points were calculated using a linear ($Y=a \cdot \text{HFF} + b$) and a log-linear ($Y=a \cdot \log(\text{HFF}) + b$) model. The best-fit model, with the highest correlations for all data points was used to investigate the individual Pearson's correlations in each of the eight individual liver

segments.

The significance of the multiple correlation analysis was adjusted by Bonferroni correction to avoid type I errors. Correlations (in absolute values) were classified as weak ($r < 0.36$), moderate ($r = 0.36$ to 0.67) and strong ($r > 0.67$) (30). For all statistical tests $P < 0.05$ was considered to indicate a statistically significant difference.

4.4 Results

4.4.1 Effect of fat on IVIM-DWI parameters

The HFFs were non-normally distributed ($p < 0.001$) and ranged between 1.5 and 29.9% for the eleven subjects. Five subjects yielded non-steatotic HFF ($\leq 5.5\%$) measurements only, two subjects had steatotic HFF ($> 5.5\%$) measurements only, and four subjects had both steatotic and non-steatotic measurements (Fig. 4.1). IVIM-DWI parameters were normally distributed ($p \geq 0.319$). Molecular diffusion (D_{slow}) differed significantly between the three groups of different HFF, and also the intergroup comparisons were significantly different ($p < 0.001$, Table 4.1).

Table 4.1: Comparison of hepatic fat fraction (HFF), IVIM-DWI parameters and $T2^*$ between groups. Measurements acquired in the liver. † Data are medians \pm median deviations and intergroup differences were assessed by Kruskal-Wallis tests and post-hoc Mann-Whitney U multiple comparisons with Bonferroni type I error correction. ‡ Data are means \pm standard deviations and intergroup differences were assessed by one-way ANOVA and post-hoc multiple comparisons using Fisher's LSD tests providing type I error protection as the number of comparisons equals 3. *P-value indicates significant difference.

	Non-steatotic		Steatotic	Inter group test	Post-hoc multiple comparisons between groups		
	Group 1 HFF $\leq 2.75\%$	Group 2 2.75 < HFF $\leq 5.5\%$	Group 3 HFF $> 5.5\%$		1-2	1-3	2-3
	n = 31	n = 30	n = 27				
HFF (%) †	2.18 \pm 0.30	3.50 \pm 0.74	19.91 \pm 9.69	<0.001*	<0.001*	<0.001*	<0.001*
D_{slow} (10^{-3} mm ² /s) ‡	0.85 \pm 0.27	0.72 \pm 0.20	0.49 \pm 0.17	<0.001*	0.023*	<0.001*	<0.001*
D_{fast} (10^{-3} mm ² /s) ‡	37.9 \pm 8.35	39.6 \pm 8.86	42.4 \pm 10.5	0.194	0.477	0.072	0.267
f_{fast} (%) ‡	36 \pm 8.5	37 \pm 8.3	39 \pm 9.0	0.279	0.601	0.116	0.288
$T2^*$ (ms) ‡	32.2 \pm 5.1	27.2 \pm 3.4	21.0 \pm 3.7	<0.001*	<0.001*	<0.001*	<0.001*

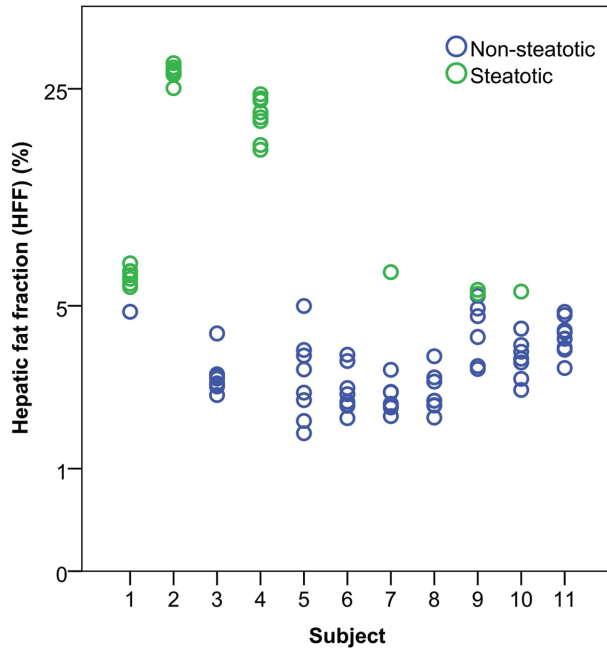


Figure 4.1: Distribution of HFF measurements in all subjects. For each subject ($n=11$), four circular regions-of-interest ($\varnothing 22.3$ mm) were drawn in each of the eight segmental regions (II – VIII) according to the Couinaud-Bismuth classification and averaged, resulting in a total of 88 measurement points. Five subjects demonstrated non-steatotic HFF ($\leq 5.5\%$) measurements only, two subjects had steatotic HFF ($> 5.5\%$) measurements only, and four subjects had both steatotic and non-steatotic measurements.

D_{slow} was 0.85×10^{-3} mm²/s for the first group ($\text{HFF} \leq 2.75\%$) and decreased steadily to 0.72×10^{-3} mm²/s in group 2 ($2.75 < \text{HFF} \leq 5.5\%$) and 0.49×10^{-3} mm²/s in group 3 ($\text{HFF} > 5.5\%$). D_{fast} and f_{fast} did not show differences between the three HFF groups ($p \geq 0.194$). Pearson's correlation analysis (Table 4.2) showed a significant negative linear relationship with moderate correlation between HFF and D_{slow} using both the linear model ($r = -0.446$, $p < 0.001$) and the log-linear model ($r = -0.514$, $p < 0.001$, Fig. 4.2). The log-linear model showed overall higher correlations compared to the linear model and was therefore used for the individual segment analysis.

The average HFF varied from $3.00 \pm 9.17\%$ to $7.32 \pm 9.36\%$ between the individual segments (Table 4.3). In segment VII a significant negative linear relationship with strong correlation ($r = -0.840$; $p \leq 0.008$) was observed between HFF and D_{slow} using the log-linear model (Table 4.4). No significant correlations between HFF and D_{fast} or f_{fast} were observed.

Table 4.2: Correlations of IVIM-DWI parameters and T_2^* with hepatic fat fraction (HFF) using two models. Two models were used to assess the effect of hepatic fat fraction (HFF) on the IVIM-DWI parameters (D_{slow} , D_{fast} and f_{fast}) or T_2^* measured in 11 patients and 8 segments (n=88). The linear model assumed a linear relationship between HFF and the IVIM-DWI parameters or T_2^* ($Y = a \cdot \text{HFF} + b$). The log-linear model assumed a linear relationship between the logarithmic of HFF and the IVIM-DWI parameters or T_2^* ($Y = a \cdot \log(\text{HFF}) + b$). Pearson's correlations increased when the log-linear model was applied. *Indicates significant correlations.

	Linear model			Log-linear model		
	Pearson's r	F	P-value	Pearson's r	F	P-value
D_{slow}	-0.446*	21.317	<0.001*	-0.514*	30.926	<0.001*
D_{fast}	+0.040	0.138	0.711	+0.101	0.892	0.348
f_{fast}	-0.041	0.148	0.701	+0.030	0.075	0.785
T_2^*	-0.607*	50.277	<0.001*	-0.714*	89.190	<0.001*

Table 4.3: Hepatic fat fraction (HFF), IVIM-DWI parameters and T_2^* per segment. For each subject four ROIs were drawn in each segment and then averaged, resulting in 11 measurements per segment. † Data are medians \pm median. ‡ Data are means \pm standard deviations.

Seg	HFF † (%)	D_{slow} ‡ (10^{-3} mm ² /s)	D_{fast} ‡ (10^{-3} mm ² /s)	f_{fast} ‡ (%)	T_2^* ‡ (ms)
II	4.99 \pm 8.80	0.48 \pm 0.28	48.4 \pm 8.5	50 \pm 5.1	25.5 \pm 5.8
III	7.32 \pm 9.36	0.65 \pm 0.16	40.9 \pm 8.8	44 \pm 6.7	28.1 \pm 5.9
IVa	3.29 \pm 8.64	0.85 \pm 0.28	40.0 \pm 7.0	38 \pm 5.4	26.8 \pm 8.4
IVb	3.00 \pm 9.17	0.85 \pm 0.19	48.4 \pm 8.6	39 \pm 6.1	29.0 \pm 7.1
V	3.46 \pm 7.38	0.60 \pm 0.25	38.0 \pm 8.1	33 \pm 5.9	27.6 \pm 4.8
VI	3.41 \pm 8.73	0.74 \pm 0.21	37.5 \pm 7.2	32 \pm 5.3	27.7 \pm 5.8
VII	3.98 \pm 9.18	0.75 \pm 0.23	34.3 \pm 6.6	31 \pm 5.6	26.2 \pm 6.0
VIII	3.27 \pm 8.54	0.59 \pm 0.26	31.4 \pm 5.8	29 \pm 5.3	25.6 \pm 5.6

Table 4.4: Correlations with hepatic fat fraction (HFF) per segment. Pearson's r correlation coefficients were calculated per segment between the HFF and the IVIM-DWI parameters (D_{slow} , D_{fast} and f_{fast}) or $T2^*$ using the log-linear model. *Indicates a significant correlation (adjusted for type I errors using Bonferroni correction).

Seg	D_{slow}		D_{fast}		f_{fast}		$T2^*$	
	r	p	r	p	r	p	r	p
II	-0.328	1.000	0.497	0.960	-0.213	1.000	-0.747	0.064
III	-0.144	1.000	0.434	1.000	-0.182	1.000	-0.406	1.000
IVa	-0.624	0.320	0.429	1.000	0.417	1.000	-0.767*	0.048*
IVb	-0.528	0.760	0.260	1.000	0.277	1.000	-0.801*	0.024*
V	-0.732	0.080	-0.345	1.000	-0.091	1.000	-0.692	0.144
VI	-0.669	0.192	-0.241	1.000	-0.043	1.000	-0.767*	0.048*
VII	-0.840*	0.008*	0.020	1.000	0.074	1.000	-0.777*	0.040*
VIII	-0.639	0.304	-0.177	1.000	-0.026	1.000	-0.804*	0.024*

4.4.2 Effect of fat on $T2^*$

$T2^*$ was normally distributed ($p=0.116$) and differed significantly between the three groups of different HFF, and also the intergroup comparisons were significantly different ($p<0.001$, Table 4.1). $T2^*$ was 32.2 ms for the first group ($\text{HFF} \leq 2.75\%$) and decreased steadily to 27.2 ms in group 2 ($2.75 < \text{HFF} \leq 5.5\%$) and 21.0 in group 3 ($\text{HFF} > 5.5\%$). Pearson's correlation analysis (Table 4.2) showed a significant negative linear relationship with moderate to strong correlation between HFF and $T2^*$ using both the linear model ($r = -0.607$, $p<0.001$) and the log-linear model ($r = -0.714$, $p<0.001$, Fig. 4.3).

The log-linear model showed overall higher correlations compared to the linear model and was therefore used for the individual segment analysis. In 5 of 8 segments a significant negative linear relationship with strong correlation ($r = -0.767$ to -0.804 ; $p \leq 0.048$) was observed between HFF and $T2^*$ using the log-linear model (Table 4.4).

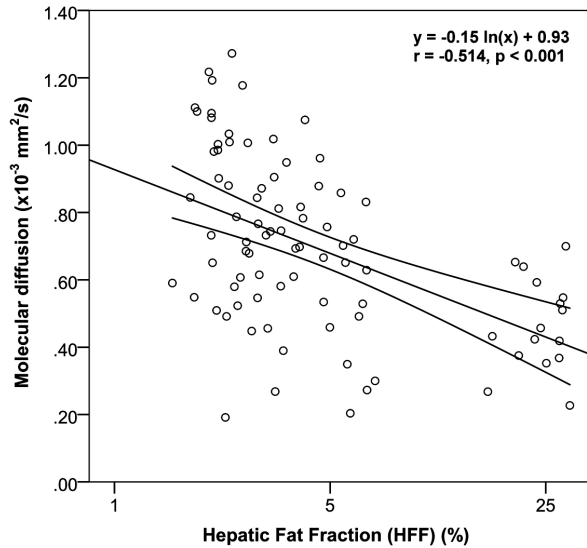


Figure 4.2: Regression plot between HFF and molecular diffusion. The correlation between HFF (%) and molecular diffusion ($\times 10^{-3} \text{ mm}^2/\text{s}$) was assessed by using a log-linear model. Pearson's product-moment correlation and its significance were calculated. The log-linear regression line is displayed together with its 95% confidence interval.

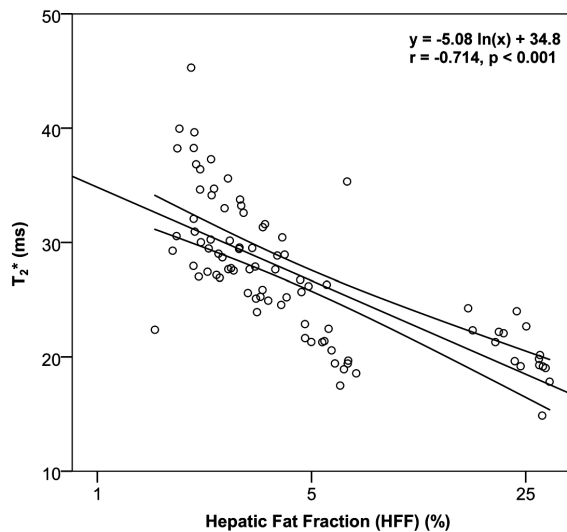


Figure 4.3: Regression plot between HFF and T_2^* . The correlation between HFF (%) and T_2^* (ms) was assessed by using a log-linear model. Pearson's product-moment correlation and its significance were calculated. The log-linear regression line is displayed together with its 95% confidence interval.

4.5 Discussion

4.5.1 Effect of fat on IVIM-DWI parameters

In this study it was demonstrated that molecular diffusion (D_{slow}) in the liver is affected by hepatic fat, also in the absence of steatosis (HFF below 5.5%). D_{slow} differed significantly between three groups of different HFF, and a steady significant decrease of D_{slow} with moderate correlation was found for increasing HFF.

These results complement existing knowledge of the reduction of molecular diffusion by steatotic HFF (>5.5%). Previous IVIM studies showed comparable negative correlations ($r = -0.59$ and $r = -0.18$) between HFF and molecular diffusion using a linear model (15, 31). In addition, Guiu et al. noticed a potential nonlinear effect between D_{slow} and HFF, especially for HFF below 3% (15). This was confirmed in our study: the relationship between HFF and D_{slow} appeared nonlinear with higher correlations for the log-linear model compared to the linear model.

Others compared non-steatotic with steatotic livers and observed a significant decrease of D_{slow} from $1.24 \times 10^{-3} \text{ mm}^2/\text{s}$ to $1.03 \times 10^{-3} \text{ mm}^2/\text{s}$ (15). Mono-exponential fitting of just a pair of DW images also indicated a significant decrease of the ADC in patients with HFF higher than 5%, with moderate correlations ($r = -0.39$) (13). Similar results were found in an animal study, increasing degrees of hepatic steatosis correlated fairly well ($r = -0.56$) with decreasing liver ADCs (12).

With regard to the effect of fat on IVIM-DWI parameters in the different segmental regions, we used the log-linear model which had the highest correlations in the overall analysis compared to the linear model. It was observed that D_{slow} correlated moderately to strong with HFF; however only in segment VII the correlation reached significance. This indicates that fat has a rather similar effect on D_{slow} throughout the liver, yet larger studies are needed to confirm these findings. In particular the segments in the left lobe (II and III) did not demonstrate a relationship between D_{slow} and HFF, which may reflect increased cardiac motion artifacts in that region, hampering DWI quantification (32).

The decrease of molecular diffusion by fat can be due to several mechanisms. MR relaxation is determined predominantly by water-macromolecular interactions (33). The MR signal from protons bound to macromolecules such as fat will interfere with the MR signal from freely diffusing water molecules. This can partly explain the observed decreased molecular diffusion in the presence of fat.

To prevent interference, fat suppression techniques serve to suppress the signal originating from protons bound to fat in order to reduce the chemical shift artifacts and eliminate signals arising from adipose tissue (34). However, fat suppression techniques are not perfect and come with disadvantages and pitfalls such as the dependency on the homogeneity of the main static magnetic field. Hence there will always be some interference of MR signal between free protons and macromolecular protons that cannot be neglected.

However, as indicated previously by the breast DWI study of Baron et al., low molecular diffusion in the presence of fat may reflect either direct contributions from the protons of the relatively immobile fat molecules or low water content, thereby restricting the diffusion of water (trapped water) (35).

Similarly, we hypothesize that the reduction of molecular diffusion in the liver is caused by physical hindrance of the movement of water molecules by the presence of macrovesicular fat droplets in hepatocytes. The fat present in the liver, is stored as triglycerides in sphere shaped vacuoles, which usually appear as large droplets with diameters larger than $15\ \mu\text{m}$ (36). These vacuoles reside in the hepatocytes, which are polygonal cells with six or more faces and a mean diameter ranging between 20 and $40\ \mu\text{m}$ (37). A considerable fraction of the volume of the hepatocyte can therefore be occupied by the macrovesicular fat droplet (Fig. 4.4).

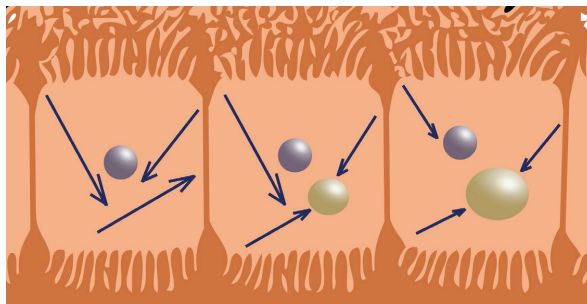


Figure 4.4: Schematic representation of the reduction of molecular diffusion in the hepatocytes by fat droplets. When fat is present in the liver, it is stored as triglycerides in sphere shaped vacuoles. Commonly, these (macrovesicular) vacuoles appear as just one large droplet (yellow spheres) with a diameter larger than $15\ \mu\text{m}$, sometimes dislocating the nucleus (purple spheres) with it. The mean diameter of a hepatocyte ranges between 20 and $40\ \mu\text{m}$. A considerable fraction of the volume of the hepatocyte can therefore be occupied by the macrovesicular fat droplet. Considering a diffusion length of about $17\ \mu\text{m}$, which is in the same order of magnitude of the hepatocyte's diameter, the movement of water molecules (blue arrows) can be physically hindered by the presence of macrovesicular fat droplets in hepatocytes. This explains the decrease of the molecular diffusion with increasing hepatic fat fractions as a mechanical process.

Considering a diffusion length (38) of about $17 \mu\text{m}$ ($l_D = \sqrt{6Dt}$, $D = 1.0 \times 10^{-3} \text{ mm}^2/\text{s}$, $t = 50 \text{ ms}$), which is in the same order of magnitude of the hepatocyte's diameter, we suspect that the movement of water molecules can be physically hindered by the presence of macrovesicular fat droplets in hepatocytes. This would be a mechanical process rather than signal interference between protons bound to fat molecules and free water protons.

The microperfusion parameters (D_{fast} and f_{fast}) were overall not affected by the HFF, neither in the individual segments. The average fraction of microperfusion f_{fast} was comparable to previously published numbers (29–35%) on healthy livers (15, 23). In agreement with earlier findings, f_{fast} was highest ($\geq 44\%$) in the left lobe (segments II and III) (39).

Microperfusion (D_{fast}) has been found to be lower in patients with steatosis compared to patients without steatosis (15). In contrast, in this study we did not find a relation between D_{fast} and HFF. This can be partially due to the limited accuracy of D_{fast} in this study. Because of software limitations on the MR system, it was not possible to acquire any data of D_{fast} between $b = 0$ and 50 s/mm^2 .

It is known that the choice of b-values is important for an accurate determination of IVIM parameters, and especially for a precise estimate of D_{fast} a number of b-values should be in the range from $b = 0$ to 50 s/mm^2 (22). The lack of b-values below 50 s/mm^2 can also explain the relatively low standard deviation of D_{fast} in our study. Previously, the ratio of D_{fast} and its standard deviation has been reported to range roughly between 1 and 3, compared to 4 – 4.5 in our study (15, 23). This suggests that in our study D_{fast} is potentially biased and forced by the fitting algorithm towards a relatively fixed value due to a lack of underlying data points, thereby reducing the overall standard deviation.

The wide range of HFF measurements (1.5–29.9%) demonstrated by our subjects was in concordance with previously published numbers. In a large population-based project conducted in northeast Germany, HFF ranged between 4.6% and 34.9% for the majority of a group of 88 healthy volunteers (40). Also in a comparative methodological study, HFF of healthy volunteers ranged up to 21.1% showing high correlations between MR spectroscopy and two-point Dixon-based MRI fat quantification (41).

4.5.2 Effect of fat on T_2^*

In this study, T_2^* differed significantly between three groups of different HFF, also for non-steatotic HFF below 5.5%, and a steady significant decrease of T_2^* with strong correlation was found for increasing HFF. Also in the different segmental regions, we found that T_2^* correlated significantly with HFF in 5 of the 8 segments. Correlations were higher for the log-linear model compared to the linear model, suggesting a nonlinear relationship between HFF and T_2^* as well.

Hepatic T_2^* variations among different segments have been shown to be low in healthy subjects, ranging between 19.3 and 29.9 ms (42), which is in accordance with our observations. Similar results were obtained in an animal study where the T_2^* of liver parenchyma of rats decreased from 31.4 ms for the control group (0.9% HFF) to 19.1 ms for rats fed by a four week choline-deficient diet (26.0% HFF) (43). A clinical study on patients with non-alcoholic fatty liver disease (NAFLD) reported significant decreases of T_2 relaxation times of water with increasing fat fractions (19). In addition, T_2^* shorting by fat has been confirmed using various phantoms with different fat-water mixtures (44).

However, for a number of studies no correlation was found between T_2^* relaxation and HFF (20, 45). For example, Hernando and Kühn et al. demonstrated that T_2^* estimations are inaccurate in tissues with high fat content due to the complex fat spectrum, and concluded that these issues can be solved when multipeak spectral modeling of fat is applied: this way they showed that T_2^* is independent of the fat fraction (18, 40). In our study, T_2^* was not corrected for the spectral complexity of the fat signal, which can explain the dependency of T_2^* on the HFF in our study.

The dependency of T_2^* on HFF can also be understood from the perspective of Bottomley et al. who suggested a fast exchange two-state (FETS) model to describe proton T_1 and T_2 relaxation in normal tissue (46). They identified three chemically different proton species: macromolecular protons (excluding fatty acids), free water protons, and mobile fatty acid protons, relaxing with T_2 times of 10-100 μ s, 50 ms and 0.2 s respectively. If the amount of fat in the liver changes, the interference pattern of the different proton signals, causing dephasing, also changes, and the overall effect can be shortening of the T_2^* relaxation time. This is in concordance with Yu et al. who suggested that when fat coexists with water in a voxel, T_2^* relaxometry may be disturbed by the chemical shift of fat, due to constructive and destructive interference of fat and water signals (47).

4.5.3 Clinical implications

It is known that the decreases of the molecular diffusion between normal liver tissue and cirrhosis or the different stages of fibrosis are relatively small and technically challenging to detect (23, 48, 49). It is therefore important to know what methodological factors can reduce molecular diffusion, regardless of the pathology itself.

One of these factors is that diffusion measurements can be heavily dependent on the MR-equipment used, which requires use of the same scanner to ensure comparable measurements (50). Also, user-dependent factors such as the choice of measurement location within the liver may affect the diffusion measurements. This was demonstrated in a recent study where the apparent diffusion coefficient significantly depended on the segmental region in the liver (39).

In the current study, we added another factor: molecular diffusion is negatively related to the hepatic fat fraction, also at non-steatotic fat levels. This is especially important when in pursuit for quantitative cut-off values for molecular diffusion in order to discriminate healthy liver tissue from pathology. Molecular diffusion is dependent on the hepatic fat fraction, also below 5.5%. This implicates that any derived cut-off value of the molecular diffusion for cirrhosis, or stages of fibrosis, is dependent on the hepatic fat fraction as well, especially because it is known that hepatic fat fractions vary between subjects (51). Therefore, we recommend that to correctly interpret quantitative hepatic DWI, acquisition of the hepatic fat fraction prior to the hepatic DWI protocol is necessary. In that way, diffusion measurements can be judged along with the fat measurement, which ensures a more reliable assessment of the diffusion properties of pathology.

Similar issues apply to quantitative evaluation of hemochromatosis using $T2^*$ (ms) estimation. The histopathologic iron grade can be classified using $T2^*$ measurement of the liver (52). For that purpose cut-off values have been defined. However, if $T2^*$ values are dependent on the HFF, then cut-off values used in the classification of hemochromatosis ought to be corrected for the hepatic fat fraction.

Next to quantitative difficulties, also non-quantitative issues may arise due to the effect of fat on hepatic DWI. Hypointensity in DWI can be a side effect of $T2^*$ shortening. DW images are $T2$ weighted and changes in $T2$ relaxation times can therefore affect the signal intensities independently of the tissue diffusion in three ways (53): shine-through (prolongation of $T2$), washout (balance between $T2$ prolongation and increased diffusion) and blackout or hypointensity (shortening of $T2$). As fat shortens $T2^*$, locally elevated levels of fat in the liver can reveal as hypointense areas, which might be incor-

rectly interpreted as increased liver diffusion.

4.5.4 Conclusions

In conclusion, we have demonstrated that hepatic fat fractions significantly decrease the molecular diffusion in the liver, also for non-steatotic fat levels ($\leq 5.5\%$). In addition, it was confirmed that hepatic fat fractions significantly decrease $T2^*$ measurements when multippeak spectral modeling is not applied. It is known that the decreases of the molecular diffusion between normal liver tissue and cirrhosis or the different stages of fibrosis are relatively small and technically challenging to be detected (23, 48, 49). The knowledge of the effect of low levels of hepatic fat on the molecular diffusion is therefore expected to be of importance in the diagnosis and staging of fibrosis and cirrhosis using quantitative DWI. Therefore, we conclude that to correctly interpret quantitative hepatic DWI, acquisition of the hepatic fat fraction prior to the hepatic DWI protocol is necessary to ensure a reliable assessment of the diffusion properties of pathology.

4.6 Acknowledgements

We thank Evelien Hans, Heike Held and Inge Vuist for their support with the recruitment and data collection.

4.7 References

- (1) Callaghan, P. T., Jolley, K. W., and Humphrey, R. S. (1983). Diffusion of fat and water in cheese as studied by pulsed field gradient nuclear magnetic resonance. *Journal of colloid and interface science* 93, 521–529.
- (2) Toussaint, J.-F., Southern, J. F., Fuster, V., and Kantor, H. L. (1997). Water diffusion properties of human atherosclerosis and thrombosis measured by pulse field gradient nuclear magnetic resonance. *Arterioscler Thromb Vasc Biol.* 17, 542–546.
- (3) Muller, M. F., Prasad, P., Siewert, B., Nissenbaum, M. A., Raptopoulos, V., and Edelman, R. R. (1994). Abdominal diffusion mapping with use of a whole-body echo-planar system. *Radiology* 190, 475–478.
- (4) Bihan, D. L., Breton, E., Lallemand, D., Aubin, M. L., Vignaud, J., and Laval-Jeantet, M. (1988). Separation of diffusion and perfusion in intravoxel incoherent motion MR imaging. *Radiology* 168, 497–505.
- (5) Yamada, I., Aung, W., Himeno, Y., Nakagawa, T., and Shibuya, H. (1999). Diffusion coefficients in abdominal organs and hepatic lesions: evaluation with intravoxel incoherent motion echo-planar MR imaging. *Radiology* 210, 617–623.

- (6) Tachibana, Y. et al. (2013). Analysis of multiple B-value diffusion-weighted imaging in pediatric acute encephalopathy. *PLoS one* 8, e63869.
- (7) Ichikawa, T., Haradome, H., Hachiya, J., Nitatori, T., and Araki, T. (1999). Diffusion-weighted MR imaging with single-shot echo-planar imaging in the upper abdomen: preliminary clinical experience in 61 patients. *Abdominal Imaging* 24, 456–461.
- (8) Amano, Y., Kumazaki, T., and Ishihara, M. (1998). Single-shot diffusion-weighted echo-planar imaging of normal and cirrhotic livers using a phased-array multicoil. *Acta Radiologica (Stockholm, Sweden : 1987)* 39, 440–442.
- (9) Kele, P. G., and van der Jagt, E. J. (2010). Diffusion weighted imaging in the liver. *World journal of gastroenterology : WJG* 16, 1567–1576.
- (10) Bakan, A. A., Inci, E., Bakan, S., Gokturk, S., and Cimilli, T. (2012). Utility of diffusion-weighted imaging in the evaluation of liver fibrosis. *European radiology* 22, 682–687.
- (11) Morelli, J. N., Michaely, H. J., Meyer, M. M., Rustemeyer, T., Schoenberg, S. O., and Attenberger, U. I. (2013). Comparison of Dynamic and Liver-Specific Gadoteric Acid Contrast-Enhanced MRI versus Apparent Diffusion Coefficients. *PLoS one* 8, e61898.
- (12) Anderson, S. W. et al. (2011). Effect of disease progression on liver apparent diffusion coefficient values in a murine model of NASH at 11.7 Tesla MRI. *Journal of magnetic resonance imaging : JMRI* 33, 882–888.
- (13) Poyraz, A. K., Onur, M. R., Kocakoc, E., and Ogur, E. (2012). Diffusion-weighted MRI of fatty liver. *Journal of magnetic resonance imaging : JMRI* 35, 1108–1111.
- (14) Wignall, O., Scurr, E., Collins, D., Thng, C. H., and Koh, D. M. (2008). Hepatic steatosis results in a reduction in the apparent diffusion coefficient (ADC) of liver parenchyma. *Proc. Intl. Soc. Mag. Reson. Med.* 16.
- (15) Guiu, B. et al. (2012). Intravoxel incoherent motion diffusion-weighted imaging in nonalcoholic fatty liver disease: a 3.0-T MR study. *Radiology* 265, 96–103.
- (16) Szczepaniak, L. S. et al. (2005). Magnetic resonance spectroscopy to measure hepatic triglyceride content: prevalence of hepatic steatosis in the general population. *American journal of physiology. Endocrinology and metabolism* 288, E462–8.
- (17) Capitan, V. et al. (2012). Macroscopic heterogeneity of liver fat: an MR-based study in type-2 diabetic patients. *European radiology* 22, 2161–2168.
- (18) Kuhn, J. P. et al. (2012). Effect of Multiplex Spectral Modeling of Fat for Liver Iron and Fat Quantification: Correlation of Biopsy with MR Imaging Results. *Radiology* 265, 133–142.
- (19) Gilman, A. J., Qayyum, A., Nystrom, M., and Noworolski, S. M. (2011). Liver Fat and Water MR T2 Values at 3T: Dependence Upon Steatosis Level. *Proc. Intl. Soc. Mag. Reson. Med.* 19.
- (20) Thomsen, C., Becker, U., Winkler, K., Christoffersen, P., Jensen, M., and Henriksen, O. (1994). Quantification of liver fat using magnetic resonance spectroscopy. *Magnetic resonance imaging* 12, 487–495.
- (21) Bihan, D. L., Turner, R., Moonen, C. T., and Pekar, J. (1991). Imaging of diffusion and microcirculation with gradient sensitization: design, strategy, and significance. *Journal of magnetic resonance imaging : JMRI* 1, 7–28.
- (22) Lemke, A. et al. (2009). Differentiation of pancreas carcinoma from healthy pancreatic tissue using multiple b-values: comparison of apparent diffusion coefficient and intravoxel incoherent motion derived parameters. *Investigative radiology* 44, 769–775.
- (23) Luciani, A. et al. (2008). Liver cirrhosis: intravoxel incoherent motion MR imaging—pilot study. *Radiology* 249, 891–899.
- (24) Turner, R., Bihan, D. L., Maier, J., Vavrek, R., Hedges, L. K., and Pekar, J. (1990). Echo-planar imaging of intravoxel incoherent motion. *Radiology* 177, 407–414.
- (25) Hussain, H. K. et al. (2005). Hepatic fat fraction: MR imaging for quantitative measurement and display—early experience. *Radiology* 237, 1048–1055.

- (26) Dixon, W. T. (1984). Simple proton spectroscopic imaging. *Radiology* 153, 189–194.
- (27) Couinaud, C., *Le foie: etudes anatomiques et chirurgicales*; Masson: Paris, 1957.
- (28) Bismuth, H. (1982). Surgical anatomy and anatomical surgery of the liver. *World journal of surgery* 6, 3–9.
- (29) Levin, J. R., Serlin, R. C., and Seaman, M. A. (1994). A controlled, powerful multiple-comparison strategy for several situations. *Psychological bulletin* 115, 153–159.
- (30) Taylor, R. (1990). Interpretation of the Correlation-Coefficient - a Basic Review. *Journal of Diagnostic Medical Sonography* 6, 35–39.
- (31) Yu, S.-M., Kim, S.-S., Paek, M.-Y., Goo, E.-H., Ji, Y.-S., and Choe, B.-Y. (2013). Correlation between Hepatic Fat Content Using 3-Echo 3-D Dixon Method and Intravoxel Incoherent Motion (IVIM) Perfusion MR Imaging. *Applied Magnetic Resonance*, 1–11.
- (32) Kwee, T. C. et al. (2009). Influence of cardiac motion on diffusion-weighted magnetic resonance imaging of the liver. *Magma (New York, N.Y.)* 22, 319–325.
- (33) Chai, J. W. et al. (2001). In vivo magnetic resonance (MR) study of fatty liver: importance of intracellular ultrastructural alteration for MR tissue parameters change. *Journal of magnetic resonance imaging : JMRI* 14, 35–41.
- (34) Delfaut, E. M., Beltran, J., Johnson, G., Rousseau, J., Marchandise, X., and Cotten, A. (1999). Fat suppression in MR imaging: techniques and pitfalls. *Radiographics : a review publication of the Radiological Society of North America, Inc* 19, 373–382.
- (35) Baron, P., Dorrius, M. D., Kappert, P., Oudkerk, M., and Sijens, P. E. (2010). Diffusion-weighted imaging of normal fibroglandular breast tissue: influence of microperfusion and fat suppression technique on the apparent diffusion coefficient. *NMR in biomedicine* 23, 399–405.
- (36) Zaitoun, A. M., Mardini, H. A., Awad, S., Ukabam, S., Makadisi, S., and Record, C. O. (2001). Quantitative assessment of fibrosis and steatosis in liver biopsies from patients with chronic hepatitis C. *Journal of clinical pathology* 54, 461–465.
- (37) Kuntz, E., Kuntz, H.-D., and SpringerLink Hepatology Textbook and Atlas., 2008.
- (38) Chawla, S., Kim, S., Wang, S., and Poptani, H. (2009). Diffusion-weighted imaging in head and neck cancers. *Future oncology (London, England)* 5, 959–975.
- (39) Dijkstra, H., Baron, P., Kappert, P., Oudkerk, M., and Sijens, P. E. (2012). Effects of microperfusion in hepatic diffusion weighted imaging. *European radiology* 22, 891–899.
- (40) Hernando, D. et al. (2013). R2* estimation using "in-phase" echoes in the presence of fat: The effects of complex spectrum of fat. *Journal of magnetic resonance imaging : JMRI* 37, 717–726.
- (41) Irwan, R., Edens, M. A., and Sijens, P. E. (2008). Assessment of the variations in fat content in normal liver using a fast MR imaging method in comparison with results obtained by spectroscopic imaging. *European radiology* 18, 806–813.
- (42) Meloni, A. et al. (2011). Single region of interest versus multislice T2* MRI approach for the quantification of hepatic iron overload. *Journal of magnetic resonance imaging : JMRI* 33, 348–355.
- (43) Okada, M. et al. (2011). Unenhanced fat fraction ratios obtained by MR and enhanced T2* values with liver-specific MR contrast agents for diagnosis of non-alcoholic steatohepatitis in rats. *Acta Radiologica (Stockholm, Sweden : 1987)* 52, 658–664.
- (44) Kamman, R. L., Bakker, C. J., van Dijk, P., Stomp, G. P., Heiner, A. P., and Berendsen, H. J. (1987). Multi-exponential relaxation analysis with MR imaging and NMR spectroscopy using fat-water systems. *Magnetic resonance imaging* 5, 381–392.
- (45) Meisamy, S. et al. (2011). Quantification of hepatic steatosis with T1-independent, T2-corrected MR imaging with spectral modeling of fat: blinded comparison with MR spectroscopy. *Radiology* 258, 767–775.

- (46) Bottomley, P. A., Hardy, C. J., Argersinger, R. E., and Allen-Moore, G. (1987). A review of ^1H nuclear magnetic resonance relaxation in pathology: are T1 and T2 diagnostic? *Medical physics* 14, 1–37.
- (47) Yu, H. et al. (2007). Multiecho reconstruction for simultaneous water-fat decomposition and T2* estimation. *Journal of magnetic resonance imaging : JMRI* 26, 1153–1161.
- (48) Dyvorne, H. A. et al. (2013). Diffusion-weighted imaging of the liver with multiple b values: effect of diffusion gradient polarity and breathing acquisition on image quality and intravoxel incoherent motion parameters—a pilot study. *Radiology* 266, 920–929.
- (49) Patel, J., Sigmund, E. E., Rusinek, H., Oei, M., Babb, J. S., and Taouli, B. (2010). Diagnosis of cirrhosis with intravoxel incoherent motion diffusion MRI and dynamic contrast-enhanced MRI alone and in combination: preliminary experience. *Journal of magnetic resonance imaging : JMRI* 31, 589–600.
- (50) Rao, R. K. et al. (2012). Implementation of dual-source RF excitation in 3 T MR-scanners allows for nearly identical ADC values compared to 1.5 T MR scanners in the abdomen. *PLoS one* 7, e32613.
- (51) Liska, D. et al. (2007). Interethnic differences in muscle, liver and abdominal fat partitioning in obese adolescents. *PLoS one* 2, e569.
- (52) Chandarana, H. et al. (2009). Hepatic iron deposition in patients with liver disease: preliminary experience with breath-hold multiecho T2*-weighted sequence. *AJR.American journal of roentgenology* 193, 1261–1267.
- (53) Hiwatashi, A. et al. (2003). Hypointensity on diffusion-weighted MRI of the brain related to T2 shortening and susceptibility effects. *AJR.American journal of roentgenology* 181, 1705–1709.

Diminished liver microperfusion in Fontan patients: a biexponential DWI study

Hildebrand Dijkstra
Djoeke Wolff
Joost P. van Melle
Beatrijs Bartelds
Tineke P. Willems
Matthijs Oudkerk
Hans Hillege
Aad P. van den Berg
Tjark Ebels
Paul E. Sijens

Submitted to NMR in Biomedicine

5.1 Abstract

Background: It has been demonstrated that hepatic apparent diffusion coefficients (ADC) are decreasing in patients with a Fontan circulation. It remains however unclear whether this is a true decrease of molecular diffusion, or rather reflects decreased microperfusion due to decreased portal blood flow.

Purpose: The purpose of this study was therefore to differentiate diffusion and microperfusion using intravoxel incoherent motion (IVIM) modeled diffusion-weighted imaging (DWI) for different liver segments in patients with a Fontan circulation, compare to a control group, and relate with liver function, chronic congestion and hepatic disease.

Materials and Methods: Livers of 59 consecutively included patients with Fontan circulation (29 men; mean-age, 19.1 years) were examined (Oct 2012–Dec 2013) with 1.5T MRI and DWI ($b=0, 50, 100, 250, 500, 750, 1500$ and 1750 s/mm²). IVIM ($D_{\text{slow}}, D_{\text{fast}}, f_{\text{fast}}$) and ADC were calculated for eight liver segments, compared to a control group (19 volunteers; 10 men; mean-age, 32.9 years), and correlated to follow-up duration, clinical variables, and laboratory measurements associated with liver function.

Results: Microperfusion was reduced ($p<0.001$) in Fontan livers compared to controls with -38.1% for D_{fast} and -32.6% for f_{fast} . Molecular diffusion (D_{slow}) was similar between patients and controls, while ADC was significantly lower (-14.3%) in patients ($p<0.001$). ADC decreased significantly with follow-up duration after Fontan operation ($r = -0.657$). D_{slow} showed significant inverse correlations ($r = -0.591$) with follow-up duration whereas D_{fast} and f_{fast} did not.

Conclusions: Decreased hepatic microperfusion was found in Fontan livers compared with controls while molecular diffusion was similar; however, since the Fontan operation molecular diffusion and ADC decreased while microperfusion remained stable.

5.2 Introduction

Diffusion-weighted imaging (DWI) has been successfully applied in the assessment of diffuse liver diseases such as cirrhosis, fibrosis and steatosis (1–6). Cirrhotic livers had significantly lower apparent diffusion coefficients (ADC) than normal livers (2, 3, 6) and negative correlations between fibrosis stages and ADC values were demonstrated (1, 4, 5).

The ADC is obtained by calculating a mono-exponential fit from multiple (at least two) diffusion-weighted images, thereby integrating molecular diffusion and microperfusion effects in one quantitative parameter (7, 8). The concept of the ADC however has been derived from the more complex intravoxel incoherent motion (IVIM) model, which separates molecular diffusion and microperfusion effects by fitting a bi-exponential model to multiple DW images (8). It has been suggested that the ADC reduction observed in cirrhotic livers could be linked to decreased microperfusion values and may be related to reduced perfusion (2).

A category of patients with altered hepatic perfusion are patients with a Fontan circulation. Fontan et al. described a palliative operation in which the right atrium (and in newer techniques the caval veins) is directly connected to the pulmonary arteries (9, 10). Additional detail about the Fontan operation is provided in the Appendix (5.6).

In the absence of a subpulmonary ventricle, this operation induces increased central venous pressure, decreased preload and increased afterload of the ventricle (11). In the Netherlands, yearly around 1200 newborns are born with a congenital heart disease and around 4–5% of these patients have a complex congenital heart disease, known as the univentricular heart, and can be subject for a Fontan operation (12–14). Over four decades, the short term survival after the Fontan operation improved significantly, resulting in an increasing cohort of Fontan patients who reach adolescence and adulthood (15). Consequently, long-term complications of the Fontan circulation are more commonly seen.

One of the implications of the Fontan circulation is liver disease resulting in fibrosis and cirrhosis (16–19). A significant positive correlation has been found between the follow-up duration (number of days since the Fontan operation) and the degree of hepatic fibrosis (20). This hepatic damage in the context of a Fontan circulation is presumably caused by the elevated venous pressure and limited cardiac output that causes decreased portal flow (14). The hepatic artery compensates the diminished portal flow by increased hepatic arterial flow, which is termed the hepatic arterial buffer response. The distribution of the microperfusion is likely to vary among the different liver seg-

ments due to the alternative distribution of the hepatic flow in Fontan patients.

In a recent report we showed that mean hepatic ADCs are decreased in Fontan patients (21). It remained unclear whether this is a true decrease of molecular diffusion, or rather reflects decreased microperfusion due to decreased portal blood flow. Therefore, the aim of our current analysis is to differentiate diffusion and microperfusion using IVIM modeled DWI for different liver segments in patients with a Fontan circulation, compare the results to a control group, and explore the relationship with follow-up duration, liver function, chronic congestion and hepatic disease.

5.3 Materials and methods

5.3.1 Study population

The protocol of this prospective study was approved by the hospital's institutional review board and patients provided informed consent. Between January 2012 and October 2013, consecutive patients with a functionally univentricular heart treated with a Fontan operation (further referred to as Fontan patients) were scheduled for cardiac MRI including diffusion-weighted imaging (DWI) of the liver (21). Inclusion criteria were: age 10 years or older. This resulted in 59 patients, 32 children and 27 adults (29 men; mean-age, 19.1 years; age-range, 9.6–44.7 years). All 59 patients have been previously reported (21). This prior article dealt with the association between the ADC and functional liver parameters; whereas in this manuscript we apply IVIM modeling to explain the previously observed decreased ADC in Fontan livers by measuring the microperfusion and molecular diffusion in each of eight liver segments.

Clinical variables were available and included body mass index (BMI), cardiac index, ejection fraction, end-diastolic volume (EDV), laboratory measurements (AST, ALT, γ -GT, FactorVIII, AST/ALRatio, bilirubin, albumin, PT), MELDXI (model for end-stage liverdisease excluding INR), Fib-4 (Fibrosis-4 score) and vena cava inferior (VCI) diameter and were obtained using previously described standardized methods (21).

In addition, a control group of 19 volunteers was included in this study: 10 men and 9 women (mean-age, 32.9 years; age-range, 20–62 years) (22). All volunteers had no relevant medical history.

This study was conducted in accordance with the declaration of Helsinki and was approved by the institutional ethics committee. Informed consent was obtained from all study participants and/or their legally authorized representative.

5.3.2 MR protocols

Diffusion-weighted imaging (DWI) of the liver was acquired by Magnetic Resonance Imaging (MRI), using a commercially available 1.5 T scanner (Magnetom Aera, Siemens Medical Solutions, Erlangen, Germany). A 32 element spine matrix coil in combination with a 4 element body matrix was used as the receiver, and the body coil as transmitter.

The protocol included a routine localizer where after 9 series ($b = 0, 50, 100, 250, 500, 750, 1000, 1500$ and 1750 s/mm²) of DWI were acquired using a spin echo based echo-planar imaging (EPI) sequence using the following parameters: TR 5900-9600 ms; TE 90 ms; slice-thickness 5 mm; slice gap 10 mm; FOV 242×300 mm²; matrix 116×144; bandwidth 1335 Hz/pixel; averages 4 and parallel acquisition technique GRAPPA with acceleration factor 2. PACE respiratory triggering was enabled and spectral adiabatic inversion recovery (SPAIR) was used for fat suppression to avoid artifacts from subcutaneous fat. In total, between 14 and 16 transverse slices were acquired to cover the whole liver within an acquisition time of 2.5 minutes.

5.3.3 DWI analysis

The control group was acquired using 7 b-values ($b = 0, 50, 100, 250, 500, 750, 1000$ s/mm²); therefore only these 7 b-values were used in the comparison between Fontan patients and controls, whereas the remaining acquired DWI series ($b = 1500$ and 1750 s/mm²) were included in all other analyses.

Drawing of regions-of-interest (ROIs) and the analysis were performed off-line using monoexponential (ADC) and biexponential fitting procedures in a programmable graphical and calculus environment (Matlab, The Mathworks, Natick, MA, USA). Circular ROIs of 21.5 mm² were drawn in 8 different segments of the liver (segment II, III, IVa, IVb, V, VI, VII, VIII) according to the Couinaud-Bismuth classification (23, 24). Extra care was taken to avoid major blood vessels in the ROIs.

In the biexponential analyses, the diffusion-weighted signal intensities S were fitted using the parameters prescribed by the IVIM model (8, 25):

$$\frac{S}{S_0} = f_{fast} \cdot e^{-b \cdot D_{fast}} + f_{slow} \cdot e^{-b \cdot D_{slow}} \quad (5.1)$$

where S_0 is the maximum signal intensity, D_{fast} is the fast component representing microperfusion, f_{fast} is the fraction of microperfusion, D_{slow} is the slow component repre-

senting molecular diffusion and f_{slow} is the fraction of molecular diffusion ($f_{\text{slow}} = 1 - f_{\text{fast}}$).

Equation 5.1 was fitted by the Nelder-Mead simplex direct search method with bound constraints, which performs a constrained non-linear minimization of the sum of the squared residuals (26, 27). The initial guess D_{slow}^0 was estimated by calculating the slope of the asymptote by monoexponential fitting of the slow signal component between $b = 500$ and 1000 s/mm^2 , and D_{slow} was bound between 0.2 and $5 \times D_{\text{slow}}^0 \times 10^{-3} \text{ mm}^2/\text{s}$. The intercept of the asymptote with the y -axis at S_0 resulted in an initial guess f_{fast}^0 , and f_{fast} was bound between 0 and 1 . The slope of the signal between $b = 0$ and $b = 50 \text{ s/mm}^2$ was used to guess the initial value of the fast signal component (D_{fast}^0), and D_{fast} was bound between D_{slow}^0 (microperfusion can never be slower than molecular diffusion) and $100 \times 10^{-3} \text{ mm}^2/\text{s}$. The ADC was obtained by using a clinically accepted method: a mono-exponential fit of all b -values was performed.

5.3.4 Statistics

Statistical analyses were performed using SPSS (SPSS 20, Chicago, IL, USA). All data were tested for normality using Shapiro–Wilk tests. IVIM parameters and ADC averaged over all liver segments were compared between Fontan patients and controls by independent samples t -tests. Subsequently, IVIM and ADC were compared per liver segment between Fontan patients and controls by independent samples t -tests. One-way ANOVA tests were used to compare IVIM parameters and ADC between the eight liver segments.

Correlations between DWI (D_{slow} , D_{fast} , f_{fast} and ADC) and clinical laboratory measurements and follow-up duration were calculated using a linear ($Y = a \cdot X + b$) model using Pearson's correlation coefficient for normally distributed variables and Spearman's rank correlation coefficient for non-normally distributed variables.

Normally distributed data were shown as means with standard deviations. Non-normally distributed data were shown as medians with interquartile range. For all statistical tests $p < 0.05$ was considered to indicate a statistically significant difference.

5.4 Results

IVIM-DWI, ADC, AST, ALT, γ -GT, FactorVIII, AST/ALRatio, EDV, EF and Cardiac index were normally distributed ($p \geq 0.071$). Microperfusion parameters (D_{fast} and f_{fast})

averaged over all segments were significantly lower in Fontan patients compared to controls. D_{fast} was $23.2 \times 10^{-3} \text{ mm}^2/\text{s}$ in the liver of Fontan patients, and $37.5 \times 10^{-3} \text{ mm}^2/\text{s}$ in controls ($p < 0.001$, -38.1%). F_{fast} was 23.6% in Fontan patients, and 35.0% in controls ($p < 0.001$, -32.6%). D_{slow} was similar in patients and controls ranging between $0.95 \times 10^{-3} \text{ mm}^2/\text{s}$ and $1.00 \times 10^{-3} \text{ mm}^2/\text{s}$ ($p = 0.171$). The ADC was significantly lower ($p < 0.001$, -14.3%) in Fontan patients ($1.08 \times 10^{-3} \text{ mm}^2/\text{s}$) compared to the controls ($1.26 \times 10^{-3} \text{ mm}^2/\text{s}$).

Also on a segmental level, the microperfusion parameters were significantly decreased for the majority of liver segments of Fontan patients compared to controls (Table 5.1). The molecular diffusion was significantly lower in half of the segments (III, IVb, VI and VII) compared to controls (Table 5.2). The ADC was significantly lower in almost all segments (except segment V).

Concerning the homogeneity of IVIM values among the segments, it was observed that for Fontan patients the microperfusion parameters differed significantly throughout the liver ($p \leq 0.045$). This was also true for the ADC ($p < 0.001$). The molecular diffusion however was similar among the segments ($p = 0.208$).

Table 5.1: Microperfusion data (using 7 b-values) per segment. Differences among the segments were tested using one-way ANOVA tests. Differences of DWI data between patients and controls were assessed by independent t-tests. The microperfusion parameters were significantly decreased for the majority of liver segments of Fontan patients compared to controls. Data are mean \pm standard deviations. *p-value indicates significant difference

Seg.	$D_{\text{fast}} (\times 10^{-3} \text{ mm}^2/\text{s})$				$F_{\text{fast}} (\%)$			
	Controls	Patients	$\Delta\%$	p	Controls	Patients	$\Delta\%$	p
II	21.5 \pm 8.8	27.0 \pm 14.1	+25.6	0.051	58.6 \pm 12.1	32.6 \pm 12.2	-79.8	<0.001*
III	37.7 \pm 22.2	24.6 \pm 8.9	-53.3	0.021*	37.9 \pm 11.0	24.9 \pm 9.8	-52.2	<0.001*
IVa	31.2 \pm 17.9	23.8 \pm 9.5	-30.5	0.095	39.4 \pm 16.9	25.1 \pm 10.4	-57.0	0.002*
IVb	46.3 \pm 16.9	22.9 \pm 8.8	-202	<0.001*	35.1 \pm 9.5	21.2 \pm 7.9	-65.6	<0.001*
V	37.5 \pm 13.2	22.2 \pm 8.0	-68.9	<0.001*	29.3 \pm 6.9	20.4 \pm 8.3	-43.6	<0.001*
VI	45.1 \pm 23.7	22.4 \pm 8.1	-201	0.001*	27.6 \pm 9.2	21.3 \pm 7.9	-29.6	0.012*
VII	42.9 \pm 25.1	21.4 \pm 8.9	-200	0.002*	27.1 \pm 7.1	21.7 \pm 6.4	-24.9	0.007*
VIII	37.8 \pm 15.2	22.0 \pm 8.6	-71.8	<0.001*	24.9 \pm 9.7	22.2 \pm 7.0	-12.2	0.293
p	0.045*	0.001*			<0.001*	<0.001*		

Table 5.2: Diffusion data (using 7 b-values) per segment. Differences among the segments were tested using one-way ANOVA tests. Differences of DWI data between patients and controls were assessed by independent samples t-tests. The molecular diffusion was significantly lower in half of the segments compared to controls. The ADC of Fontan patients was significantly lower in almost all segments compared to controls (except segment V). Data are mean \pm standard deviations. *p-value indicates significant difference

Seg.	ADC ($\times 10^{-3}$ mm ² /s)				D _{slow} ($\times 10^{-3}$ mm ² /s)			
	Controls	Patients	$\Delta\%$	p	Controls	Patients	$\Delta\%$	p
II	1.42 \pm 0.29	1.15 \pm 0.28	-23.5	<0.001*	0.79 \pm 0.40	0.95 \pm 0.36	+16.8	0.123
III	1.38 \pm 0.15	1.10 \pm 0.15	-25.5	<0.001*	1.12 \pm 0.21	0.96 \pm 0.19	-16.7	0.009*
IVa	1.40 \pm 0.24	1.12 \pm 0.16	-25.0	<0.001*	1.05 \pm 0.38	0.97 \pm 0.23	-8.2	0.422
IVb	1.32 \pm 0.15	1.09 \pm 0.11	-21.1	<0.001*	1.12 \pm 0.14	0.98 \pm 0.14	-14.3	0.001*
V	1.09 \pm 0.18	1.05 \pm 0.12	-3.8	0.391	0.92 \pm 0.21	0.96 \pm 0.17	+4.2	0.482
VI	1.18 \pm 0.08	1.06 \pm 0.15	-11.3	<0.001*	1.02 \pm 0.09	0.95 \pm 0.17	-7.4	0.021*
VII	1.21 \pm 0.10	1.06 \pm 0.14	-14.2	<0.001*	1.05 \pm 0.13	0.93 \pm 0.18	-12.9	0.005*
VIII	1.09 \pm 0.16	1.00 \pm 0.15	-9.0	0.024*	0.94 \pm 0.21	0.88 \pm 0.20	-6.8	0.213
p	<0.001*	<0.001*			0.001*	0.208		

The DWI data averaged over all segments were correlated to the clinical laboratory measurements (Table 5.3). The median follow-up time was 11.2 years (min: 2.5 years; max: 33.6 years). The ADC showed a significant negative linear relationship with the follow-up duration after Fontan operation with a correlation coefficient $r = -0.657$ (Fig. 5.1), with the highest correlations found in segments II and VIII (Table 5.4).

Also the molecular diffusion showed a significant negative linear relationship ($r = -0.591$) with the follow-up duration (Fig. 5.1), with the highest correlations found in segments V and VIII. The microperfusion was stable over time and did not correlate with the follow-up duration ($r = -0.158$). The fraction of microperfusion on the other hand showed a significant positive linear relationship ($r = +0.401$) with the follow-up duration (Fig. 5.2(b)), with the highest correlations in segments V and VIII.

The FIB-4 score showed weak though significant relationships, negative with molecular diffusion ($r = -0.322$) and positive with the fraction of microperfusion ($r = +0.324$). Some other clinical laboratory parameters also showed significant correlations with IVIM-DWI parameters, most notably gamma GT with ADC and D_{slow} ($r = -0.450$ and $r = -0.424$, respectively; Table 5.3).

Table 5.3: Correlations between DWI parameters and clinical variables. †Pearson's correlation coefficient. ‡Spearman's rank correlation coefficient. *p-value indicates significant difference.

	ADC	D _{slow}	D _{fast}	F _{fast}
Laboratory measurements				
AST†	+0.199	+0.275*	+0.250	-0.132
ALT†	-0.173	-0.188	+0.045	+0.218
gamma GT†	-0.450*	-0.424*	-0.047	+0.199
Bilirubin‡	-0.258	-0.275	+0.198	+0.301*
Albumin‡	+0.127	+0.100	+0.238	+0.110
PT‡	-0.143	-0.180	-0.321*	-0.033
Factor VIII†	+0.046	-0.003	-0.058	+0.005
Liver disease scores				
MELDXI‡	-0.259	-0.271	+0.266	+0.402*
AST-ALT ratio†	+0.330*	+0.405*	+0.203	-0.317*
Fib-4‡	-0.344*	-0.322*	-0.020	+0.324*
Cardiac function				
EDV†	+0.153	+0.093	+0.031	+0.131
EF†	+0.043	+0.076	+0.070	-0.106
Cardiac-index†	+0.270*	+0.266*	+0.220	+0.005
VCI diameter‡	-0.222	-0.211	0.034	0.180
Follow-up duration†				
	-0.657*	-0.591*	-0.158	+0.401*

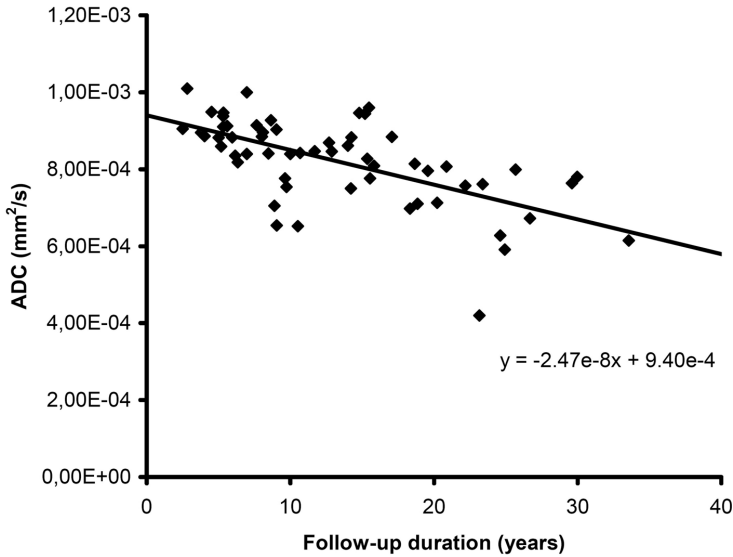
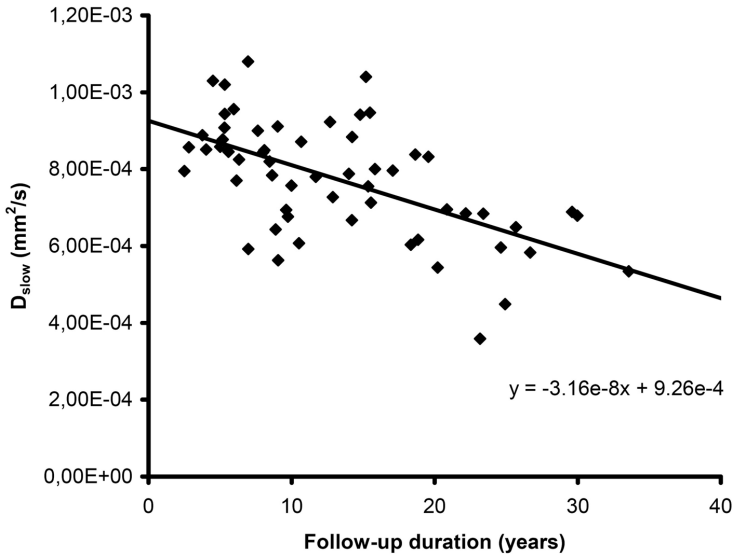


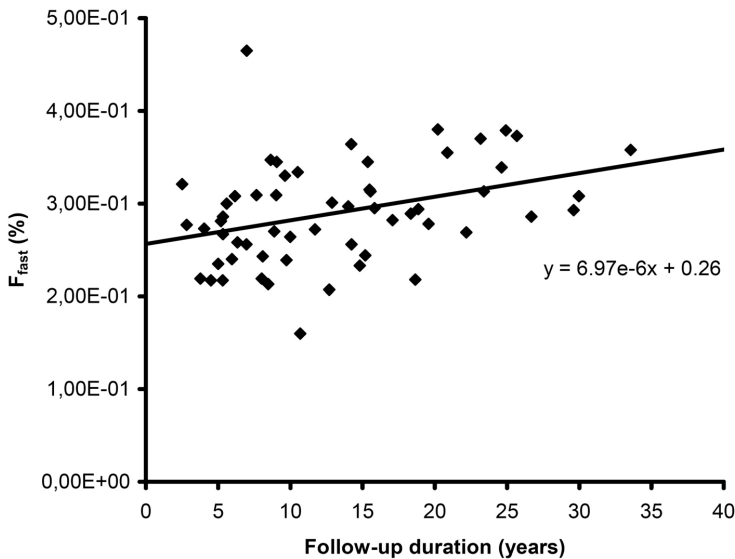
Figure 5.1: Correlation between follow-up duration and apparent diffusion coefficient (ADC). The mean hepatic ADC for each patient ($n = 59$) is plotted against the number of years since the Fontan operation (follow-up duration). The ADC showed a significant negative linear relationship with the follow-up duration ($r = -0.657$).

Table 5.4: Follow-up duration and DWI parameters correlated per segment. Data are Spearman's rank correlation coefficients. *p-value indicates significant difference.

Segment	ADC	D _{slow}	D _{fast}	F _{fast}
II	-0.632*	-0.307*	+0.002	-0.167
III	-0.447*	-0.397*	+0.067	+0.239
IVa	-0.555*	-0.453*	-0.216	+0.212
IVb	-0.367*	-0.258	+0.013	+0.221
V	-0.562*	-0.556*	-0.120	+0.440*
VI	-0.494*	-0.488*	-0.123	+0.269*
VII	-0.328*	-0.367*	-0.207	+0.203
VIII	-0.612*	-0.567*	-0.154	+0.371*



((a)) Follow-up duration vs. molecular diffusion (D_{slow}).



((b)) Follow-up duration vs. fraction of microperfusion (f_{fast}).

Figure 5.2: Correlation between follow-up duration and molecular diffusion (top) and microperfusion (bottom). The mean is plotted for each patient ($n = 59$) against the number of years since the Fontan operation (follow-up duration). D_{slow} showed a significant negative linear relationship ($r = -0.591$) with the follow-up duration, whereas the f_{fast} showed a significant positive linear relationship ($r = +0.401$)

5.5 Discussion

This study demonstrates that decreased hepatic ADC measurements of Fontan patients can be explained by significantly lower microperfusion in the Fontan liver rather than by decreased diffusion. It was observed that the molecular diffusion (D_{slow}) was similar between Fontan patients and controls, while the microperfusion parameters (D_{fast} and f_{fast}) and ADC were significantly lower in the Fontan liver. A previously formulated hypothesis relating hypoperfusion of the liver to the reduced ADC in Fontan patients is thus substantiated (21).

However, the currently and previously (21) reported strong negative dependency of the hepatic ADC on the follow-up duration after the Fontan operation, reflects changes of the molecular diffusion with time rather than changes of the microperfusion with time. This potentially indicates that in the Fontan patient's follow-up true cellular changes leading to fibrosis and cirrhosis dominate over changes in microperfusion.

The evidence in the current study that hypoperfusion of the liver in Fontan patients causes the reduced ADC values as compared with controls, confirms the high degree of sensitivity to microperfusion of the mono-exponential model which was already shown decades ago by Le Bihan et al. in DWI of the brain (8). When the DWI sequence contains b-values in the microperfusion range ($b \leq 100 \text{ s/mm}^2$), and the microperfusion is diminished, the ADC measurements will decrease (22). With a bi-exponential IVIM model, the cellular diffusion component can be distinguished from the microperfusion component, in order to improve our understanding of the underlying pathophysiology of liver disease in the Fontan circulation, and to provide important additional information on the degree of congestion and liver fibrosis and cirrhosis in clinical practice.

It was observed that the ADC values and molecular diffusion decreased with the follow-up duration after Fontan operation, whereas the microperfusion was stable over time. In other words, structural liver disease (i.e. liver fibrosis or cirrhosis) seems not present at first but develops progressively in time after Fontan operation whereas the hepatic congestion is chronically present and stable over time.

All patients had some derangement of laboratory liver measurements; potentially laboratory disturbance is not only associated with advanced liver disease, but also influenced by chronic liver damage, due to congestion and hypoperfusion. Increased gamma GT, a sign of congestive hepatopathy, was related to D_{slow} and unrelated to the microperfusion. This suggests that D_{slow} is potentially related to liver fibrosis and cirrhosis, and suggests that in the liver these processes might develop faster in context of more liver congestion (as in the first case report by Lemmer in 1983) (28).

Previous histological studies have demonstrated, on a microscopic level, that in patients with chronic hepatic congestion, the poorly arterially supplied hepatocytes in the centrilobular zone show atrophy (29, 30). In patients with a Fontan circulation, atrophy of centrilobular hepatocytes seems related to the degree of right sided pressure and to the time after Fontan operation (20, 30). Likewise, on a macroscopic level, the arterial blood supply is not homogenously distributed over the various liver segments. It has been reported that the ratio of the arterial liver perfusion (ALP) and portal venous perfusion (PVP) varies and is the lowest in segments V to VIII and highest in segments I to IV (31, 32). When the ALP over-compensates the PVP in Fontan patients, it is expected that the microperfusion increases in segments I to IV, and diminishes in segments V to VIII. This is confirmed by our data. This suggests that, in a Fontan circulation, the development of liver fibrosis or cirrhosis varies between the different liver segments, depending on the degree of arterial blood supply.

Altogether, this study demonstrated that the degree of congestion is generally stable with time after Fontan operation, whereas liver fibrosis/-cirrhosis develops progressively. With the bi-exponential model, the DWI-MR technique provides the opportunity to distinguish between these two components. For clinical practice, this provides a major advantage compared to the other non-invasive alternatives for liver biopsy. Potentially, a decrease in the microperfusion component could indicate an adverse change in the Fontan circulation, for instance more congestion due to a conduit stenosis or pulmonary vascular remodeling. With a routine follow-up of the cellular diffusion, the development of liver fibrosis/-cirrhosis can be safely monitored.

We suggest further research to investigate changes in microperfusion and cellular diffusion longitudinally, and want to highlight that, with progressive liver disease being apparently inherent to the Fontan circulation, steps have to be taken concerning potential treatment options for liver disease in Fontan patients. Therefore, future studies should focus on reversibility of this liver disease, and the effects and timing of potential treatment options, including heart transplantation, Fontan conversion or a late Fontan takedown.

5.5.1 Limitations

Liver damage in the Fontan circulation presents with disturbed transaminases, coagulation disorders, and can eventually lead to liver fibrosis-, cirrhosis and even hepatocellular carcinoma (33–35). It was assumed that the severity of fibrosis increases with

the follow-up duration after Fontan operation. The stage of liver fibrosis or cirrhosis was however not confirmed by liver biopsy, thereby limiting the study.

Although the segmental differences in microperfusion strongly point to the reported variation in the ALP and PVP in Fontan patients, this might also be related to cardiac pulsation artifacts in DWI which are known to result in deviating values between right and left liver lobe. The increase in the ADC in the left lobe is usually explained from the increased cardiac motion in the left lobe (36–40). However, it was also demonstrated that the increased ADC in the left lobe may be caused by extensive microperfusion contamination of the ADC and this does not affect the molecular diffusion obtained by IVIM (22). This effect of microperfusion contamination in the left lobe is also supported by the observed tendency of increased D_{fast} in segment II against the trend in all other segments.

5.5.2 Conclusions

Decreased hepatic microperfusion was found in Fontan livers compared with controls while the molecular diffusion was similar. The molecular diffusion and ADC decreased since the Fontan operation while the microperfusion remained stable. The current study is the first to show with IVIM-DWI that, in a Fontan circulation, the development of liver fibrosis or cirrhosis varies between the different liver segments, depending on the degree of arterial blood supply.

5.6 Appendix: The Fontan operation

The Fontan operation is currently the treatment-of-choice for patients who are born with a univentricular heart which is not suitable for a biventricular repair (9, 10). With the Fontan operation, the right atrium or both caval veins are surgically connected to the pulmonary artery, thereby bypassing the subpulmonary ventricle. This means that the systemic venous return flows passively through the pulmonary vascular bed, without the aid of a pumping ventricle. As a consequence, Fontan patients suffer from chronically elevated systemic venous pressure and decreased cardiac output due to decreased ventricular preload and increased ventricular afterload.

Over four decades, the short term survival after the Fontan operation improved significantly (15). However, patients who underwent a Fontan operation are prone to develop several complications on the long-term. The liver is one of the organs that suffer

from the unphysiologic circumstances. Both the increased systemic venous pressure and the decreased cardiac output are thought to be underlying causes of the progressive liver damage in the Fontan circulation.

The liver damage in the Fontan circulation was first recognized in a 15-year-old girl with severe systemic hypertension due to a conduit stenosis (28). Nowadays, more evidence is emerging that liver damage is not restricted to single patients with adverse hemodynamic complications, but is inherently related to the un-physiological circumstances of the Fontan circulation (21).

Liver damage in the Fontan circulation presents with disturbed transaminases, coagulation disorders, and can eventually lead to liver fibrosis-, cirrhosis and even hepatocellular carcinoma (33–35). Because a liver biopsy (which is considered the golden standard) is hazardous in Fontan patients, the search for alternative measures to assess liver fibrosis and cirrhosis is ongoing.

5.7 References

- (1) Bakan, A. A., Inci, E., Bakan, S., Gokturk, S., and Cimilli, T. (2012). Utility of diffusion-weighted imaging in the evaluation of liver fibrosis. *European radiology* 22, 682–687.
- (2) Luciani, A. et al. (2008). Liver cirrhosis: intravoxel incoherent motion MR imaging—pilot study. *Radiology* 249, 891–899.
- (3) Patel, J., Sigmund, E. E., Rusinek, H., Oei, M., Babb, J. S., and Taouli, B. (2010). Diagnosis of cirrhosis with intravoxel incoherent motion diffusion MRI and dynamic contrast-enhanced MRI alone and in combination: preliminary experience. *Journal of magnetic resonance imaging : JMIRI* 31, 589–600.
- (4) Lewin, M. et al. (2007). Diffusion-weighted magnetic resonance imaging for the assessment of fibrosis in chronic hepatitis C. *Hepatology (Baltimore, Md.)* 46, 658–665.
- (5) Wang, Y. et al. (2011). Assessment of chronic hepatitis and fibrosis: comparison of MR elastography and diffusion-weighted imaging. *AJR.American journal of roentgenology* 196, 553–561.
- (6) Amano, Y., Kumazaki, T., and Ishihara, M. (1998). Single-shot diffusion-weighted echo-planar imaging of normal and cirrhotic livers using a phased-array multicoil. *Acta Radiologica (Stockholm, Sweden : 1987)* 39, 440–442.
- (7) Namimoto, T., Yamashita, Y., Sumi, S., Tang, Y., and Takahashi, M. (1997). Focal liver masses: characterization with diffusion-weighted echo-planar MR imaging. *Radiology* 204, 739–744.
- (8) Bihan, D. L., Breton, E., Lallemand, D., Aubin, M. L., Vignaud, J., and Laval-Jeantet, M. (1988). Separation of diffusion and perfusion in intravoxel incoherent motion MR imaging. *Radiology* 168, 497–505.
- (9) Fontan, F., and Baudet, E. (1971). Surgical repair of tricuspid atresia. *Thorax* 26, 240–248.
- (10) Kreutzer, G., Galindez, E., Bono, H., Palma, C. D., and Laura, J. P. (1973). An operation for the correction of tricuspid atresia. *The Journal of thoracic and cardiovascular surgery* 66, 613–621.
- (11) Fredenburg, T. B., Johnson, T. R., and Cohen, M. D. (2011). The Fontan procedure: anatomy, complications, and manifestations of failure. *Radiographics : a review publication of the Radiological Society of North America, Inc* 31, 453–463.

- (12) Cornel, M. Aangeboren afwijkingen van het hartvaatstelsel: prevalentie en sterfte naar leeftijd en geslacht. In: Volksgezondheid Toekomst Verkenning, Nationaal Kompas Volksgezondheid. Bilthoven: RIVM, <http://www.nationaalkompas.nl/gezondheid-en-ziekte/ziekten-en-aandoeningen/aangeboren-afwijkingen/hartvaatstelsel/hoe-vaak-komen-aangeboren-afwijkingen-van-het-hartvaatstelsel-voor/>, 2010.
- (13) Hoffman, J. I., and Kaplan, S. (2002). The incidence of congenital heart disease. *Journal of the American College of Cardiology* 39, 1890–1900.
- (14) Rychik, J. et al. (2012). The precarious state of the liver after a Fontan operation: summary of a multidisciplinary symposium. *Pediatric cardiology* 33, 1001–1012.
- (15) Wolff, D., van Melle, J. P., Ebels, T., Hillege, H., van Slooten, Y. J., and Berger, R. M. (2014). Trends in mortality (1975–2011) after one- and two-stage Fontan surgery, including bidirectional Glenn through Fontan completion. *European journal of cardio-thoracic surgery : official journal of the European Association for Cardio-thoracic Surgery* 45, 602–609.
- (16) Greenway, S. C. et al. (2015). Fontan-associated liver disease: Implications for heart transplantation. *The Journal of heart and lung transplantation : the official publication of the International Society for Heart Transplantation*.
- (17) Pundi, K. et al. (2015). Liver Disease in Patients After the Fontan Operation. *The American Journal of Cardiology*.
- (18) Ozkurt, H., Keskiner, F., Karatag, O., Alkim, C., Erturk, S. M., and Basak, M. (2014). Diffusion Weighted MRI for Hepatic Fibrosis: Impact of b-Value. *Iranian journal of radiology : a quarterly journal published by the Iranian Radiological Society* 11, e3555.
- (19) Sandrasegaran, K. et al. (2009). Value of diffusion-weighted MRI for assessing liver fibrosis and cirrhosis. *AJR.American journal of roentgenology* 193, 1556–1560.
- (20) Kiesewetter, C. H. et al. (2007). Hepatic changes in the failing Fontan circulation. *Heart (British Cardiac Society)* 93, 579–584.
- (21) Wolff, D. et al. (2016). The Fontan circulation and the liver: A magnetic resonance diffusion-weighted imaging study. *International journal of cardiology* 202, 595–600.
- (22) Dijkstra, H., Baron, P., Kappert, P., Oudkerk, M., and Sijens, P. E. (2012). Effects of microperfusion in hepatic diffusion weighted imaging. *European radiology* 22, 891–899.
- (23) Couinaud, C., *Le foie: etudes anatomiques et chirurgicales*; Masson: Paris, 1957.
- (24) Bismuth, H. (1982). Surgical anatomy and anatomical surgery of the liver. *World journal of surgery* 6, 3–9.
- (25) Bihan, D. L., Turner, R., Moonen, C. T., and Pekar, J. (1991). Imaging of diffusion and microcirculation with gradient sensitization: design, strategy, and significance. *Journal of magnetic resonance imaging : JMRI* 1, 7–28.
- (26) Muller, M. F., Prasad, P., Siewert, B., Nissenbaum, M. A., Raptopoulos, V., and Edelman, R. R. (1994). Abdominal diffusion mapping with use of a whole-body echo-planar system. *Radiology* 190, 475–478.
- (27) Turner, R., Bihan, D. L., Maier, J., Vavrek, R., Hedges, L. K., and Pekar, J. (1990). Echo-planar imaging of intravoxel incoherent motion. *Radiology* 177, 407–414.
- (28) Lemmer, J. H., Coran, A. G., Behrendt, D. M., Heidelberger, K. P., and Stern, A. M. (1983). Liver fibrosis (cardiac cirrhosis) five years after modified Fontan operation for tricuspid atresia. *The Journal of thoracic and cardiovascular surgery* 86, 757–760.
- (29) Safran, A. P., and Schaffner, F. (1967). Chronic passive congestion of the liver in man. Electron microscopic study of cell atrophy and intralobular fibrosis. *The American journal of pathology* 50, 447–463.
- (30) Ghaferi, A. A., and Hutchins, G. M. (2005). Progression of liver pathology in patients undergoing the Fontan procedure: Chronic passive congestion, cardiac cirrhosis, hepatic adenoma, and hepatocellular carcinoma. *The Journal of thoracic and cardiovascular surgery* 129, 1348–1352.

- (31) Kanda, T. et al. (2012). Perfusion measurement of the whole upper abdomen of patients with and without liver diseases: initial experience with 320-detector row CT. *European Journal of Radiology* 81, 2470–2475.
- (32) Wang, X. et al. (2013). Quantitative hepatic CT perfusion measurement: comparison of Couinaud's hepatic segments with dual-source 128-slice CT. *European Journal of Radiology* 82, 220–226.
- (33) Johnson, J. A. et al. (2013). Identifying predictors of hepatic disease in patients after the Fontan operation: a postmortem analysis. *The Journal of thoracic and cardiovascular surgery* 146, 140–145.
- (34) Asrani, S. K. et al. (2012). Congenital heart disease and the liver. *Hepatology (Baltimore, Md.)* 56, 1160–1169.
- (35) Asrani, S. K., Warnes, C. A., and Kamath, P. S. (2013). Hepatocellular carcinoma after the Fontan procedure. *The New England journal of medicine* 368, 1756–1757.
- (36) Boulanger, Y. et al. (2003). Diffusion-weighted MR imaging of the liver of hepatitis C patients. *NMR in biomedicine* 16, 132–136.
- (37) Nasu, K., Kuroki, Y., Sekiguchi, R., Kazama, T., and Nakajima, H. (2006). Measurement of the apparent diffusion coefficient in the liver: is it a reliable index for hepatic disease diagnosis? *Radiation Medicine* 24, 438–444.
- (38) Koh, D. M. et al. (2006). Colorectal hepatic metastases: quantitative measurements using single-shot echo-planar diffusion-weighted MR imaging. *European radiology* 16, 1898–1905.
- (39) Kandpal, H., Sharma, R., Madhusudhan, K. S., and Kapoor, K. S. (2009). Respiratory-triggered versus breath-hold diffusion-weighted MRI of liver lesions: comparison of image quality and apparent diffusion coefficient values. *AJR. American journal of roentgenology* 192, 915–922.
- (40) Kwee, T. C. et al. (2009). Influence of cardiac motion on diffusion-weighted magnetic resonance imaging of the liver. *Magma (New York, N.Y.)* 22, 319–325.

Part III

Breast

**Effects of b-values and
pre-admission of contrast media on
the diagnostic accuracy of 1.5T
breast DWI: a systematic review
and meta-analysis**

Monique D. Dorrius
Hildebrand Dijkstra
Matthijs Oudkerk
Paul E. Sijens

Published in *European Radiology*
2014, vol. 24, no. 11, pp. 2835-2847.

6.1 Abstract

Purpose: To evaluate the effect of the choice of b-values and prior use of contrast medium on ADCs of breast lesions derived from DWI, and on the discrimination between benign and malignant lesions.

Materials and Methods: A literature search was performed of relevant DWI studies. The accuracy of DWI to characterize lesions by using b-value ≤ 600 s/mm² and b-value > 600 s/mm² was presented as pooled sensitivity and specificity, and the ADC was calculated for both groups. Also, lesions were pooled as pre- or post-contrast DWI.

Results: Of 198 articles, 26 met the inclusion criteria. Median ADCs were significantly higher (13.2–35.1%, $p < 0.001$) for the group of b-values ≤ 600 s/mm² compared to > 600 s/mm². The sensitivity in both groups was similar (91% and 89%, $p = 0.495$) as well as the specificity (75% and 84%, $p = 0.237$). Contrast medium had no significant effects on the ADCs ($p \geq 0.08$). The differentiation between benign and malignant lesions was optimal (58.4%) for the combination of b = 0 and 1000 s/mm².

Conclusions: The wide variety of b-value combinations applied in different studies significantly affects the ADC of breast lesions and therefore confounds quantitative DWI. If only a couple of b-values are used, those of b = 0 and 1000 s/mm² are recommended for the best improvement of differentiating between benign and malignant lesions.

6.2 Introduction

Contrast-enhanced Magnetic Resonance Imaging (MRI) of the breast has turned out to be a clinically useful additional diagnostic tool. Breast MR includes both diagnostic and screening indications (1). Imaging analysis is based on the enhancement pattern of lesions in dynamic breast MRI and on morphological changes (2–4). With these two criteria, breast MRI has an excellent sensitivity for cancer detection, which usually exceeds 90%. However, an overlap between benign and malignant lesions still exists and the overall specificity of MRI has generally been modest, ranging from 67% to 72% (5–7), and in some studies higher ($\geq 90\%$) owing to the use of a superior contrast agent (8) or a high magnetic field strength (9).

In addition to morphologic and kinetic analysis, new techniques are implemented; one of these techniques is diffusion weighted imaging (DWI), an extensively reviewed method reflecting the diffusion of water molecules through biologic tissues (10). Basically, a T_2^* -weighted control MRI series is made without application of a dephasing gradient ($b=0$ s/mm²) followed by one or more repeats with brief application of dephasing gradients for, typically, up to $b=1000$ s/mm² to allow for water to diffuse away leading to decreased signal intensities. The gradient factor b is a function of the third power of the gradient pulse duration (δ) and of the second power of the gradient strength (G), and is also affected by the time between the onsets of the diffusion gradients (Δ).

The apparent diffusion coefficient (ADC) map is a reconstructed image representing the slope in the graphics with on the X-axis the b values and on the Y-axis the logarithm of the signal intensities. This important tissue diffusion parameter already plays a major role in the evaluation of acute cerebral infarction. DWI has also been used in the diagnosis of neoplasms, for example the characterization of lesions in brain, liver, pancreas, prostate and ovary (11–17).

Nowadays, DWI can thus help to differentiate between benign and malignant breast lesions (18–43). However, the ADC obtained in the monoexponential analysis of DWI data of breast lesions, and the subsequently derived ADC thresholds which allow for optimal discrimination between malignant and benign lesions, show considerable variation (18–43). The problem is that besides true molecular diffusion, based on the thermally driven motion of water molecules (mean diffusivity), which is known as “Brownian motion”, there may be substantial contributions of additional faster components due to contributions of blood vessels (microperfusion) (10). The microperfusion term reflecting microcirculation of blood in the capillary network, is substantial in tumors, but not in normal glandular breast tissue, whereas a very slow diffusion term prevails in

fatty tissue (44). Therefore, both diffusion and perfusion affect the ADC values. ADCs tend to increase by the contributions from perfusion when small b-values are used, and decrease when reconstructed from DWI series measured with mainly higher b-values (reflecting diffusion) (44). Different ADC values can also be caused by contrast medium. Two studies showed that ADC decreased when DWI was acquired after contrast administration (45, 46).

Therefore, the purpose of this systematic review and meta-analysis is to evaluate the influence of different b-values on the ADC values obtained in DWI and on discriminating benign from malignant breast lesions in terms of sensitivity and specificity. Furthermore, the effects of contrast medium on the ADC of benign and malignant lesions are assessed.

6.3 Materials and methods

6.3.1 Search strategy

A computerized search was performed to identify relevant studies in Medline and Embase until December 2012. The following search terms were used in Medline: DWI[TIAB] OR diffusion[TIAB] OR "Diffusion Magnetic Resonance Imaging"[Mesh] AND ("Magnetic Resonance Imaging"[Mesh] OR "Magnetic Resonance Imaging"[TIAB] OR MRI[TIAB] OR "MR imaging"[TIAB] OR "MR mammography"[TIAB]) AND ("Breast Neoplasms"[Mesh] OR mamma carcinoma*[TIAB] OR breast[TIAB]) AND (specificity[TIAB] OR sensitivity[TIAB] OR "Sensitivity and Specificity"[Mesh] OR accura*[TIAB] OR predictive value[TIAB]). In Embase the same strategy was used. All languages were considered.

6.3.2 Eligibility criteria and study selection

Studies assessing the clinical value of DWI for a radiologist in the discrimination between benign and malignant breast lesions were searched. Studies were included if the following inclusion criteria were met (1) all patients underwent a breast DWI; (2) 1.5T MRI scanner was used; (3) study population had benign and malignant breast lesions, which were confirmed by pathology or at least a diagnostic follow-up of 1 or 2 years; (4) the type of analysis was tumor-based; (5) the mean ADC for malignant and

benign lesions were measured; (6) an ADC threshold was used for the calculations of sensitivity and specificity; (7) accuracy, sensitivity, specificity, positive predictive value and/or negative predictive value was/were measured or could be derived, and (8) published studies with original data in peer-reviewed journals. Reviews, editorials, and case-reports were excluded.

Two researchers (MDD, HD) independently selected relevant studies based on title and abstract or full article. Any discrepancies concerning the study selection were resolved by discussion of the full article. The complete search yielded 317 studies. After removing duplicates (n=119), 159 out of 198 studies were excluded based on the title and/or abstract. 13 out of 39 studies did not meet the inclusion criteria (no mean ADC or threshold (n=6), 3.0T MRI scanner (n=5), no sensitivity and specificity (n=1) and no histopathology (n=1)). The exclusion of the minority of studies performed at 3T rather than 1.5T was based on potential compromization of ADC values by increased image distortions by susceptibility artefacts and field inhomogeneities at the higher field strength (47).

Twenty-six studies fulfilled our inclusion criteria (Fig. 6.1). Twenty-one studies were in the English language; four studies were written in Chinese and the remaining one in Spanish. The non-English studies were assessed in cooperation with native speakers of the foreign language who had a background in radiology as well.

6.3.3 Data collection and quality assessment

The following study descriptives were extracted: population descriptives (age, number of patients, number of benign and malignant lesions), study design, type of MRI, scanning before or after contrast medium, b-values, mean ADC of benign lesions, mean ADC of malignant lesions, the threshold of the ADC and diagnostic accuracy numbers (true positives, false positives, true negatives and false negatives).

Study quality was assessed independently using the Quality Analysis of Data from Any Sensor (QUADAS) tool by the same two observers (48, 49), disagreement was resolved by arbitration. This evidence based tool was developed specifically to assess the quality of diagnostic accuracy studies and includes 14 quality items. The 14 items can be scored as “yes”, “no” or “unclear”. The total score can range from 0 to 14, in which 14 is the maximum attainable score.

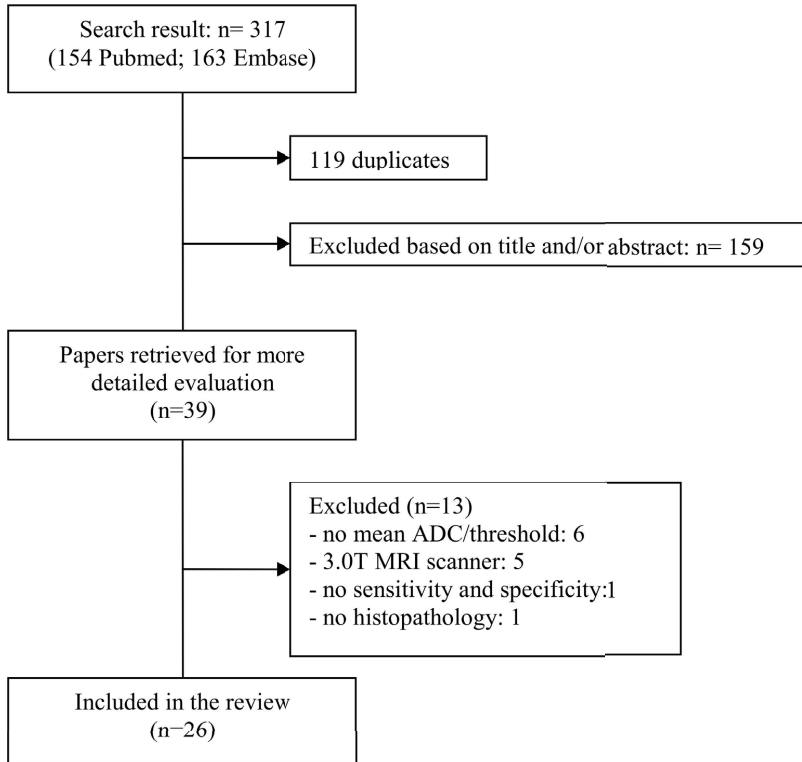


Figure 6.1: Flow chart of search results

6.3.4 Statistical analysis

The performance of DWI to discriminate benign and malignant breast lesions was assessed by evaluating study data rather than patient data, thus limiting the value of data pooling. Lesions were pooled in two distinct groups: ADCs obtained with a maximal b-value lower than or equal to 600 s/mm^2 and ADCs obtained with a maximal b-value higher than 600 s/mm^2 . This choice of cut-off was motivated by earlier findings in a breast DWI study of healthy volunteers, demonstrating that at b-values smaller than 600 s/mm^2 the DW signal is monoexponential (44).

All data were tested for normality using Shapiro–Wilk tests. Primary outcome was sensitivity and specificity at tumor level. Pooling of data was performed within the bivariate mixed-effects binary regression modelling framework. Model specification, estimation and prediction were carried out with the function XTMELOGIT in STATA (Ver-

sion 11, StataCorp, College Station, Texas, USA). The sensitivity and specificity were calculated using the model summary. A forest plot was generated containing the individual study sensitivities and specificities with 95% confidence intervals (CI) and the pooled sensitivity and specificity estimates. Significance was tested using Mann-Whitney tests.

To study the effect of b-values on the ADCs, the mean ADCs were not only calculated for the group of b-values ≤ 600 s/mm² and >600 s/mm², but also divided in five categories of maximum b-value: 250, 500-600, 700-800, 1000 and 1500-2000 s/mm². The effect of contrast medium on the ADCs of malignant and benign lesions was assessed by pooling lesions as pre- or post-contrast DWI.

For normally distributed data the mean ADCs and standard deviations were calculated for malignant and benign lesions and significance of differences between groups were tested with independent t-tests.

For non-normally distributed data the median ADCs and interquartile range were calculated and tested with Mann-Whitney U tests. $P < 0.05$ was considered to indicate a statistically significant difference. A test of heterogeneity was applied, using the I^2 statistics (50). The statistic calculates the percentage of total variation across studies that can be attributed to inter-study heterogeneity, ranging from 0% (no heterogeneity) to 100% (all variance due to heterogeneity).

Publication bias of the diagnostic accuracy test was evaluated using Deeks' funnel plot asymmetry test where $p > 0.10$ suggests a low likelihood of publication bias. Data were analysed in SPSS 20.0 (SPSS, Chicago, IL, USA) and STATA version 11.0 (StataCorp, College Station, Texas, USA).

Table 6.1: The sensitivity and specificity of DWI by using b-values > 600 s/mm².

Study Pereira: a: b-value 750; f: b-value 1000; l: b-value 0,250,500,750,1000

Study Fornasa: b: threshold 1.48; c: threshold 1.52

Study Belli: d: threshold 1.6; e: threshold 1.4

Study Yili: g: reader 1; h: reader 2

Study Gu: i: b-value 1000; m: b-value 2000

Study Rubesova: j: reader 1; k: reader 2

Study (author, ref, year of publication)	Contrast medium	B-values	Mean ADC malignant	Mean ADC benign	Thres- -hold	Sensitivity	Specificity
Barcelo (34) 2009	Before	0, 700	1,12	1,61	0,95	52	100
Pereira ^a (32) 2009	After	0, 750	0,96	1,58	1,24	92,3	96,2
Woodhams (41) 2005	Before	0, 750	1,22	1,67	1,6	93	46
Fornasa ^b (23) 2011	After	0-800	1,3	1,68	1,48	88,6	95,3
Fornasa ^c (23) 2011	After	0-800	1,3	1,68	1,52	100	86
Xie (26) 2010	NR	0-800	1,14	1,55	1,3	79,5	81,5
Luo (39) 2007	NR	0-800	0,87	1,59	1,22	88,9	87,9
Imamura (21) 2010	Before	0-1000	0,97	1,21	1,1	68,8	72,7
Baltzer (24) 2011	After	0-1000	0,87	1,62	1,16	87	88,2
Jin (27) 2010	Before	0-1000	1,08	1,61	1,18	77,5	95
Belli ^d (31) 2010	Before	0-1000	0,97	1,66	1,6	97	56
Belli ^e (31) 2010	Before	0-1000	0,97	1,66	1,4	94	72
Pereira ^f (32) 2009	After	0-1000	0,68	1,44	1,14	92,3	88,5
Stadlbauer (35) 2009	After	0-1000	0,84	1,5	1,21	69,2	100
Yili ^g (37) 2009	Before	0-1000	1,01	1,72	1,22	93	96
Yili ^h (37) 2009	Before	0-1000	1,01	1,75	1,38	97	92
Marini (38) 2007	Before	0-1000	0,95	1,48	1,1	80	81
Tang (42) 2008	NR	0-1000	1,08	1,42	1,38	86,7	76

Gu ⁱ (43) 2007	Before	0-1000	1,18	1,39	1,3	70,7	75,7
Baltzer (29) 2010	After	0, 750, 1000	0,99	1,53	1,23	90,6	76,5
Baltzer (36) 2009	After	0, 750, 1000	1,05	1,63	1,23	87,2	82,9
Sonmez (19) 2011	Before	0, 50, 200, 500, 1000	0,82	1,49	1	95	100
Rubesova ^j (40) 2006	After	0, 200, 400, 600, 1000	0,95	1,51	1,15	82	86
Rubesova ^k (40) 2006	After	0, 200, 400, 600, 1000	0,99	1,47	1,1	86	86
Inoue (20) 2011	After	0, 250, 500, 750, 1000	0,98	1,5	1,29	94,5	80
Pereira ^l (32) 2009	After	0, 250, 500, 750, 1000	0,92	1,5	1,21	92,3	92,3
Kul (22) 2011	Before	50-1000	0,75	1,26	0,92	91,5	86,5
Ochi (18) 2011	Before	0-1500	0,9	1,21	1,11	93,2	55,6
Tozaki (33) 2009	Before	500, 1500	0,73	1,19	1,13	97	67
Gu ^m (43) 2007	Before	0, 2000	0,82	1	0,9	69,8	54,8

6.4 Results

6.4.1 Study descriptives

The 26 studies included a total of 2111 patients (range 27-219) with a total of 2151 breast lesions (range 27-191) of which 1286 (59.8%) were histology proven malignant (range 9-167) and 865 (40.2%) benign (range 11-91) (16-41). All studies included patients with a suspect finding on mammography, ultrasound, MRI or presented with a palpable breast lesion. All DWI examinations were performed on a 1.5 Tesla MR scanner with a sequence based on echo planar imaging (EPI). In all studies histology was used as the gold standard. Six studies applied a diagnostic follow-up of one or two years (21, 24, 25, 28, 32, 38); biopsy provided further histological assessment in the case of a positive finding.

The QUADAS score ranged from 10 to 14. Two studies complied to all QUADAS queries (Table 6.2) (18, 33). The main omissions to the QUADAS tool concerned query

6 (did patients receive the same reference standard regardless of the index result) and query 10 (were the index test results interpreted without knowledge of the results of the reference standard), by 13 and 8 studies respectively.

Table 6.2: Study characteristics of the 26 included studies. All studies used a 1.5T MR scanner (*SD* standard deviation, *NR* not reported, *P* prospective tumour-based, *R* retrospective tumour based)

Study (author, ref, year of publication)	No. of patients	Mean age (SD or range)	No. of lesions	No. of malignant	No. of benign	Contrast medium	B-value combination	Study design	QUADAS query failure (total score)
Ochi (18) 2013	219	55 (13-92)	104	59	45	before	0-1500	<i>P</i>	- (14)
Sonmez (19) 2011	41	34 (23-49)	41	23	18	before	0-50-200-500-1000	<i>P</i>	9 (13)
Inoue (20) 2011	105	54 (26-85)	106	91	15	after	0-250-500-750-1000	<i>R</i>	6 (13)
Imamura (21) [21] 2010	27	50 (31-81)	27	16	11	before	0-1000	<i>P</i>	2, 6 (12)
Kul (22) 2011	84	47 (25-75)	84	47	37	before	50-1000	<i>P</i>	6 (13)
Fornasa (23) 2011	78	44 (18-77)	78	35	43	after	0-800	<i>P</i>	6,7,10,11 (10)
Baltzer (24) 2011	59	55 (nr)	71	54	17	after	0-1000	<i>P</i>	9 (13)
Partridge (25) 2010	91	49 (22-76)	116	29	87	after	0-600	<i>R</i>	6 (13)
Xie (26) 2010	53	44 (30-62)	66	39	27	<i>NR</i>	0-500 0-800	<i>P</i>	9,10 (12)
Jin (27) 2010	56	nr (18-80)	60	40	20	before	0-600 0-1000	<i>R</i>	6 (13)
Partridge (28) 2010	91	49 (22-76)	118	27	91	after	0-600	<i>R</i>	12 (13)
Baltzer (29) 2010	94	54 (nr)	81	54	27	after	0-750-1000	<i>R</i>	6 (13)
Partridge (30) 2009	70	52 (27-85)	83	31	52	after	0-600	<i>R</i>	12 (13)
Belli (31) 2010	86	50 (23-84)	126	100	26	before	0-1000	<i>R</i>	6 (13)
Pereira (32) 2009	45	46 (22-80)	52	26	26	after	0-250 0-500 0-750 0-250-500-750-1000	<i>P</i>	6, 10 (12)
Tozaki (33) 2009	111	49 (16-89)	111	63	48	before	500-1500	<i>R</i>	- (14)
Barcelo (34) 2009	88	57 (nr)	94	80	14	before	0-700	<i>P</i>	6 (13)
Stadlbauer (35) 2009	30	50 (22-75)	36	9	27	after	0-1000	<i>P</i>	10, 12 (12)
Baltzer (36) 2009	65	55 (nr)	74	39	35	after	0-750-1000	<i>P</i>	6, 10 (12)
Yili (37) 2009	54	46 (31-77)	57	35	22	before	0-500 0-1000	<i>P</i>	10 (13)
Marini (38) 2007	60	53 (24-79)	63	42	21	before	0-1000	<i>P</i>	6, 10 (12)
Luo (39) 2007	52	47 (nr)	60	27	33	<i>NR</i>	0-800	<i>P</i>	9,11 (12)
Rubesova (40) 2006	77	52 (25-74)	87	65	22	after	0-200-400-600-1000	<i>P</i>	6, 10 (12)
Woodhams (41) 2005	190	53 (14-88)	191	167	24	before	0-750	<i>P</i>	10 (13)
Tang (42) 2008	48	51 (33-76)	70	45	25	<i>NR</i>	0-1000	<i>P</i>	9,11 (12)
Gu (43) 2007	83	51 (33-83)	95	43	52	before	0-500 0-1000 0-2000	<i>P</i>	11 (13)

6.4.2 The effect of b-value combinations on sensitivity and specificity

In most studies ($n=21$) the analysis of the DWI examinations were based on the combination of two b-values, two studies used three b-values, and four studies used five b-values (Table 6.2). The b-values ranged, besides $b = 0 \text{ s/mm}^2$, between 250 s/mm^2 and 2000 s/mm^2 .

The study of Patridge et al. (25) contained two groups of lesions ($\leq 1 \text{ cm}$ and $> 1 \text{ cm}$) for which sensitivity and specificity were obtained. The studies of Fornasa et al. (23) and Belli et al. (31) contained two groups with each a different ADC threshold for which the sensitivity and specificity were obtained. In all studies one reader assessed the data, except in the studies of Yili et al. (37) and Rubesova et al. (40) two readers were involved, resulting in a sensitivity and specificity for both readers. In total, 11 datasets (8 studies) were included for the group of b-values $\leq 600 \text{ s/mm}^2$ (Table 6.3) (25–28, 30, 32, 37, 43) and 30 datasets (23 studies) for the group of b-values $> 600 \text{ s/mm}^2$ (Table 6.1) (18–24, 26, 27, 29, 31–43).

In the group of b-values $\leq 600 \text{ s/mm}^2$ the mean ADC threshold (Table 6.3) was 1.50 (range 1.29 to 1.81) with a pooled sensitivity and specificity of 91% (95% CI: 84–95%) and 75% (95% CI: 61–85%) respectively (Fig. 6.2), resulting in an area under the curve (AUC) of 0.92 (Fig 6.4(a)).

In the group of b-values $> 600 \text{ s/mm}^2$ the mean ADC threshold (Table 6.1) was 1.23 (range 0.90–1.60) with a pooled sensitivity and specificity of 89% (95% CI: 85–92%) and 84% (95% CI: 78–89%) respectively (Fig. 6.3), resulting in an AUC of 0.93 (Fig 6.4(b)). There was no significant difference between both groups in terms of sensitivity ($p=0.495$) and specificity ($p=0.237$).

6.4.3 The effect of different b-value combinations and contrast media on the ADC

In total, 10 datasets (8 studies) (25–28, 30, 32, 37, 43) were included in the group of b-values $\leq 600 \text{ s/mm}^2$ and 26 datasets (23 studies) (18–24, 26, 27, 29, 31–43) for the group of b-values $> 600 \text{ s/mm}^2$. For both groups of b-values ADCs were non-normally distributed ($p \leq 0.02$). For the group of b-values $\leq 600 \text{ s/mm}^2$ the median ADC was significantly ($p < 0.001$) higher than for the group obtained with a maximal b-value $> 600 \text{ s/mm}^2$ for both benign (+13.2%) and malignant (+35.1%) lesions (Table 6.4).

When ADCs of malignant and benign lesions were differentiated in five groups ac-

Table 6.3: The sensitivity and specificity of DWI by using b-values ≤ 600 s/mm².
 Study Pereira: a: b-value 250; b: b-value 500
 Study Yili: c: reader 1; d: reader 2
 Study Partridge: e: lesions ≤ 1 cm; f: lesions > 1 cm

Study (author, ref, year of publication)	Contrast medium	B-values	Mean ADC malignant	Mean ADC benign	Threshold	Sensitivity	Specificity
Pereira ^a (32) 2009	after	0, 250	1,25	1,77	1,52	84,6	80,8
Xie (26) 2010	NR	0, 500	1,31	1,71	1,44	82,1	81,5
Pereira ^b (32) 2009	after	0, 500	1,06	1,65	1,36	92,3	84,6
Yili ^c (37) 2009	before	0, 500	1,04	1,78	1,29	93	91
Yili ^d (37) 2009	before	0,5	1.04	1.79	1.39	93	96
Gu (43) 2007	before	0, 500	1,36	1,64	1,5	76,9	77,2
Partridge ^e (25) 2010	after	0-600	1,33	1,75	1,57	92	56
Partridge ^f (25) 2010	after	0-600	1,31	1,64	1,59	95	50
Jin (27) 2010	before	0-600	1,33	1,82	1,44	80	95
Partridge (28) 2010	after	0-600	1,32	1,71	1,6	96	55
Partridge (30) 2009	after	0-600	1,3	1,7	1,81	100	32,7

According to the maximum b-value, ADCs were normally distributed ($p \geq 0.165$) in each group and mean ADCs decreased accordingly when the maximal b-value increased (Fig. 6.5). The highest differentiation (58.4%) between benign and malignant lesions was obtained with a combination of $b = 0$ and 1000 s/mm².

In 16 datasets (12 studies) DWI were acquired before the injection of a gadolinium-based contrast medium (18, 19, 21, 22, 27, 31, 33, 34, 37, 38, 41, 43) and in 16 datasets (11 studies) after administration of contrast medium (20, 23–25, 28–30, 32, 35, 36, 40). In three studies it was not reported whether the DWI were acquired before or after contrast administration (26, 39, 42). Pre- and post-contrast groups were normally distributed ($p \geq 0.09$) and no significant effects of contrast medium on the ADCs of benign and malignant lesions were found ($p \geq 0.08$) (Table 6.4).

Table 6.4: The effect of microperfusion and contrast agent on the ADCs was assessed for both benign and malignant lesions. For the comparison between studies differentiated by the maximum b-value, the median and interquartile range were calculated and statistically tested with Mann-Whitney U tests. For the effect of contrast agent mean and standard deviations were calculated, and statistical differences between groups were tested with independent samples t-tests. Number of datasets indicates the pool of available ADCs for which the average was calculated (for some studies multiple ADCs were available for different b-value sets).

a: Studies Patridge (25), Xie (26), Jin (27), Patridge (28), Patridge (30), Pereira (31), Yili (37), Gu (43)

b: Studies Ochi (18), Sonmez (19), Inoue (20), Imamura (21), Kul (22), Fornasa (23), Baltzer (24), Xie (26), Jin (27), Baltzer (29), Belli (31), Pereira (32), Tozaki (33), Barcelo (34), Stadlbauer (35), Baltzer (36), Yili (37), Marini (38), Luo (39), Rubesova (40), Woodhams (41), Tang (42), Gu (43)

c: Studies Ochi (18), Sonmez (19), Imamura (21), Kul (22), Jin (27), Belli (31), Tozaki (33), Barcelo (34), Yili (37), Marini (38), Woodhams (41), Gu (43)

d: Studies Inoue (20), Fornasa (23), Baltzer (24), Patridge (25), Patridge (28), Baltzer (29), Patridge (30), Pereira (32), Stadlbauer (35), Baltzer (36), Rubesova (40)

	Number of datasets	ADC benign	ADC malignant
Max b-value ≤ 600 s/mm²	10 ^a	1.71 (1.65-1.78)	1.31 (1.20-1.33)
Max b-value > 600 s/mm²	26 ^b	1.51 (1.41-1.61)	0.97 (0.86-1.08)
		p < 0.001	p < 0.001
Pre-contrast DWI	16 ^c	1.49 \pm 0.25	1.02 \pm 0.19
Post-contrast DWI	16 ^d	1.61 \pm 0.10	1.07 \pm 0.21
		p = 0.08	p = 0.45

6.4.4 Analysis of heterogeneity and publication bias

For the group of b-values ≤ 600 s/mm², moderate to high heterogeneity was observed for the sensitivity ($I^2=52\%$, $p=0.02$) and the specificity ($I^2=88\%$, $p=0.00$). A low likelihood of publication bias ($p=0.42$) was found, suggesting that we most likely did not miss studies with a negative outcome (Fig 6.6(a)).

For the group of b-values > 600 s/mm², high heterogeneity was observed for the sensitivity ($I^2=86\%$, $p=0.00$) and specificity ($I^2=79\%$, $p=0.00$). Also, evidence of publication bias was found ($p=0.05$), suggesting that small studies reporting a higher diagnostic accuracy are easier to be published (Fig. 6.6(b)).

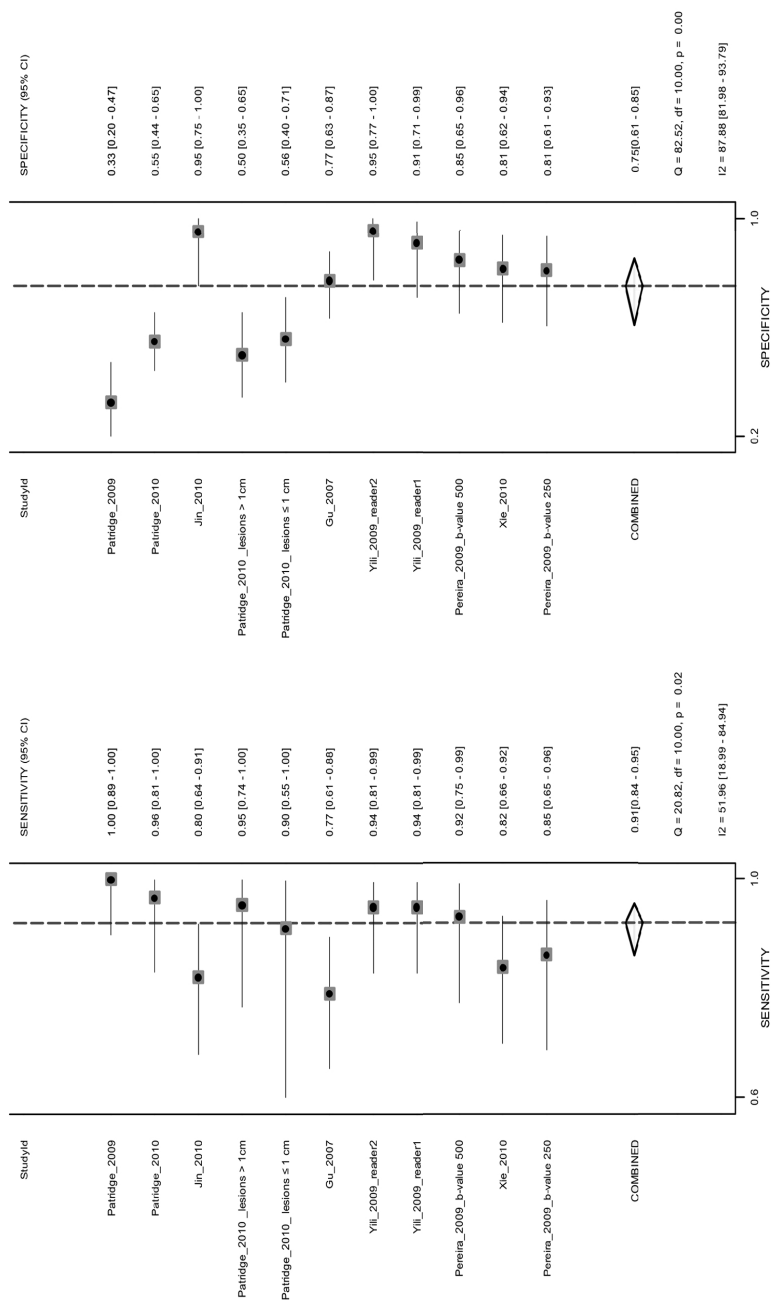


Figure 6.2: The forest plot of pooled sensitivity and specificity of DWI with b-values ≤ 600 s/mm² in discriminating benign from malignant breast lesions

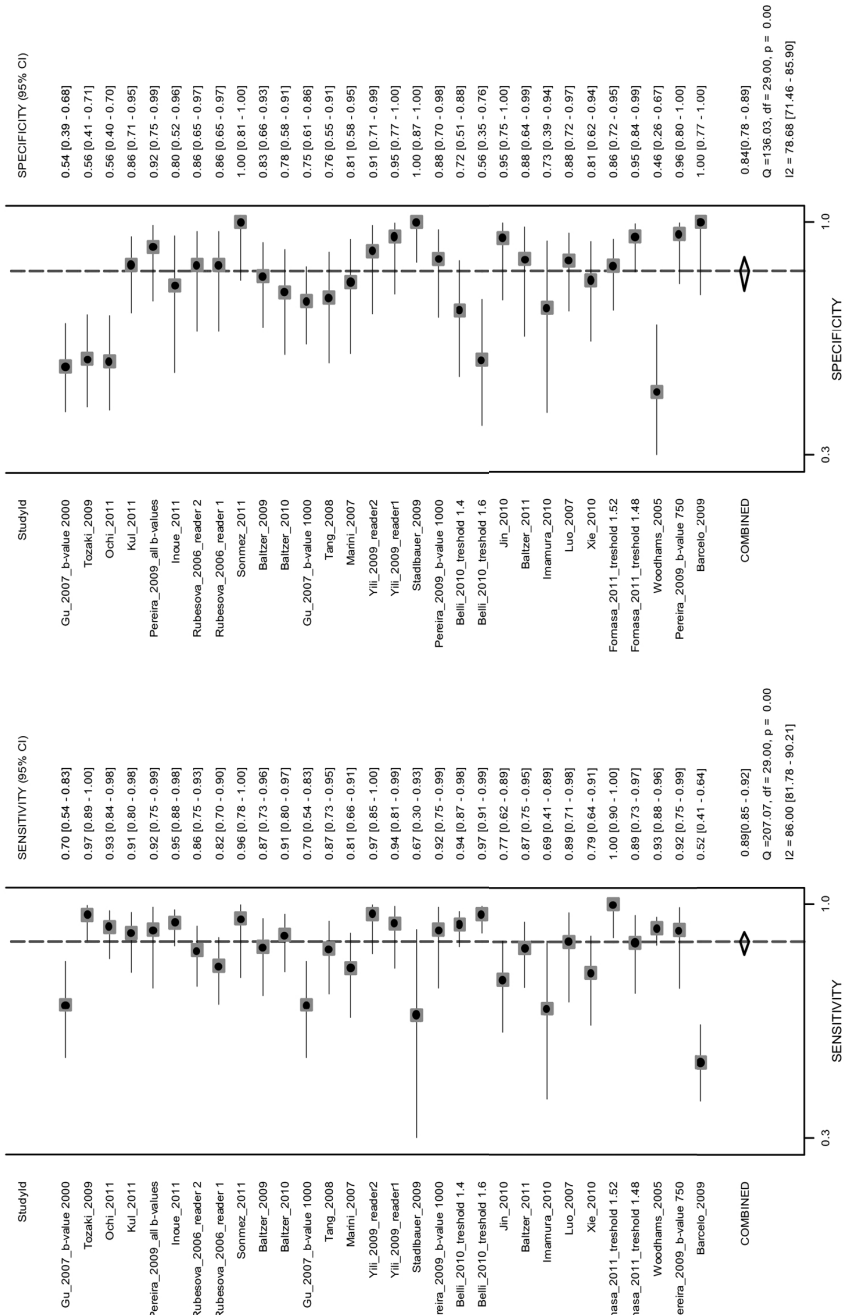


Figure 6.3: The forest plot of pooled sensitivity and specificity of DWI with b-values > 600 s/mm² in discriminating benign from malignant breast lesions

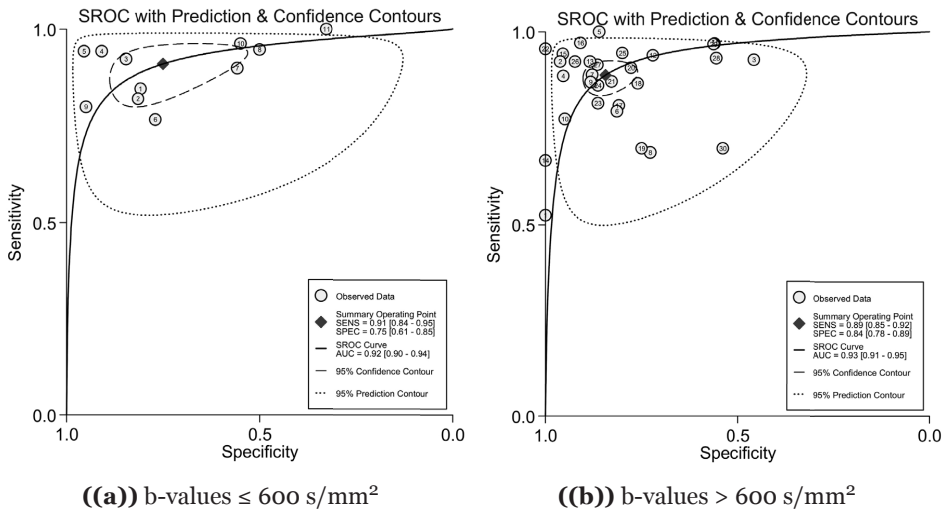


Figure 6.4: Summary ROC curve regarding the studies of DWI with b-values ≤ 600 s/mm² (left) and with b-values > 600 s/mm² (right)

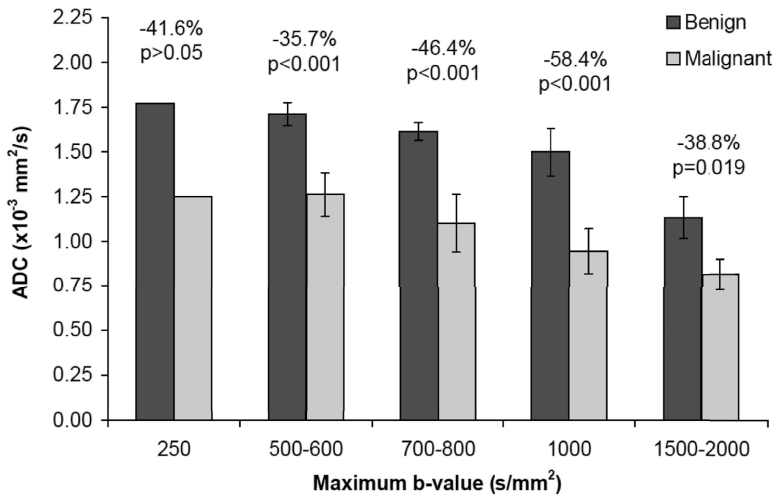
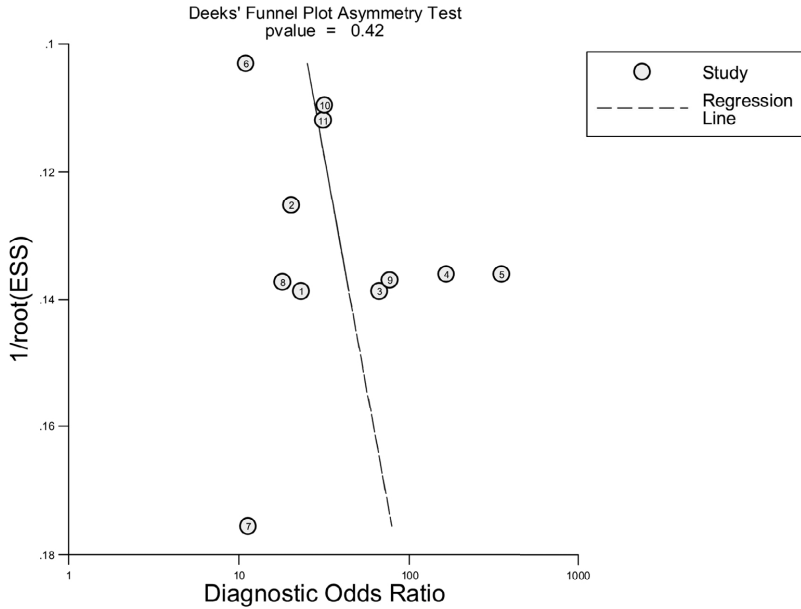
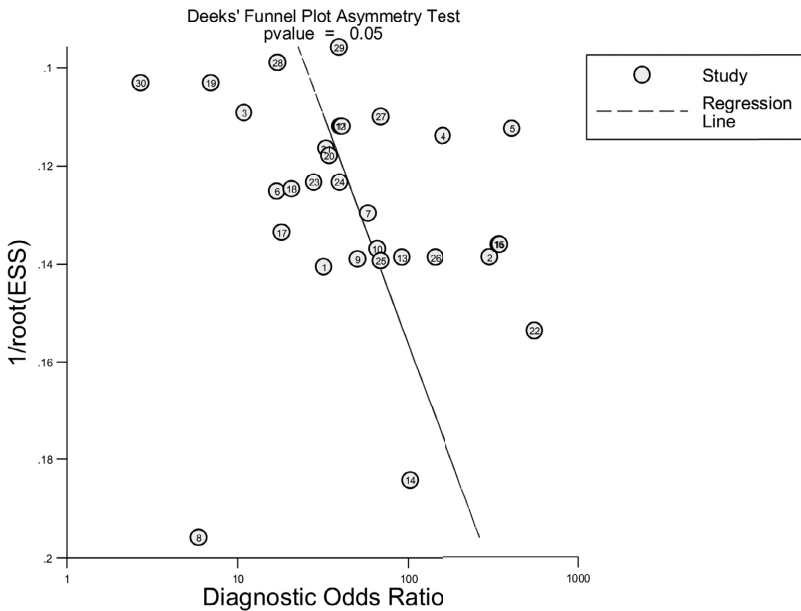


Figure 6.5: The effect of microperfusion on the ADCs was assessed for both benign and malignant lesions. All studies were included (18–43). Studies were pooled according to the maximal b-value used for the DWI acquisition. Only one study was found with a maximum b-value of 250 s/mm² (32). Indicated are the percentage differences between the ADC of benign lesions and malignant lesions, and its significance was tested using a two-tailed Student's t-test with equal variance. The percentage difference between benign and malignant lesions was the highest (58.4%) for sequences with a maximal b-value of 1000 s/mm².



((a)) $b\text{-values} \leq 600 \text{ s/mm}^2$



((b)) $b\text{-values} > 600 \text{ s/mm}^2$

Figure 6.6: Funnel plot with log odds ratios on the inverse root of effective sample sizes for visualization of publication bias in the studies using $b\text{-values} \leq 600 \text{ s/mm}^2$ (top) and $b\text{-values} > 600 \text{ s/mm}^2$ (bottom).

6.5 Discussion

This meta-analysis shows that the wide variety of b-value combinations applied in different studies significantly affects the ADC of breast lesions and therefore confounds quantitative DWI. The combination of $b = 0$ and 1000 s/mm^2 was found to yield highest differentiation between benign and malignant lesions. For the assessment of breast lesions using DWI, the pooled sensitivity was similar between combinations of b-values $\leq 600 \text{ s/mm}^2$ (91%) and combinations of b-values $> 600 \text{ s/mm}^2$ (89%). The pooled specificity increased from 75% to 84% by the use of b-values $> 600 \text{ s/mm}^2$, but this result was not significant.

One must take into account that the ADC threshold used for calculating the sensitivity and specificity, varied between different studies, even when similar b-values were used. Each published ADC threshold presumably reflects optimal differentiation between malignant and benign breast lesions based on the ADC outcomes of that study. The ADC outcomes, amongst numerous other factors that will be discussed below, also depend on how the region of interest was drawn in the lesion. The sensitivity of DWI in the detection of cancer was in concordance with published results of contrast-enhanced breast MRI ($>90\%$) (5–9).

The specificity of DWI was higher (75–84%) than generally achieved in contrast-enhanced breast MRI (67–72%) (7), especially when b-values $> 600 \text{ s/mm}^2$ were used. In the meta-analysis of Tsushima et al. the pooled sensitivity and specificity for detecting breast cancer were 89% and 77%, respectively (51). The pooled sensitivity is in accordance with our results while their specificity was lower (77% versus 84%). They included only 12 articles for the meta-analysis, from which 11 out of 12 articles had a b-value $\geq 700 \text{ s/mm}^2$ and 1 article used a maximum b-value of 300 s/mm^2 (51). This may explain the differences with our study; including 30 publications with a b-value $>600 \text{ s/mm}^2$. Another meta-analysis by Chen et al. revealed a pooled sensitivity and specificity for 11 studies using maximum $b = 1000 \text{ s/mm}^2$ of 84% and 84%, respectively (52). In comparison with our study their sensitivity was lower (84% versus 89%) while the specificity was similar.

The expected bi-exponential behaviour of the ADC in breast tissue was tested by comparing ADCs acquired with maximal b-values below and above 600 s/mm^2 . The reason for this subdivision was that in normal fibroglandular breast tissue the relationship between logarithmic DW attenuation was shown to be linear up to 600 s/mm^2 (44). This indicates that there is no microperfusion effect in fibroglandular breast tissue. At higher b-values, a second term with a very low diffusion value, representing

unsuppressed signal from fatty tissue, starts to contribute to the ADC in a non-linear manner (44). These effects were confirmed in this meta-analysis, showing a significant decrease of ADCs when DWI was acquired with maximal b-values higher than 600 s/mm² for both benign and malignant lesions.

However, the picture is different in the presence of tumor tissue, typically characterized by a substantial vasculature, and therefore a substantial microperfusion. In that case, three terms are expected: a fast microperfusion term, a slower tumor/glandular tissue diffusion term, and a very slow fatty tissue term. This is in agreement with Figure 6.5 showing a continuous decrease of the ADC with increasing maximum b-value, both in benign and malignant tumors. This figure also makes clear that the differentiation between benign and malignant tumors is optimal for combinations of b = 0 and 1000 s/mm² when only 1.5T MRI systems are considered. However, this combination approaches the recommendations of Bogner et al. who showed on a 3.0T MRI system that the optimum ADC determination together with optimum DWI quality such as CNR is obtained using a selection of b values of 50 and 850 s/mm² (53).

Concerning the effects of contrast media on the ADC, our results showed no significant differences on the respective ADCs of benign and malignant breast lesions derived from DWI data obtained before or after contrast administration, that is, apart from a trend of ADC increase in the benign lesions (p=0.08). Although it might still be possible that in time, with a larger sample size, a significantly improved differentiation between benign and malignant tumors after contrast can be shown, for the time being this meta analysis does not substantiate earlier findings suggesting a decrease of the ADC of breast carcinoma when DWI was acquired after administering extracellular Gd-DTPA (45, 46).

The latter reference by Janka et al. concluded that DWI of the breast may as well be performed after contrast application and they even indicated a slightly better ADC discrimination between benign (n=20) and malignant (n=59) lesions after contrast administration (46). In the study of Yuen et al., however, no benign lesions were studied (45) while in the study of Janke et al. for maximum impact the post-contrast DWI measurements were done within 6 min after the contrast administration (46). This contrasts with the normal clinical routine of acquiring post-contrast T1-weighted series prior to the DWI. Normally DWI is thus performed about 15 min post contrast, whereas, at least in brain lesions, initial ADC reductions measured at 5 min post Gd-DTPA contrast already have become insignificant at 10 min thereafter (54).

6.5.1 Limitations

Specific limitations in our meta-analysis with regard to the impact of contrast agents in the 16 pooled studies, beyond the general issues mentioned in the second next paragraph, are in the various Gd-containing contrast agents used and in their dosage. Most studies used gadopentate dimeglumine (Gd-DTPA) or gadoterate meglumine (Dotarem), 4 studies used gadodiamide and one study used gadobenated dimeglumine (BOPTA). The dosage in most studies was 0.1 mmol/kg, in 3 studies 0.2 mmol/kg and 1 study used 0.3 mmol/kg. The influence of the use of b-values in the comparison of pre- and post-contrast may be considered negligible since in the pre- and post-contrast groups similar proportions used b values smaller than 600 s/mm² (3 of 16 studies vs. 4 of 16 studies, respectively).

All studies selected in this meta-analysis were of high quality with a QUADAS score of at least 10, so it was assumed that the quality of the studies did not have significant impact on the results of the meta-analysis. However, evidence of publication bias was found for the group of b-values > 600 s/mm², it is therefore anticipated that the meta-analysis overestimates the performance of DWI in terms of sensitivity and specificity for this group. However, it also reflects that small studies, reporting a higher diagnostic accuracy, were more easily published (Fig. 6.6).

The sources of heterogeneity found in this study, can be explained from the wide variation of data, data acquisition and data analysis in the 26 studies. A number of different tissue types were included and the number of lesions varied between the studies. Secondly, there was a wide variation in MRI protocol between the studies such as the use of different b-values and unwanted variations in the magnitude of b-values. The latter reflects variations in the three separate acquisition parameters, gradient strength, gradient duration (δ) and interpulse delay (Δ). Also the same b-value can be obtained by using different sets of acquisition parameters, causing potential measurement heterogeneity between studies.

Other differences in acquisition protocols include DWI measurement before or after contrast administration, not every study using fat saturation (or not reporting it) or using different fat suppression schemes, number of averages, DW directions and DWI sequence (spin-echo echo planar imaging (SE-EPI) or echo planar imaging (EPI); often not specified). Furthermore, there were systematic discrepancies in the determination of region-of-interest (ROI) for the calculation of the ADCs between studies. Some studies used ROIs larger than 10 mm², or placed the ROI in the whole breast lesion, others used the most enhancing area of the lesion. These issues cause heterogeneity, thus

contaminating our comparisons. Therefore, we used a random-effects model that interprets these results with caution. However, the sources of heterogeneity could not be assessed quantitatively in this meta-analysis, due to the often poorly documented methodological aspects of the studies considered. Noted here is that the QUADAS quality score used for study inclusion fails to account for lack of experimental detail such as in the DWI acquisition parameters.

A similar meta-analysis on diffusion-weighted MRI of lung lesions however demonstrated that the main source of heterogeneity in their study was the ADC threshold effect; each study uses another diagnostic threshold to differentiate benign from malignant lesions. Other effects, such as QUADAS score, b-values, study design and MRI field strength did not contribute significantly to the heterogeneity (55).

6.5.2 Conclusions

It has been well over a decade since Le Bihan et al. demonstrated that multiexponential analysis of DWI data, referred to as incoherent intravoxel motion (IVIM) analysis, is needed to differentiate true diffusion from contamination with perfusion or very slow diffusion effects (10). Nevertheless, even now a fast majority of the clinical DWI studies still relies on monoexponential analysis yielding a single ADC value. Although in the previous paragraphs we have outlined that many factors do influence the reported ADC values, in our opinion the discrepant ADC values observed in previous DWI studies differentiating breast lesions, essentially reflect the use of different sets of b-values. This is elaborated by the differential outcomes for studies pooled according to b_{\max} smaller or larger than 600 s/mm^2 .

Furthermore, the wide discrepancy between ADCs obtained in different studies even when the same combinations of b-values are used, underlines the importance of at least settling to the same measurement protocols and methods of data-analysis within the same patient and institution, to decrease the proportions of false-negatives and false positives results.

In conclusion, this is the first meta-analysis of breast cancer DWI studies demonstrating that the wide variety of b-value combinations applied in different studies significantly affects the ADC of breast lesions and therefore confounds quantitative DWI. In clinical practice when time restraints allow for diffusion images acquired at a couple of b-values only, the combination of $b = 0$ and 1000 s/mm^2 is recommended for optimal differentiation between benign and malignant lesions.

6.6 References

- (1) Orel, S. G., and Schnall, M. D. (2001). MR imaging of the breast for the detection, diagnosis, and staging of breast cancer. *Radiology* 220, 13–30.
- (2) Macura, K. J., Ouwerkerk, R., Jacobs, M. A., and Bluemke, D. A. (2006). Patterns of enhancement on breast MR images: interpretation and imaging pitfalls. *Radiographics : a review publication of the Radiological Society of North America, Inc* 26, 1719–34, quiz 1719.
- (3) Schnall, M. D. et al. (2006). Diagnostic architectural and dynamic features at breast MR imaging: multicenter study. *Radiology* 238, 42–53.
- (4) Szabo, B. K., Aspelin, P., Wiberg, M. K., and Bone, B. (2003). Dynamic MR imaging of the breast. Analysis of kinetic and morphologic diagnostic criteria. *Acta Radiologica (Stockholm, Sweden : 1987)* 44, 379–386.
- (5) Bluemke, D. A. et al. (2004). Magnetic resonance imaging of the breast prior to biopsy. *Jama* 292, 2735–2742.
- (6) Hrung, J. M., Sonnad, S. S., Schwartz, J. S., and Langlotz, C. P. (1999). Accuracy of MR imaging in the work-up of suspicious breast lesions: a diagnostic meta-analysis. *Academic Radiology* 6, 387–397.
- (7) Peters, N. H., Rinkes, I. H. B., Zuithoff, N. P., Mali, W. P., Moons, K. G., and Peeters, P. H. (2008). Meta-analysis of MR imaging in the diagnosis of breast lesions. *Radiology* 246, 116–124.
- (8) Martincich, L. et al. (2011). Multicenter, double-blind, randomized, intraindividual crossover comparison of gadobenate dimeglumine and gadopentetate dimeglumine for Breast MR imaging (DETECT Trial). *Radiology* 258, 396–408.
- (9) Pinker, K. et al. (2014). Clinical application of bilateral high temporal and spatial resolution dynamic contrast-enhanced magnetic resonance imaging of the breast at 7 T. *European radiology* 24, 913–920.
- (10) Bihan, D. L., Breton, E., Lallemand, D., Aubin, M. L., Vignaud, J., and Laval-Jeantet, M. (1988). Separation of diffusion and perfusion in intravoxel incoherent motion MR imaging. *Radiology* 168, 497–505.
- (11) Gourtsoyianni, S., Papanikolaou, N., Yarmenitis, S., Maris, T., Karantanis, A., and Gourtsoyianis, N. (2008). Respiratory gated diffusion-weighted imaging of the liver: value of apparent diffusion coefficient measurements in the differentiation between most commonly encountered benign and malignant focal liver lesions. *European radiology* 18, 486–492.
- (12) Namimoto, T., Yamashita, Y., Sumi, S., Tang, Y., and Takahashi, M. (1997). Focal liver masses: characterization with diffusion-weighted echo-planar MR imaging. *Radiology* 204, 739–744.
- (13) Michielsen, K. et al. (2014). Whole-body MRI with diffusion-weighted sequence for staging of patients with suspected ovarian cancer: a clinical feasibility study in comparison to CT and FDG-PET/CT. *European radiology* 24, 889–901.
- (14) Cha, J. et al. (2013). Analysis of the layering pattern of the apparent diffusion coefficient (ADC) for differentiation of radiation necrosis from tumour progression. *European radiology* 23, 879–886.
- (15) Kartalis, N., Lindholm, T. L., Aspelin, P., Permert, J., and Albiin, N. (2009). Diffusion-weighted magnetic resonance imaging of pancreas tumours. *European radiology* 19, 1981–1990.
- (16) Yamashita, Y. et al. (1998). Mucin-producing tumor of the pancreas: diagnostic value of diffusion-weighted echo-planar MR imaging. *Radiology* 208, 605–609.
- (17) Ueno, Y. et al. (2013). Computed diffusion-weighted imaging using 3-T magnetic resonance imaging for prostate cancer diagnosis. *European radiology* 23, 3509–3516.
- (18) Ochi, M. et al. (2013). Diffusion-weighted imaging (b value = 1500 s/mm²) is useful to decrease false-positive breast cancer cases due to fibrocystic changes. *Breast cancer (Tokyo, Japan)* 20, 137–144.

- (19) Sonmez, G. et al. (2011). Value of diffusion-weighted MRI in the differentiation of benign and malign breast lesions. *Wiener klinische Wochenschrift* 123, 655–661.
- (20) Inoue, K. et al. (2011). Usefulness of diffusion-weighted imaging of breast tumors: quantitative and visual assessment. *Japanese journal of radiology* 29, 429–436.
- (21) Imamura, T. et al. (2010). Diagnostic performance of ADC for Non-mass-like breast lesions on MR imaging. *Magnetic resonance in medical sciences : MRMS : an official journal of Japan Society of Magnetic Resonance in Medicine* 9, 217–225.
- (22) Kul, S., Cansu, A., Alhan, E., Dinc, H., Gunes, G., and Reis, A. (2011). Contribution of diffusion-weighted imaging to dynamic contrast-enhanced MRI in the characterization of breast tumors. *AJR.American journal of roentgenology* 196, 210–217.
- (23) Fornasa, F., Pinali, L., Gasparini, A., Toniolli, E., and Montemezzi, S. (2011). Diffusion-weighted magnetic resonance imaging in focal breast lesions: analysis of 78 cases with pathological correlation. *La Radiologia medica* 116, 264–275.
- (24) Baltzer, P. A. et al. (2011). Diffusion tensor magnetic resonance imaging of the breast: a pilot study. *European radiology* 21, 1–10.
- (25) Partridge, S. C. et al. (2010). Apparent diffusion coefficient values for discriminating benign and malignant breast MRI lesions: effects of lesion type and size. *AJR.American journal of roentgenology* 194, 1664–1673.
- (26) Xie, C. M. et al. (2010). Diagnostic value of ADC and rADC of diffusion weighted imaging in malignant breast lesions. *Zhonghua zhong liu za zhi [Chinese journal of oncology]* 32, 217–220.
- (27) Jin, G., An, N., Jacobs, M. A., and Li, K. (2010). The role of parallel diffusion-weighted imaging and apparent diffusion coefficient (ADC) map values for evaluating breast lesions: preliminary results. *Academic Radiology* 17, 456–463.
- (28) Partridge, S. C., Demartini, W. B., Kurland, B. F., Eby, P. R., White, S. W., and Lehman, C. D. (2010). Differential diagnosis of mammographically and clinically occult breast lesions on diffusion-weighted MRI. *Journal of magnetic resonance imaging : JMRI* 31, 562–570.
- (29) Baltzer, P. A., Benndorf, M., Dietzel, M., Gajda, M., Camara, O., and Kaiser, W. A. (2010). Sensitivity and specificity of unenhanced MR mammography (DWI combined with T2-weighted TSE imaging, ueMRM) for the differentiation of mass lesions. *European radiology* 20, 1101–1110.
- (30) Partridge, S. C., DeMartini, W. B., Kurland, B. F., Eby, P. R., White, S. W., and Lehman, C. D. (2009). Quantitative diffusion-weighted imaging as an adjunct to conventional breast MRI for improved positive predictive value. *AJR.American journal of roentgenology* 193, 1716–1722.
- (31) Belli, P., Costantini, M., Bufi, E., Magistrelli, A., Torre, G. L., and Bonomo, L. (2010). Diffusion-weighted imaging in breast lesion evaluation. *La Radiologia medica* 115, 51–69.
- (32) Pereira, F. P. et al. (2009). Assessment of breast lesions with diffusion-weighted MRI: comparing the use of different b values. *AJR.American journal of roentgenology* 193, 1030–1035.
- (33) Tozaki, M., and Fukuma, E. (2009). 1H MR spectroscopy and diffusion-weighted imaging of the breast: are they useful tools for characterizing breast lesions before biopsy? *AJR.American journal of roentgenology* 193, 840–849.
- (34) Barcelo, J. et al. (2009). Breast MRI: the usefulness of diffusion-weighted sequences for differentiating between benign and malignant lesions. *Radiologia* 51, 469–476.
- (35) Stadlbauer, A. et al. (2009). Diffusion-weighted MR imaging with background body signal suppression (DWIBS) for the diagnosis of malignant and benign breast lesions. *European radiology* 19, 2349–2356.
- (36) Baltzer, P. A. et al. (2009). Diffusion-weighted imaging (DWI) in MR mammography (MRM): clinical comparison of echo planar imaging (EPI) and half-Fourier single-shot turbo spin echo (HASTE) diffusion techniques. *European radiology* 19, 1612–1620.
- (37) Yili, Z. et al. (2009). The value of diffusion-weighted imaging in assessing the ADC changes of tissues adjacent to breast carcinoma. *BMC cancer* 9, 2407–9.

- (38) Marini, C., Iaconi, C., Giannelli, M., Cilotti, A., Moretti, M., and Bartolozzi, C. (2007). Quantitative diffusion-weighted MR imaging in the differential diagnosis of breast lesion. *European radiology* 17, 2646–2655.
- (39) Luo, J. D., Liu, Y. Y., Zhang, X. L., and Shi, L. C. (2007). Application of diffusion weighted magnetic resonance imaging to differential diagnosis of breast diseases. *Ai zheng = Aizheng = Chinese journal of cancer* 26, 168–171.
- (40) Rubesova, E., Grell, A. S., Maertelaer, V. D., Metens, T., Chao, S. L., and Lemort, M. (2006). Quantitative diffusion imaging in breast cancer: a clinical prospective study. *Journal of magnetic resonance imaging : JMRI* 24, 319–324.
- (41) Woodhams, R. et al. (2005). ADC mapping of benign and malignant breast tumors. *Magnetic resonance in medical sciences : MRMS : an official journal of Japan Society of Magnetic Resonance in Medicine* 4, 35–42.
- (42) Tang, J. -.-H., Yan, F. -.-H., Zhou, M. -.-L., Ye, F., and Xu, P. -.-J. (2008). Comparative study of diffusion weighted imaging and dynamic contrast enhanced MRI for the detection of small breast cancers. *Chinese Journal of Radiology* 42, 152–156.
- (43) Gu, Y. -.-J., Feng, X. -.-Y., Tang, F., Peng, W. -.-J., Mao, J., and Yang, W. -.-T. (2007). Diffusion-weighted MRI of the breast: Lesion characterization and parameter selection. *Chinese Journal of Radiology* 41, 451–456.
- (44) Baron, P., Dorrius, M. D., Kappert, P., Oudkerk, M., and Sijens, P. E. (2010). Diffusion-weighted imaging of normal fibroglandular breast tissue: influence of microperfusion and fat suppression technique on the apparent diffusion coefficient. *NMR in biomedicine* 23, 399–405.
- (45) Yuen, S., Yamada, K., Goto, M., Nishida, K., Takahata, A., and Nishimura, T. (2009). Microperfusion-induced elevation of ADC is suppressed after contrast in breast carcinoma. *Journal of magnetic resonance imaging : JMRI* 29, 1080–1084.
- (46) Janka, R., Hammon, M., Geppert, C., Nothhelfer, A., Uder, M., and Wenkel, E. (2014). Diffusion-weighted MR imaging of benign and malignant breast lesions before and after contrast enhancement. *RoFo : Fortschritte auf dem Gebiete der Rontgenstrahlen und der Nuklearmedizin* 186, 130–135.
- (47) Matsuoka, A. et al. (2008). Comparison of 3.0- and 1.5-tesla diffusion-weighted imaging in the visibility of breast cancer. *Radiation Medicine* 26, 15–20.
- (48) Whiting, P., Rutjes, A. W., Reitsma, J. B., Bossuyt, P. M., and Kleijnen, J. (2003). The development of QUADAS: a tool for the quality assessment of studies of diagnostic accuracy included in systematic reviews. *BMC medical research methodology* 3, 25.
- (49) Whiting, P. F., Weswood, M. E., Rutjes, A. W., Reitsma, J. B., Bossuyt, P. N., and Kleijnen, J. (2006). Evaluation of QUADAS, a tool for the quality assessment of diagnostic accuracy studies. *BMC medical research methodology* 6, 9.
- (50) Higgins, J. P., Thompson, S. G., Deeks, J. J., and Altman, D. G. (2003). Measuring inconsistency in meta-analyses. *BMJ (Clinical research ed.)* 327, 557–560.
- (51) Tsushima, Y., Takahashi-Taketomi, A., and Endo, K. (2009). Magnetic resonance (MR) differential diagnosis of breast tumors using apparent diffusion coefficient (ADC) on 1.5-T. *Journal of magnetic resonance imaging : JMRI* 30, 249–255.
- (52) Chen, X., Li, W. L., Zhang, Y. L., Wu, Q., Guo, Y. M., and Bai, Z. L. (2010). Meta-analysis of quantitative diffusion-weighted MR imaging in the differential diagnosis of breast lesions. *BMC cancer* 10, 2407–10.
- (53) Bogner, W. et al. (2009). Diffusion-weighted MR for differentiation of breast lesions at 3.0 T: how does selection of diffusion protocols affect diagnosis? *Radiology* 253, 341–351.
- (54) Firat, A. K., Sanli, B., Karakas, H. M., and Erdem, G. (2006). The effect of intravenous gadolinium-DTPA on diffusion-weighted imaging. *Neuroradiology* 48, 465–470.
- (55) Chen, L. et al. (2013). Meta-analysis of diffusion-weighted MRI in the differential diagnosis of lung lesions. *Journal of magnetic resonance imaging : JMRI* 37, 1351–1358.

Semi-automated quantitative IVIM analysis and its implementation in breast DWI

Hildebrand Dijkstra
Monique D. Dorrius
Mirjam Wielema
Karolien Jaspers
Ruud M. Pijnappel
Matthijs Oudkerk
Paul E. Sijens

Published in the Journal of Magnetic Resonance Imaging
2016, vol. 43, no. 5, pp. 1122-1131.

7.1 Abstract

Purpose: To optimize and validate intravoxel incoherent motion (IVIM) modeled diffusion-weighted imaging (DWI) compared to the apparent diffusion coefficient (ADC) for semi-automated analysis of breast lesions using a multi-reader setup.

Materials and Methods: Patients (n=176) with breast lesions (≥ 1 cm) and known pathology were prospectively examined (1.5T MRI) with DWI (b=0, 50, 200, 500, 800 and 1000 s/mm²) between November 2008 and July 2014 and grouped into a training and test set. Three independent readers applied a semi-automated procedure for setting regions-of-interest for each lesion and recorded ADC and IVIM parameters: molecular diffusion (D_{slow}), microperfusion (D_{fast}), and the fraction of D_{fast} (f_{fast}). In the training set (24 lesions, 12 benign) a semi-automated method was optimized to yield maximum true negatives (TN) with minimal false negatives (FN): only the optimal fraction (F_0) of voxels in the lesions was used and optimal thresholds were determined. The optimal F_0 and thresholds were then applied to a consecutive test set (139 lesions, 23 benign) to obtain specificity and sensitivity.

Results: In the training set, optimal thresholds were 1.44×10^{-3} mm²/s (D_{slow}), 18.55×10^{-3} mm²/s (D_{fast}), 0.247 (f_{fast}) and 2.00×10^{-3} mm²/s (ADC) with F_0 set to 0.61, 0.85, 1.0 and 1.0 respectively, this resulted in TN=5 (IVIM) and TN=1 (ADC), with FN=0. In the test set, sensitivity and specificity among the readers were 90.5-93.1% and 43.5-52.2% respectively for IVIM, and 94.8-95.7% and 13.0-21.7% for ADC ($p \leq 0.0034$) without inter-reader differences ($p=1.000$).

Conclusion: The presented semi-automated method for breast lesion evaluation is reader independent and yields significantly higher specificity for IVIM compared to the ADC.

7.2 Introduction

Diffusion-weighted imaging (DWI) of breast lesions is usually quantified using a mono-exponential model such as the apparent diffusion coefficient (ADC) or a bi-exponential model such as intravoxel incoherent motion (IVIM), the latter quantifying molecular diffusion more accurately and additionally providing microperfusion properties of breast lesions (1–3).

Currently, DWI is however not generally implemented for detecting breast pathology due to its lower sensitivity and specificity compared to dynamic contrast-enhanced (DCE-) MRI. Recently, meta-analysis of DWI for detecting breast pathology showed a sensitivity between 84 and 91% and specificity between 75 and 84% (4, 5). In contrast, DCE-MRI has sensitivity and specificity of 100% and 82.5% respectively in non-calcified breast lesions, resulting in a negative predictive value (NPV) higher than 98%, thereby able to safely exclude malignancy (6, 7). Hence, for DWI to be implemented successfully along DCE-MRI, the sensitivity should be high (>98%) while the specificity is optimized as high as possible.

One potential area to improve the sensitivity of quantitative DWI is to implement IVIM. Recently, for breast lesions increased diagnostic performance of IVIM was found compared to the ADC and increased sensitivity was suggested when combining information of molecular diffusion and microperfusion (3).

Another potential area for improving sensitivity and specificity in quantitative DWI is the selection of the region-of-interest (ROI). Several studies have shown that important information is lost when one relies just on the average values of lesions and that higher sensitivity (92.6% vs. 87.0%) can be obtained when the minimum diffusion is used instead of average diffusion (1, 8, 9). That approach however usually depends on just a single voxel defining the lesion's minimum value and is therefore prone to a high degree of uncertainty. For optimal sensitivity it is therefore preferable to characterize the diffusion properties of the lesions, by values representing a number of voxels with low diffusion instead of just a single voxel.

In reply to these questions an optimization algorithm might be the solution, by converging to the optimal number of voxels with low diffusion needed to obtain the maximum sensitivity. Independent optimization and validation test groups are required to successfully implement such an algorithm; this reduces the chance that the output of the optimization algorithm is only valid for a certain specific patient group. Recently, this approach was also applied by Park et al. grouping patients chronologically into an independent training set and test set in pursuit for an optimal cutoff to differentiate

between pseudoprogression and early tumor progression in patients with glioblastoma (10). Also, a multi-reader setup is mandatory, to prevent that the results are dependent on a specific reader with a certain amount of experience.

Thus the purpose of this study was to optimize and validate IVIM compared to the ADC for the semi-automated analysis of breast lesions using a multi-reader setup.

7.3 Materials and Methods

7.3.1 Study population

The protocol of the study was approved by the hospital's institutional review board and informed consent was obtained from each patient. Between November 2008 and July 2014, patients scheduled for breast MRI and diffusion-weighted imaging (DWI) were recruited. Inclusion criteria were: lesion diameter larger than or equal to 1 cm on MRI, no history of breast cancer, no hematomas and no previous breast surgery or breast implants. This resulted in 176 patients (mean age, 47 years; age range, 22–75 years) with 206 breast lesions: 165 malignant and 41 benign. Seven lesions were excluded (1 malignant and 6 benign) because the lesions were not visible on DWI.

Independent training and test sets without overlap were defined to perform optimization and validation of the IVIM and ADC methods (Fig. 7.1). The training subgroup (mean age, 43 years; age range, 22–67 years) contained the first 12 benign and 12 malignant lesions, consecutively included between November 2008 and May 2010; the remainder of malignant lesions ($n=36$) were not analyzed.

The test subgroup (mean age, 48 years; age range, 23–75 years) contained the lesions in the second part of the database, consecutively included between May 2010 and July 2014: 116 malignant and 23 benign lesions. The number of lesions in the training set resulted from the criteria that we aimed for 1) a ratio of about 1 to 4 lesions in the training set versus test set, and 2) an equal number of benign and malignant lesions, and 3) consecutive and chronological inclusion of lesions (without too many malignant lesions in the database not being used).

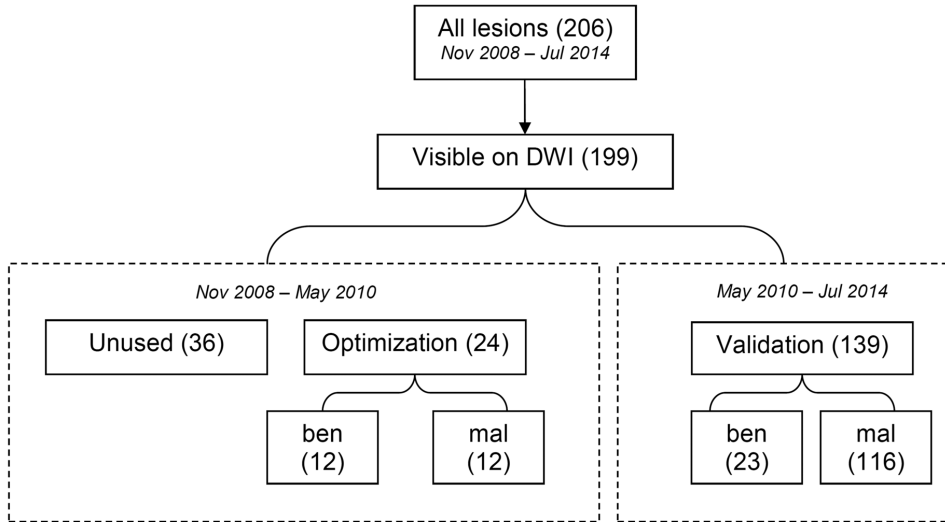


Figure 7.1: Flow chart of division of lesions in training and test subgroups. 176 patients with 206 lesions underwent DWI. In 7 cases (6 benign and 1 malignant) the lesion was not visible on DWI and therefore excluded from the database. A training and test subgroup were defined to perform optimization and validation of the IVIM method. The subgroups were independent and did not overlap. The lesions in the test subgroup were assessed by three independent readers.

7.3.2 Pathology

Histopathology, cytology or follow-up with a 6-months interval of the 206 breast lesions defined lesions as benign or malignant. Tissue samples were obtained after modified radical mastectomy ($n = 109$), lumpectomy ($n = 52$), ultrasonographically (US) guided core biopsy ($n = 21$), US-guided fine-needle aspiration ($n = 4$), MRI-guided core biopsy ($n = 1$) and other procedures ($n = 4$). For 15 lesions the diagnosis was benign during repetitive follow-up MRI ($n = 14$) and follow-up US ($n = 1$).

7.3.3 MR protocols

All subjects were examined on a 1.5T MRI system (Magnetom Avanto, Siemens Medical Solutions, Erlangen, Germany). The body coil served as transmitter and a commercially available circularly polarized bilateral breast phased-array coil with automatic tuning and electronic decoupling as receiver (Siemens Medical Solutions, Erlangen, Germany).

After the localizer scans, diffusion-weighted images (DWI) were obtained using a spin echo based single shot echo-planar imaging (SS-EPI) sequence in combination with spectral adiabatic inversion recovery (SPAIR) fat suppression. DWI acquisitions ($b = 0, 50, 200, 500, 800, 1000 \text{ s/mm}^2$) were tuned with the following parameters: TR 9300 ms; TE 91 ms; FA 90° ; slice-thickness 4 mm; slice-gap 2 mm; FOV $170 \times 340 \text{ mm}^2$; matrix 192×384 ; bandwidth 1628 Hz/pixel; 2 averages. Diffusion gradients (25 mT/m) were applied in the phase-, read-, and z-directions separately. In total, 28 transverse slices were acquired in interleaved mode to cover both breasts within an acquisition time of 2.5 minutes.

Finally, eight series of transversal dynamic contrast-enhanced (DCE-) T1-weighted spoiled gradient echo sequences were obtained with a temporal resolution of 76 seconds using gadoterate meglumine (Gd-DOTA, Dotarem, Guerbet, 0.1 mmol/kg): TR 4.17 ms; TE 1.29 ms; FA 10° ; slice-thickness 0.97 mm; no slice-gap; FOV $340 \times 340 \text{ mm}^2$; matrix 384×384 ; bandwidth 318 Hz/pixel; no averages. Parallel acquisition technique GRAPPA with acceleration factor 2 was enabled in all acquisitions.

7.3.4 DWI analysis

Three independent readers analyzed the lesions: an expert breast radiologist with more than 15 years experience (reader 1), a radiology resident (reader 2), and a radiology researcher without any experience on mammography (reader 3). The analysis was performed off-line using bi-exponential fitting procedures in a programmable graphical and calculus environment (Matlab R2014a, The Mathworks, Natick, MA, USA). For all analyses, the diffusion-weighted signal intensities S were fitted bi-exponentially using the parameters described by the IVIM model (11, 12):

$$\frac{S}{S_0} = f_{fast} \cdot e^{-b \cdot D_{fast}} + f_{slow} \cdot e^{-b \cdot D_{slow}} \quad (7.1)$$

where S_0 is the maximum signal intensity, D_{fast} is the fast component representing microperfusion, f_{fast} is the fraction of microperfusion, D_{slow} is the slow component representing molecular diffusion and f_{slow} is the fraction of molecular diffusion ($f_{slow} = 1 - f_{fast}$).

Equation 7.1 was fitted by the Nelder-Mead simplex direct search method with bound constraints, which performs a constrained non-linear minimisation of the sum of the squared residuals (13, 14). For that it requires a first (initial) guess of the fitting

parameters D_{slow} , D_{fast} and f_{fast} . The first guess is then optimized during a number of iteration steps until the equation fits the input diffusion-weighted signal intensities S . D_{slow} reflects the molecular diffusion, which is most accurately represented by the tail of the diffusion curve, weighted with high b -values. Therefore, the initial guess of D_{slow} (D_{slow}^0) was estimated by calculating the slope of the tail between $b = 500$ and 1000 s/mm^2 . In contrast, the microperfusion (D_{fast}) is reflected by the steep descent of the diffusion curve, at low b -values. The initial guess of D_{fast} (D_{fast}^0) was therefore estimated by calculating the slope of the descent of the diffusion curve between $b = 0$ and $b = 50$ s/mm^2 . Thirdly, the fraction of microperfusion (f_{fast}) is simply the amount of microperfusion present in the diffusion curve; if $f_{\text{fast}} = 0$ no microperfusion is present in the diffusion curve (essentially mono-exponential), and if $f_{\text{fast}} = 0.1$ the measured diffusion curve is reflected for 10% by microperfusion and for 90% by molecular diffusion. The initial guess of f_{fast} (f_{fast}^0) can therefore be estimated simply by solving equation 7.1 for f_{fast} as all other parameters are known and $f_{\text{slow}} = 1 - f_{\text{fast}}$.

Another prerequisite of the Nelder-Mead simplex direct search method is that it needs boundaries to prevent any non-physical results. For D_{slow} the boundaries were defined by assuming a maximum factor of 5 of uncertainty in the initial guess (D_{slow}^0), i.e. D_{slow} was bound between $0.2 \times D_{\text{slow}}^0 \times 10^{-3}$ mm^2/s and $5 \times D_{\text{slow}}^0 \times 10^{-3}$ mm^2/s . For D_{fast} the lower boundary was defined equal as D_{slow}^0 (microperfusion can never be slower than molecular diffusion) and the upper boundary was defined as 100×10^{-3} mm^2/s . The fraction of microperfusion (f_{fast}) was not restricted (bound between 0.0 and 1.0). The ADC was obtained by using a clinically accepted method: a mono-exponential fit of all 6 b -values was performed.

7.3.5 Optimization of the IVIM method

The optimization using the training subset was performed by reader 2. For all lesions, the reader included voxels by drawing a freeform margin around the lesion; the voxels within it were used in the optimization process (Fig. 7.2). There were no further instructions to the reader.

The optimization of IVIM to discriminate benign and malignant lesions was performed using a script based algorithm (Matlab R2014a, The Mathworks, Natick, MA, USA). The algorithm consisted of three nested layers (Fig. 7.3): the first layer yielded different combinations of the optimal fraction (Fo), the second layer different combinations of the threshold (TH) and the third layer calculated the diagnostic performance

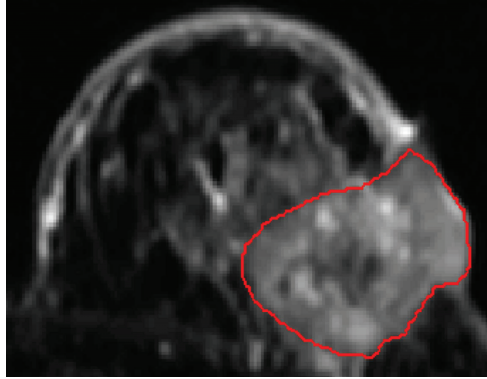


Figure 7.2: Example of an invasive ductal carcinoma (IDC) on DWI. Voxels were included within a freeform margin around the lesion.

for all different combinations of Fo and TH.

The Fo defined which voxels of the lesions were used based on the magnitude of D_{slow} , D_{fast} and f_{fast} (and similar for ADC as well). Three nested loops went through the Fo (0.0 – 1.0) in steps of 0.1 for D_{slow} , D_{fast} and f_{fast} individually. For instance, when Fo = 0.1, only the 10% lowest D_{slow} voxels in the lesion were used to calculate the median D_{slow} of the lesion, yet when Fo = 1.0, all voxels in the lesion were used to calculate the median. Similarly, the other two loops in the first layer calculated the median for D_{fast} and f_{fast} , yielding independent sets of Fo for D_{fast} and f_{fast} .

In the second layer of the algorithm again three nested loops were defined which went through a range of thresholds (TH) for D_{slow} ($0.5\text{--}3.0 \times 10^{-3} \text{ mm}^2/\text{s}$), D_{fast} ($5\text{--}20 \times 10^{-3} \text{ mm}^2/\text{s}$) and f_{fast} (0.01-1.00) individually. The incremental steps were $0.05 \times 10^{-3} \text{ mm}^2/\text{s}$ for D_{slow} , $0.1 \times 10^{-3} \text{ mm}^2/\text{s}$ for D_{fast} and 0.01 for f_{fast} .

Subsequently, all sets of TH and Fo for D_{slow} , D_{fast} and f_{fast} resulting from the first and second layer were used in the third layer where the diagnostic performance in terms of TN, FN, TP and FP was calculated for all combinations of TH and Fo. The diagnostic performance was calculated by combining the three IVIM parameters in parallel in a single test using the “AND rule” to discriminate malignant from benign lesions, based on the three TH (15). That is, if D_{slow} was lower than the TH, and if D_{fast} was lower than the TH, and if f_{fast} was lower than the TH, then the combined result was defined positive (malignant), but in all other cases, the combined result was negative (benign). Finally, in the evaluation step the optimal TH and Fo for D_{slow} , D_{fast} and f_{fast} which resulted in the maximum number of TN and minimal number of FN were selected.

For the ADC the same algorithm was applied with the exception that the “AND rule” was not applicable and the first and second layer only consisted of one nested loop each

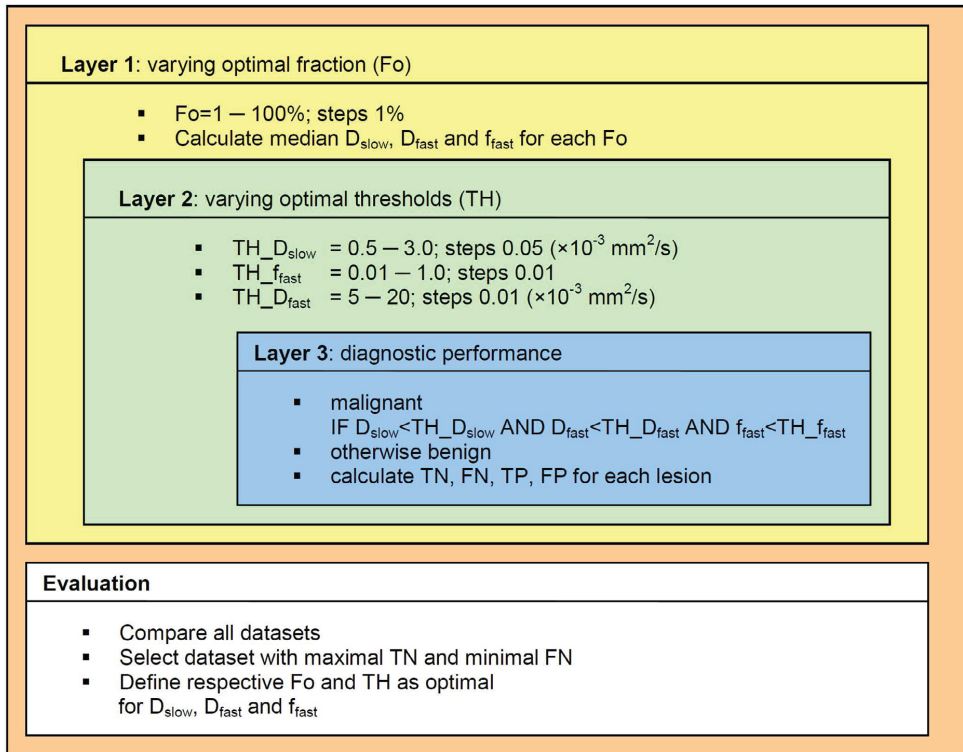


Figure 7.3: Schematic representation of the optimization algorithm for IVIM. The algorithm consisted of three nested layers: the first layer yielded different combinations of the optimal fraction (Fo) for D_{slow} , D_{fast} and f_{fast} individually, the second layer yielded different combinations of the threshold (TH) for D_{slow} , D_{fast} and f_{fast} individually and the third layer calculated the diagnostic performance for all different combinations of Fo and TH. Finally, in the evaluation step the optimal TH and Fo for D_{slow} , D_{fast} and f_{fast} which resulted in the maximum number of TN and minimal number of FN were selected. For the ADC the algorithm was similar.

to vary Fo and TH and select the optimum accordingly.

To verify the stability of the optimization algorithm and resulting variation in TH and Fo, two additional subgroups were defined. Stability set 1 contained the first 12 benign and 12 malignant lesions, consecutively included between June 2010 and September 2012. Stability set 2 contained the remainder of 11 benign lesions and the first 11 malignant lesions, consecutively included between October 2012 and July 2014. To guarantee independency between training set and test set, the resulting TH and Fo from the stability subgroups were not used in the multi-reader analysis of the test set, as the stability subgroups contained lesions already included in the test set as well.

7.3.6 Validation of the IVIM method

The validation was performed by the three independent readers using the test set. For all 139 lesions, the readers included voxels by drawing a freeform margin around the lesion: the voxels within it were used in the analysis. There were no further instructions to the readers. The T1 DCE images and individual DW images were used to locate the lesion. The optimal Fo and TH for the three IVIM parameters and ADC resulting from the optimization of the training set were applied to the test set for validation.

Subsequently, the diagnostic performance for IVIM was calculated by combining the three IVIM parameters in parallel in a single test using the “AND rule” to discriminate malignant from benign lesions, based on the three TH resulting from the training set (15). In addition, the diagnostic performance was calculated also for D_{slow} only. Next, Se, Sp, negative predictive value (NPV) and accuracy (ACC) were calculated. Next, also the diagnostic performance for the ADC was calculated by applying the optimal Fo and TH resulting from the training set.

7.3.7 Statistics

Statistical analyses were performed using SPSS (SPSS 22, Chicago, IL, USA). All data were tested for normality using Shapiro–Wilk tests. IVIM parameters and ADC were given as median and interquartile range. Mann-Whitney U tests were used to test the significance of the difference between benign and malignant lesions for the ADC, D_{slow} , D_{fast} and f_{fast} . Differences between readers were tested using non-parametric Kruskal-Wallis one-way analysis of variance. McNemar’s test based on the binomial distribution was used to statistically compare the diagnostic performance of the readers and between IVIM and ADC. Receiver operator characteristics (ROC) curves in the training group were calculated for IVIM and the ADC.

The agreement of the lesion segmentation between the readers was tested using the Dice Similarity Coefficient (DSC), which ranges between 0 (no spatial overlap of the ROIs) and 1 (perfect agreement of ROIs) (16). For all statistical tests, $p < 0.05$ was considered to indicate a statistically significant difference.

7.4 Results

7.4.1 Optimization using a training subset

For benign lesions (n=12), pathology (PA) analysis resulted in fibroadenoma (n=5), adenosis (n=1), epithelial hyperplasia (n=1), intraductal papilloma (n=1), juvenile papillomatosis (n=1) and 3 other lesions benign on follow-up. The diameter varied between 10 and 53 mm.

For malignant lesions (n=12), PA resulted in invasive ductal carcinoma (IDC, n=3), IDC + ductal carcinoma in situ (DCIS) grade 3 (n=1), IDC + DCIS grade 2 (n=1), IDC + DCIS grade 1 (n=1), pure DCIS grade 3 (n=1), pure DCIS grade 2 (n=1) invasive lobular carcinoma (ILC, n=1), ILC + DCIS grade 2 (n=1), metaplastic carcinoma (n=1) and mucous carcinoma (n=1). The diameter was between 12 and 91 mm.

The different combinations of Fo and TH generated by the optimization algorithm resulted for IVIM in varying sensitivity and specificity (Fig. 7.4). Maximum specificity in combination with 100% sensitivity was 41.7%. (TP = 12; TN = 5; FP = 7; FN = 0) when all three IVIM parameters were combined in parallel in a single test using the “AND rule”. The highest reachable number of TN was 5 of 12 using the optimal selection of TH and Fo (Table 7.1).

Table 7.1: Optimal parameters yielded from training subset and stability tests. Optimization resulted in the optimal threshold (TH) and optimal fraction (Fo) for the three IVIM parameters and ADC. To verify the stability of the optimization algorithm and resulting variation in TH and Fo, two additional subgroups (stability subgroup 1 and 2) were defined. D_{slow} , D_{fast} and ADC are given in $\times 10^{-3} \text{ mm}^2/\text{s}$ and f_{fast} as a unitless fraction.

	Training set		Stability test 1		Stability test 2	
	TH	Fo	TH	Fo	TH	Fo
D_{slow}	1.44	0.61	1.59	0.54	1.37	0.67
D_{fast}	18.55	0.85	17.89	0.99	15.17	0.97
f_{fast}	0.247	1.00	0.134	1.00	0.25	0.98
ADC	2.00	1.00	1.94	0.97	2.06	0.96

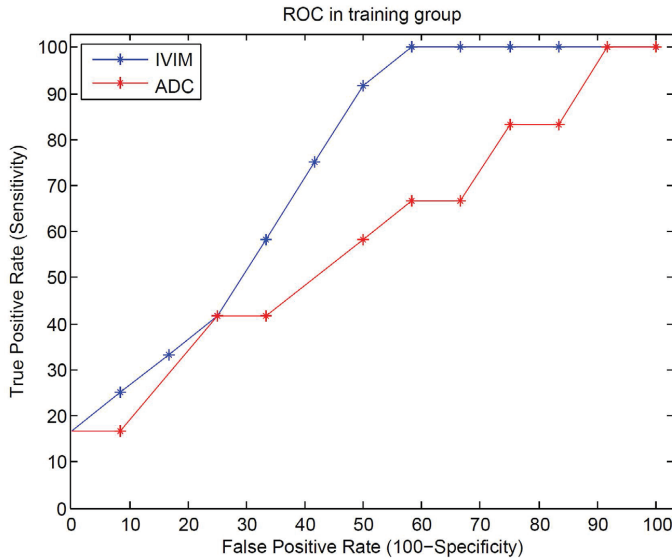


Figure 7.4: Receiver operator characteristics (ROC) in the training group for IVIM and ADC. Varying thresholds (TH) and optimal fraction (Fo) resulted in different sensitivity and specificity. The maximum specificity obtained with a sensitivity of 100% was used to select the optimal values of TH and Fo.

Median D_{slow} was $1.10 \times 10^{-3} \text{ mm}^2/\text{s}$ and varied between 0.73 and $1.79 \times 10^{-3} \text{ mm}^2/\text{s}$ for benign lesions and for malignant lesions the median D_{slow} was $1.13 (0.60\text{--}1.43) \times 10^{-3} \text{ mm}^2/\text{s}$ ($p = 0.428$). Median D_{fast} was $4.0 (0.0\text{--}19.5) \times 10^{-3} \text{ mm}^2/\text{s}$ for benign lesions and $6.9 (0.0\text{--}14.6) \times 10^{-3} \text{ mm}^2/\text{s}$ for malignant lesions ($p = 0.350$). Median f_{fast} was $8.8\% (0.0\text{--}26.7\%)$ for benign lesions and $9.4\% (0.0\text{--}17.2\%)$ for malignant lesions ($p = 0.834$).

For the ADC, the highest reachable number of TN was 1 of 12, using a threshold of $2.00 \times 10^{-3} \text{ mm}^2/\text{s}$, resulting in a specificity and sensitivity of 8.3% and 100% respectively. The median ADC was $1.39 \times 10^{-3} \text{ mm}^2/\text{s}$ and varied between 1.04 and $2.07 \times 10^{-3} \text{ mm}^2/\text{s}$ for benign lesions and for malignant lesions the median ADC was $1.36 (0.84\text{--}1.92) \times 10^{-3} \text{ mm}^2/\text{s}$ ($p = 0.599$).

For the ADC the TH and Fo resulting from the stability subsets was within 5% of the results from the training set (Table 7.1). For D_{slow} , TH varied between -4.9% and $+10.4\%$ and Fo between -11.5% and $+9.8\%$. For the microperfusion components the variation was relatively larger varying between -45.7% and $+1.2\%$ for TH, and between -2.0% and 16.5% for Fo.

7.4.2 Validation using a test subset

For benign lesions (n=23), PA resulted in adenosis (n=7), fibroadenoma (n=4), chronic inflammation (n=4), intraductal papilloma (n=2), epithelial hyperplasia (n=1), benign phyllodes (n=1), tubular adenoma (n=1), fibrotic parenchyma (n=1) and 2 other lesions benign on follow-up. The diameter varied between 10 and 90 mm.

For malignant lesions (n=116), PA diagnosed IDC (n=43), IDC + DCIS grade 3 (n=12), IDC + DCIS grade 2 (n=20), IDC + DCIS grade 1 (n=7), DCIS grade 3 (n=2), DCIS grade 2 (n=4), ILC (n=12), ILC + LCIS (n=3), invasive micropapillary carcinoma (n=4), mixed invasive ductolobular carcinoma (n=2), mixed invasive ductolobular carcinoma + DCIS grade 2 (n=1), mixed ductolobular adenocarcinoma + DCIS grade 2 (n=1), mucinous carcinoma (n=1), adenosquamous carcinoma (n=1), adenocarcinoma (n=1), malignant phyllodes (n=1) and medullary carcinoma (n=1), and the diameter was between 10 and 100 mm. For malignant lesions, the diffusion (D_{slow} and ADC) was significantly lower than in benign lesions and the measurements were similar among readers (Table 7.2, Fig. 7.5).

Table 7.2: Diffusion obtained with IVIM and the ADC. In malignant lesions (n = 116) the diffusion was significantly lower than in benign lesions (n = 23). The measurements were similar among readers. Data are given as median and interquartile range.

	$D_{\text{slow}} (\times 10^{-3} \text{ mm}^2/\text{s})$			ADC ($\times 10^{-3} \text{ mm}^2/\text{s}$)		
	Benign	Malignant	p	Benign	Malignant	p
Reader 1	1.34 (0.99-1.57)	0.90 (0.62-1.06)	<0.001	1.63 (1.35-1.83)	1.18 (1.01-1.37)	<0.001
Reader 2	1.45 (1.02-1.61)	0.87 (0.68-1.07)	<0.001	1.68 (1.38-1.86)	1.15 (0.99-1.41)	<0.001
Reader 3	1.33 (1.11-1.57)	0.85 (0.66-1.05)	<0.001	1.63 (1.30-1.83)	1.14 (0.99-1.38)	<0.001
p	0.844	0.934		0.925	0.906	

Fibroadenomas were classified as true negatives by IVIM in 3 out of 7 cases, while for the ADC this number was of 1 out of 7 (Fig. 7.5). For the microperfusion parameters D_{fast} and f_{fast} no significant differences were found between malignant and benign lesions, and also measurements were similar among readers (Table 7.3).

For the three IVIM parameters and the ADC, the respective TH and Fo obtained from the training set were applied to the test set. For IVIM, the average sensitivity and specificity were 91.4% and 49.3% when the “AND rule” was implemented using all three

IVIM parameters, and 92.8% and 47.8% respectively for D_{slow} only.

The results were not significantly different ($p = 1.000$) among the three readers (Table 7.4). Also the agreement of the lesion segmentation was high between the readers with a median DSC of 0.78 (reader 1 vs. 2), 0.77 (reader 1 vs. 3) and 0.85 (reader 2 vs. 3) (Fig. 7.6).

For the ADC, the average sensitivity and specificity was 95.1% and 17.4% respectively and was not significantly different ($p \geq 0.500$) among the three readers (Table 7.5). The specificity of IVIM was significantly ($p \leq 0.003$) higher compared to the ADC.

Table 7.3: Microperfusion obtained with IVIM. The measurements were similar among readers. Microperfusion parameters D_{fast} and f_{fast} were not significantly different between malignant ($n = 116$) and benign lesions ($n = 23$). Data are given as median and interquartile range.

	$D_{\text{fast}} (\times 10^{-3} \text{ mm}^2/\text{s})$			$F_{\text{fast}} (\%)$		
	Benign	Malignant	p	Benign	Malignant	p
Reader 1	3.0 (0.0-6.2)	4.8 (0.0-6.9)	0.930	7.9 (2.5-11.2)	10.0 (5.6-12.5)	0.561
Reader 2	0.0 (0.0-5.3)	5.3 (0-7.2)	0.305	6.1 (0-9.9)	9.5 (5.9-12.3)	0.233
Reader 3	0.0 (0.0-6.7)	5.3 (0.0-8.3)	0.100	6.5 (0.0-10.7)	9.5 (6.1-12.7)	0.129
p	0.693	0.550		0.711	0.941	

Table 7.4: Diagnostic performance of IVIM compared among readers. In total 116 malignant and 23 benign lesions were analyzed. McNemar's test showed no differences between readers ($p = 1.000$). The average specificity of IVIM among all readers was 49.3% when the "AND rule" was implemented using all three IVIM parameters, and 47.8% for D_{slow} only.

	Reader 1		Reader 2		Reader 3	
	IVIM 3-parameters	IVIM D_{slow}	IVIM 3-parameters	IVIM D_{slow}	IVIM 3-parameters	IVIM D_{slow}
Se	91.4	92.2	92.2	93.1	90.5	93.1
Sp	47.8	43.5	52.2	52.2	47.8	47.8
NPV	52.4	52.6	57.1	60.0	50.0	57.9
ACC	84.2	84.2	85.6	86.3	83.5	85.6
TP	106	107	107	108	105	108
FP	12	13	11	11	12	12
FN	10	9	9	8	11	8
TN	11	10	12	12	11	11

Table 7.5: Diagnostic performance of ADC compared among readers. In total, 116 malignant and 23 benign lesions were analyzed. The average specificity of the ADC was 17.4%, which is significantly ($p \leq 0.0034$) lower than IVIM (47.8-49.3%, Table 7.4). McNemar's test showed no differences between readers ($p \geq 0.500$).

	Reader 1	Reader 2	Reader 3
Se	94.8	95.7	94.8
Sp	13	17.4	21.7
NPV	33.3	44.4	45.5
ACC	81.3	82.7	82.7
TP	110	111	110
FP	20	19	18
FN	6	5	6
TN	3	4	5

7.5 Discussion

For the optimization of IVIM, we used a semi-automated method of including voxels of the breast lesion. A commonly used method has been to draw a circular ROI with fixed diameter and subsequently ascertain the mean (17) and sometimes the maximum and minimum diffusion values or the difference between the minimal and maximal value (1, 18). Another study performed a similar analysis by looking for the peak diffusion of the lesion on the DWI maps. They observed a higher sensitivity (92.6% vs. 87.0%) when utilizing the peak diffusion of the lesion compared to the average diffusion of the entire lesion (19). Thus important information can be lost when one relies just on the average values of lesions.

Therefore, we developed and applied a semi-automated method requiring the definition of a freeform margin around the lesion resulting in automated inclusion of a selection of voxels within it. Voxels within the lesion were analyzed objectively by the algorithm, and only the optimal fraction of voxels, yielding the optimal specificity, was used. For D_{slow} and D_{fast} this resulted respectively in collecting 61% and 85% of the lowest voxels (in terms of the magnitude of D_{slow} and D_{fast} respectively) in each lesion and taking the median of those voxels for each lesion. For f_{fast} the optimization resulted in

using all voxels of each lesion. The advantage of this method is that for example for D_{slow} the median molecular diffusion is obtained from a number of voxels, and does not rely on only one minimum voxel, which could be strongly affected by noise and artifacts.

The ADCs of breast lesions are strongly affected by the selection of b-values (17, 18). This effect has been shown very clearly in invasive ductal carcinomas (IDCs), demonstrating decreasing ADCs (1.22, 0.87 and $0.97 \times 10^{-3} \text{ mm}^2/\text{s}$) with increasing maximal b-values of 700, 1000 and $1500 \text{ s}/\text{mm}^2$ respectively (2, 19, 20). This information shows the strong dependency of the ADC with microperfusion and explains why decreasing ADCs of breast tumors can be interpreted as restricted diffusion instead of a reduction of the microperfusion component (21). IVIM separates microperfusion and diffusion, and is thereby less dependent on the choice of b-values.

We observed that IVIM had a significantly higher specificity compared to the ADC for evaluation of breast lesions. This demonstrates the potentially added value of IVIM. It is however important to note that the primary cause of increase in IVIM specificity is the molecular diffusion (D_{slow}). When the molecular diffusion was compared between malignant and benign lesions, a strong significant difference was found, with a lower molecular diffusion for malignant lesions compared to benign lesions. This difference between benign and malignant lesions was absent for the microperfusion and fraction of microperfusion. The molecular diffusion alone yielded an average specificity almost similar to when microperfusion and fraction of microperfusion are added to the analysis using the "AND rule". This indicates that the use of IVIM for discriminating breast lesions is beneficial over the ADC mainly because IVIM results in a more accurate measurement of the molecular diffusion and to a lesser extent by its additional description of the microperfusion. Another way of looking at it is that the ADC performs worse than IVIM because the ADC is strongly influenced by microperfusion effects.

The biexponential diffusion characteristics of breast lesions were also previously shown helpful: a combined sensitivity of f_{fast} (microperfusion) and D_{slow} (diffusion) of 98.75% was demonstrated with a combined specificity of 49.73% (3, 22, 23) which is confirmed by our results using IVIM. The increased specificity of IVIM in our study yielded a lower number of false positives compared to the ADC. Also, fibroadenomas, which are usually difficult to analyze by DCE-MRI because they often appear as malignant lesions, were more frequently diagnosed correctly as benign using IVIM compared to the ADC.

Between the readers, the results were comparable and not statistically different, con-

firming that the presented semi-automated method is independent of the experience of the reader. This was also emphasized by the inter-reader analysis of the lesions segmentation between the readers, showing a high level of agreement. In our knowledge, no previous published studies used all three IVIM parameters simultaneously to increase the specificity in breast DWI.

Various strategies have been used to discriminate benign from malignant lesions using the ADC and IVIM. Some groups raised the sensitivity (93-96%) of the ADC, reducing specificity (55-56%) (19, 24). Others aimed the opposite, reducing sensitivity (52-70%) with high specificity (85-100%) (2, 25, 26), or optimized sensitivity and specificity simultaneously (86-92%) (27, 28). Recently, meta-analysis of DWI for detecting breast pathology showed a sensitivity between 84 and 91% and specificity between 75 and 84% (4, 5).

However, thresholds vary among publications and can only be compared between studies when aiming for similar sensitivity and specificity (29), in our case aiming at excluding cancer by maximizing specificity while maintaining sensitivity at 100%, rather than simply going for optimization of the receiver operator characteristic curve. This approach aims at substantial clinical benefit as it provides improved MRI analysis methods in order to reduce the number of biopsies and surgical removals of breast lesions turning out to be benign.

One of the potential limitations of this study may be the stability of the parameters (TH and Fo) resulting from the optimization of the algorithm using the training set. For the ADC the parameters ranged within 5% when three independent training groups were compared. For D_{slow} the variability of TH and Fo was also acceptable with values differing around 10%. The TH and Fo optimized for the microperfusion parameters D_{fast} and f_{fast} however were subject to a higher degree of uncertainty ranging up to 45.7%. This indicates that the microperfusion parameters resulting from IVIM are more difficult to implement in quantitative evaluation of breast lesions using an automated algorithm compared to the molecular diffusion. This is confirmed by our results demonstrating an almost similar specificity when only D_{slow} was used compared to implementing all three IVIM parameters. We expect that the stability of the microperfusion related parameters would improve when the first part of the diffusion curve, representing microperfusion, is sampled using more b-values especially between $b = 0$ and 50 s/mm^2 .

The implementation of the “AND rule” in our study to assess the three IVIM parameters in parallel, was based on the assumption that D_{slow} , D_{fast} and f_{fast} were lower in malignant lesions compared to benign lesions. In malignant lesions, the

diffusion is generally assumed to be lower due to a more dense structure compared to benign lesions. The difference in microperfusion between malignant and benign lesions is however more difficult to describe. Two studies found lower D_{fast} in malignant lesions but higher f_{fast} (3, 30). Another study found that both D_{fast} and f_{fast} were lower in malignant lesions (21). Nakagawa et al. showed the opposite with higher D_{fast} in invasive ductal carcinoma versus fibroadenoma (31). This shows that there is no established consensus on the difference between microperfusion components in malignant versus benign lesions. In addition, recently it was reported that in about half of all breast cancers and normal breast tissue voxels, the microperfusion components are not present (32). In our study we chose to implement D_{fast} and f_{fast} lower than the threshold for malignant lesions. It would be however interesting to observe the effect of D_{fast} and f_{fast} higher than the threshold in a future study.

7.5.1 Limitations

This study may be biased by the method incorporated to delineate the lesions. The margin around the lesions was drawn by different readers relying on the contrast between the surrounding breast tissue and the lesion itself. The contrast will be diminished in case of partial volume effect. When a voxel is relatively large, it contains various tissues which are represented on MRI as an average. At the transition of two tissue types (i.e. normal breast tissue and a tumor) this is especially reflected in blurring of the contrast. Higher resolution and the use of thin DWI slices mean smaller voxels and more accurate delineation of the lesions, reducing partial volume effects. The DWI resolution in our study was 0.89 mm in-plane, which is acceptable for DWI. However, an alternative acquisition of DWI images with a higher spatial resolution might have improved delineation and potentially diagnostic performance.

Another relevant issue is the relatively high noise floor in DWI, especially at high b-values. This is inherent to the principle of DWI which measures signal loss due to moving hydrogen protons in a relatively long time frame. During this time frame a large amount of noise is acquired compared to the small signal of the remaining stationary hydrogen protons. A possible solution might be a higher field strength such as 3.0T which increases overall SNR. However, a higher field strength can also compromise DWI by increased image distortions due to susceptibility artefacts and field heterogeneities at the higher field strength (33). Repeating this study at 3.0T rather

than at 1.5T is recommended, especially for lesions smaller than 1 cm.

7.5.2 Conclusions

In conclusion, this study demonstrates that IVIM has a significantly higher specificity compared to the ADC for the evaluation of breast lesions, and the semi-automated breast lesion analysis is independent of the reader.

7.5.3 Acknowledgements

The authors thank MRI system specialist Peter Kappert for acquisition of the data.

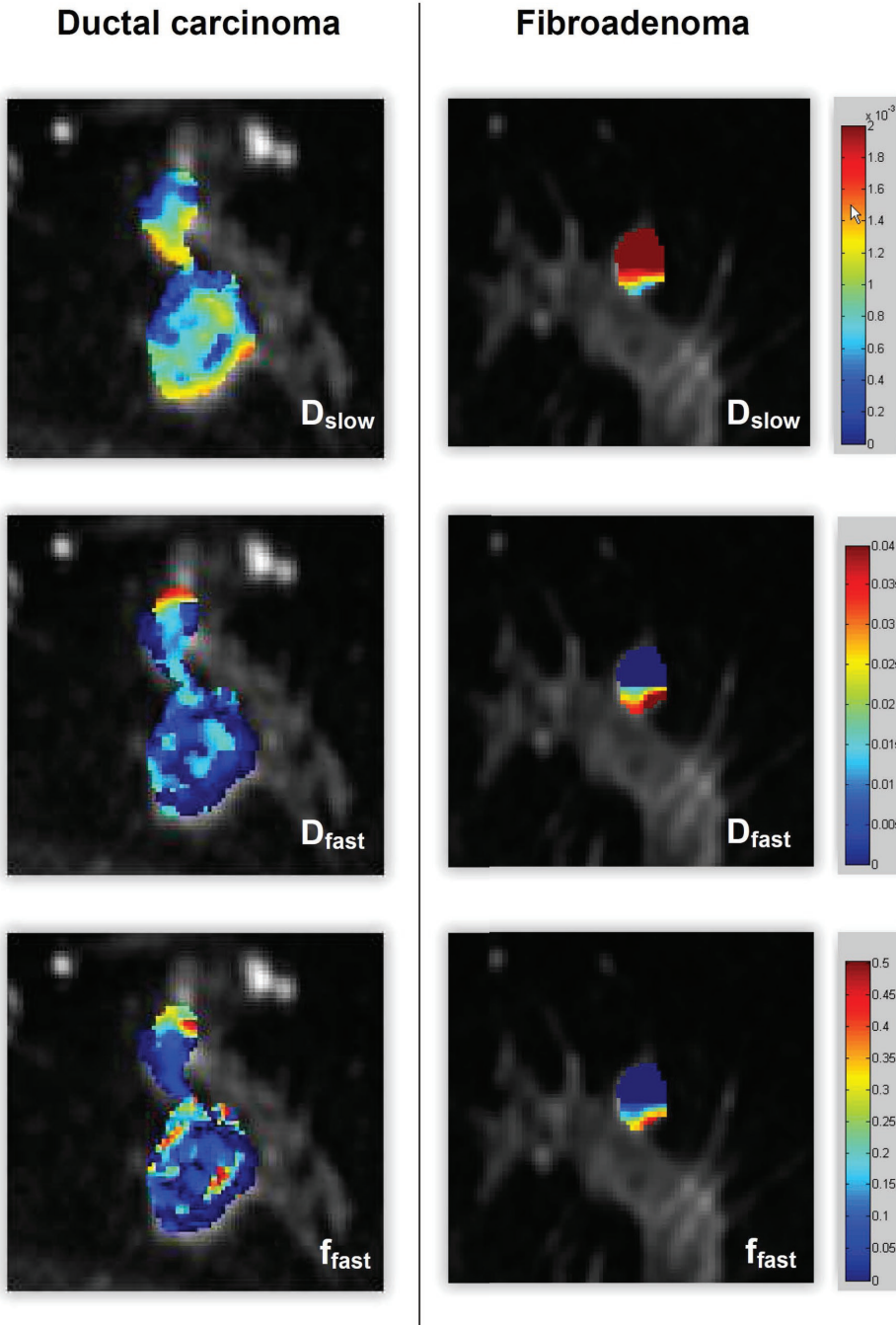


Figure 7.5: Example of a malignant ductal carcinoma (left) and a benign fibroadenoma (right). The fibroadenoma was successfully identified as benign using IVIM due to the increased diffusion D_{slow} (top) compared to the ductal carcinoma. The microperfusion parameters D_{fast} (middle) and f_{fast} (bottom) were not distinctive between the two lesions.

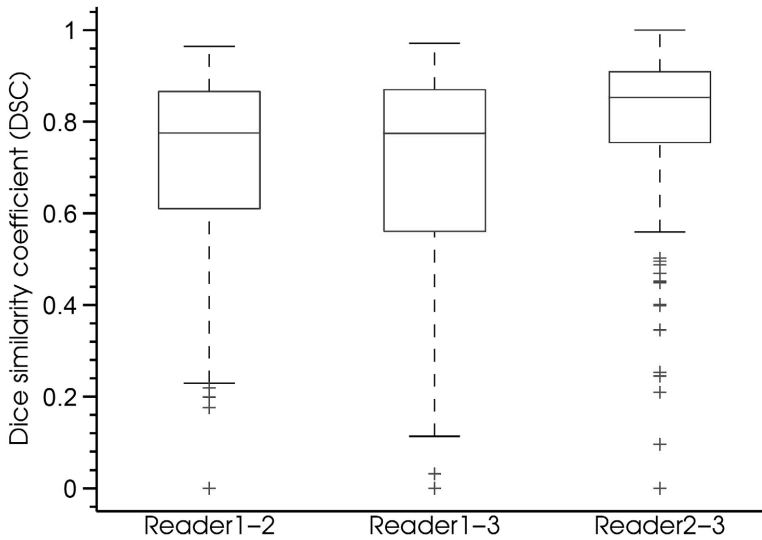


Figure 7.6: Agreement of the lesion segmentation between the readers. The agreement of the lesion segmentation between the readers was tested using the Dice Similarity Coefficient (DSC), which ranges between 0 (no spatial overlap of the ROIs) and 1 (perfect agreement of ROIs).

7.6 References

- (1) Hirano, M., Satake, H., Ishigaki, S., Ikeda, M., Kawai, H., and Naganawa, S. (2012). Diffusion-weighted imaging of breast masses: comparison of diagnostic performance using various apparent diffusion coefficient parameters. *AJR.American journal of roentgenology* 198, 717–722.
- (2) Cheng, L. et al. (2013). Optimization of apparent diffusion coefficient measured by diffusion-weighted MRI for diagnosis of breast lesions presenting as mass and non-mass-like enhancement. *Tumour biology : the journal of the International Society for Oncodevelopmental Biology and Medicine* 34, 1537–1545.
- (3) Liu, C., Liang, C., Liu, Z., Zhang, S., and Huang, B. (2013). Intravoxel incoherent motion (IVIM) in evaluation of breast lesions: comparison with conventional DWI. *European Journal of Radiology* 82, e782–9.
- (4) Chen, X., Li, W. L., Zhang, Y. L., Wu, Q., Guo, Y. M., and Bai, Z. L. (2010). Meta-analysis of quantitative diffusion-weighted MR imaging in the differential diagnosis of breast lesions. *BMC cancer* 10, 2407–10.
- (5) Dorrius, M. D., Dijkstra, H., Oudkerk, M., and Sijens, P. E. (2014). Effect of b value and pre-admission of contrast on diagnostic accuracy of 1.5-T breast DWI: a systematic review and meta-analysis. *European radiology*.
- (6) Dorrius, M. D., Pijnappel, R. M., Sijens, P. E., van der Weide, M. C., and Oudkerk, M. (2012). The negative predictive value of breast Magnetic Resonance Imaging in noncalcified BIRADS 3 lesions. *European Journal of Radiology* 81, 209–213.
- (7) Strobel, K., Schradling, S., Hansen, N. L., Barabasch, A., and Kuhl, C. K. (2015). Assessment of BI-RADS category 4 lesions detected with screening mammography and screening US: utility of MR imaging. *Radiology* 274, 343–351.
- (8) Mori, N. et al. (2013). Detection of invasive components in cases of breast ductal carcinoma in situ on biopsy by using apparent diffusion coefficient MR parameters. *European radiology* 23, 2705–2712.
- (9) Baltzer, P. A. et al. (2011). Diffusion tensor magnetic resonance imaging of the breast: a pilot study. *European radiology* 21, 1–10.
- (10) Park, J. E., Kim, H. S., Goh, M. J., Kim, S. J., and Kim, J. H. (2015). Pseudoprogression in Patients with Glioblastoma: Assessment by Using Volume-weighted Voxel-based Multiparametric Clustering of MR Imaging Data in an Independent Test Set. *Radiology* 275, 792–802.
- (11) Bihan, D. L., Turner, R., Moonen, C. T., and Pekar, J. (1991). Imaging of diffusion and microcirculation with gradient sensitization: design, strategy, and significance. *Journal of magnetic resonance imaging : JMRI* 1, 7–28.
- (12) Bihan, D. L., Breton, E., Lallemand, D., Aubin, M. L., Vignaud, J., and Laval-Jeantet, M. (1988). Separation of diffusion and perfusion in intravoxel incoherent motion MR imaging. *Radiology* 168, 497–505.
- (13) Muller, M. F., Prasad, P., Siewert, B., Nissenbaum, M. A., Raptopoulos, V., and Edelman, R. R. (1994). Abdominal diffusion mapping with use of a whole-body echo-planar system. *Radiology* 190, 475–478.
- (14) Turner, R., Bihan, D. L., Maier, J., Vavrek, R., Hedges, L. K., and Pekar, J. (1990). Echo-planar imaging of intravoxel incoherent motion. *Radiology* 177, 407–414.
- (15) Weinstein, S., Obuchowski, N. A., and Lieber, M. L. (2005). Clinical evaluation of diagnostic tests. *AJR.American journal of roentgenology* 184, 14–19.
- (16) Zou, K. H. et al. (2004). Statistical validation of image segmentation quality based on a spatial overlap index. *Academic Radiology* 11, 178–189.
- (17) Nilsen, L. B., Fangberget, A., Geier, O., and Seierstad, T. (2013). Quantitative analysis of diffusion-weighted magnetic resonance imaging in malignant breast lesions using different b value combinations. *European radiology* 23, 1027–1033.

- (18) Peters, N. H., Vincken, K. L., van den Bosch, M. A., Luijten, P. R., Mali, W. P., and Bartels, L. W. (2010). Quantitative diffusion weighted imaging for differentiation of benign and malignant breast lesions: the influence of the choice of b-values. *Journal of magnetic resonance imaging : JMRI* 31, 1100–1105.
- (19) Ochi, M. et al. (2013). Diffusion-weighted imaging (b value = 1500 s/mm²) is useful to decrease false-positive breast cancer cases due to fibrocystic changes. *Breast cancer (Tokyo, Japan)* 20, 137–144.
- (20) Kinoshita, T., Yashiro, N., Ihara, N., Funatu, H., Fukuma, E., and Narita, M. (2002). Diffusion-weighted half-Fourier single-shot turbo spin echo imaging in breast tumors: differentiation of invasive ductal carcinoma from fibroadenoma. *Journal of computer assisted tomography* 26, 1042–1046.
- (21) Tamura, T. et al. (2010). Biexponential Signal Attenuation Analysis of Diffusion-weighted Imaging of Breast. *Magnetic resonance in medical sciences : MRMS : an official journal of Japan Society of Magnetic Resonance in Medicine* 9, 195–207.
- (22) Baron, P., Dorrius, M. D., Kappert, P., Oudkerk, M., and Sijens, P. E. (2010). Diffusion-weighted imaging of normal fibroglandular breast tissue: influence of microperfusion and fat suppression technique on the apparent diffusion coefficient. *NMR in biomedicine* 23, 399–405.
- (23) Tamura, T. et al. (2012). Comparisons of multi b-value DWI signal analysis with pathological specimen of breast cancer. *Magnetic resonance in medicine : official journal of the Society of Magnetic Resonance in Medicine / Society of Magnetic Resonance in Medicine* 68, 890–897.
- (24) Partridge, S. C., Demartini, W. B., Kurland, B. F., Eby, P. R., White, S. W., and Lehman, C. D. (2010). Differential diagnosis of mammographically and clinically occult breast lesions on diffusion-weighted MRI. *Journal of magnetic resonance imaging : JMRI* 31, 562–570.
- (25) Stadlbauer, A. et al. (2009). Diffusion-weighted MR imaging with background body signal suppression (DWIBS) for the diagnosis of malignant and benign breast lesions. *European radiology* 19, 2349–2356.
- (26) Sahin, C., and Aribal, E. (2013). The role of apparent diffusion coefficient values in the differential diagnosis of breast lesions in diffusion-weighted MRI. *Diagnostic and interventional radiology (Ankara, Turkey)* 19, 457–462.
- (27) Pereira, F. P. et al. (2009). Assessment of breast lesions with diffusion-weighted MRI: comparing the use of different b values. *AJR. American journal of roentgenology* 193, 1030–1035.
- (28) Rubesova, E., Grell, A. S., Maertelaer, V. D., Metens, T., Chao, S. L., and Lemort, M. (2006). Quantitative diffusion imaging in breast cancer: a clinical prospective study. *Journal of magnetic resonance imaging : JMRI* 24, 319–324.
- (29) Orguc, S., Basara, I., and Coskun, T. (2012). Diffusion-weighted MR imaging of the breast: comparison of apparent diffusion coefficient values of normal breast tissue with benign and malignant breast lesions. *Singapore medical journal* 53, 737–743.
- (30) Bokacheva, L. et al. (2014). Intravoxel incoherent motion diffusion-weighted MRI at 3.0 T differentiates malignant breast lesions from benign lesions and breast parenchyma. *Journal of magnetic resonance imaging : JMRI* 40, 813–823.
- (31) Nakagawa, M. et al. (2014). Triexponential diffusion analysis in invasive ductal carcinoma and fibroadenoma. *Nihon Hoshasen Gijutsu Gakkai zasshi* 70, 199–205.
- (32) Panek, R. et al. (2015). Evaluation of diffusion models in breast cancer. *Medical physics* 42, 4833–4839.
- (33) Matsuoka, A. et al. (2008). Comparison of 3.0- and 1.5-tesla diffusion-weighted imaging in the visibility of breast cancer. *Radiation Medicine* 26, 15–20.

Quantitative DWI implemented after DCE-MRI yields increased specificity for BI-RADS 3 and 4 breast lesions

Hildebrand Dijkstra
Monique D. Dorrius
Mirjam Wielema
Ruud M. Pijnappel
Matthijs Oudkerk
Paul E. Sijens

Published in the Journal of Magnetic Resonance Imaging
2016, doi 10.1002/jmri.25331.

8.1 Abstract

Purpose: To assess if specificity can be increased when semi-automated breast lesion analysis of quantitative diffusion-weighted imaging (DWI) is implemented after dynamic contrast-enhanced (DCE-) MRI in the workup of BI-RADS 3 and 4 breast lesions larger than 1 cm.

Materials and Methods: 120 consecutive patients (mean age, 48 years; age range, 23–75 years) with 139 breast lesions (≥ 1 cm) were examined (2010–2014) with 1.5T DCE-MRI and DWI ($b=0, 50, 200, 500, 800$ and 1000 s/mm²) and the BI-RADS classification and histopathology were obtained. For each lesion malignancy was excluded using voxelwise semi-automated breast lesion analysis based on previously defined thresholds for the apparent diffusion coefficient (ADC) and the three intravoxel incoherent motion (IVIM) parameters: molecular diffusion (D_{slow}), microperfusion (D_{fast}), and the fraction of D_{fast} (f_{fast}). The sensitivity (Se), specificity (Sp) and negative-predictive-value (NPV) based on only IVIM parameters combined in parallel (D_{slow} , D_{fast} and f_{fast}), or the ADC or the BI-RADS classification by DCE-MRI were compared. Subsequently, the Se, Sp and NPV of the combination of the BI-RADS classification by DCE-MRI followed by the IVIM parameters in parallel (or the ADC) were compared.

Results: Twenty-three of 139 breast lesions were benign. Se and Sp of DCE-MRI were 100% and 30.4% (NPV=100%). Se and Sp of IVIM parameters in parallel were 92.2% and 52.2% (NPV=57.1%) and for the ADC 95.7% and 17.4%, respectively (NPV=44.4%). 26 of 139 lesions were classified as BI-RADS 3 ($n=7$) or BI-RADS 4 ($n=19$). DCE-MRI combined with ADC (Se=99.1%, Sp=34.8%) or IVIM (Se=99.1%, Sp=56.5%) did significantly improve ($p=0.016$) Sp of DCE-MRI alone for workup of BI-RADS 3 and 4 lesions (NPV=92.9%).

Conclusion: Quantitative DWI has a lower NPV compared to DCE-MRI for evaluation of breast lesions and may therefore not be able to replace DCE-MRI; when implemented after DCE-MRI as problem solver for BI-RADS 3 and 4 lesions the combined specificity improves significantly.

8.2 Introduction

Diffusion-weighted imaging (DWI) is currently not generally implemented in the diagnostic workup of breast pathology. After the combination of mammography and ultrasound, dynamic contrast-enhanced (DCE-) MRI is the second most used modality. DCE-MRI has the highest overall negative predictive value (NPV) of all imaging techniques, and is usually able to safely exclude malignancy (NPV > 98%) (1–4). However, enhancement patterns of benign and malignant breast lesions can show considerable overlap on DCE-MRI, especially for BI-RADS 3 and 4 lesions (1, 3, 4). For those breast lesions it is often unclear if the lesion is a cancer based on only the enhancement curve, for example a fibro adenoma often appears as malignant due to late wash-out of the kinetic curve. In clinical practice the majority of patients with these difficult to differentiate breast lesions on DCE-MRI will undergo a biopsy with its known complications (5). At this point in the diagnostic algorithm, quantitative DWI might have the potential to be implemented for excluding malignancy in this group of equivocal breast lesions on DCE-MRI (6).

DWI of breast lesions can be quantified using a mono-exponential model yielding the apparent diffusion coefficient (ADC) or a bi-exponential model such as intravoxel incoherent motion (IVIM) (7). The ADC has been shown already to be a valuable noninvasive quantitative biomarker to assess breast cancer (8). Also IVIM has the potential to provide additional diagnostic performance and proves generally a higher specificity for breast cancer compared to the ADC (9–11).

In a preceding optimization and validation study, IVIM and ADC were optimized for excluding malignancy of breast lesions using semi-automated breast lesion analysis (12). The included lesions were larger than 1 cm to allow for optimal voxelwise analysis using DWI, which has generally a relatively low spatial resolution. The effect of lesion size on the NPV was suspected to be minimal; the NPV of the ADC has been reported similar (96%) for small (≤ 1 cm) and large (> 1 cm) lesions (13). The statistics will be affected though by the high percentage of malignancy (66.7–95.9%) when only large lesions are included (14, 15).

The potential value of combined quantitative DWI and DCE-MRI for breast lesion differentiation has been indicated already, but is generally based on the ADC, and the selection of the region-of-interest usually relies on drawing a circular area and taking the average (16–18). Additionally, for DWI to be implemented successfully along DCE-MRI, the sensitivity should be high ($>98\%$) while the specificity is maximized. These opportunities were implemented in a method defined as semi-automated breast lesion

analysis and is described in the previous study (12).

This prior article dealt with the optimization and validation of IVIM compared with the ADC for the semi-automated analysis of breast lesions using a multi-reader setup, which requires the definition of a freeform margin around the lesion resulting in automated inclusion of a selection of voxels within it, thereby maximizing specificity while aiming for a sensitivity near 100%. In the current manuscript we apply the previously validated and optimized semi-automated breast lesion analysis by implementing it after DCE-MRI.

The purpose of this study was therefore to assess if specificity can be increased when semi-automated breast lesion analysis of quantitative DWI is implemented after DCE-MRI in the workup of BI-RADS 3 and 4 breast lesions larger than 1 cm.

8.3 Materials and methods

8.3.1 Study population

The protocol of this prospective study was approved by the hospital's institutional review board and all patients provided informed consent. Between May 2010 and July 2014, patients with an inconclusive mammogram or part of the BRCA screening population and scheduled for breast MRI and DWI were recruited. Inclusion criteria were: lesion diameter larger than or equal to 1 cm on MRI, no hematomas, pathology available, and no previous breast surgery or breast implants. This resulted in the inclusion of 120 consecutive patients (mean age, 48 years; age range, 23–75 years) with 139 breast lesions: 116 malignant and 23 benign. All 120 patients have been previously reported (12).

8.3.2 Pathology

Histopathology, cytology or at least 6 months follow-up of the 139 breast lesions defined lesions as benign or malignant. Tissue samples were obtained after modified radical mastectomy (n = 75), lumpectomy (n = 39), ultrasonographically (US) guided core biopsy (n = 16), US-guided fine-needle aspiration biopsy (n = 3) and MRI-guided core biopsy (n = 1). Five lesions were negative during MRI follow-up (mean follow-up time: 1.5 years; mean follow-up frequency: 11 months).

8.3.3 MR protocols

All subjects were examined on a 1.5T MRI system (Magnetom Avanto, Siemens Medical Solutions, Erlangen, Germany). The body coil served as transmitter and a commercially available circularly polarized bilateral breast phased-array coil with automatic tuning and electronic decoupling as receiver (Siemens Medical Solutions). After the localizer scans, DWI was performed using a spin echo based single shot echo-planar imaging (SS-EPI) sequence in combination with spectral adiabatic inversion recovery (SPAIR) fat suppression. DWI acquisitions ($b = 0, 50, 200, 500, 800$ and 1000 s/mm^2) were tuned with the following parameters: TR 9300 ms; TE 91 ms; FA 90° ; slice-thickness 4 mm; slice-gap 6 mm; FOV $170 \times 340 \text{ mm}^2$; matrix 192×384 ; bandwidth 1628 Hz/pixel; 2 averages. Diffusion gradients (25 mT/m) were applied in the phase-, read-, and z-directions separately. In total, 28 transverse slices were acquired in interleaved mode to cover both breasts within an acquisition time of 2.5 minutes.

Finally, eight series (six series from July 2013) of transversal DCE T1-weighted spoiled gradient echo sequences were obtained with a temporal resolution of 76 seconds using gadoterate meglumine (Gd-DOTA, Dotarem, Guerbet, 0.1 mmol/kg): TR 4.17 ms; TE 1.29 ms; FA 10° ; slice-thickness 0.97 mm; no slice-gap; FOV $340 \times 340 \text{ mm}^2$; matrix 384×384 ; bandwidth 318 Hz/pixel; no averages. Parallel acquisition technique GRAPPA with acceleration factor 2 was enabled in all acquisitions.

8.3.4 DWI analysis

All 139 lesions were analyzed off-line (Matlab 2014a, The Mathworks, Natick, MA, USA) by a radiologist (R.M.P.) with 25 years of experience in mammography using the semi-automated method as described in the preceding optimization and validation study (12). For all lesions, the radiologist included voxels by drawing a freeform region-of-interest (ROI) around the lesion. The voxels included in the ROI were then fitted using both the bi-exponential IVIM model and a mono-exponential model using all 6 b-values yielding the ADC.

For the IVIM model the diffusion-weighted signal intensities S were fitted as follows (7, 19):

$$\frac{S}{S_0} = f_{fast} \cdot e^{-b \cdot D_{fast}} + f_{slow} \cdot e^{-b \cdot D_{slow}} \quad (8.1)$$

where S_0 is the maximum signal intensity, D_{fast} is the fast component representing microperfusion, f_{fast} is the fraction of microperfusion, D_{slow} is the slow component representing molecular diffusion and f_{slow} is the fraction of molecular diffusion ($f_{slow} = 1 - f_{fast}$).

Equation 8.1 was fitted by the Nelder-Mead simplex direct search method with bound constraints, which performs a constrained non-linear minimisation of the sum of the squared residuals (20, 21). The initial guess D_{slow}^0 was estimated by calculating the slope of the asymptote of the slow signal component between $b = 500$ and 1000 s/mm², and D_{slow} was bound between $0.2 \times D_{slow}^0 \times 10^{-3}$ mm²/s and $5 \times D_{slow}^0 \times 10^{-3}$ mm²/s. The slope of the signal between $b = 0$ and $b = 50$ s/mm² was used to guess the initial value of the microperfusion (D_{fast}^0), and was bound between D_{slow}^0 and 100×10^{-3} mm²/s. The initial guess of f_{fast} (f_{fast}^0) was estimated simply by solving equation 8.1 for f_{fast} as all other parameters are known and $f_{slow} = 1 - f_{fast}$, and no restrictions were applicable (bound between 0.0 and 1.0).

Subsequently, the voxels within the ROI were automatically processed off-line according to the two previously determined optimized parameters as described in the preceding optimization and validation study (12): optimal fraction (Fo) and thresholds (TH). The Fo defined which voxels of the lesions were used based on the magnitude of D_{slow} , D_{fast} and f_{fast} (and similar for ADC as well), and were respectively 61%, 85%, 100% and 100%. This means that for instance for D_{slow} , only the 61% lowest D_{slow} voxels in the lesion are used to calculate the median D_{slow} of the lesion. The optimized TH were 1.44×10^{-3} mm²/s, 18.55×10^{-3} mm²/s and 0.247 for D_{slow} , D_{fast} and f_{fast} respectively.

The sensitivity (Se), specificity (Sp) and negative-predictive-value (NPV) resulted from combining the three IVIM parameters in parallel in a single test using the “AND rule” to discriminate malignant from benign lesions, based on the TH resulting from the preceding optimization and validation study. That is, if D_{slow} was lower than the TH, and if D_{fast} was lower than the TH, and if f_{fast} was lower than the TH, then the combined result was defined positive (malignant), but in all other cases, the combined result was negative (benign). For the ADC one TH was applied (2.00×10^{-3} mm²/s) and the result was defined malignant if ADC was lower than the TH.

8.3.5 DCE-MRI analysis

All patients’ images were clinically interpreted by two radiologists with 3 and 30 years of experience in mammography and the findings were recorded in structured ra-

diology reports. The Breast Imaging-Reporting and Data System (BI-RADS) classification was extracted retrospectively from the structured radiology reports for all 139 lesions. Lesions which MRI classified as BI-RADS 1 or 2 were considered negative for malignancy. Next, Se, Sp and NPV were calculated.

8.3.6 Statistics

Statistical analyses were performed using SPSS (SPSS 22, Chicago, IL, USA). All data were tested for normality using Shapiro–Wilk tests. IVIM parameters and ADC were given as median. The diagnostic performance in terms of Se, Sp and NPV was compared between DWI (IVIM and ADC) and DCE-MRI (BI-RADS classification) using McNemar’s test based on the binomial distribution. In addition, the combinations of IVIM or ADC following DCE-MRI were compared.

For Se and Sp, the 95% confidence intervals (CI) for proportions were calculated according to the efficient-score method (corrected for continuity) described by Newcombe et al. (22). For all statistical tests $P < 0.05$ was considered to indicate a statistically significant difference.

8.4 Results

8.4.1 Comparison of DCE-MRI and quantitative DWI as individual techniques

All 139 breast lesions exceeding 1 cm on DCE-MRI were classified according to the BI-RADS classification: BI-RADS 2 ($n = 7$), BI-RADS 3 ($n = 7$), BI-RADS 4 ($n = 19$), BI-RADS 5 ($n = 73$) and BI-RADS 6 ($n = 33$). One hundred sixteen out of 139 breast lesions (83.5%) were proven malignant by pathology.

After reviewing all 139 lesions, the overall Se and Sp of DCE-MRI were 100% and 30.4% respectively when lesions classified as BI-RADS ≥ 3 were considered malignant (Table 8.1). Using DCE-MRI, 7 out of 23 benign lesions were true negatives (TN) that could be safely excluded from further diagnostic workup (BI-RADS 2), and there were no false negatives (NPV = 100%). The overall NPV of DWI using IVIM was 57.1% with a Se of 92.2% and Sp of 52.2% (significantly different from DCE-MRI, $p = 0.003$), and as many as 12 benign lesions would have been excluded from further diagnostic workup;

at the same time there would have been 9 false negatives. The overall NPV of the ADC was 44.4% with a Se of 95.7% and Sp of 17.4%, and based on the ADC alone, only 4 benign lesions would have been excluded from further diagnostic workup while there were 5 false negatives.

When only BI-RADS 3 and 4 lesions were considered, the NPV was 50.0% and 85.7% respectively for the ADC and IVIM individually.

Table 8.1: Comparison of the diagnostic performance of DCE-MRI and quantitative DWI as individual techniques. Demonstrated is the diagnostic performance and 95% CI to exclude breast cancer compared between DCE-MRI, IVIM and ADC as individual techniques. Data are provided for all lesions ($n = 139$) and also for BI-RADS 3 and 4 lesions only ($n = 26$). Quantitative DWI has a lower NPV compared to DCE-MRI for evaluation of breast lesions and may therefore not be able to replace DCE-MRI. * indicates a significant difference.

	TP	TN	FP	FN	Se (%)	Sp (%)	NPV (%)	
<i>all lesions (n = 139)</i>								
DCE-MRI	116	7	16	0	100 (96.0-100)	30.4 (14.0-53.0)	100 (56.0-100)	
ADC	111	4	19	5	95.7 (89.7-98.4)	17.4 (0.06-39.5)	44.4 (15.3-77.3)	p = 0.77 vs. DCE-MRI
IVIM	107	12	11	9	92.2 (85.4-96.2)	52.2 (31.1-72.6)	57.1 (34.4-77.4)	p = 0.003* vs. DCE-MRI
<i>BI-RADS 3 and 4 lesions (n = 26)</i>								
ADC	14	1	10	1	93.3 (66.0-99.7)	9.1 (0.0-42.9)	50.0 (2.6-97.3)	
IVIM	14	6	5	1	93.3 (66.0-99.7)	54.5 (24.6-81.9)	85.7 (42.0-99.2)	

8.4.2 Quantitative DWI following DCE-MRI as problem solver for BI-RADS 3 and 4 lesions

Pathology proved 11 out of 26 BI-RADS 3 and 4 lesions as benign (Fig. 8.1, Table 8.2). The overall Sp increased significantly ($p = 0.016$) from 30.4% (DCE-MRI only) to 56.5% (DCE-MRI + IVIM) with a NPV of 92.9%, when IVIM followed DCE-MRI as problem solver for BI-RADS 3 and 4 lesions (Table 8.3). For the ADC the overall Sp showed little change from 30.4% to 34.8%. IVIM identified 6 out of 11 benign lesions correctly as negative (Table 8.2). One of those benign lesions was proven adenosis and the parametric maps (D_{slow} , D_{fast} and f_{fast}) of this lesion obtained using IVIM are shown

in Fig. 8.2 for illustrative purposes. The ADC identified 1 out of 11 benign lesions correctly as negative.

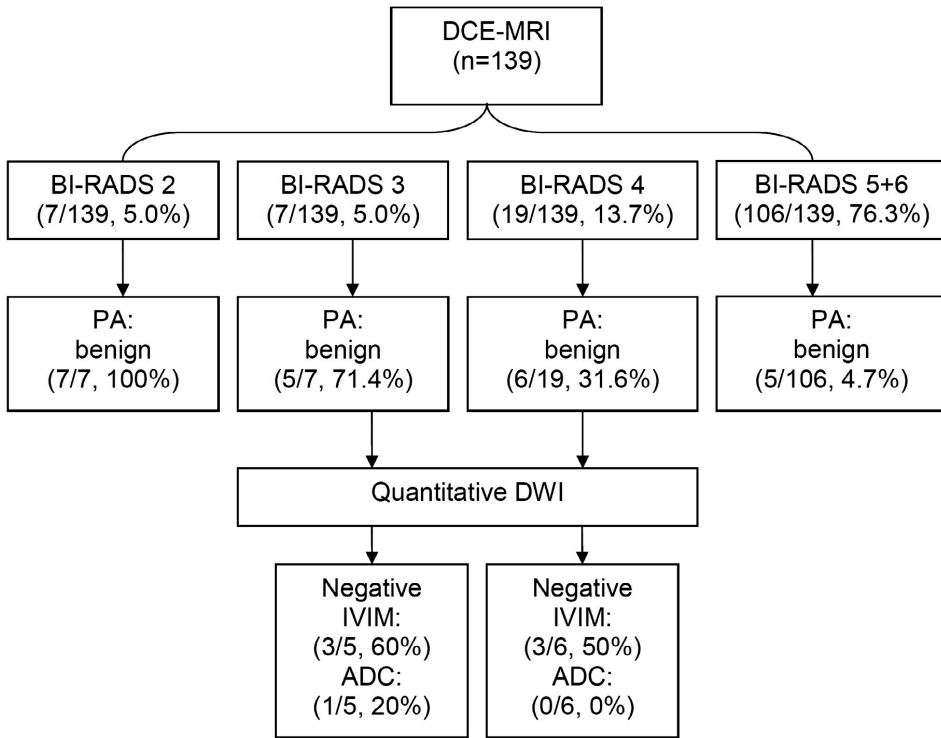


Figure 8.1: Flow chart of diagnostic workup. Lesions identified on DCE-MRI as BI-RADS 3 or 4 ($n = 26$) were additionally evaluated by quantitative DWI. For the remainder of the lesions ($n = 113$) the endpoint was DCE-MRI. DCE-MRI classified 11 benign lesions as BI-RADS 3 or 4; IVIM identified 6 of those lesions correctly as negative, for ADC this was 1 out of 11. This indicates the potential added value of DWI when implemented after DCE-MRI in the diagnostic workup of breast lesions, especially for BI-RADS 3 and 4 lesions.

Table 8.2: BI-RADS 3 and 4 lesions on DCE-MRI Listed are 26 lesions classified by DCE-MRI as inconclusive (BI-RADS 3 or 4). 11 out of 26 inconclusive lesions were proven benign by pathology, and IVIM identified 6 out of those 11 benign lesions correctly as negative. For the ADC this number was 1 out of 11 lesions.

† Lesion was defined as positive (malignant) if the apparent diffusion coefficient (ADC) < $2.00 \times 10^{-3} \text{ mm}^2/\text{s}$, otherwise negative (benign).

‡ The three intravoxel incoherent motion (IVIM) parameters were combined in parallel in a single test using the "AND rule" to discriminate malignant from benign lesions, based on three thresholds. If molecular diffusion (D_{slow}), fraction of microperfusion (f_{fast}) and microperfusion (D_{fast}) were lower than their threshold ($1.44 \times 10^{-3} \text{ mm}^2/\text{s}$, 0.247 and $18.55 \times 10^{-3} \text{ mm}^2/\text{s}$ respectively) then the combined result was defined positive (malignant), but in all other cases, the combined result was negative (benign). Data are medians.

* Lesion is shown in Fig. 8.2

Pathology	BI-RADS DCE- MRI	ADC ($\times 10^{-3} \text{ mm}^2/\text{s}$)	ADC test †	D_{slow} ($\times 10^{-3} \text{ mm}^2/\text{s}$)	D_{fast} ($\times 10^{-3} \text{ mm}^2/\text{s}$)	f_{fast} (%)	3-param IVIM test ‡
Benign							
epithelial hyperplasia	3	1.32	+	0.64	6.09	0.18	+
fibroadenoma	3	2.27	-	1.86	0.00	0.00	-
	3	1.93	+	1.57	12.5	0.27	-
adenosis	3	1.77	+	1.56	7.62	0.15	- *
	4	1.25	+	1.05	4.47	0.08	+
	4	1.16	+	0.75	0.00	0.06	+
chronic inflammation	4	1.63	+	1.32	3.66	0.08	+
	4	1.78	+	1.61	0.00	0.06	-
intraductal papilloma	3	1.68	+	1.33	0.00	0.05	+
	4	1.92	+	1.61	0.00	0.00	-
fibrotic parenchyma	4	1.66	+	1.46	22.9	0.15	-

Malignant									
	3	1.52	+	1.04	6.51	0.15	+		
	3	1.44	+	1.08	4.59	0.08	+		
IDC	4	1.29	+	1.18	0.00	0.00	+		
	4	0.93	+	0.58	3.97	0.15	+		
	4	0.99	+	0.81	0.00	0.00	+		
	4	2.00	-	1.71	0.00	0.00	-		
IDC + DCIS grade 2	4	0.96	+	0.55	11.1	0.16	+		
IDC + DCIS grade 1	4	1.70	+	1.11	5.31	0.10	+		
DCIS grade 3	4	1.38	+	1.21	7.09	0.09	+		
	4	1.11	+	0.80	6.12	0.18	+		
invasive micro- papillary carcinoma	4	1.26	+	0.74	4.74	0.19	+		
mixed ductolobular adeno- carcinoma + DCIS grade 2	4	1.05	+	0.54	6.67	0.15	+		
mixed invasive ductolobular carcinoma + DCIS grade 2	4	0.98	+	0.42	6.46	0.24	+		
ILC + LCIS	4	1.07	+	0.60	3.74	0.16	+		
mucinous carcinoma	4	1.37	+	1.17	6.55	0.11	+		

Table 8.3: Comparison of the diagnostic performance of quantitative DWI following DCE-MRI as problem solver for BI-RADS 3 and 4 lesions. Demonstrated is the diagnostic performance and 95% CI of ADC and IVIM implemented after DCE-MRI as problem solver for lesions classified as BI-RADS 3 and 4. The analysis was performed on all lesions ($n = 139$). Lesions identified on DCE-MRI as BI-RADS 3 or 4 ($n = 26$) were additionally evaluated by quantitative DWI. For the remainder of the lesions ($n = 113$) the endpoint was DCE-MRI. * indicates a significant difference.

	TP	TN	FP	FN	Se (%)	Sp (%)	NPV (%)	
DCE-MRI	116	7	16	0	100 (96.0-100)	30.4 (14.0-53.0)	100 (56.0-100)	
DCE-MRI + ADC	115	8	15	1	99.1 (94.6-100)	34.8 (17.2-57.2)	88.9 (50.7-99.4)	$p = 0.5$ vs. DCE-MRI
DCE-MRI + IVIM	115	13	10	1	99.1 (94.6-100)	56.5 (34.9-76.1)	92.9 (64.2-99.6)	$p = 0.016^*$ vs. DCE-MRI

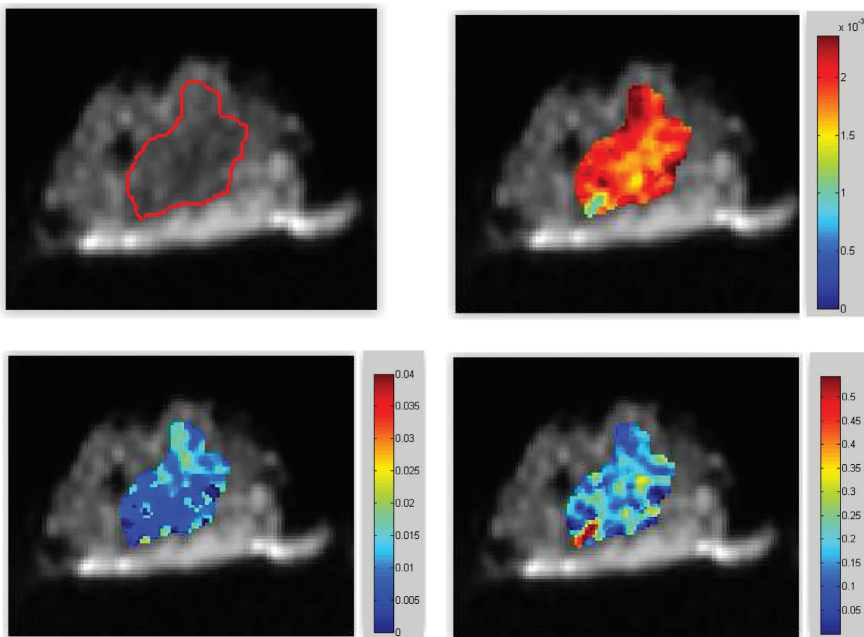


Figure 8.2: Example of adenosis. Voxels were included within a freeform margin around the lesion (top left) and the three IVIM parameters were calculated: molecular diffusion (top right), microperfusion (bottom left) and fraction of microperfusion (bottom right).

8.5 Discussion

The aim of this study was to validate the diagnostic use of quantitative DWI implemented after DCE-MRI in the workup of BI-RADS 3 and 4 breast lesions by implementing a previously validated method for semi-automated breast lesion analysis (12). The Se and NPV of DCE-MRI alone in this study were 100% with a Sp of 30.4%, thereby yielding no false negatives, and therefore safe exclusion of malignancy. The NPV of IVIM was 57.1% with a Se and Sp of respectively 92.2% and 52.2%, which is generally too low to allow safe exclusion of malignancy. This means that IVIM may not be able to replace DCE-MRI in the diagnostic workup of breast lesions.

DCE-MRI alone generally results in a negative predictive value of more than 98%, which is confirmed in this study and is enough to safely exclude malignancy (1–3). This is mainly based on non-enhancement of breast lesions. However, enhancement patterns of benign and malignant breast lesions can show considerable overlap on DCE-MRI, especially for BI-RADS 3 and 4 lesions which are then mostly scheduled for invasive procedures. To reduce the number of invasive procedures, DCE-MRI followed by quantitative DWI can have potential. The Se and NPV of IVIM or ADC however needs to be sufficient (>98%) to allow for safe exclusion of malignancy.

When IVIM was implemented after DCE-MRI as problem solver for BI-RADS 3 and 4 lesions, the combined Sp of DCE-MRI followed by IVIM increased significantly from 30.4% to 56.5%; this contradicts previous findings on the integration of DCE-MRI and DWI for breast lesion classification, which suggested no benefit of combining DCE-MRI and DWI (23). The likely reasons for that are the differences in the approach of optimizing the differentiation between benign and malignant lesions.

The semi-automated method of breast lesion analysis presented in this and previous paper was optimized for excluding breast cancer and preventing biopsies by aiming for a high Se (>98%) with maximal Sp. This approach is inherently different from detecting cancer by optimizing the receiver operating curve and maximizing the area under the curve such that an optimal set of Se and Sp is obtained. DCE-MRI already has a Se and Sp near 100% and 82.5% respectively in non-calcified breast lesions, resulting in a negative predictive value (NPV) higher than 98%, and is thereby able to safely exclude malignancy (1, 4). Therefore for DWI to be implemented successfully along DCE-MRI, the Se should be high (>98%) while the Sp is optimized as high as possible. In the current paper we show that this approach is beneficial for BI-RADS 3 and 4 lesions by proving additional Sp and potentially a reduced number of unnecessary biopsies.

For 11 benign lesions classified as BI-RADS 3 or 4 on DCE-MRI, IVIM was negative

for 6 lesions and the ADC was negative for 1 lesion. However, the combined NPV of DCE-MRI followed by IVIM was too low (92.9%) to allow safe exclusion of malignancy. This indicates that additional optimization of the semi-automated method and possibly a larger group of BI-RADS 3 and 4 lesions are necessary to utilize the gained Sp with sufficient NPV.

For DCE-MRI followed by the ADC, no improvement of the Sp compared to DCE-MRI alone was observed. The ADC can therefore not replace DCE-MRI. These findings are comparable to a previous study investigating whether adding an ADC threshold to DCE-MRI could improve the positive predictive value of breast MRI (24). They found a Sp of 47% in combination with 100% Se, however significance was not reached. Also, a study to differentiate between DCIS and invasive breast carcinoma did not find a significant improvement of the diagnostic performance when ADC was compared to DCE-MRI (25). A meta-analysis found a Se and Sp of 91.6% and 85.5% respectively (16). They optimized their Se and Sp by aiming for the optimum in the receiver-operating curve. Although the Se and Sp of combined DCE-MRI and ADC were higher than either DCE-MRI or ADC alone, this optimization strategy yields a Se which is still too low to safely exclude malignancy.

The diagnostic performance of quantitative DWI depends heavily on the strategy which is used to discriminate benign from malignant lesions using the ADC and IVIM. Some groups raised the Se (93-96%) of the ADC, reducing Sp (55-56%) (26, 27). Others aimed the opposite, reducing Se (52-70%) with high Sp (85-100%) (10, 28, 29), or simply optimized the receiver-operator curve (86-92%) (30, 31).

In the current study a recently published method was implemented which was designed and validated for excluding cancer by maximizing Sp while maintaining Se near 100% (12). This explains the relatively lower Sp presented in this study compared to literature values. However, all Sp of DWI which is gained using this strategy is profitable and can be used to potentially reduce invasive procedures which are indecisive after DCE-MRI by ruling out malignancy, as long as the Se of DWI is high enough. This approach is inherently different to previously published studies that aimed to prove malignancy by increasing the positive predictive value of DWI following DCE-MRI (24).

8.5.1 Limitations

A technical limitation in this study is that with the use of additional b-values, especially additional ones in the range between 0 and 50 s/mm² and beyond 1000 s/mm²,

the assessed IVIM parameters might become more robust and potentially yield a higher Sp (32). Another limitation is that despite the sizable number of 139 breast lesions included in this prospective study, the demonstration that IVIM analysis of DWI data has additional value for correctly identifying benign BI-RADS 3 and 4 lesions, relies on observations made in 26 lesions only. Also, the study is limited by the retrospective acquisition of the BI-RADS classification from DCE-MRI structured reports. In addition, two malignant BI-RADS 3 lesions were under-classified in retrospect because they had not the typical characteristics of a malignant lesion.

The inclusion criterion of at least 1 cm in diameter, whilst beneficial to the accuracy and reproducibility of the outcomes, limits this study to only a portion of those breast lesions assessable by DCE-MRI. The NPV of the ADC is however reported similar (96%) for small (≤ 1 cm) and large (> 1 cm) lesions (13).

Our study included 83.5% malignant lesions, which is comparable to previously published studies (66.7-95.9%) including only lesions of at least 1 cm (14, 15). In addition, our hospital is a center for high risk patients groups (i.e. BRCA) as well as advanced breast cancer. This may explain the relatively high number of malignancies over 1 cm found in our patients, and also the relatively low Sp of DCE-MRI alone. We expect that for this group of complex patients the BI-RADS classification is more frequently over-classified, resulting in more biopsies, to be on the safe side.

8.5.2 Conclusions

In conclusion, this study demonstrates that quantitative DWI has a lower NPV compared to DCE-MRI for evaluation of breast lesions and may therefore not be able to replace DCE-MRI; when implemented after DCE-MRI as problem solver for BI-RADS 3 and 4 lesions the combined specificity improves significantly.

8.6 Acknowledgements

The authors thank MRI system specialist Peter Kappert for acquisition of the data.

8.7 References

- (1) Dorrius, M. D., Pijnappel, R. M., Sijens, P. E., van der Weide, M. C., and Oudkerk, M. (2012). The negative predictive value of breast Magnetic Resonance Imaging in noncalcified BIRADS 3 lesions. *European Journal of Radiology* 81, 209–213.
- (2) Gokalp, G., and Topal, U. (2006). MR imaging in probably benign lesions (BI-RADS category 3) of the breast. *European Journal of Radiology* 57, 436–444.
- (3) Moy, L. et al. (2009). Is breast MRI helpful in the evaluation of inconclusive mammographic findings? *AJR.American journal of roentgenology* 193, 986–993.
- (4) Strobel, K., Schradang, S., Hansen, N. L., Barabasch, A., and Kuhl, C. K. (2015). Assessment of BI-RADS category 4 lesions detected with screening mammography and screening US: utility of MR imaging. *Radiology* 274, 343–351.
- (5) Nassar, A. (2011). Core needle biopsy versus fine needle aspiration biopsy in breast—a historical perspective and opportunities in the modern era. *Diagnostic cytopathology* 39, 380–388.
- (6) Iima, M. et al. (2011). Apparent diffusion coefficient as an MR imaging biomarker of low-risk ductal carcinoma in situ: a pilot study. *Radiology* 260, 364–372.
- (7) Bihan, D. L., Breton, E., Lallemand, D., Aubin, M. L., Vignaud, J., and Laval-Jeantet, M. (1988). Separation of diffusion and perfusion in intravoxel incoherent motion MR imaging. *Radiology* 168, 497–505.
- (8) Bickel, H. et al. (2015). Quantitative apparent diffusion coefficient as a noninvasive imaging biomarker for the differentiation of invasive breast cancer and ductal carcinoma in situ. *Investigative radiology* 50, 95–100.
- (9) Hirano, M., Satake, H., Ishigaki, S., Ikeda, M., Kawai, H., and Naganawa, S. (2012). Diffusion-weighted imaging of breast masses: comparison of diagnostic performance using various apparent diffusion coefficient parameters. *AJR.American journal of roentgenology* 198, 717–722.
- (10) Cheng, L. et al. (2013). Optimization of apparent diffusion coefficient measured by diffusion-weighted MRI for diagnosis of breast lesions presenting as mass and non-mass-like enhancement. *Tumour biology : the journal of the International Society for Oncodevelopmental Biology and Medicine* 34, 1537–1545.
- (11) Liu, C., Liang, C., Liu, Z., Zhang, S., and Huang, B. (2013). Intravoxel incoherent motion (IVIM) in evaluation of breast lesions: comparison with conventional DWI. *European Journal of Radiology* 82, e782–9.
- (12) Dijkstra, H. et al. (2015). Semi-automated quantitative intravoxel incoherent motion analysis and its implementation in breast diffusion-weighted imaging. *Journal of magnetic resonance imaging : JMRI*.
- (13) Partridge, S. C. et al. (2010). Apparent diffusion coefficient values for discriminating benign and malignant breast MRI lesions: effects of lesion type and size. *AJR.American journal of roentgenology* 194, 1664–1673.
- (14) Kul, S., Cansu, A., Alhan, E., Dinc, H., Gunes, G., and Reis, A. (2011). Contribution of diffusion-weighted imaging to dynamic contrast-enhanced MRI in the characterization of breast tumors. *AJR.American journal of roentgenology* 196, 210–217.
- (15) Vignati, A. et al. (2011). Performance of a fully automatic lesion detection system for breast DCE-MRI. *Journal of magnetic resonance imaging : JMRI* 34, 1341–1351.
- (16) Zhang, L., Tang, M., Min, Z., Lu, J., Lei, X., and Zhang, X. (2015). Accuracy of combined dynamic contrast-enhanced magnetic resonance imaging and diffusion-weighted imaging for breast cancer detection: a meta-analysis. *Acta Radiologica (Stockholm, Sweden : 1987)*.
- (17) de Almeida, J. R. M., Gomes, A. B., Barros, T. P., Fabel, P. E., and de Seixas Rocha, M. (2015). Subcategorization of Suspicious Breast Lesions (BI-RADS Category 4) According to MRI Criteria: Role of Dynamic Contrast-Enhanced and Diffusion-Weighted Imaging. *AJR.American journal of roentgenology* 205, 222–231.

- (18) Pinker, K. et al. (2014). Improved diagnostic accuracy with multiparametric magnetic resonance imaging of the breast using dynamic contrast-enhanced magnetic resonance imaging, diffusion-weighted imaging, and 3-dimensional proton magnetic resonance spectroscopic imaging. *Investigative radiology* 49, 421–430.
- (19) Bihan, D. L., Turner, R., Moonen, C. T., and Pekar, J. (1991). Imaging of diffusion and microcirculation with gradient sensitization: design, strategy, and significance. *Journal of magnetic resonance imaging : JMRI* 1, 7–28.
- (20) Muller, M. F., Prasad, P., Siewert, B., Nissenbaum, M. A., Raptopoulos, V., and Edelman, R. R. (1994). Abdominal diffusion mapping with use of a whole-body echo-planar system. *Radiology* 190, 475–478.
- (21) Turner, R., Bihan, D. L., Maier, J., Vavrek, R., Hedges, L. K., and Pekar, J. (1990). Echo-planar imaging of intravoxel incoherent motion. *Radiology* 177, 407–414.
- (22) Newcombe, R. G. (1998). Two-sided confidence intervals for the single proportion: comparison of seven methods. *Statistics in medicine* 17, 857–872.
- (23) Fusco, R. et al. (2015). Integration of DCE-MRI and DW-MRI Quantitative Parameters for Breast Lesion Classification. *BioMed research international* 2015, 237863.
- (24) Partridge, S. C., DeMartini, W. B., Kurland, B. F., Eby, P. R., White, S. W., and Lehman, C. D. (2009). Quantitative diffusion-weighted imaging as an adjunct to conventional breast MRI for improved positive predictive value. *AJR.American journal of roentgenology* 193, 1716–1722.
- (25) Wang, Y. et al. (2015). Diffusion-tensor imaging as an adjunct to dynamic contrast-enhanced MRI for improved accuracy of differential diagnosis between breast ductal carcinoma in situ and invasive breast carcinoma. *Chinese journal of cancer research = Chung-kuo yen cheng yen chiu* 27, 209–217.
- (26) Partridge, S. C., Demartini, W. B., Kurland, B. F., Eby, P. R., White, S. W., and Lehman, C. D. (2010). Differential diagnosis of mammographically and clinically occult breast lesions on diffusion-weighted MRI. *Journal of magnetic resonance imaging : JMRI* 31, 562–570.
- (27) Ochi, M. et al. (2013). Diffusion-weighted imaging (b value = 1500 s/mm²) is useful to decrease false-positive breast cancer cases due to fibrocystic changes. *Breast cancer (Tokyo, Japan)* 20, 137–144.
- (28) Stadlbauer, A. et al. (2009). Diffusion-weighted MR imaging with background body signal suppression (DWIBS) for the diagnosis of malignant and benign breast lesions. *European radiology* 19, 2349–2356.
- (29) Sahin, C., and Aribal, E. (2013). The role of apparent diffusion coefficient values in the differential diagnosis of breast lesions in diffusion-weighted MRI. *Diagnostic and interventional radiology (Ankara, Turkey)* 19, 457–462.
- (30) Pereira, F. P. et al. (2009). Assessment of breast lesions with diffusion-weighted MRI: comparing the use of different b values. *AJR.American journal of roentgenology* 193, 1030–1035.
- (31) Rubesova, E., Grell, A. S., Maertelaer, V. D., Metens, T., Chao, S. L., and Lemort, M. (2006). Quantitative diffusion imaging in breast cancer: a clinical prospective study. *Journal of magnetic resonance imaging : JMRI* 24, 319–324.
- (32) Peters, N. H., Vincken, K. L., van den Bosch, M. A., Luijten, P. R., Mali, W. P., and Bartels, L. W. (2010). Quantitative diffusion weighted imaging for differentiation of benign and malignant breast lesions: the influence of the choice of b-values. *Journal of magnetic resonance imaging : JMRI* 31, 1100–1105.

Part IV

Appendix



Summary

Diffusion-weighted imaging (DWI) is a biomedical application of magnetic resonance imaging (MRI). The technique measures the diffusion of hydrogen protons in, for example, the human body. Diffusion is the random walk, or Brownian motion of particles. In a glass of water the hydrogen protons move around freely in all directions, in a random fashion called isotropic diffusion. In the human body diffusion is restricted by obstacles including macromolecules such as lipids or proteins, and by the large gadolinium based complexes injected during contrast-enhanced imaging. Diffusion also relates to the number of cells within a volume. When the cell density increases, as in cancer, there is less space to allow diffusion, thus the diffusion drops. The diffusion also drops when the cell volume increases, for example by ischemia. Increases of diffusion can be observed when the space around the cells (the extracellular space) increases and fills with edema, for example by inflammation.

DWI is applied in a wide range of imaging protocols to assess for example the brain, liver, kidney, prostate or breasts. Its use in the clinic is however mostly qualitative and based on visual assessment of DWI images resulting in a classification of either “low” or “high” diffusion. If a quantitative measurement of the diffusion is required, usually the apparent diffusion coefficient (ADC) is used, which expresses the diffusion into a number with units of mm^2/s . The ADC derives from a simplified (mono-exponential) model assuming that diffusion in the tissue can be represented by only one parameter: molecular diffusion. However, most tissues have an additional faster diffusion component: microperfusion. The microperfusion term reflects the microcirculation of blood

in the capillary network, and is for example substantial in tumors, but almost negligible in normal glandular breast tissue. The thus imperfect representation of molecular diffusion by a single coefficient ADC is expressed by the A of apparent.

Preferable for quantifying DWI data is the intravoxel incoherent motion (IVIM) model. Contrary to the mono-exponential ADC model, the IVIM model separates diffusion into molecular diffusion and microperfusion. This provides the opportunity to perform accurate measurements of molecular diffusion and simultaneously obtain additional microperfusion parameters. IVIM analysis is however a niche in clinical practice because it is not implemented in commercially available software, and depends on off-line analysis in custom software. More importantly, the interpretation of IVIM parameters is challenging.

Quantitative end results of DWI depend on several factors acting during the acquisition, data modeling and data analysis. One important acquisition parameter is the so called b -value, which defines the sensitivity of the DWI sequence for proton motion. To obtain the ADC a minimum of two DWI images with different sensitivities have to be obtained (two b -values), where for the IVIM model at least 6 b -values have to be acquired, which results in a longer study time.

The quantitative outcome of DWI, especially the ADC, is affected strongly by the choice of b -values. The acquisition settings, including the (number of) b -values are therefore main confounders in quantitative DWI. In addition, patient related properties such as the amount of contrast agent and fat fractions affect quantitative DWI. In this thesis these confounders were identified and the scale of their effect on DWI data quantification and on the clinical workflow of liver and breast imaging were assessed.

First part

Currently, clinical hepatic DWI generally relies on mono-exponential diffusion expressed in the ADC. However, a significant amount of microperfusion can be expected in the liver. In **chapter 2** it was demonstrated that the ADC of normal liver tissue varies with the measurement location due to regional differences of the microperfusion. By applying the IVIM model it was shown that molecular diffusion was similar throughout the liver and that the microperfusion varied regionally. The ADC is to a high degree sensitive to microperfusion, especially when the DWI sequence contains several b -values in the lower range. By a simulation study we showed that the variety of ADC values of healthy liver tissue published in the literature, reflected the choice of b -values, and the mono-exponential model itself. It follows that the choice of b -values is a pitfall when

using the ADC as a quantitative measure for molecular diffusion; there is no optimal combination of b-values because the a priori unknown amount of microperfusion determines the optimal sequence of b-values. The IVIM model however separates molecular diffusion and microperfusion, and can therefore be safely implemented in quantitative hepatic DWI.

Although the IVIM model describes separation of molecular diffusion and microperfusion, the concept has remained under debate since its introduction. Especially the linkage to classical perfusion obtained from techniques such as (dynamic) contrast enhanced MRI has been discussed. In **chapter 3** a further understanding of what is measured by IVIM was intended for the liver. We observed that microperfusion obtained with IVIM, and measured in pre-contrast conditions in liver parenchyma, increased significantly with wash-in rates of an hepatospecific gadolinium-based contrast agent (Gd-EOB-DTPA) during the early portal-venous phase. Additionally, microperfusion increased significantly with the uptake rate of Gd-EOB-DTPA by a specific type of liver lesions (focal nodular hyperplasia) in the late hepatobiliary phase. Interestingly, we also found that IVIM was able to separate intra- and extracellular MR contrast media. Microperfusion and diffusion were compared before and after injecting either Gd-DOTA (extracellular) or Gd-EOB-DTPA (intracellular). It was observed that microperfusion increased after administering Gd-EOB-DTPA, while it decreased after Gd-DOTA. This observation was additionally investigated by simulation to assess the question whether parameters such as diffusion and microperfusion are actually affected biophysically by a contrast agent, or that the assumptions of the quantitative DWI model are violated. The theoretical simulation confirmed that the observed in- and decreases of the microperfusion after injection contrast agent, were caused by violating specific assumptions of the IVIM model (equal T₂-relaxation times for microperfusion and diffusion). From these results we concluded that IVIM reflects perfusion in a way resembling CE-MRI, and the observations add to the ongoing debate and understanding of what is measured by IVIM.

One of the confounders in hepatic DWI is steatosis. The ADC decreases significantly in patients with hepatic steatosis and this may hamper for example the determination of hepatic fibrosis with DWI. Less is known however of the effect of normal (non-steatotic) fat fractions on quantitative DWI, which was the topic of **chapter 4**. The hepatic fat fractions (HFF), molecular diffusion and microperfusion were measured and compared. It was demonstrated that molecular diffusion in the liver is affected by hepatic fat, also in the absence of steatosis (HFF below 5.5%). A steady significant decrease of the molec-

ular diffusion with moderate correlation was found for increasing HFF. These results complement existing knowledge of the reduction of molecular diffusion by steatotic HFF (>5.5%). These observations are especially important when in pursuit of quantitative cut-off values for molecular diffusion in order to discriminate healthy liver tissue from pathology. It is known that the decreases of the molecular diffusion between normal liver tissue and cirrhosis or the different stages of fibrosis are relatively small and technically challenging to detect. This implicates that any derived cut-off value for molecular diffusion used in the assessment of cirrhosis, or stages of fibrosis, is dependent on the HFF as well, especially because it is known that HFFs vary between subjects. Therefore, we recommend that to correctly interpret quantitative hepatic DWI, acquisition of the HFF prior to the hepatic DWI protocol is necessary. In that way, diffusion measurements can be judged along with the fat measurement, which ensures a more reliable assessment of the diffusion properties of pathology.

Liver diseases often assessed by DWI are fibrosis and cirrhosis. Fibrosis is characterized by the generation of more than normal amounts of collagen fibers in the extracellular space thereby hardening the tissue. This process develops in four stages and the final stage is known as cirrhosis. The ADC has been shown to decrease from stage to stage and, as a result, cirrhotic livers have a significantly lower ADC compared to normal livers. A patient group implicated with fibrosis and cirrhosis are patients with a Fontan circulation. The Fontan operation is a palliative operation in which the right atrium (and in newer techniques the caval veins) is directly connected to the pulmonary arteries. In the Netherlands, yearly around 1200 newborns are born with a congenital heart disease. Around 4-5% of these patients have a complex congenital heart disease (univentricular heart) and can benefit from a Fontan operation.

One of the implications of the Fontan circulation is a decreased portal flow due to elevated venous pressure and limited cardiac output. The decreased portal flow is compensated by an increased hepatic arterial flow, which is termed the hepatic arterial buffer response. We expected that the distribution of the microperfusion is likely to vary among the different liver segments due to the alternative distribution of the hepatic flow in Fontan patients. In **chapter 5** it was therefore investigated if previously observed decreases of the ADC in the liver of Fontan patients can be explained by a true decrease of molecular diffusion, or rather reflects decreased microperfusion due to the decreased portal blood flow.

Observations indeed showed that decreased hepatic ADC measurements are caused by a lower microperfusion in Fontan livers instead of a decreased molecular diffusion. The molecular diffusion was similar between Fontan patients and controls, while the

microperfusion parameters (and ADC) were significantly lower in Fontan livers. We also found that the molecular diffusion decreases with time since the Fontan operation. In other words, structural liver disease (i.e. liver fibrosis or cirrhosis) seems not present at first but develops progressively in time after Fontan operation whereas hepatic congestion (decreased microperfusion) is chronically present and stable over time. IVIM provides the opportunity to distinguish between these two components.

In clinical practice, IVIM-DWI might provide a major advantage compared to the other non-invasive alternatives for liver biopsy. Potentially, a decrease in the microperfusion component could indicate an adverse change in the Fontan circulation, for instance more congestion due to a conduit stenosis or pulmonary vascular remodeling. With a routine MRI follow-up of cellular diffusion, the development of liver fibrosis/cirrhosis can be safely monitored.

Second part

In the second part of this thesis the potential added value of quantitative breast DWI was investigated. DWI can help to differentiate between benign and malignant breast lesions. However, the ADCs of breast lesions and the subsequently derived ADC thresholds show considerable variation. Besides molecular diffusion, there are substantial contributions of microperfusion in tumors, but not in normal glandular breast tissue. Therefore, both diffusion and microperfusion affect the ADC values. ADCs tend to increase by the contributions from microperfusion when small b-values are used, and decrease when reconstructed from DWI series measured with mainly higher b-values (reflecting diffusion). Also different ADC values can be caused by use of contrast agents. Therefore, in **chapter 6** a systematic review and meta-analysis was performed to assess the effect of the choice of b-values, and the effect of contrast agents, on the ADCs of breast lesions.

It was observed that the wide variety of b-value combinations applied in different studies significantly affects the ADC of breast lesions and therefore confounds quantitative DWI. The combination of $b = 0$ and 1000 s/mm^2 was found to yield highest differentiation between benign and malignant lesions. The pooled sensitivity was similar between combinations of b-values $\leq 600 \text{ s/mm}^2$ (91%) and combinations of b-values $> 600 \text{ s/mm}^2$, (89%). The pooled specificity increased from 75% to 84% by the use of b-values $> 600 \text{ s/mm}^2$.

The meta-analysis also confirmed that at higher b-values, a second term with a very low diffusion value, representing unsuppressed signal from fatty tissue, results in a de-

crease of the ADC. Also a continuous decrease of the ADC with increasing maximum b-value was observed both in benign and malignant tumors, which substantiates the hypothesis that tumor tissue is characterized by substantial microperfusion and thereby affects the ADC. Our results showed no significant effect of contrast agents on the respective ADCs of benign and malignant breast lesions.

Currently, DWI is not generally implemented for detecting breast pathology due to its lower sensitivity and specificity compared to dynamic contrast-enhanced (DCE-) MRI. DWI has a sensitivity between 84 and 91% and specificity between 75 and 84%. In contrast, DCE-MRI has sensitivity and specificity of 100% and 82.5% respectively in non-calcified breast lesions. To implement DWI successfully along DCE-MRI, the sensitivity should be high while the specificity is optimized as high as possible. In **chapter 7** we proposed a semi-automated method for breast lesions analysis. The method required the definition of a freeform margin around the lesion resulting in automated inclusion of a selection of voxels within it. Voxels within the lesion were analyzed objectively by the algorithm, and only the optimal fraction of voxels, yielding the optimal specificity, was used. A novel approach of this method was that we combined all three IVIM parameters (molecular diffusion, microperfusion and its fractions) simultaneously to increase the specificity of breast DWI.

A group of 176 patients with breast lesions and known pathology was divided into an independent training (24 lesions, 12 benign) and test set (139 lesions, 23 benign). The training set was used to optimize the method such that a maximum number of true negatives and a minimal number of false negatives was obtained. The test set was used to validate the method for breast lesion analysis by assessing the sensitivity and specificity by three independent readers. We observed that between the readers the results were comparable and not statistically different, confirming that the presented semi-automated method is independent of the experience of the reader. Also IVIM performed better than the ADC. For IVIM, the average sensitivity and specificity were 91.4% and 49.3%, and for the ADC 95.1% and 17.4% respectively. This indicates that the use of IVIM for discriminating breast lesions is beneficial over the ADC. The increased specificity of IVIM in our study yielded a lower number of false positives compared to the ADC. Also, fibroadenomas, which are usually difficult to analyze by DCE-MRI because they often appear as malignant lesions, were more frequently diagnosed correctly as benign using IVIM compared to the ADC.

DCE-MRI has the highest overall negative predictive value (NPV) of all imaging techniques, and is usually able to safely exclude malignancy (NPV > 98%). However,

enhancement patterns of benign and malignant breast lesions can show considerable overlap on DCE-MRI, especially for BI-RADS 3 and 4 lesions. For those breast lesions it is often unclear if the lesion is a cancer based on only the enhancement curve, for example a fibro adenoma often appears as malignant due to late wash-out of the kinetic curve. In clinical practice the majority of patients with these difficult to differentiate breast lesions on DCE-MRI will undergo a biopsy with its known complications. At this point in the diagnostic algorithm, quantitative DWI might have the potential to be implemented for excluding malignancy in this group of equivocal breast lesions on DCE-MRI.

In **chapter 8** it was therefore investigated if the specificity can be increased when the semi-automated method for breast lesion analysis (presented in chapter 7) was implemented after DCE-MRI in the workup of BI-RADS 3 and 4 breast lesions. For that purpose 120 consecutive patients with 139 breast lesions and known pathology were included.

The sensitivity and NPV of DCE-MRI alone in this study were 100% with a specificity of 30.4%, thereby yielding no false negatives, and therefore safe exclusion of malignancy. The NPV of IVIM was 57.1% with a sensitivity and specificity of respectively 92.2% and 52.2%, which is generally too low to allow safe exclusion of malignancy. This means that IVIM may not be able to replace DCE-MRI in the diagnostic workup of breast lesions. However, when IVIM was implemented after DCE-MRI as problem solver for BI-RADS 3 and 4 lesions, the combined specificity of DCE-MRI followed by IVIM increased significantly from 30.4% to 56.5%. Also, for 11 benign lesions classified as BI-RADS 3 or 4 on DCE-MRI, IVIM was negative for 6 lesions and the ADC was negative for 1 lesion. This showed that all specificity of DWI which is gained using the presented strategy is profitable and can be used to potentially reduce invasive procedures which are indecisive after DCE-MRI by ruling out malignancy, as long as the sensitivity of DWI is high enough.

In this thesis the value of the IVIM model has been demonstrated, with recognition of its limitations. The ADC, though widely used in the clinic, neglects valuable tissue characteristics which are exposed using IVIM. It is expected that IVIM can play a major role as non-invasive problem solver in breast cancer, however more research is needed.

Nederlandse Samenvatting

Diffusie-gewogen beeldvorming (DWI) is een biomedische toepassing van MRI. De techniek meet de diffusie van waterstof protonen in bijvoorbeeld het menselijk lichaam. Diffusie is de willekeurige verplaatsing van deeltjes (Browniaanse beweging). In een glas met water bewegen de waterstof protonen vrij in alle richtingen, op een willekeurige manier, genaamd isotrope diffusie. In het menselijk lichaam wordt diffusie beperkt door obstakels zoals grote moleculen (vet en proteïnen), en door grote gadolinium complexen die worden geïnjecteerd bij een contrast-versterkt onderzoek. Diffusie is gerelateerd aan het aantal cellen in een volume. Wanneer de celdichtheid toeneemt, zoals in een tumor, dan is er minder ruimte voor diffusie, dus de diffusie neemt af. De diffusie neemt ook af als het volume van de cellen toeneemt, bijvoorbeeld bij onvoldoende zuurstof. Een toename van de diffusie kan worden geconstateerd wanneer de ruimte rondom de cellen (de extracellulaire ruimte) toeneemt en vult met oedeem, bijvoorbeeld bij een ontsteking.

DWI wordt toegepast in een groot aantal MRI onderzoeken naar bijvoorbeeld het brein, de lever, de nieren, prostaat of borsten. De toepassing in de dagelijkse praktijk is echter voornamelijk kwalitatief en gebaseerd op visuele beoordeling van DWI plaatjes, resulterend in een “lage” of “hoge” diffusie. Als een kwantitatief onderzoek nodig is, dan wordt de apparent diffusion coefficient (ADC) gebruikt om de diffusie uit te drukken in een getal. De ADC heeft de eenheid mm^2/s . De ADC is afgeleid van een simpel (mono-exponentieel) model. Dit model heeft als aanname dat de diffusie in een weefsel kan worden samengevat in één parameter: molecuulair diffusie. Echter, voor

de meeste weefsels gaat deze aanname niet op omdat er ook nog een snellere diffusie component aanwezig is: de microperfusie. De microperfusie representeert de microcirculatie van bloed in het capillaire netwerk, en is bijvoorbeeld sterk verhoogd in tumoren, maar bijna afwezig in normaal borstweefsel. De moleculaire diffusie kan dus niet simpelweg weergegeven worden door één parameter zoals de ADC. De “A” in ADC staat dan ook voor apparent (schijnbaar of ogenschijnlijke) diffusie coëfficiënt.

Het intravoxel incoherent motion (IVIM) model kwantificeert DWI beelden op een andere manier. In tegenstelling tot het mono-exponentiële ADC model, is het IVIM model in staat om diffusie te scheiden in moleculaire diffusie en microperfusie. Dit biedt de mogelijkheid om tegelijkertijd betrouwbare metingen te verrichten van de moleculaire diffusie en daarnaast extra metingen te verrichten van de microperfusie. IVIM wordt echter niet veel toegepast in de klinische praktijk omdat het niet beschikbaar is als commerciële software, en afhankelijk is van analyse met zelfgeschreven software modules op research werkstations. Een andere reden is dat de interpretatie van IVIM lastig is.

Kwantitatieve DWI resultaten zijn afhankelijk van verschillende factoren tijdens de acquisitie, modelering en data analyse. Een belangrijke parameter is de zogenaamde b-waarde, die definieert de gevoeligheid van de DWI sequentie voor de beweging van waterstof protonen. Om de ADC te kunnen meten zijn er tenminste twee DWI plaatjes nodig met elk een verschillende gevoeligheid (twee b-waarden). Voor IVIM zijn er tenminste 6 b-waarden nodig, wat dus resulteert in een langere scan tijd.

De kwantificering van DWI, in het bijzonder van de ADC, wordt sterk beïnvloed door de keuze van b-waarden. De instellingen die worden gemaakt voor de acquisitie van de beelden, inclusief het aantal en keuze van de b-waarden, zijn daarom sterk van invloed op het uiteindelijke resultaat. Daarnaast beïnvloeden ook patiënt gerelateerde eigenschappen zoals de hoeveelheid contrastmiddel of het vetpercentage het eindresultaat. In dit proefschrift wordt de invloed van deze en ook andere factoren op DWI kwantificatie in lever en borst onderzocht.

Deel 1

Bij DWI opnamen van de lever maakt men in de klinische praktijk op dit moment alleen gebruik van de ADC. Er wordt vanuit gegaan dat leverweefsel zich vrij simpel gedraagt op een mono-exponentiële wijze. Deze aanname is van grote invloed op het uiteindelijke kwantitatieve resultaat. In **hoofdstuk 2** zijn de effecten van het gebruik van de ADC of IVIM onderzocht. In normaal lever weefsel werd een groot aandeel mi-

croperfusie aangetroffen. Dit aandeel varieerde op verschillende plaatsen in de lever. Als gevolg hiervan varieerde de ADC waarde ook op verschillende plaatsen in de lever. Dit komt doordat de ADC niet alleen de langzame diffusie representeert maar ook sterk gevoelig is voor variaties in de microperfusie, met name als er lage b-waarden worden toegepast. Echter, de diffusie gemeten met het IVIM model bleek onafhankelijk van de meetlocatie in de lever. Dit is verklaarbaar omdat het IVIM model de diffusie en microperfusie van elkaar onderscheidt, waardoor de metingen van de diffusie onafhankelijk zijn van variaties in microperfusie. Een simulatie toonde dat de verschillen in ADC waarden die zijn gepubliceerd van normaal lever weefsel verklaard kunnen worden door de verscheidenheid aan toegepaste b-waarden. Hieruit blijkt dat de keuze van b-waarden sterk van invloed is op de ADC, en dat er geen optimale combinatie van b-waarden bestaat omdat voorafgaand aan een onderzoek het niet duidelijk is of en hoeveel microperfusie er in het weefsel aanwezig is. Het IVIM is echter in staat om moleculaire diffusie en microperfusie van elkaar te onderscheiden waardoor het een betrouwbare manier is om DWI te kwantificeren.

Er is in de wetenschappelijke literatuur echter nog steeds discussie over wat er nu precies wordt gemeten met het IVIM model, en of diffusie en microperfusie ook echt gescheiden kunnen worden. Met name de overeenkomsten met bestaande gevestigde perfusie technieken, zoals contrast versterkte (CE-) MRI, zijn onduidelijk. In **hoofdstuk 3** is deze discussie verder voortgezet en het begrip van het IVIM model in de lever verder uitgebouwd. Hierbij maakten we gebruik van contrastmiddelen. Een contrastmiddel kan zeer plaatselijk het te onderzoeken orgaan of weefsel laten oplichten (aankleuren) en wordt met een infuus ingebracht voor of tijdens een MRI onderzoek. We zagen dat microperfusie in normaal leverweefsel gemeten met IVIM (en vóór contrast injectie) significant toenam wanneer de aankleuringsnelheid tijdens de vroege fase van een intracellulair contrastmiddel (Gd-EOB-DTPA) toenam. Daarnaast zagen we in specifieke lever laesies (focal nodular hyperplasia) dat de microperfusie significant toenam wanneer de aankleuringsnelheid van Gd-EOB-DTPA in de late fase toenam. Een interessant resultaat was dat IVIM in staat bleek om intra- en extracellulaire contrast middelen van elkaar te kunnen onderscheiden. Microperfusie en diffusie werden vergeleken voor en na injectie van ofwel Gd-DOTA (extracellulair) of Gd-EOB-DTPA (intracellulair). De resultaten lieten zien dat de microperfusie toenam na injectie van Gd-EOB-DTPA maar juist afnam na injectie van Gd-DOTA. Deze observaties werden daarna getoetst in een simulatie waarmee werd aangetoond dat deze resultaten verwacht kunnen worden na injectie van contrastmiddelen. De simulatie liet echter ook zien dat de oorzaak van toe- en afname van de microperfusie gevonden moet worden in

de schending van een aantal aannames van het IVIM model (gelijkwaardige T2 relaxatie tijden voor microperfusie en diffusie). Al deze resultaten dragen bij aan het debat over wat IVIM precies weerspiegelt, en concluderend in dit hoofdstuk kan er worden gezegd dat microperfusie gemeten met IVIM gelijkwaardige processen meet als CE-MRI.

Steatose is een bepalende factor in lever DWI. Steatose is vervetting van de lever, waarbij meer dan 5,5% vet als steatose gezien wordt. Het is bekend dat de ADC significant afneemt bij patiënten met steatose en dit kan de beoordeling van lever fibrose (verstijving van de lever door overmatig bindweefsel) beïnvloeden. Er is echter minder bekend over de invloed van normale vetpercentages op de kwantificatie van DWI; dit was het onderwerp van **hoofdstuk 4**. Lever vetpercentages, moleculaire diffusie en microperfusie werden gemeten en vergeleken. Hieruit bleek dat de moleculaire diffusie ook bij normale vetpercentages (geen steatose) beïnvloed wordt door de hoeveelheid vet. De moleculaire diffusie nam significant af naar mate het vetpercentage toenam, met een matige correlatie. Deze resultaten zijn in de lijn van bestaande kennis over afname van de diffusie bij patiënten met een steatotische lever. De resultaten zijn ook met name belangrijk wanneer er wordt gezocht naar afkapwaarden voor de diffusie om zo normaal leverweefsel van pathologie te kunnen onderscheiden. Het is bekend dat de diffusie verschillen tussen normaal weefsel en de verschillende stadia van fibrose klein zijn, en moeilijk te meten. Dit betekent dat afkapwaarden voor diffusie afhankelijk kunnen zijn van het vetpercentage, en kunnen variëren tussen verschillende patiënten groepen. Op basis van deze studie raden we dan ook aan om voorafgaand aan kwantitatieve DWI studies een lever vetbepaling te doen, wat ook mogelijk is met MRI. Op die manier kunnen de diffusie resultaten beter worden geïnterpreteerd, wat resulteert in een betrouwbaardere evaluatie van de diffusie eigenschappen van pathologie.

DWI wordt vaak gebruikt om leverziekten zoals fibrose en cirrose te onderzoeken. Fibrose ontstaat doordat er teveel collageenstrengen worden aangemaakt waardoor het weefsel harder of stijver wordt. Het ontstaan van fibrose vindt plaats in vier stadia waarbij in het laatste stadium wordt gesproken van cirrose. Het is al eerder aangetoond dat de ADC afneemt in elk opeenvolgend stadium, en om die reden worden cirrotische levers gekenmerkt door een significant lagere ADC vergeleken met gezonde levers.

Een patiëntengroep bij wie fibrose en cirrose vaker voorkomen, zijn patiënten met een Fontan circulatie, naar aanleiding van een aangeboren hartafwijking. In Nederland worden jaarlijks rond de 1200 kinderen geboren met een aangeboren hart afwijking. Ongeveer 4 tot 5% van deze kinderen hebben een complexe hart afwijking waarbij het

hart bestaat uit één in plaats van twee kamers (univentriculair). Deze patiënten hebben baat bij een Fontan operatie. Een Fontan operatie is een ingreep waarbij het rechter atrium (en bij recentere ingrepen ook de vena cava) rechtstreeks wordt verbonden met de pulmonale aderen.

Eén van de implicaties van een Fontan circulatie is een verminderde portale bloedtoevoer doordat de veneuze druk verhoogd is en de pomp prestaties van het hart beperkt zijn. De verminderde portale toevoer wordt gecompenseerd door een verhoogde toevoer door de aderen vanaf de lever. In deze studie gingen wij ervan uit dat de microperfusie in verschillende delen van de lever varieert bij Fontan patiënten doordat de toevoer van bloed afwijkend is. Eerder was al aangetoond dat de ADC lager is in de lever van Fontan patiënten. In **hoofdstuk 5** is onderzocht of deze afname wordt veroorzaakt door een echte afname van de diffusie of dat dit een gevolg is van verminderde microperfusie doordat de portale toevoer is verlaagd.

De experimenten toonden aan dat de verlaagde ADC in de lever wordt veroorzaakt door een verlaagde microperfusie bij Fontan patiënten en niet door verlaagde diffusie. De diffusie was vergelijkbaar tussen Fontan patiënten en een controle groep, echter de microperfusie was significant lager bij Fontan patiënten. We zagen ook dat de diffusie afnam naarmate de tijd sinds de Fontan operatie toenam. In andere woorden, het lijkt erop dat fibrose en cirrose langzaam ontwikkelen na een Fontan operatie, en een verminderde perfusie stabiel maar voortdurend aanwezig is. Met IVIM is het mogelijk om deze twee processen van elkaar te onderscheiden op een niet-invasieve manier, wat van groot belang is in de dagelijkse klinische praktijk. Een verlaagde microperfusie gemeten in de lever kan er namelijk op wijzen dat er nadelige veranderingen plaatsvinden in de Fontan circulatie, bijvoorbeeld door de aanwezigheid van een verstopping. Daarnaast kan de ontwikkeling van fibrose/cirrose in de gaten worden gehouden door regelmatig de diffusie te meten.

Deel 2

In het tweede gedeelte van dit proefschrift is er gekeken naar de mogelijke voordelen van kwantitatieve DWI metingen in de borst. DWI kan worden ingezet om onderscheid te maken of een tumor in de borst goedaardig of kwaadaardig is. Echter, de ADC metingen en ADC afkapwaarden tonen behoorlijke variaties. Naast diffusie is er in tumoren ook een aanzienlijk aandeel microperfusie te vinden. De ADC van tumoren wordt daarom beïnvloed door zowel de diffusie als de microperfusie. ADC waarden nemen toe wanneer er in het meetprotocol wordt gekozen voor kleine b-waarden, omdat

daardoor de microperfusie de overhand neemt. Wanneer er hoge b-waarden worden gekozen dan wordt met name de diffusie gemeten. Een verklaring voor de verscheidenheid aan ADC waarden in de literatuur kan daarnaast worden gevonden in het gebruik van contrastmiddelen. In **hoofdstuk 6** is er daarom in een meta-analyse systematisch gekeken welk effect b-waarden en contrastmiddelen hebben op de uiteindelijke ADC waarde van borsttumoren. De resultaten laten zien dat de ADC van borsttumoren significant wordt beïnvloed door het gebruik van verschillende b-waarden. Dit heeft dus een nadelige invloed op het toepassen van kwantitatieve DWI analyses. De combinatie van $b = 0$ en 1000 s/mm^2 toonde de beste differentiatie tussen goed- en kwaadaardige tumoren. De sensitiviteit was vergelijkbaar tussen combinaties van b-waarden kleiner dan 600 s/mm^2 (91%) en combinaties van b-waarden groter dan 600 s/mm^2 (89%). De specificiteit nam toe van 75% tot 84% wanneer b-waarden groter dan 600 s/mm^2 werden toegepast.

De meta-analyse bevestigde ook dat bij hogere b-waarden een tweede, zeer lage, diffusie component kan worden aangetroffen die wordt veroorzaakt door resterend signaal uit vetweefsel. Een andere observatie was dat de ADC evenredig afnam naarmate de maximale b-waarde toenam, in zowel goed- als kwaadaardige tumoren. Dit bevestigt nog eens dat tumor weefsel gekenmerkt wordt door een aanzienlijk aandeel microperfusie. In de resultaten was geen bewijs te vinden dat contrastmiddelen een significant effect hebben op ADC metingen in borst tumoren.

Op dit moment wordt DWI niet breed ingezet om pathologie in de borst aan te tonen omdat de sensitiviteit en specificiteit lager zijn dan dynamisch contrast versterkte (DCE-) MRI. DWI heeft een sensitiviteit tussen de 84 en 91% en een specificiteit tussen 75 en 84%. DCE-MRI heeft echter een sensitiviteit en specificiteit van 100% en 82,5% respectievelijk in het geval van borsttumoren zonder verkalkingen. Om DWI succesvol te implementeren naast DCE-MRI is het nodig dat de sensitiviteit hoog is en de specificiteit wordt geoptimaliseerd. In **hoofdstuk 7** werd een semiautomatische methode geïntroduceerd voor de analyse van borsttumoren. Met deze methode kan een tumor worden geselecteerd door er een omtrek om heen te tekenen. De beeldpunten (voxels) binnen de omtrek werden automatisch geselecteerd en geïncludeerd in de analyse op basis van een optimale fractie die de beste specificiteit opleverde. Het nieuwe aan de aanpak was dat de diffusie, de microperfusie, en hun verhoudingen tegelijk werden geanalyseerd om op die manier de beste specificiteit te verkrijgen. Een groep van 176 patiënten met borsttumoren waarvan de pathologie bekend was, werd verdeeld in een trainingsgroep (24 tumoren, 12 goedaardig) en een testgroep (139 tumoren, 23 goedaardig). De train-

ingsgroep werd gebruikt om de methode te optimaliseren zodanig dat er een maximaal aantal echt negatieven en een minimaal aantal fout negatieven werd behaald. De testgroep werd gebruikt om de methode te valideren door de sensitiviteit en specificiteit te bepalen door drie onafhankelijke gebruikers.

We zagen dat de resultaten tussen de drie gebruikers vergelijkbaar waren. Dit geeft aan dat de methode onafhankelijk is van de ervaring van de gebruikers. Daarnaast zagen we dat IVIM beter presteert dan de ADC. De sensitiviteit en specificiteit van IVIM waren 91,4% en 49,3%, en voor de ADC 95,1% en 17,4% respectievelijk. Dit geeft aan dat het gebruik van de IVIM voordelen oplevert ten opzichte van de ADC. De verhoogde specificiteit van IVIM resulteerde in een lager aantal fout positieven vergeleken met de ADC. Ook specifieke goedaardige borst tumoren zoals fibroadenomen, die moeilijk te beoordelen zijn met DCE-MRI omdat ze er vaak uit zien als kwaadaardige tumoren, werden door IVIM vaker als goedaardige gekenmerkt vergeleken met de ADC.

DCE-MRI heeft de hoogste negatief voorspelende waarde (NPV) vergeleken met andere beeldvormende technieken, en is in staat om betrouwbaar maligniteiten uit te sluiten (NPV > 98%). Echter de aankleuring van goed- en kwaadaardige tumoren kan veel overeenkomsten tonen en is in sommige gevallen lastig om van elkaar te onderscheiden, in het bijzonder voor BI-RADS 3 en 4 tumoren. Voor deze borsttumoren is het vaak onduidelijk of er sprake is van een goedaardige of kwaadaardige tumor wanneer men alleen afgaat op de aankleuringskenmerken na contrast toediening. In de dagelijkse praktijk ondergaat het merendeel van deze patiënten daarom een invasieve procedure, waarbij er wat weefsel wordt afgenomen uit de tumor (een biopt). Voor deze patiënten kunnen kwantitatieve DWI metingen mogelijk uitkomst bieden.

In **hoofdstuk 8** is er gekeken of de diagnose kan worden verbeterd (specificiteit verhogen) door de semiautomatische methode (die is geïntroduceerd in hoofdstuk 7) te implementeren na DCE-MRI en toe te passen voor deze lastige BI-RADS 3 en 4 borsttumoren. In deze studie werden 120 opeenvolgende patiënten opgenomen met 139 borsttumoren en bekende pathologie.

De sensitiviteit en NPV van DCE-MRI was 100% met een specificiteit van 30,4%. DCE-MRI is daarom in staat om betrouwbaar maligniteiten uit te sluiten. De NPV van IVIM was 57,1% met een sensitiviteit en specificiteit van 92,2% en 52,2%, wat te laag is om maligniteiten betrouwbaar uit te sluiten. Dit betekent dan ook dat IVIM geen vervanger is voor DCE-MRI. Echter, wanneer IVIM werd ingezet als aanvulling op DCE-MRI om moeilijke tumoren te beoordelen, dan verhoogde de specificiteit significant van 30,4% naar 56,5%. In het geval van 11 moeilijk te beoordelen goedaardige

tumoren gaf IVIM het juiste uitsluitsel voor 6 tumoren, waar de ADC maar 1 tumor correct als goedaardige identificeerde. Dit geeft aan dat de semiautomatische methode die wordt toegepast voordelen biedt voor de diagnose van borsttumoren. Daarnaast biedt de methode mogelijk kansen om het aantal invasieve procedures (biopten) te reduceren bij patiënten met moeilijk te beoordelen borsttumoren.

In dit proefschrift zijn de voordelen van het IVIM model beschreven, maar er is ook gekeken naar de beperkingen. Hoewel de ADC breed wordt toegepast, negeert deze parameter waardevolle weefselkenmerken die juist wel met IVIM worden blootgelegd. De verwachting is dat IVIM een grote rol kan spelen om op een niet-invasieve manier de diagnose van borst tumoren te verbeteren, hiervoor is echter meer onderzoek noodzakelijk.



Dankwoord

Op 1 november 2006 begon ik de opleiding tot klinisch fysicus in het UMCG. Onderdeel van de opleiding is o.a. het uitvoeren van een wetenschappelijk project, wat mij goed beviel. Naarmate de opleiding vorderde kwam ik steeds vaker in aanraking met onderzoek en schreef mee aan verschillende manuscripten. In de zomer van 2010, met het eind van de opleiding in zicht, realiseerde ik mij dat ik naast het werk als klinisch fysicus ook graag verder zou willen in het onderzoek. Wat volgde was een gesprek met Prof. Oudkerk en Paul Sijens over de mogelijkheden en enkele maanden daarna de start van een promotietraject met als onderwerp “diffusion-weighted imaging”. Vlak daarna werd ik aangesteld als klinisch fysicus bij radiologie.

Nu, bijna 6 jaar later, ligt er een proefschrift dat er zeker niet was gekomen zonder de hulp en motivatie van anderen.

Allereerst wil ik graag mijn promotor, Prof. Oudkerk, bedanken voor het mogelijk maken van dit proefschrift. De vele discussies en gesprekken hebben me laten zien dat een manuscript toch net altijd nog wat beter kan. De kleurige anekdotes die hierbij aan te pas kwamen hebben daar zeker aan bij gedragen.

Ook Paul, mijn co-promotor, wil ik van harte bedanken voor de uitstekende praktische begeleiding. Wanneer ik een manuscript ter revisie naar je opstuurde had ik het vaak de volgende dag al retour met waardevolle correcties. Je stippelde altijd de perfecte publicatiestrategie uit en gaf de manuscripten altijd nog even die extra zet in de goede richting. Wanneer een manuscript daarna toch niet geaccepteerd werd, lag het in ieder geval niet aan ons, maar zeker aan de reviewers.

De leden van de beoordelingscommissie, Prof. dr. G.A.P. Hospers, Prof. dr. J. Stoker en Prof. dr. T. Leiner, bedankt voor het lezen en beoordelen van dit proefschrift.

Marcel, zonder jou was dit proefschrift er ook zeker niet gekomen. Ik zal de reisjes nooit vergeten die we maakten tijdens mijn stage BMT, in het najaar 2006. Met de fantomen achterin de auto reden we naar Münster, of één van die andere steden met een geschikte CT scanner. Nadat je weer het halve rek aan pepermunt had leeggekocht bij de eerste de beste Esso, vroeg je me wat ik na mijn studie zou willen gaan doen, en of ik misschien interesse had om in opleiding te gaan voor klinisch fysicus in de radiologie. Volgens mij heb ik hier slechts enkele dagen over nagedacht, omdat ik op zoek was naar een richting waarbinnen ik mijn opleiding technische natuurkunde maatschappelijk relevant zou kunnen maken. Tijdens de opleiding klinische fysica en ook daarna heb je me, ondanks mijn overstap naar MRI, altijd gestimuleerd om door te gaan met wetenschappelijk onderzoek. Ik hoop nog vele jaren met je samen te kunnen werken binnen de klinische fysica.

Ook mijn collega's van de klinisch fysica, Arjen, Enouschka, Wim, Karolien, Sèvrin, en sinds kort ook Hinke en Jenny; bedankt voor jullie support in al die jaren, en in het bijzonder ook Peter voor het begeleiden en scannen van patiënten en vrijwilligers. Groep MT, Marcel, Hylko, Vincent, Clement, Wim, Gert, bedankt voor de fijne samenwerking en interesse.

Stella, van harte bedankt voor al de adviezen die je hebt gegeven in de loop der jaren, en het accuraat bijhouden van de reguliere discussies met Oudkerk. De G2 kan zich geen betere researchcoördinator wensen.

Ook alle collega's en kamergenoten van G2, toen en nu, teveel om op te noemen, maar ik doe het toch, Gert Jan, Wout, Daiwei, Peter, Wiard, Jonathan, Volkan, Hendrik, Martijn, Petra, Floris, Marjolein, Monique, Paul, Astri, Karolien, Sèvrin, Wiktor, Kadek, Thomas, Pandji, Wisnu, Yingru, Ying, Jaap, Marjolein, Mieneke, Daniël, Jolanda, Jordy, Marleen, Randy, Merel, Marly, Rozemarijn, bedankt voor de "proofreading" en alle gezelligheid tijdens lunch, congressen, borrels, feestjes en ook gewoon op het werk. Voor diegenen die nog gaan promoveren; veel succes met de laatste loodjes!!

Alle coauteurs, veel dank voor de waardevolle bijdragen aan de manuscripten en constructieve samenwerking. In het bijzonder Monique, ik vond het geweldig samen stukken te schrijven en hoop dat we ook in de toekomst hiermee door kunnen gaan.

Marc, we kennen elkaar nu zo'n 10 jaar en ervaar onze vriendschap als zeer waardevol. Je hebt zeker bijgedragen aan dit proefschrift door je aanhoudende interesse in mijn werk. Ook de film avondjes hebben me er zeker doorheen gesleept.

Eelko, het is alweer even geleden, maar je herinnerde me er altijd aan dat er naast werk ook nog een wereld van ontspanning bestaat. De ski-weekenden en natuurlijk de bands waarin we samen hebben gespeeld, zal ik niet snel weer vergeten.

Douwe, Johanna, Willem, Aukje, Ronald, Wies, Leen, Nanny, alle Heeringa's; jullie getoonde interesse in de afgelopen jaren was van grote steun. En Lolke, ik hoop dan nu toch eindelijk tijd te hebben de Pluto's af te maken.

Bedankt voor de foto's Willem!

Waarde paranimfen, Wout en Gert Jan, met jullie aan mijn zijde ga ik de verdediging met vertrouwen tegemoet. Bedankt voor de organisatie van de laatste dingen de afgelopen weken. Heel veel succes met de afronding van jullie eigen proefschrift!!

Families Dijkstra, Lautenbag, De Jonge, Bootsma, Ribôt, Van der Werff, bedankt voor jullie interesse tijdens de talrijke gezellige familiedagen, weekenden, verjaardagen en feestjes. Ook de skiweekenden met de "koude kant" wisten mijn aandacht positief van het werk te onttrekken.

Mijn ouders wil ik graag bedanken voor hun onbeperkte inzet om mij en mijn broertjes te ondersteunen bij alles wat we ondernemen. Jullie raad en adviezen zijn voor mij altijd van grote waarde geweest. Hoewel wij als Friezen het motto "doch mar gewoan, dan doche jo wol gek genôch" een warm hart toedragen, wisten jullie toch het beste in mij naar boven te halen. Freerk, Annemarie, Durk en Eci en Chris, bedankt voor alle interesse en gezelligheid!

Tenslotte, Gonda, zonder jou had ik het waarschijnlijk al lang opgegeven. Je wist me altijd weer te motiveren met lieve kaartjes en verrassingsweekendjes als een manuscript voor de zoveelste keer met de kerende post terug kwam. Bedankt voor je geduld en steun als ik weer eens de hele avond aan research zat te werken, terwijl Kirsten beneden de papieren uit de kast trok, of een viltstift omgekeerd in de mond had. Ik zie erg uit naar onze volgende kruimel :) Ik hou van jullie.



Bibliography

Publications in peer reviewed journals

1. Quantitative DWI implemented after DCE-MRI yields increased specificity for BI-RADS 3 and 4 breast lesions. *J Magn Reson Imaging* 2016. Dijkstra H, Dorrius MD, Wielema M, Pijnappel RM, Oudkerk M, Sijens PE.
2. Semi-automated quantitative intravoxel incoherent motion analysis and its implementation in breast diffusion-weighted imaging. *J Magn Reson Imaging* 2016. *May*;43(5):1122-31. Dijkstra H, Dorrius MD, Wielema M, Jaspers K, Pijnappel RM, Oudkerk M, Sijens PE.
3. Quantitative myocardial perfusion with dynamic contrast-enhanced imaging in MRI and CT: theoretical models and current implementation. *BioMed Res Int* 2016. Pelgrim GJ, Handayani A, Dijkstra H, Prakken N, Slart HJA, Oudkerk M, van Ooijen PMA, Vliegenthart R, Sijens PE.
4. Contrast-optimized composite image derived from multigradient echo cardiac magnetic resonance imaging improves reproducibility of myocardial contours and T2* measurement. *MAGMA*. 2016 Feb;29(1):17-27. Triadyaksa P, Handayani A, Dijkstra H, Aryanto KY, Pelgrim GJ, Xie X, Willems TP, Prakken NH, Oudkerk M, Sijens PE.
5. The Fontan circulation and the liver: A magnetic resonance diffusion-weighted imaging study. *Int J Cardiol*. 2015 Sep 28;202:595-600. Wolff D, van Melle JP, Dijkstra H, Bartelds B, Willems TP, Hillege H, van den Berg AP, Ebels T, Sijens PE, Berger RM.
6. Intermodel agreement of myocardial blood flow estimation from stress-rest myocardial perfusion magnetic resonance imaging in patients with coronary artery

- disease. *Invest Radiol.* 2015 Apr;50(4):275-82. Handayani A, Triadyaksa P, Dijkstra H, Pelgrim GJ, van Ooijen PM, Prakken NH, Schoepf UJ, Oudkerk M, Vliegenthart R, Sijens PE.
7. Effect of b-value and pre-admission of contrast on diagnostic accuracy of 1.5T breast DWI: a systematic review and meta-analysis. *Eur Radiol.* 2014 Nov;24(11):2835-47. Dorrius MD, Dijkstra H, Oudkerk M, Sijens PE.
 8. The Cumulative Risk of Multiple CT Exposures Using Two Different Methods. *Health Phys.* 2014 Apr;106(4):475-83. Dijkstra H, Groen JM, Bongaerts FA, van der Jagt EJ, de Bock TG, Greuter MJ.
 9. Clinical implications of non-steatotic hepatic fat fractions on quantitative diffusion-weighted imaging of the liver. *PLoS One.* 2014 Feb 4;9(2):e87926. Dijkstra H, Handayani A, Kappert P, Oudkerk M, Sijens PE.
 10. Quantitative and qualitative assessment of structural magnetic resonance imaging data in a two-center study. *BMC Med Imaging.* 2012 Aug 6;12:27. Chalavi S, Simmons A, Dijkstra H, Barker GJ, Reinders AA.
 11. Effects of microperfusion in hepatic diffusion weighted imaging. *Eur Radiol.* 2012 Apr;22(4):891-9. Dijkstra H, Baron P, Kappert P, Oudkerk M, Sijens PE.
 12. A model for quantitative correction of coronary calcium scores on multidetector, dual source, and electron beam computed tomography for influences of linear motion, calcification density, and temporal resolution: a cardiac phantom study. *Med Phys.* 2009 Nov;36(11):5079-88. Greuter MJ, Groen JM, Nicolai LJ, Dijkstra H, Oudkerk M.
 13. Coronary calcium mass scores measured by identical 64-slice MDCT scanners are comparable: a cardiac phantom study. *Int. J. Cardiovasc Imaging* 2009. Dijkstra H, Greuter MJW, Groen JM, Vliegenthart-Proença R, Renema WKJ, de Lange F, Oudkerk M.
 14. Threshold adjusted calcium scoring using CT is less susceptible to cardiac motion and more accurate. *Med Phys.* 2009 Feb;36(2):438-46. Groen JM, Dijkstra H, Greuter MJW, Oudkerk M.
 15. 64 slice MDCT generally underestimates coronary calcium scores as compared to EBT: a phantom study. *Med Phys.* 2007 Sep;34(9):3510-9. Greuter MJW, Dijkstra H, Groen JM, Vliegenthart R, de Lange F, Renema WKJ, de Bock GH, Oudkerk M.

Oral presentations (as presenter)

1. *European Congress of Radiology, Vienna, 2016.* Inter-observer agreement of semi-automated quantitative lesion analysis in breast diffusion-weighted imaging. Dijkstra H, Dorrius MD, Wielema M, Jaspers K, Pijnappel RM, Oudkerk M, Sijens PE.

2. *Radiologendagen, 's Hertogenbosch, 2015 (invited lecture)*. Veilige implementatie van een nieuwe modaliteit. Dijkstra H.
3. *European Congress of Radiology, Vienna, 2015*. Breast lesion differentiation by 3-parameter IVIM analysis. Dijkstra H, Dorrius MD, Wielema M, Oudkerk M, Sijens PE.
4. *European Congress of Radiology, Vienna, 2013*. Clinical implications of fatty liver on hepatic diffusion-weighted imaging studied in healthy subjects. Dijkstra H, Handayani A, Kappert P, Oudkerk M, Sijens PE.
5. *Radiological Society of North America 98th Annual Meeting, Chicago, 2012*. Gd-EOB-DTPA affects hepatic diffusion weighted imaging (DWI). Dijkstra H, Oudkerk M, Handayani A, Kappert P, Sijens PE.
6. *Radiological Society of North America 98th Annual Meeting, Chicago, 2012*. Comparison of the fast diffusion component in intravoxel incoherent motion (IVIM) modeled hepatic diffusion-weighted imaging (DWI) and perfusion MRI. Dijkstra H, Oudkerk M, Handayani A, Kappert P, Sijens PE.
7. *European Congress of Radiology, Vienna, 2012*. Effects of Gd-EOB-DTPA on hepatic diffusion weighted imaging (DWI) based on the mono- and bi-exponential model. Dijkstra H, Oudkerk M, Kappert P, Sijens PE.
8. *Radiological Society of North America 97th Annual Meeting, Chicago, 2011*. The Role of Perfusion Artifacts in Hepatic Diffusion-weighted Imaging: The Requirement of a Multi-exponential Approach. Dijkstra H, Baron P, Kappert P, Oudkerk M, Sijens PE.
9. *International Radiation Protection Association, Helsinki, 2010*. Radiation-induced cancer risk from recurrent CT scanning. Dijkstra H, Groen JM, Bongaerts AHH, van der Jagt EJ, Greuter MJW.
10. *European Congress of Radiology, Vienna, 2010*. Apparent Diffusion Coefficient of Normal Liver Tissue Depends on Measurement Location. Dijkstra H, Kele P, Dorrius MD, Kappert P, Baron P, Oudkerk M, Sijens PE.
11. *Nederlandse Vereniging voor Stralingshygiëne, Scheveningen, 2010*. Radiation-induced cancer risk from recurrent CT scanning. Dijkstra H, Groen JM, Bongaerts AHH, van der Jagt EJ, Greuter MJW.
12. *Radiological Society of North America 94th Annual Meeting, Chicago, 2008*. Quality parameters measured on four mammography systems: NPS, MTF and DQE. Dijkstra H, Greuter MJW, Visser R, van Engen R, Oudkerk M.
13. *European Society of Cardiac Radiology, Rome, 2008*. Coronary calcium mass score determination on 64-MDCT systems as compared to the physical calcium mass value. Dijkstra H, Greuter MJW, Vliegthart R, Oudkerk M.



Curriculum Vitae

Hildebrand Dijkstra werd op 12 maart 1983 geboren te Smallerland, en groeide op in het kleine Friese dorp Sumar. Na twee jaar middelbare school in Burgum, vervolgde hij zijn opleiding in Drachten op het CSG Liudger, locatie De Raai, waar hij zijn VWO diploma behaalde in 2001. Aansluitend begon hij de studie Technische Natuurkunde aan de Rijksuniversiteit Groningen, na drie jaar aangevuld met de specialisatie Biomedische Technologie. Op 30 september 2006 slaagde hij voor het doctoraal examen. In datzelfde jaar behaalde hij ook het Stralingsdeskundigheids niveau 3.

Op 1 november 2006 begon hij als klinisch fysicus in opleiding bij de afdeling radiologie van het Universitair Medisch Centrum Groningen (UMCG). Na verschillende projecten en stages bij o.a. de Isala Klinieken en het Landelijk Referentiecentrum voor Bevolkingsonderzoek (LRCB) ronde hij vier jaar later de opleiding met succes af.

Aansluitend werd hij in februari 2011 aangenomen als klinisch fysicus bij het UMCG. In deeltijd startte hij tevens een promotietraject met als hoofdonderwerp “diffusion-weighted imaging”. In 2012 verscheen de eerste publicatie in het internationale tijdschrift *European Radiology*. Het werk beschreven in dit proefschrift heeft hij gepresenteerd op verschillende nationale en internationale congressen zoals het European Congress of Radiology (ECR), in Wenen, en de Radiological Society of North America (RSNA), in Chicago.

Op dit moment is hij aangesteld als klinisch fysicus in het UMCG en zal vanuit deze functie ook betrokken blijven bij uitvoer en ondersteuning van toekomstig wetenschappelijk onderzoek.

